Hydrothermal geochemistry: what can we learn from autoclaves and photons?

Denis Testemale

To cite this version:

Denis Testemale. Hydrothermal geochemistry: what can we learn from autoclaves and photons?. Geochemistry. Université Grenoble Alpes, 2020. tel-04482439

UGA
Université
Grenoble Alpes

Habilitation à diriger des recherches
Ecole doctorale Terre Univers Environnement (TUE)

Hydrothermal geochemistry : what can we learn from autoclaves and photons ?

Présentée par

Denis TESTEMALE

Institut Néel – CNRS

HDR soutenue publiquement **le 29 septembre 2020**
devant le jury composé de :

Mme Carmen SANCHEZ-VALLE (Rapporteur)
Mr Laurent TRUCHE (Rapporteur)
Mr Max WILKE (Rapporteur)
Mr Fabrice BRUNET (Président)
Mr Gleb POKROVSKI (Membre)

Hydrothermal geochemistry: what can we learn with autoclaves and photons?

Contents

Contents **2**

Introduction **4**

1 X-ray Absorption Spectroscopy to explore metal transport in hydrothermal fluids. And the case of iron. **6**
1.1 Speciation and solubility by XAS - Introduction . . . 6
1.2 Speciation and solubility by XAS - Methods and examples . . . 7
1.2.1 Iron(II) at hydrothermal conditions. . . . 8
1.2.2 Iron(III) at hydrothermal conditions. . . . 41
1.3 The contribution of XANES in hydrothermal geochemistry . . . 49
1.4 15 years of using autoclaves at FAME: the progress of knowledge in hydrothermal metal transport. . . . 51
1.4.1 Methodological advances . . . 52
1.4.2 Scientific advances . . . 52
1.4.3 The autoclave equipment installed at FAME beamlines . . . 89

2 High-pressure and high-temperature technological developments. **91**
2.1 Context . . . 91
2.2 The Néel autoclave . . . 106
2.2.1 Introduction, general principles . . . 106
2.2.2 Design and usage highlights . . . 112
2.2.3 Autoclave MarkII . . . 113
2.3 Autoclave collaborations . . . 115
2.3.1 Generation of organic compounds in hydrothermal fluids . . . 115
2.3.2 Microbial redox transformation of metals under subsurface pressure and temperature conditions . . . 116
2.3.3 Solvothermal synthesis of size-controlled single-nanocrystals and *in situ* monitoring . . . 118
2.3.4 Technology transfer . . . 118

3 Beamline scientist **120**
3.1 User support . . . 120
3.2 Outreach and teaching . . . 120
3.3 XAS database . . . 121
3.4 Pivotal role . . . 122

4 Perspectives **124**
4.1 Hydrothermal transport of metals . . . 125
4.1.1 X-ray absorption spectroscopies . . . 125
4.1.2 Raman spectroscopy . . . 125
4.2 Physical-chemistry of supercritical fluids . . . 126
4.2.1 Supercritical water: short and medium scale structure . . . 126
4.2.2 $H_2O - CO_2$ hydrothermal solvents . . . 128
4.2.3 Supercritical solvents and Small Organic Molecules (SOM) . . . 130

Remerciements **131**

Bibliography **132**

Introduction

This manuscript finally came to life. After 20 years of studying hydrothermal fluids by *in situ* spectroscopy, it was about time to look back and summarize the main outcomes, both the successful ones and the less so.

The attraction for the physical sciences led me to the *Ecole Nationale Supérieure de Physique de Grenoble* (1997-2000): the diversity of its teaching and the fundamental colouring of a large part of its courses convinced me of this choice. One of the peculiarities of my curriculum is that I trained as a physicist engineer and nowadays I carry out my research mainly in the field of earth sciences. The transition between the two corresponds to the period of master and PhD thesis (2000-2003) carried out at the *Laboratoire de Cristallographie* (Joseph Fourier University and CNRS, Grenoble, France) during which I specialized in the study of hydrothermal fluids (a theme precisely at the interface of physics, chemistry and earth sciences) and in instrumental development. I joined the *'Supercritical Fluids'* team of Jean Louis Hazemann. There the research topics were the structural characterization of fluids (especially aqueous solutions) in supercritical conditions, using synchrotron X-ray spectroscopy techniques. During these first three years, we studied As and U solvation structures in supercritical aqueous solutions, and extended the research to the study of the solvent H_2O itself, using small-angle and inelastic X-ray scattering methods. During this period, an important work was to develop an innovative autoclave, dedicated to the *in situ* study of aqueous solutions in high temperature and pressure conditions (up to 600°C and 2000 bar). Our objective was to study 'synthetic' solutions, i.e., samples which composition is controled and are not natural, and to avoid the use of existing high-pressure technological solutions (hydrothermal diamond anvil cell, Paris-Edinburgh cell) that are not optimized for the range of pressure investigated. Another objective was to adapt the device to the different measurement techniques envisaged (spectroscopy, diffusion, Raman, etc.). The large proportion of time and energy given to this technological development clearly matched my engineering background. This is actually still the case to this day. This PhD work was rewarded by the 2004 Haüy-Lacroix prize of the Société Française de Minéralogie et Cristallographie, and the J. M. Besson 2004 prize from the French high-pressure network.

My first post-doctoral position was at ESRF, as a scientist on the Swiss-Norwegian beamline. I was in charge of user support on the X-ray absorption and high-resolution powder diffraction instruments. As far as my research was concerned, I worked in continuity of my PhD by deepening the studies I had initiated (metal speciation in hydrothermal conditions, structure of supercritical water). It is also during this period that I started collaborations with earth science laboratories (such as IMPMC, Paris, on the dissolution of iron minerals, solubility and kinetics). My second post-doctoral contract was at the South Australian Museum in Adelaide, Australia, on a fellowship I obtained from the Australian Research Council (ARC Linkage Fellowship). I joined the 'Metals and Solutions' team of Pr. J. Brugger. There my research project was the study of iron (II) and copper (I) speciation using XAS data and *ab initio* calculations of XANES spectra. I also helped them to finalize a high-pressure experimental cell for UV-Vis measurements.

I was recruited at CNRS (section 18, "Earth and the Terrestrial Planets: structure, history and models") in 2007 at Néel Institute, back in the 'Supercritical Fluids' team. The project was in the continuity of my research topics and consisted in developing our methods to study metal speciation in hydrothermal conditions, based on X-ray absorption data obtained at FAME beamline. A related objective was to make this tool available to the entire earth science community in France and internationally. Finally, another mission of this CNRS position was to provide user support at FAME beamline.

The core of my research activity is the study of metal transport in hydrothermal fluids. It is oriented along several complementary axes:

(i) study of the speciation of dissolved metals; fluid/rock interaction and study of the solubility of minerals;

(ii) physical chemistry of hydrothermal fluids, in particular the structure of hydrothermal solvents;

(iii) establishing the methods used for these studies, mainly based on Raman and X-ray absorption spectroscopy techniques, and the use of high-pressure high-temperature (HP-HT) experimental cells specifically developed for these *in situ* measurements;

(iv) beamline scientist activity at FAME and FAME-UHD beamlines.

For clarity and brevity reasons in this manuscript I chose to present only a portion of my results, related to **(i)** (chapter 1, in particular the scientific case of iron), **(iii)** (the methods are explained in chapter 1 and the HP tools in chapter 2), and some aspects of my beamline activity **(iv)** that I find important (chapter 3). I decided to treat **(ii)** differently, without a dedicated chapter, but I deal with this aspect of my research in the perspectives (chapter 4) where I included some related results.

Regarding the form of this manuscript, I integrated several (5) published manuscripts in the text. I'm aware that this can be a rather indigestible form of presentation; in consequence, for each of them I highlighted the key elements both in the text and as a summary. Also, I wanted to make each chapter quite self-consistent: for this reason some ideas are sometimes briefly reiterated in different chapters.

Chapter 1

X-ray Absorption Spectroscopy to explore metal transport in hydrothermal fluids. And the case of iron.

In this chapter we'll describe the methodology and analytical tools we developed in the last 15 years, and which constitute an **integrated micro-batch reactor setup**, particularly suited (and successful) for the study of **metal transport in hydrothermal fluids**. The scientific case that will underpin this description is the fate of iron at hydrothermal conditions.

1.1 Speciation and solubility by XAS - Introduction

In order to explore the mechanisms of metal transport in hydrothermal solutions, one needs:

- techniques to have access to the speciation and the concentration of the dissolved metals. Indeed, with these data available and measurable, it is possible to monitor the complexation of metals by the ligands in solution and/or dissolution/precipitation of minerals. X-ray Absorption Spectroscopy is one of the most (if not the most) powerful tool to derive local structure + redox (i.e. speciation) and density information of a sample. I recommend the reference by Kelly et al. (1) as a general but very comprehensive and clear source of information on that topic. Within this manuscript we'll focus on the methods that we set for this purpose, and the specificities of dealing with aqueous solutions and solubility experiments;
- techniques to conduct these measurements *in situ* at hydrothermal conditions. Indeed, when the speciation and concentration data are obtained at hydrothermal conditions, they make geochemical models more robust, instead of having to rely on extrapolated data from low temperature and pressure measurements. Autoclaves are invaluable tools to perform such challenging measurements and target with precision the desired pressures and temperatures. In addition XAS is particularly suited for that type of *in situ* measurements. The technological details about the development of our autoclaves are presented in chapter 2.

The methodology of using XAS to derive speciation and solubility data of metals in fluids is schematized in figure 1.1. It is based on the measurement of XAS spectra in transmission and/or fluorescence mode. In summary:

Transmission mode: With appropriate detectors, the intensity of photons before and after the sample are measured. From these numbers, the absorption coefficient μ is calculated. μ varies with the energy E of the incident photos, and the offset of μ over the absorption edge (of the element/metal that is being measured) is a function of the density of this element/metal. As a consequence, its concentration can then be calculated in an absolute manner. Furthermore, the transmitted spectra also allow an EXAFS (and XANES) analysis from which the local structure and redox are derived. So both the concentration/solubility and the speciation of the dissolved metals can be determined.

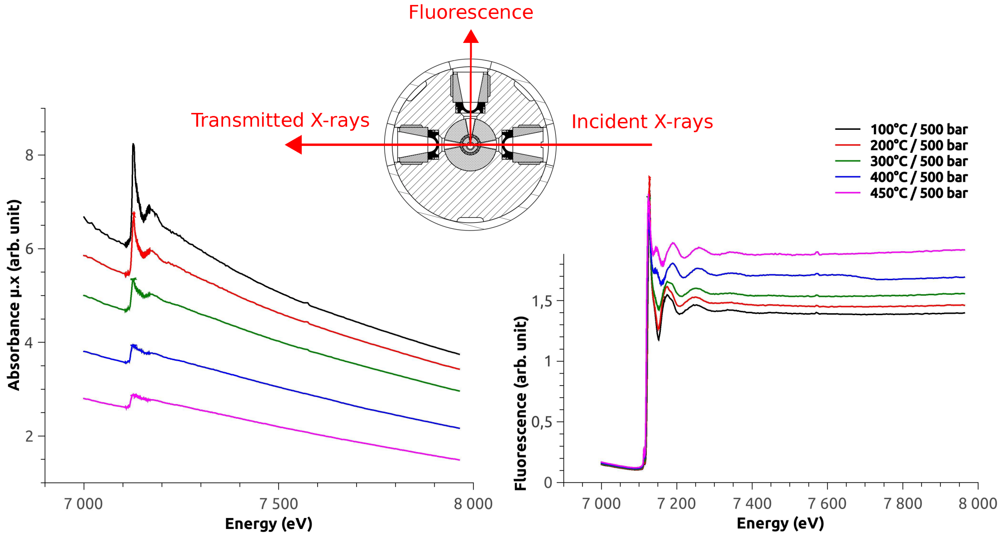

Figure 1.1: Schematic abstract of the methodology used with the autoclave setup: both transmission (left) and fluorescence (right) spectra can be collected simultaneously. This is possible thanks to the geometry of the autoclave with 3 dedicated windows (top). This graph is from the reference (2) (see section 2.1, page 91).

Fluorescence mode: In some experimental circumstances the transmitted signal may not be measureable (typically when the metal concentrations are too low, or the photons cannot cross the sample because of the sample environment), and one has to turn to fluorescence measurements. The fluorescence signal is typically measured at 90° of the incident beam. Fluorescence XAS measurements are ideally suited for very diluted samples, with much better signal-to-noise (S/N) than with transmission (see the striking difference of S/N in figure 1.1), and make possible the determination of the low concentration metal speciation. But, on the other hand, the determination of its solubility is not as straightforward as in the case of transmission, since the fluorescence intensity is only proportional to the absorption coefficient µ: as a consequence deriving its value, and then the metal concentration, entails painstaking and careful experimental work and the use of calibrants. This is clearly a drawback of the method, and the use of transmission signal shall be favored if possible (but that can become an experimental challenge in itself).

The first studies of our research group using a similar methodology in our autoclaves were conducted 20 years ago (3, 4). At the same period, during the year 2000 (start of my PhD), Gleb Pokrovski started his collaboration with us to make use of our tools for applications in geochemistry (5, 6): the momentum was established and the numbers of experiments has been growing ever since. In the rest of this chapter the results of our studies about the fate of Fe^{II} and Fe^{III} are presented. Why iron? As stated in the introduction of one of our iron paper (7): *Iron is a ubiquitous element in the Earth's crust, as well as one of the most critical elements in engineered hydrothermal systems (e.g., corrosion in mineral processing, deep injection and production wells, and power plants). Iron(III) chlorocomplexes are important under near-surface saline conditions (e.g., (8), and references therein), whereas Fe(II) chlorocomplexes are the predominant form of Fe in chloride-bearing hydrothermal aqueous solutions which are typical of crustal fluids (e.g., (9)). Despite this, the speciation and its effect on the transport of Fe (II) in hydrothermal aqueous solutions are not well understood.*

1.2 Speciation and solubility by XAS - Methods and examples

In this section I present results about iron(II) (published results) and iron(III) (unpublished data), respectively in section 1.2.1 and section 1.2.2.

1.2.1 Iron(II) at hydrothermal conditions.

Collaborations:

- *Local: Néel Institute (Y. Joly) + FAME staff*
- *Adelaide and Melbourne University (J. Brugger, B. Etschmann), CSIRO Melbourne (W. Liu, L. Mei)*
- *IMPMC and IPGP (F. Guyot, I. Martinez, D. Daval)*

The studies devoted to iron transport in hydrothermal fluids were initiated in 2005 along two directions: the speciation of Fe^{II} chloride complexes (in collaboration with J. Brugger at Adelaide University) (7), the dissolution of Fe^{II} carbonates and silicates in the context of mineral CO_2 sequestration (in collaboration with F. Guyot and I. Martinez at IMPMC and IPG, Paris) (10, 11). Two resulting publications were included in this manuscript, excluding the one dedicated to the solubility of siderite (10): the reasons are that in the context of this manuscript, these publications also serve as an example of all the methodological tools developed during the last 15 years, and it appears that the work devoted to fayalite and siderite are very similar, but the former is a more integrated study and may have more pedagogical value.

1.2.1.1 In-situ X-ray absorption study of Iron(II) speciation in brines up to supercritical conditions

Key ideas of the publication:

- XAS measurements were used to determine the speciation of Fe^{II} at hydrothermal conditions, and more particularly at high temperature and/or high salinity where previous solubility and spectroscopic results differed. Our results show that in these conditions **the tetrahedral species $FeCl_4^{2-}$ is predominant**, and must be taken into account to model Fe^{II} geochemistry. See figure 10 (of the publication) for a graphical summary of the thermodynamical analysis and the predominance of iron species.
- The set of samples was composed of several solutions containing Fe^{II} at different chloride concentrations (0.5-12 m), and for each one XANES spectra were collected at constant pressure (500 bar) and varying temperature (25-450°C). This set of XANES spectra was analysed through a Principal Component Analysis (PCA)-based method (developed by J. Brugger (12)) to derive **the number of individual iron species, their nature and their formation constants**. The thermodynamical data allowed to model iron solubility, which compared favourably with existing experimental data: see figure 12 (of the publication).
- In parallel, EXAFS spectra were collected for the 2 end-members (i.e. conditions where only one iron species is expected to be predominant): low T/low salinity, and high T/high salinity. These data could then be analyzed by classical EXAFS, and XANES *ab initio* calculations to confirm the presence of the **tetrahedral species** $FeCl_4^{2-}$.

Chemical Geology 264 (2009) 295–310

Contents lists available at ScienceDirect

Chemical Geology

journal homepage: www.elsevier.com/locate/chemgeo

In-situ X-ray absorption study of Iron(II) speciation in brines up to supercritical conditions

Denis Testemale [a,b,*], Joël Brugger [a,c], Weihua Liu [d], Barbara Etschmann [d], Jean-Louis Hazemann [b]

[a] School of Earth and Environmental Sciences, University of Adelaide, Adelaide, SA 5005, Australia
[b] Institut Néel, Département MCMF, CNRS-Grenoble, 25 Avenue des Martyrs, BP166 38042 Grenoble Cedex 09, France
[c] South Australian Museum, North Terrace, Adelaide, SA 5000, Australia
[d] CSIRO Exploration and Mining, School of Geosciences, Monash University, Clayton, Vic 3800, Australia

ARTICLE INFO

Article history:
Received 29 September 2008
Received in revised form 9 March 2009
Accepted 10 March 2009

Editor: J. Fein

Keywords:
X-ray absorption spectroscopy
Iron-chloride complexes
Thermodynamic properties
XANES
Hydrothermal conditions

ABSTRACT

X-ray absorption spectroscopy (XAS) measurements were used to determine the coordination structure and to derive the speciation of aqueous ferrous chloride complexes in acidic chloride brines over a wide range of conditions (25–450 °C, 500 bar, 0.5–12 m chloride molality), covering the range from sedimentary brines to magmatic hydrothermal fluids. EXAFS analysis coupled with *ab initio* free potential XANES calculations confirmed the octahedral geometry of the different Fe chlorocomplexes at low temperature (<200 °C) and low (<1 m) chloride concentration ($[FeCl_x(H_2O)_{6-x}]^{2-x}$, $x=0$–2), and attest the stability of a high-order tetrahedral Fe(II)-chloride complex at high-temperature (>300 °C) and high (>2 m) chloride molality ($[FeCl_y]^{2-y}$; $y=4$ or $y=3$; Fe–Cl distance $=2.31\pm0.01$ Å). These spectroscopic results contrast with the interpretation of most recent high-temperature studies of Fe(II) speciation in brines, which assumed that $[FeCl_2]^0$ is the predominant species in brines at high temperature. A reinterpretation of the experimental Fe solubilities measured by Fein et al. [Fein, J.B., Hemley, J.J., D'Angelo, W.M., Komninou, A., Sverjensky, D.A., 1992. Experimental study of iron-chloride complexing in hydrothermal fluids. Geochim. Cosmochim. Acta 56, 3179–3190.] for the magnetite–pyrite–pyrrhotite–quartz–muscovite–K-feldspar assemblage in KCl solutions at 300 °C/500 bar and 400 °C/500 bar shows that these solubility data can be explained using the high-order $[FeCl_4]^{2-}$ complex. This study illustrates the complementarity between solubility and spectroscopic studies, and provides further evidence of the importance of high-order chlorocomplexes for the transport of transition metals (e.g., Zn, Ni) in high-temperature and/or supercritical fluids.

1. Introduction

The ability to model accurately the transport of metals by aqueous fluids over wide ranges of pressure, temperature, fluid composition and fluid density is essential to predict and control hydrothermal processes such as the formation of ore deposits in the Earth's crust, scale deposition in pipes used for geothermal energy production and deep-aquifer CO_2 geosequestration, hydrothermal ore processing, aquifers waste contamination, and hydrothermal corrosion in power plants. Essential knowledge underpinning this modelling are the speciation of each relevant chemical element transported in the fluid and the thermodynamic properties for each of the species involved i.e. minerals, aqueous complexes, gases, as well as melts in hydrothermal systems (e.g., Heinrich et al., 1996; Seward and Barnes, 1997; Anderson, 2005; Tooth et al., 2009). The nature and thermodynamic properties of the aqueous complexes of many geochemically and industrially valuable elements are well constrained experimentally at ambient conditions, but fewer experimental studies have been conducted under hydrothermal conditions, especially near and beyond the critical point of water (see e.g. Table 1 for Fe(II) chlorocomplexes). This stems from the difficulties inherent in conducting solubility, spectroscopic or electrochemical experiments at high temperature, pressure, and/or salinity. As a result, many properties for important aqueous complexes under hydrothermal conditions have been obtained via empirical and semi-empirical extrapolation methods (e.g., Anderson et al., 1991; Johnson et al., 1992; Gu et al., 1994; Sverjensky et al., 1997). High quality experimental studies are required in order to test and improve extrapolation techniques, and to extend our understanding of "frontier" conditions such as high salinity, near supercritical, or volatile-rich, low density fluids, for which no well established extrapolation technique is available.

Recent advances in high-temperature/pressure technology combined with the development of synchrotron sources and related analysis techniques have improved considerably our knowledge about metal complexation in hydrothermal environments (e.g., review by Seward and Driesner, 2004). X-ray absorption spectroscopic (XAS) techniques are particularly suitable for determining metal speciation in those demanding experimental environments (e.g., Seward et al.,

---

* Corresponding author. Institut Néel, Département MCMF, CNRS-Grenoble, 25 Avenue des Martyrs, BP166 38042 Grenoble Cedex 09, France.
E-mail address: denis.testemale@grenoble.cnrs.fr (D. Testemale).

0009-2541/$ – see front matter © 2009 Elsevier B.V. All rights reserved.
doi:10.1016/j.chemgeo.2009.03.014

Table 1
Previous work on Fe(II) speciation in chloride brines under hydrothermal conditions.

Study	*T*, *P* and salinity range	Species identified or postulated
Solubility		
Chou and Eugster (1977)	500–650 °C, 2 kbar, $Cl \leq 5.0$ m (as $FeCl_2$)	$FeCl_{2(aq)}$
Crerar et al. (1978)	200–350 °C, P_{sat}, $Cl \leq 5.0$ m	Fe^{2+}, $FeCl^+$, $FeCl_2(aq)$
Boctor et al. (1980)	400–600 °C, 1–2 kbar, $Cl \leq 0.15$ m	$FeCl_2(aq)$
Wood et al. (1987)	200–350 °C, P_{sat}, $Cl \leq 5.0$ m, CO_2 partial pressure 0.69–172 bar	$FeCl^+$, $FeCl_2(aq)$
Ding and Seyfried (1992)	200–450 °C, 0.3–0.5 kbar, $Cl \leq 1.24$ m	$FeCl_{2(aq)}$
Fein et al. (1992)	300–600 °C, 0.5–2.0 kbar, $Cl \leq 2.0$ m	$FeCl_2(aq)$, $FeCl^+$ (minor)
Ohmoto et al. (1994)	250–350C, P_{sat}, $Cl \leq 4.0$ m	$FeCl^+$, $FeCl_2(aq)$
Potentiometry		
Palmer and Hyde (1993)	125–295 °C, P_{sat}, $Cl \leq 0.97$ m	$FeCl^+$
UV–Vis spectrophotometry		
Koplitz et al. (1987)	25–82 °C, $Cl \leq 11$ m	Fe^{2+}, $FeCl^+$, $FeCl_2(aq)$, $FeCl_3^-$, $FeCl_4^{2-}$
Heinrich and Seward (1990)	25–200 °C, P_{sat}, $Cl \leq 3.4$ m	Fe^{2+}, $FeCl^+$, $FeCl_2(aq)$
Zhao and Pan (2001)	10–100 °C, P_{sat}, $Cl \leq 6$ m	Fe^{2+}, $FeCl^+$, $FeCl_2(aq)$, $FeCl_4^{2-}$
XAS spectroscopy		
Liu et al. (2007)	25–150 °C, P_{sat}, $Cl \leq 16$ m	Fe^{2+}, $FeCl^+$, $FeCl_2(aq)$, $FeCl_4^{2-}$

1996; Bassett et al., 2000; Hoffmann et al., 2000; Testemale et al., 2005a). The penetrative nature of X-rays enables collection of information *in-situ* at high pressures and temperatures, while the chemical, local and electronic sensitivities of XAS allow the determination of the geometrical features of the metal complexes existing in solution, together with electronic information such as the oxidation state. In addition, recent studies show that the thermodynamic properties of these complexes can be derived from XAS measurements. Inada and Funahashi (1999) used Extended X-ray Absorption Fine Structure (EXAFS) to study chlorocomplexation of iron(III), Pokrovski et al. (2006) combined EXAFS and solubility measurements to determine the structure and stability of antimony complexes in NaCl–HCl–H_2O hydrothermal solutions, and Brugger et al. (2007) and Liu et al. (2007) demonstrated how both the formation constants and the structure of metal complexes can be obtained from X-ray Absorption Near Edge Structure (XANES) data.

Iron is a ubiquitous element in the Earth's crust, as well as one of the most critical elements in engineered hydrothermal systems (e.g., corrosion in mineral processing, deep injection and production wells, and power plants; e.g., Kritzer et al., 1999). Iron(III) chlorocomplexes are important under near-surface saline conditions (e.g., Liu et al., 2006, and references therein), whereas Fe(II) chlorocomplexes are the predominant form of Fe in chloride-bearing hydrothermal aqueous solutions which are typical of crustal fluids (e.g., Heinrich and Seward, 1990). Despite this, the speciation and its effect on the transport of Fe (II) in hydrothermal aqueous solutions are not well understood. The available knowledge on iron(II) chlorocomplexes in hydrothermal acidic Cl-rich aqueous solutions is summarised in Table 1.

There exists a discrepancy between spectroscopic studies and solubility and potentiometric studies regarding the nature of Fe(II) chlorocomplexes at high salinity and high temperature (Table 1): while the latter consider $FeCl_2(aq)$ as the limiting species, spectroscopic studies emphasise the importance of higher order chlorocomplexes. For example, Liu et al. (2007) concluded on the basis of XANES spectroscopy that the stability of the tetrahedral $FeCl_4^{2-}$ complex increases relative to that of the lower order octahedral chlorocomplexes $[FeCl_x(H_2O)_{6-x}]^{2-x}$ (with $x = 0, 1, 2$) as either temperature (25 °C to 150 °C) and/or Cl^- concentrations increase. This result is consistent with the spectrophotometric study of Zhao and Pan (2001). The same trend was observed by Hoffmann et al. (1999) in the case of a transition from octahedral $Ni(H_2O)_6^{2+}$ to tetrahedral $NiCl_4^{2-}$, and studies of zinc in natural fluid inclusions and in synthetic systems to 500 °C also support the stability of the high-order complex $ZnCl_4^{2-}$ up to supercritical conditions (Mayanovic et al., 1997; Anderson et al., 1998; Mayanovic et al., 1999; Mibe et al., 2009). However, the stability at high temperatures of such high-order complexes is surprising: the corresponding low permittivity conditions should favour neutral or weakly charged species (e.g., Crerar et al., 1985; Susak and Crerar, 1985) such as $FeCl_2(H_2O)_{x(aq)}$ (where $x = 2$ or 4). Indeed, the results of all available high *P*–*T* solubility experiments seem to support a lower chloride coordination for Fe(II) in supercritical solutions (e.g., Ding and Seyfried, 1992; Fein et al., 1992; Ohmoto et al., 1994; see Table 1).

This study attempts to resolve this discrepancy by characterising the stoichiometry, structure and geometry of Fe(II) chloride complexes using both EXAFS and XANES techniques. While current iron spectroscopic data are limited to ≤200 °C, this paper extends this range to temperatures and pressures relevant for magmatic hydrothermal conditions (up to 450 °C and 500 bars). In particular, *ab initio* free potential XANES calculations are used to constrain the sensitivity of XANES spectra to local order, to small geometrical distortions, and to ordering in the second shell. We also integrate the XAS results with existing thermodynamic properties and experiments to construct a preliminary set of thermodynamic properties that reflect the new spectroscopic results and can be used for comparison with other experimental methods. Using this approach, we demonstrate that it is possible to reproduce Fein et al. (1992) solubility data (Table 1) accurately even if $[FeCl_4]^{2-}$ is the dominant form of Fe(II) in high-temperature chloride brines.

2. Materials and methods

The aqueous solutions were prepared by dissolving $FeCl_2 \cdot 4H_2O$ powder (Sigma Aldrich, Reagent Plus, >99%) in pure water (milliQ™) under an argon atmosphere to prevent oxidation of the iron. The solutions were acidified by addition of up to 0.1 M HCl in order to prevent hydrolysis: the logarithm of the stability constant for the reaction $Fe^{2+} + H_2O = Fe(OH)^+ + H^+$ changes from −9.31 at 25 °C to −4.84 at 300 °C. NaCl was added to obtain a set of different chloride molalities at varying ionic strength. For the highest chloride concentration (12.031 m), LiCl was used instead of NaCl for solubility reasons. The composition and ionic strengths of the solutions are summarised in Table 2.

Table 2
Composition of the sample solutions.

Solution label	$Fe_{\_total}$	$Na_{\_total}$	$Li_{\_total}$	$Cl_{\_total}$	$HCl_{\_added}$	*I* (mol/kg)	Density [g/cm^3] at 450 °C, 500 bars
A	0.045	0.356	–	0.547	0.100	0.592	0.45 (SC)
B	0.044	0.744	–	0.932	0.100	0.977	0.50 (SC)
C	0.046	1.901	–	2.092	0.100	2.138	0.60 (SC)
D	0.056	2.813	–	3.024	0.100	3.080	0.67
E	0.060	3.784	–	4.003	0.100	4.063	0.73
F	0.065	4.825	–	5.055	0.100	5.120	0.78
G	0.075	–	11.825	12.031	0.100	12.129	1.02

The temperature and pressure investigated for each solution are 500 bar and 25 up to 450 °C. The densities at 450 °C, 500 bar are estimated from the equation of state for the NaCl–H_2O system of Anderko and Pitzer (1993), as coded in the loner program of Bakker (2003) (the concentration of chloride ion was taken as representing the total NaCl concentration). At 500 bar, the critical point of a NaCl–H_2O mixture is ~2.18 m NaCl at *T*~475 °C (Bischoff and Pitzer, 1989), and hence solutions A, B and probably C were in the supercritical state (SC) at the highest temperature investigated. All concentrations are expressed in mol/kg H_2O, and *I* is the stoichiometric ionic strength (mol/kg H_2O).

2.1. Generation of high pressure and high temperature

As indicated in Table 2, the experiments were conducted along the 500 bar isobar, by varying the temperature from ambient up to 450 °C, using the autoclave developed by Testemale et al. (2005a). This versatile high-pressure (HP) setup has been used successfully for *in-situ* XAS studies of melts (Coulet et al., 2005), inelastic scattering (Wernet et al., 2005) and small angle X-ray scattering (Testemale et al., 2005b) on supercritical water, and XAS and mineral solubility studies in hydrothermal conditions (e.g., Pokrovski et al., 2002, 2005, 2006; Brugger et al., 2007; Liu et al., 2008; Pokrovski et al., 2009). It consists of an external autoclave made of stainless steel which is pressurised by helium, and is fitted with three Be windows: one entrance window for the incoming beam, one exit window for detection of the transmission signal (both located along the X-ray beam), and one fluorescence exit window which is placed at 90° relative to the incoming beam. The high temperature is obtained by using a resistive heater which surrounds an internal cell. This internal cell contains the sample (loaded at ambient conditions), and its material can be chosen according to the specific chemical, mechanical and spectroscopic requirements of the experiment. In this study, given the relatively low energy of the photons at the Fe K-edge (about 7 keV), and the corrosive nature of hydrothermal acidic samples, glassy carbon was chosen for its low density, low chemical reactivity and the low X-ray absorption of carbon. Furthermore, the thinnest possible Be windows were used in the autoclave (0.8 mm each). This choice imposed a relatively low working pressure for the experiment (500 bars), but still enabled us to explore conditions well beyond the critical point of water. An external automatic regulation of the pressure (Bruyère et al., 2008) has been incorporated into the system since its description by Testemale et al. (2005a). As pressure is continuously and precisely regulated, the changes in pressure resulting from changes in temperature during isobaric experiments, or from small helium leaks, are compensated. Both measurement precision and stability of temperature and pressure are within 0.1 °C and 0.5 bar respectively.

2.2. Spectroscopic measurements and analyses

2.2.1. XAS measurements

The spectroscopic and thermodynamic analyses were based on XAS fluorescence measurements. The XAS spectra were measured at the iron K-edge (7112 eV), from 150 eV before the edge to 800 eV above the edge, on the Collaborative Research Group beamline FAME (French Absorption beamline in Material and Environmental sciences) at the European Synchrotron Radiation Facility (ESRF), in Grenoble, France. The details of the beamline and its optical devices were described by Proux et al. (2005, 2006). The beam was focused to 300 × 200 µm, and the focusing point was kept at a constant position using the dynamically sagittal focusing of the second crystal of the monochromator (Hazemann et al., 1995). For this study, a (220) monochromator was used to get a better energy resolution (about 0.8 eV FWHM, Full Width at Half Maximum), which is of critical importance when it comes to the analysis of the pre-edge and edge regions of a spectrum. The presence of the two Rh-coated mirrors ensured the rejection of the harmonics to better than 0.1%, i.e., the intensity of the harmonics was less than 0.1% of the intensity of the fundamental X-rays. The incident (I0) and transmitted (I1) intensities were measured by Si photodiodes collecting the X-rays diffused by Kapton foils placed in the beam. The fluorescence photons were measured by a Canberra™ 30 element solid state detector. The energy was calibrated by regularly measuring the spectrum of a reference metallic foil (first maximum of the derivative set at 7112 eV). This reference foil could not be measured simultaneously behind the sample due to the low intensity of the transmitted photons, resulting from the high absorbance of the high-pressure cell and of the solutions at 7.1 keV.

To trace the speciation change as a function of temperature and Cl concentration, and to retrieve thermodynamic properties for ligand exchange reactions from XAS data, a reasonable number of points must be explored both in concentration and temperature spaces. For the present study, our approach was to collect XANES spectra (up to 200 eV above the edge) for five NaCl-based solutions with chlorinities between 0.547 and 5.055 m, plus one solution with 12.031 m LiCl (Table 2). The use of LiCl as salt enables one to extend the range of chloride concentration and thus better characterise the Fe complexes stable under very high salt concentrations. These solutions were measured at temperatures of 25, 100, 200, 300, 400 and 450 °C, at a constant pressure of 500 bar. Good quality EXAFS data, obtained by averaging 4 to 6 scans of 30 min each, were collected only for end-member solutions (e.g., solutions A and G in Table 2) and are used to constrain the nature of the end-member species. We define an 'end-member' solution as a solution in which one Fe(II) aqueous complex is predominant (ideally alone) so that the mean XAS spectrum contains only the features of this species. These 'end-members' are recognised because the spectra become stable and insensitive to further changes in temperature or composition, and are typically found at the extremes of the temperature and chloride concentration ranges investigated. The multiple scans also allowed us to check that no change, e.g. due to beam damage, was detectable in the EXAFS signal over time.

2.2.2. EXAFS analysis

EXAFS data were analysed using the HORAE package (Ravel and Newville, 2005), which is a graphical interface to the AUTOBK and IFEFFIT codes (Newville et al., 1993; Newville, 2001). The following fitting procedure was used: normalisation of the spectra, extraction of the oscillations with an evaluation of the baseline, and fitting of the following structural parameters: coordination number (N), distance to the neighbouring shells (R), and EXAFS Debye–Waller factor (noted σ^2, and referring to the mean-square relative displacement to which this technique is sensitive). The parameter ΔE_0, which accounts for the error in determining the edge energy, was also fitted. The effective scattering functions and mean free path necessary in the fit were calculated with FEFF6.0 (Mustre de Leon et al., 1991) within the clusters FeO_6 and $FeCl_4$. The amplitude factor (S_0^2) was fixed to 0.7 as determined by fitting the first shell structure of natural siderite $FeCO_3$ (from Ivigtut, Greenland); the EXAFS of this powder reference sample of siderite was measured in transmission mode. k^3 weighting was used. The possible reduction of the amplitude of the signal due to self-absorption effects in the solutions was considered: its intensity was calculated using both the Booth (Booth and Bridges, 2005) and the Tröger (Tröger et al., 1992) algorithms, and was found to be below 1% of the intensity of the oscillations in both cases. The asymmetry of the distance distribution was accounted for with the use of C_3 and C_4 cumulant parameters (Bunker, 1983), and multiple scattering paths within the octahedral and/or tetrahedral clusters were taken into account. Finally, the fitting code IFEFFIT allows a further refinement of the residual background during the fitting procedure itself, to improve the background modelling done with AUTOBK. We employed this option, and obtained correlations between the background and structural parameters below 25%, which were considered adequate. The goodness of fit is expressed with two figures of merit: the reduced chi-square χ^2 and the R-factor. The former is the sum-of-squares of the difference between model and data XAFS, normalised to the number of degrees of freedom of the fit, and the latter is a sum-of-squares of the fractional misfit between model and EXAFS data (Newville et al., 1995).

2.2.3. Ab initio free potential XANES calculations

XANES is usually a useful complement to EXAFS analysis. Indeed, in this low energy part of the spectrum extending to about 60 eV above the edge where the mean free path of the photoelectron is relatively large, XANES can be thought of as a localised probe (a few angstroms) that is sensitive to the three-dimensional and electronic environment of the absorbing atom, whereas EXAFS is mainly sensitive to the radial structure of this environment. Qualitative interpretation of XANES is current practice, as it allows the derivation of structural and redox information in a straightforward way by comparing the measured spectral features with those of standards of known coordination geometry and oxidation state (Parsons et al., 2002; and references therein). Quantitative *ab initio* XANES calculations are more difficult than quantitative EXAFS analyses as there is no simple analytical expression of the XANES (Joly, 2001). *Ab initio* XANES calculations on aqueous complexes attracted early interest for the simplicity and high symmetry of their structures (e.g., Garcia et al., 1986). The derivation of structural information from *ab initio* XANES modelling is more recent (e.g., Benfatto et al., 1997; Bugaev et al., 1998; Benfatto et al., 2002, 2003; Chaboy et al., 2006; D'Angelo et al., 2006), and includes results up to supercritical conditions (Testemale et al., 2004). With *ab initio* XANES calculations it is sometimes possible to distinguish between two similar ligands, such as N and O in systems of biological interest, in situations where EXAFS cannot (e.g., Hayakawa et al., 2004). In the present study, *ab initio* XANES calculations were used either to independently confirm EXAFS results or to obtain additional information regarding the structure of the Fe(II) complexes when the EXAFS results were ambiguous.

All the *ab initio* XANES analyses were carried out with the FDMNES package developed by Joly (2001). This code uses full potential calculations within the real space cluster, and the final states and resulting absorbing cross sections can be calculated by either of two ways:

1) multiple scattering (MS) theory, where the cross section is calculated in terms of path operators by solving the Lippman–Schwinger equation. The Muffin Tin (MT) approximation is used to model the shape of the potential, which is spherically averaged over the atoms and constant between them;
2) solving the Schrödinger equation in the cluster using the Finite Difference Method (FDM). The FDM method avoids the limitations of the MT approximation by allowing a totally free potential shape. This is of particular interest for asymmetrical or non-dense structures (Joly, 2001), such as aqueous complexes at high temperature, but it comes at the cost of increased computing time.

Regardless of the method, the raw calculations are convoluted with 1) a Lorentzian function of energy dependent width in order to reproduce the core-hole lifetime broadening (1.25 eV at the iron K-edge, Krause and Oliver, 1979) and the inelastic plasmon interactions with the photoelectron, and 2) a Gaussian function to reproduce the experimental resolution determined to be 0.8 eV FWHM in our case. These values were set *a priori* and not fitted in the subsequent steps of the analysis.

The origin and nature of the XANES spectra, and the effects of choosing different values of structural and electronic parameters, were determined by comparing calculated (FDMNES code) with observed spectra. Other recent codes add the possibility of fitting structural parameters; e.g., MXAN by Benfatto and Della Longa (2001), and recent works by Smolentsev and Soldatov (2006) and Smolentsev et al. (2007). Instead, we calculated the XANES spectra of the complexes whose presence was inferred either from the EXAFS results or from literature data, and compared them to the experimental spectra.

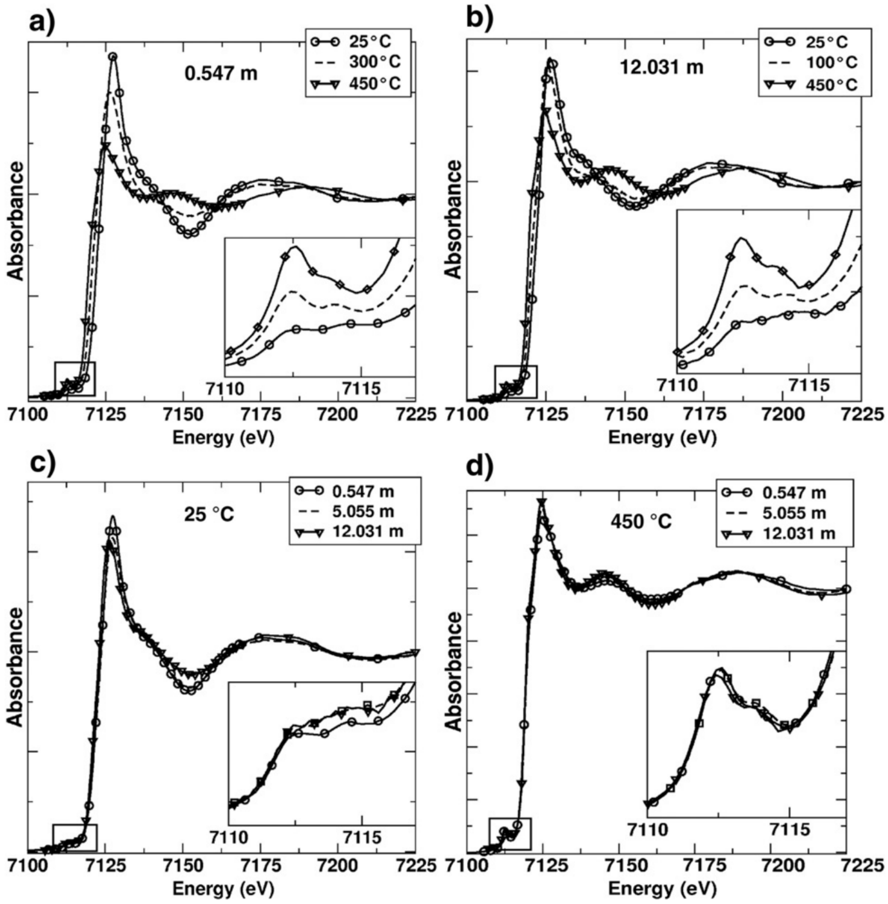

Fig. 1. Normalised Fe K-edge XANES spectra of solutions measured a) in experiment A at constant chloride concentration 0.547 m, b) in experiment G at constant chloride concentration 12.031 m, c) at the same temperature 25 °C in experiments A, F and G and d) at the same temperature 450 °C in experiments A, F and G. Only a limited number of spectra are presented in this figure in order to clearly show the differences in the XANES features. The insets in the graphs correspond to the pre-edge region for the same temperatures as in the main graph.

It should be noted that neither structural nor thermal disorder was taken into account in the distribution of distances, i.e. there is no equivalent to the EXAFS Debye–Waller factor in our XANES calculations. While such a parameter has almost no influence around the edge, for higher energies (above 60 eV that are considered to be part of the EXAFS regime) the calculated amplitudes are expected to be higher than the experimental ones. Finally, all calculations were done with neutral atoms.

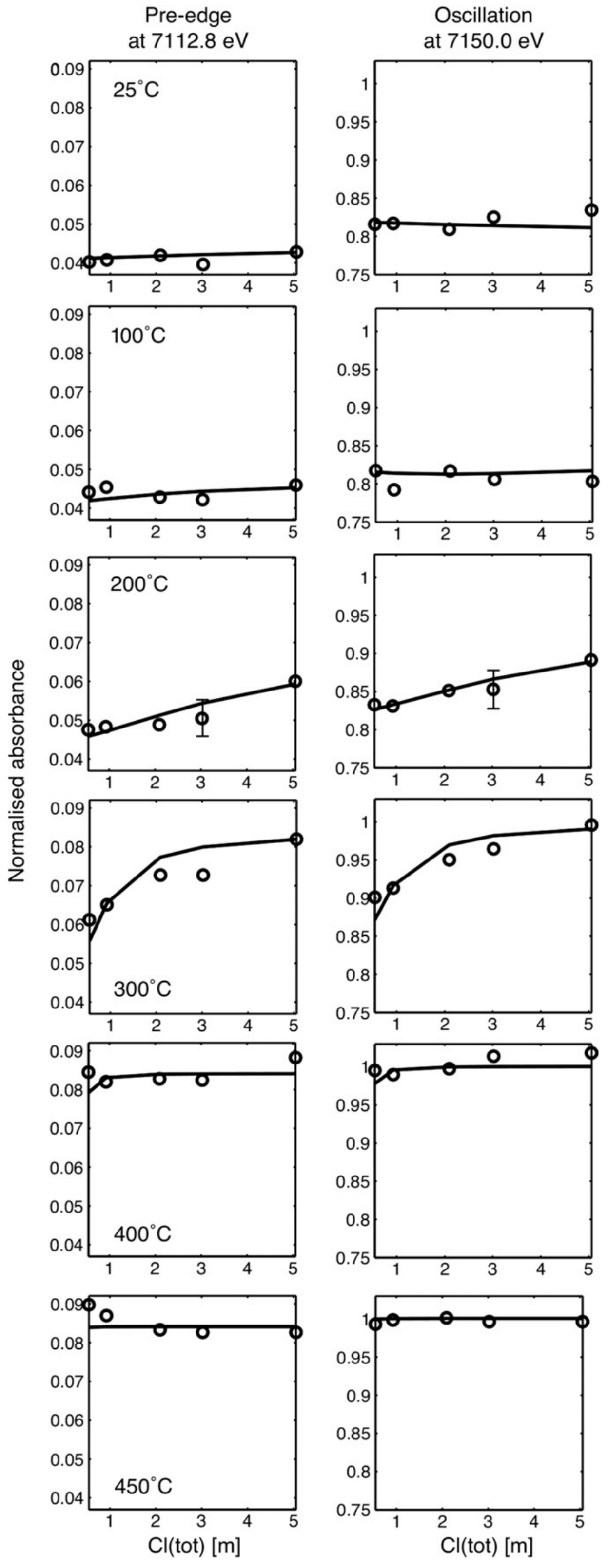

Fig. 2. Variation of normalised fluorescence signal at two different energies (corresponding to the pre-edge and first oscillation in the XANES spectra) as a function of temperature and salinity (expressed at total chlorine concentration). The circles represent the experimental data, and the lines the fits using the BEEROZ model (see Section 4 for details). 1-σ errors (experimental + normalisation) are estimated to be about +/− 0.005 (pre-edge 7112.8 eV) and +/− 0.0025 (7150.0 eV), and are shown on the 200 °C plots.

2.3. Thermodynamic analysis and comparison with solubility data

While *ab initio* XANES calculations provide information on the geometry of the Fe(II) chlorocomplexes, the distribution of species, i.e. the proportion of each species in a particular solution, can be retrieved from XANES data by using the Beer–Lambert law (e.g. Liu et al., 2007). Under optimal circumstances, i.e. with each complex/species having a different XAS spectrum and a sufficient number of spectra to describe the transition from one species to another, this information can be used to retrieve thermodynamic properties for the aqueous species present (Inada and Funahashi, 1999; Brugger et al., 2007; Liu et al., 2007). Such a thermodynamic model then enables comparison of the spectroscopic results with results from solubility experiments.

The determination of the speciation and thermodynamic properties for Fe(II)-chlorocomplexes from the XANES data was done using the BeerOz program (Brugger, 2006). BeerOz consists of a set of Matlab routines dedicated to analysing spectroscopic data on ligand exchange reactions qualitatively (e.g., Principal Component Analysis) as well as quantitatively. In the latter case, the concentrations of aqueous species and their spectra were retrieved from the experimental data using calculated distributions of species and non-linear least square fitting. BeerOz's output consists of the extracted XANES spectra of the individual species, their formation constants (log(K)), their concentration in each of the experimental solution, and residual maps in the n-dimensional space of the results. These residual maps are used to determine the nature of the local minimum corresponding to the end result and to estimate uncertainties for the formation constants. This method can be applied to any spectroscopic data that follow the Beer–Lambert law, and was initially applied to UV–Vis data (Brugger et al., 2001; Liu et al., 2002, 2006) and only recently to XANES data (Brugger et al., 2007; Liu et al., 2007). Due to the underdetermined nature of the problem of interest here (*ab initio* XANES calculations confirm that all octahedral species have similar XANES spectrum, so that species such as $FeCl^+$ and $FeCl_2(aq)$ are difficult to distinguish; the octahedral to tetrahedral transition was observed only at 200 °C and 300 °C), the XAS information had to be combined with literature data to provide a consistent thermodynamic model.

3. Spectroscopic results

3.1. Qualitative interpretation

The normalised Fe K-edge XANES spectra shown in Fig. 1 are for the two sets of experiments (A and G in Table 2) with the lowest (0.547 m) and highest (12.031 m) chloride concentrations (Fig. 1a and b respectively), and for the two extreme temperatures (25 and 450 °C) used in this study (Fig. 1c and d respectively). For purposes of clarity, only the spectra for the intermediate experiment F (5.055 m total chloride concentration) are shown in Fig. 1c and d: they give an indication of the trend from A (0.547 m chloride) to G (12.031 m chloride) spectra. Similarly, a limited number of temperatures are plotted in Fig. 1 in order to keep the evolution of the XANES features distinguishable on the graphs. In addition, the evolution of the XANES

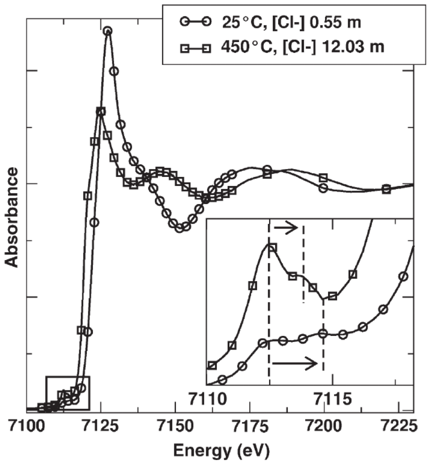

Fig. 3. Normalised Fe K-edge XANES spectra of the 2 end-members (25 °C/0.547 m chloride concentration and 450 °C/12.031 m chloride concentration). The inset corresponds to the pre-edge region. The dotted lines in the inset point to the 2 main peaks visible in the pre-edges, and the arrows are here to stress the difference in the relative positions of the 2 peaks (see text).

signal at two different energies (7112.8 eV and 7150.0 eV) is shown in Fig. 2.

It can be seen in Fig. 1a and c that increasing the temperature and the chloride concentration have the same effect on the speciation of Fe in solution, the effect of temperature being stronger than that of the chloride concentration. At 25 °C, the spectra, and consequently the speciation, change little with the addition of chloride (Fig. 1c). At 450 °C, the similarity between the spectra of the 5.055 m NaCl and 12.031 m LiCl solutions suggests that Fe speciation is dominated by the same aqueous complex in both solutions. Fig. 2 further illustrates the changes observed as a function of temperature and salinity: little significant change is observed at 25 °C and 100 °C upon addition of salt, but the speciation changes dramatically at 200 °C and 300 °C as salinity increases from 0.5 to 5 m. At 400 and 450 °C, a change in salinity again causes only minimal effect on the XANES spectrum. Based on the graphs in Figs. 1 and 2, we can define the spectra of two end-members (see Section 2.2.1) from the two most extreme conditions: 25 °C with 0.547 m chloride concentration and 450 °C with 12.031 m chloride concentration. These two spectra are compared in Fig. 3. The intermediate solutions may consist of a mixture of these two end-members and of several other iron complexes of mixed coordination, as the addition of chloride ligands to the iron metal centre is expected to be progressive.

There is a broad agreement that under ambient conditions Fe(II) exists mainly as the octahedral $Fe(H_2O)_6^{2+}$ complex in aqueous solutions (e.g., Baes and Mesmer, 1976). Then, several features in the XANES spectra indicate that the changes observed (Fig. 3) are related to a transition of the geometry of the dominant Fe(II) complex from octahedral to tetrahedral upon heating or upon increase in chlorinity. First, the increase of the intensity of the pre-edge is in agreement with a structural transition from an octahedral species, where the weak pre-edge is due to quadrupolar transitions, to a tetrahedral species where the

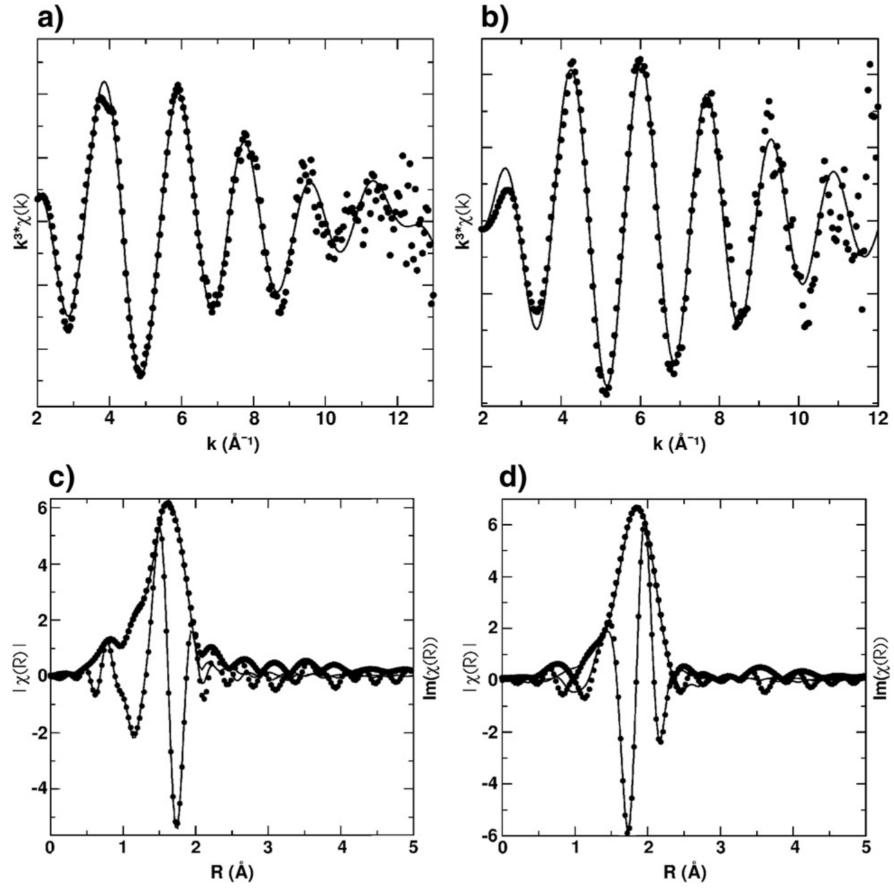

Fig. 4. a) EXAFS k^3-weighted oscillations extracted from fluorescence spectra of the 1st end-member (experiment A at 25 °C); b) EXAFS k^3-weighted oscillations extracted from fluorescence spectra of the 2nd end-member (experiment G at 450 °C); c) magnitude and imaginary part of the Fourier transform (not corrected for the phase shift) of the oscillations in a); d) magnitude and imaginary part of the Fourier transform of the oscillations in b). Dots are the experimental spectra, solid lines are the best fits.

dipolar transition 1s–3d is allowed by a mixing of 4p and 3d orbitals in this non centro-symmetric geometry (e.g., Waychunas et al., 1983; Apted et al., 1985; Galoisy et al., 2001). Then, two components are discernible in the pre-edges and the energy splitting between them is reduced from 2 eV for the first end-member to 1.5 eV for the second end-member: these values correspond to a transition from octahedral to tetrahedral symmetry as demonstrated theoretically and verified experimentally (Westre et al., 1997; Wilke et al., 2001; Rueff et al., 2004). Finally, the intensity of the white line (maximum absorbance), which corresponds to the main 1s–4p dipole transition, is reduced and its position shifted to lower energy, in agreement with what is observed in tetrahedral structures (Galoisy et al., 2001). This transition has been observed at lower temperature (up to 150 °C) and wider chloride concentration (up to 15.6 m Cl) by Liu et al. (2007), in their XANES study of Fe(II) and Zn(II) chloride complexes. The same evolution of features was also observed by Hoffmann et al. (1999) in the case of a transition from octahedral $Ni(H_2O)_6^{2+}$ to tetrahedral $NiCl_4^{2-}$.

3.2. Quantitative EXAFS results

The EXAFS data for the two end-member solutions are plotted together with the final fits in Fig. 4. The results of the EXAFS analysis, including the fitting parameters, are reported in Table 3. It can be inferred from these results that 1) the first end-member (experiment A at 25 °C) corresponds most likely to the (octahedral) complex $Fe(H_2O)_6^{2+}$, a result consistent with earlier studies (see below); and 2) the second end-member (experiment G at 450 °C) most likely to the (tetrahedral) $FeCl_4^{2-}$ complex. Note that the exact three-dimensional (3D) symmetry (octahedral and tetrahedral) cannot be inferred from the EXAFS results. In the absence of multiple scattering peaks, EXAFS constrains only the coordination number and the distance, i.e., the radial structure. In our case, the multiple scattering peaks were too weak to be measured, and the 3D geometry of the complexes was studied using *ab initio* XANES calculations. Also, our EXAFS data are sensitive only to the structure of the first shell; i.e. the presence of cations in the second shell and hence the true formal charge of the complex cannot be assessed.

The values of the EXAFS Debye–Waller factors, about 8×10^{-3} Å^2, are typical for the hydration shell of divalent ions in solutions: similar values were found by Simonet et al. (2002) for $Zn(H_2O)_6^{2+}$ (8.3×10^{-3} Å^2) and by Hoffmann et al. (1999) for $Ni(H_2O)_6^{2+}$ (8.1×10^{-3} Å^2). The anharmonic term C_3 is also shown in Table 3: its values remain low (about 3×10^{-4}), indicating a small correction to symmetrical radial distribution for Cl and O. C_4 was also refined, but its value always converged to 0.

A Fe–O distance of 2.09(2) Å was obtained from the refinement of the EXAFS data for the first end-member (experiment A at 25 °C). This distance is similar to the value of about 2.10 Å determined by previous researchers for the Fe(II) hexaaquo complex (Apted et al., 1985; Herdman and Neilson, 1992, and references therein). This value is also in agreement with the value of 2.12 Å of D'Angelo and Benfatto (2004). This latter agreement confirms D'Angelo and Benfatto's (2004) result that the contribution of the 1s–3s and 1s–3p multielectronic channels to the EXAFS is weak in the case of Fe(II)-hydration, thus we did not take into account these multielectronic channels in our analysis. Because a large number of studies have detected the presence of chloride ions in the oxygen coordination shell for the octahedral Fe^{2+} ion (Table 1), we considered a mixed coordination with both oxygen and chloride ligands (Table 3). The refined parameters for Cl coordination are in agreement within the uncertainties with the values determined by Pokrovski et al. (2003) (0.3 ± 0.2 chloride ions at 2.30 ± 0.03 Å). However, this 2-shells fit has a larger number of variables, for the same limited amount of information available in the experimental spectrum: this makes this fit of slightly worse quality (larger χ^2 value, see Table 3), although the *R*-factor is lower. The presence of a small number of chloride ligands in the first shell cannot be totally ruled out.

In the case of the second end-member (experiment G at 450 °C), the Fe–Cl distance of 2.31 Å retrieved from our EXAFS analysis is in agreement with the average value of 2.29 Å found in the crystallographic study of Lauher and Ibers (1975) on the tetramethylammonium tetrachloroferrate(II), and with the value of 2.30 Å determined by Poiarkova (1999) using *ab initio* quantum chemical calculations on the $FeCl_4^{2-}$ complex. The addition of oxygen in the scattering shell noticeably degraded the fit (not shown). Together with the robustness of the primary EXAFS fit indicated by the low *R*-factor and the small EXAFS Debye–Waller factor for such high temperatures (Table 3), the coordination of 3.9 ± 0.4 is a strong indication that the $FeCl_4^{2-}$ cluster is the predominant Fe(II) species in experiment G.

The recent work by Ferlat et al. (2005) stressed the limitations of EXAFS fitting in disordered systems, particularly high-temperature aqueous solutions, where the continuous distribution of atomic environments beyond the first shell is not taken in consideration. This simplification results in a misleading determination of the amplitude parameters, particularly the number of neighbours: this occurs essentially when one tries to determine the reduction in the number of water molecules in the first shell. As far as the present EXAFS results are concerned for the two end-members, we are not dealing with a progressive reduction in the number of neighbours, but with a strong change in the first shell (nature, number and distance of neighbours). For these reasons, and given the stability of the two end-member clusters as inferred essentially from the low amplitude of the EXAFS Debye–Waller factors, we believe that our results do not suffer from this problem.

3.3. Ab initio XANES calculations

3.3.1. Calculation framework and effect of the second shell

The FDM method was used for XANES calculations throughout this study. The reason is that the tetrahedral structure expected at high temperatures or high chlorinity (second end-member) is less symmetric than the octahedral end-member, a situation in which the FDM calculations are more sensitive than the MS method in the low energy part of the spectrum (Joly, 2001).

As indicated by Benfatto et al. (1997) and D'Angelo et al. (2006), the influence of hydrogen atoms and the second hydration shell must be considered when looking for a good agreement between data and

Table 3

Local structure of the two end-members (experiment A at 25 °C and experiment G at 450 °C) as determined by fitting of the EXAFS K-edge fluorescence spectra.

End-member	Shell	*N*	*R* (Å)	σ^2 (Å$^2\times10^{-3}$)	ΔE_0 (eV)	C_3 (Å$^3\times10^{-4}$)	*R*-factor/χ^2
Exp A/25 °C	O	6.4 (0.9)	2.09 (6)	8 (1)	0.0 (2.7)	4 (2)	0.034/14.0
Exp A/25 °C	O	6.1 (0.6)	2.11 (2)	8 (1)	3.1 (1.0)	–[a]	0.010/25.0
	Cl	0.8 (0.8)	2.17 (2)	40 (40)	11.0 (1.0)	–[a]	
Exp G/450 °C	Cl	3.9 (0.4)	2.31 (5)	8 (1)	1.9 (1.7)	3 (3)	0.005/18.0

In the case of the first end-member, two possible structures are proposed (one with oxygen coordination only, and one with mixed oxygen and chloride coordination, see text). The parameters are the coordination number *N*, the distance to the scattering shell (*R*), the EXAFS Debye–Waller factor (σ^2), the energy misfit (ΔE_0), the third order cumulant C_3, and the goodness of fit *R*-factor and reduced chi-square χ^2. The data used in the fit ranged in [2.4–12.5 Å^{-1}] (first end-member) and [2.4–10.5 Å^{-1}]) (second end-member). The fitting was done in *R*-space in the range [1.6–3.2 Å] and k^3 weighting was used.

[a] Anharmonicity was not introduced in this fit.

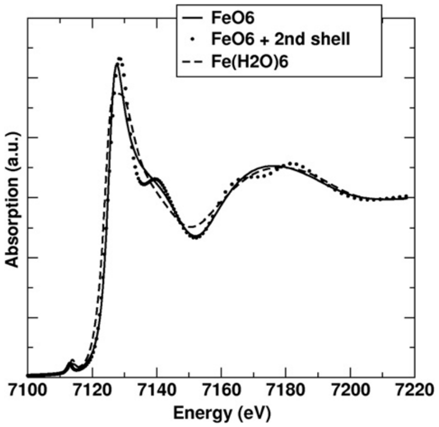

Fig. 5. Convoluted calculated spectra for FeO_6 (solid line), $Fe(H_2O)_6$ (dashed line) and FeO_6 with a second shell of oxygens (dotted line). For $Fe(H_2O)_6$, the water molecules are considered rigid with d(O–H) = 0.96 Å, the angle H–O–H = 105° and the hydrogens are placed in the 'dipole' configurations (Benfatto et al., 1997; D'Angelo et al., 2002). For the cluster FeO_6 with a second shell of oxygens, the 12 second shell oxygens are placed at 4.27 Å (D'Angelo et al., 2006), each facing one edge of the octahedron. The differences between the spectra are visible in the white line (maximum absorbance) and the first shoulder around 7140 eV.

theory, especially in the low energy region of the spectra. D'Angelo et al. (2006) insisted on the necessity of taking into account the disorder among these more distant atoms, by means of Molecular Dynamics (MD) for example. In our case this point is not critical because we consider large changes in the XANES spectra (from the first to the second end-member), of much larger amplitude than the effect of hydrogen atoms and/or a second hydration shell. This is demonstrated in Fig. 5 where the convoluted calculated spectra are shown for different 'extreme' configurations of the hydrogen bonding and the second shell for the FeO_6 cluster: i) FeO_6, ii) $Fe(H_2O)_6$ and iii) FeO_6 with a second shell of oxygens. For ii), the water molecules are considered rigid with d(O–H) = 0.96 Å, the angle H–O–H = 105° and the hydrogens are placed in the 'dipole' configurations (Benfatto et al., 1997; D'Angelo et al., 2002). For the cluster iii), twelve second shell oxygens are placed at 4.27 Å (D'Angelo et al., 2006), each facing one edge of the octahedron. The configurations ii) and especially iii) are very structured and unrealistic: as shown by many MD results (e.g., Remsungnen and Rode, 2003), these shells are much more disordered in reality. For that reason, the real effect on the XANES spectra will be smaller than shown in Fig. 5, which represents a 'worst case' scenario. Consequently we did not consider the hydrogen atoms and second hydration shells in the subsequent calculations. For the same reasons, the partial charges (in the sense of orbital populations) of the atoms constituting the clusters were not varied, as can be done with the FDMNES program (Joly et al., 1999; Testemale et al., 2004).

In the following, we investigated whether the experimental spectra obtained are consistent with the octahedral and tetrahedral structures proposed by previous studies, and tested the sensitivity of the XANES to different types of structural changes and geometrical distortions.

3.3.2. The first end-member: an octahedral complex

The XANES spectrum of the first end-member was calculated based on a FeO_6 octahedron with a Fe–O distance of 2.09 Å, i.e., the distance derived from the EXAFS analysis (see Table 3), and is compared to the experimental spectrum in Fig. 6a. Both the pre-edge and post-edge regions of the spectrum are well reproduced. The main discrepancy around 7175 eV, which is already in the EXAFS region, is due to the absence of thermal disorder in the calculations (see Section 2.2.3). The agreement for the position of all the peaks up to 7220 eV adds support to the EXAFS Fe–O distance of 2.09 Å. The XANES spectra of octahedral $M(H_2O)_6$ clusters (where M is a transition metal) have already been calculated to a close agreement by different authors using multiple scattering (MS) theory: Ni^{2+} and Co^{2+} by Benfatto et al. (1997); Ni^{2+} by Benfatto and Della Longa (2001); Ni^{2+}, Co^{2+} and Zn^{2+} by D'Angelo et al. (2002, 2006). And as stated by Joly (2001), the MS and FDM methods provide similar results in the case of highly symmetrical octahedral structures. Regarding the pre-edge, two peaks are calculated and match the experimental data and the energy split between them (the calculated value of 1.6 eV is within 20% of the experimental value of 2.0 eV). However, as shown by Westre et al. (1997), the experimental pre-edge is in fact made of three peaks (the two extremes being split by 2 eV), as derived from the ligand-field splitting of 3d orbitals into the t_{2g}–e_g set, and the multielectronic coupling between two one-hole intermediate states of t_{2g} and e_g character. The monoelectronic approach of FDMNES is not capable of taking these multielectronic effects into account, but it still deals correctly with the ligand-field splitting: this is the reason why the calculated pre-edge (for neutral atoms) matches the experimental one to first order.

We also calculated the spectra of the following intermediate octahedral chlorocomplexes: $FeCl(H_2O)_5^+$, trans-$FeCl_2(H_2O)_{4(aq)}$ and $FeCl_3(H_2O)_3^-$ (Fig. 7). No firm conclusions about the presence or absence of these complexes can be drawn from the observation of the spectra as the differences between them are small. Nevertheless, the trend in the features of the spectra is in very good agreement with

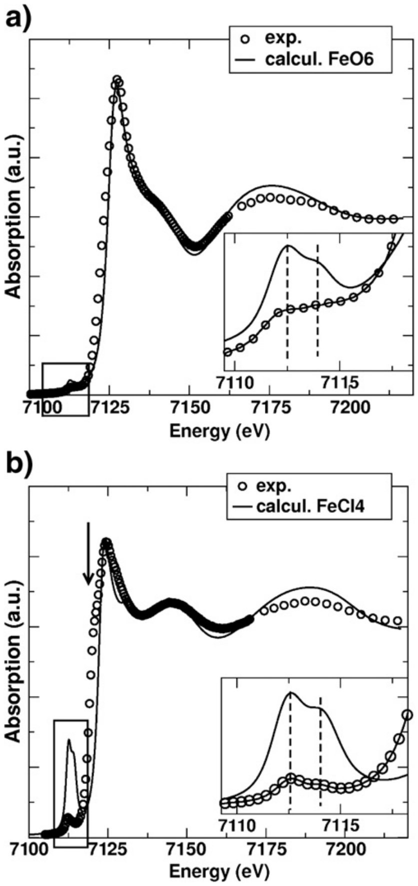

Fig. 6. a) Experimental (open circles) and convoluted calculated (solid line) spectra for the first end-member. The structure calculated is an octahedron FeO_6 with a distance Fe–O of 2.09 Å. b) Experimental (open circles) and convoluted calculated (solid line) spectra for the second end-member. The structure calculated is a regular tetrahedron $FeCl_4$ with a distance Fe–Cl of 2.31 Å. The insets correspond to the pre-edge regions. The dotted lines in the insets point to the 2 main peaks visible in the pre-edges. The arrow in the main graph points to the shoulder on the low energy part of the white line (see text).

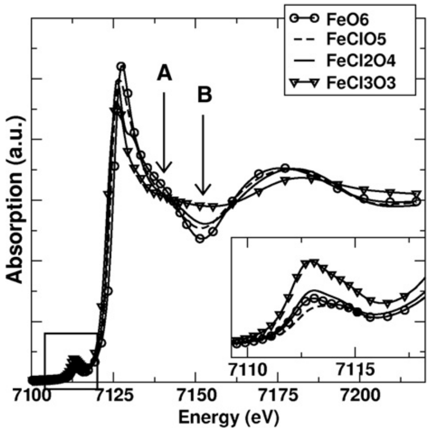

Fig. 7. Convoluted calculated spectra for the possible intermediate octahedral complexes, corresponding to $FeCl(H_2O)_5^+$, trans-$FeCl_2(H_2O)_{4(aq)}$ and $FeCl_3(H_2O)_3^-$. The inset corresponds to the pre-edge regions. The arrows point to the features A and B at 7140 and 7150 eV for comparison with Fig. 11 (see text, end of Section 4.1).

what is observed experimentally when T or $[Cl^-]$ are increased (see Fig. 1a for example). In other words, the intermediate experimental spectra have features that could be reproduced by linearly combining several of those chlorinated complexes. This is consistent with the expected progressive stepwise replacement of water molecules by chloride ions in the first shell of Fe^{2+} (e.g., Liu et al., 2007).

3.3.3. The second end-member: a tetrahedral complex

The XANES spectrum of the second end-member was calculated based on a $FeCl_4$ tetrahedron with a Fe–Cl distance of 2.31 Å, as determined from EXAFS. As can be seen in Fig. 6b, the agreement with the experimental spectrum is good. Above 7130 eV, the position of the peaks and relative intensities of the oscillations closely match the experimental data. Above 7150 eV, the calculated amplitude of the oscillations is larger than the experimental one: this is most likely due to the absence of thermal disorder in our calculations (see Section 2.2.3). In the edge region, the experimental white line (maximum absorbance) is wider than in the case of the first end-member, and is especially asymmetric on the high energy side. This asymmetry may correspond, in the calculations, to the presence of a small bump at 7130 eV on the high energy side of the main white line. The small difference could find its origin in a possible distortion of the tetrahedral structure (see below and Fig. 8b) and/or in the influence of a second hydration shell in this region of the spectrum (see Fig. 5; Benfatto et al., 1997). As shown in the inset in Fig. 6b, the pre-edge is well reproduced: two peaks are discernible in the convoluted calculated spectrum, due to ligand-field splitting, in correspondence with the two features of the experimental pre-edge. This pre-edge is formally composed of 4 peaks (Westre et al., 1997), but the energy resolution of Fe K-edge spectroscopy allows to distinguish only two features (e.g., Wilke et al., 2001; Rueff et al., 2004).

This overall good agreement is a strong argument in favour of the existence of the $FeCl_4^{2-}$ complex at high temperatures and high chlorinity, but as mentioned in the introduction the stability of a charged species in these conditions of low permittivity is questionable. For that reason, the spectrum of a tetrahedron $FeCl_2O_2$ was calculated, corresponding to the neutral species $FeCl_2(H_2O)_{2(aq)}$. Many distances and angular distortions of this complex were considered, but none of them was found to match the experimental data. This can be seen in Fig. 8a where the experimental spectrum is compared to the closest calculated spectrum. Hence, both XANES and EXAFS fitting results do not support the possibility of two different neighbours in the first shell around Fe in this end-member. Finally, the ion pairing of two Na^+ cations with the $FeCl_4^{2-}$ complex was also considered as a possibility to ensure a neutral charge with the $FeCl_2(NaCl)_2$ complex: the results are not shown here but it appeared that the presence of sodium cations only affects the intensity of the XANES features in the edge region, and to such a small extent (about 2% in the intensity of the edge region) that it was not possible to conclude whether these cations were present or not. This result is in agreement with the conclusions of D'Angelo et al. (2006) who showed that a second shell has a detectable but very small influence on the XANES spectra of hydrated transition metals. Consequently, as in the case of the EXAFS analysis which is not sensitive to the second shell, the presence of these Na^+ ions cannot be reliably assessed.

Finally, as can be seen in Fig. 6b, there still remains a disagreement between the calculated and experimental spectra of the second end-member: on the low energy side of the white line, the shoulder visible experimentally (arrow in Fig. 6b) is not present in the calculations. Since it is quite a discernible feature, it is necessary to track down its origin. One possibility is a trigonal $FeCl_3$ structure, corresponding to a $FeCl_4$ tetrahedron from which one chloride is removed, the other three remaining in the same geometry. This would correspond to a $[FeCl_3]^-$ complex. As can be seen in Fig. 8b, this structure gives rise to a

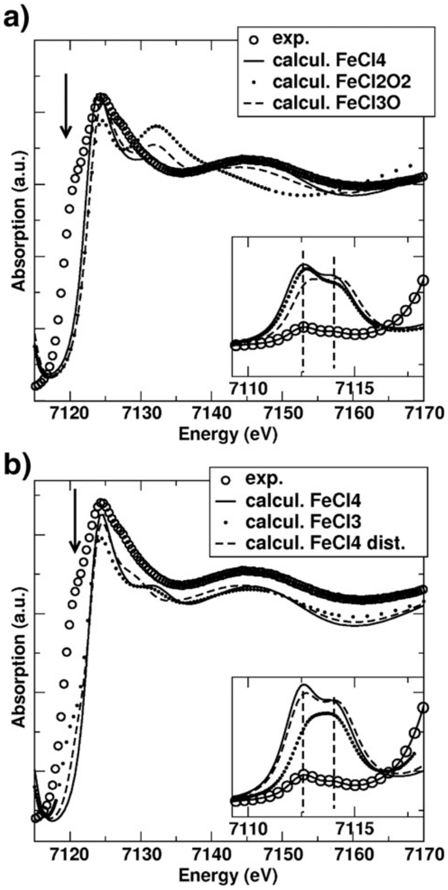

Fig. 8. a) Experimental (open circles) and convoluted calculated spectra for the second end-member. The structures calculated correspond to: the same regular tetrahedron $FeCl_4$ as in Fig. 6b (solid line); a tetrahedron $FeCl_2O_2$ (dotted line, d(Fe–O) = 2.20 Å and d(Fe–Cl) = 2.40 Å); and the $FeCl_3O$ complex with a tetrahedral configuration (dashed line, d(Fe–O) = 2.20 Å and d(Fe–Cl) = 2.40 Å). b) Experimental (open circles) and convoluted calculated spectra for the second end-member. The structures calculated correspond to: the same regular tetrahedron $FeCl_4$ as in Fig. 6b (solid line); the $FeCl_3$ complex with a tetrahedral configuration, see text (dotted line, d(Fe–Cl) = 2.31 Å); an angularly distorted tetrahedral $FeCl_4$ structure (dashed line, d(Fe–Cl) = 2.31 Å, three Cl–Fe–Cl angles changed from 109° to 90°). In b), the experimental curve is shifted upwards for clarity reasons. The arrow points to the shoulder on the low energy part of the white line (see text).

shoulder about 4 eV below the main transition (the white line), the rest of the spectrum being similar to the regular tetrahedral $FeCl_4$ cluster. This figure shows a good agreement with the experimental data. It is worth noting that adding a fourth oxygen neighbour, i.e. the tetrahedral $[FeCl_3(H_2O)]^-$ complex, results in a poorer agreement (Fig. 8a). Another structural possibility that has been considered is the distortion of the tetrahedral $FeCl_4$ structure: the existence of a complex such as $FeCl_2(NaCl)_2(aq)$ or $FeCl_2(LiCl)_2(aq)$ could be at the origin of such a distortion from ideal Td geometry. Several possibilities for structural distortions were considered, mainly angular distortions. One of them is shown in Fig. 8b (three Cl–Fe–Cl angles changed from 109° to 90°). This distortion results in the mixing of the p and s orbitals, otherwise symmetry-forbidden in perfect tetrahedral structures, which shows up on the low energy side of the white line as well (the rest of the spectrum being almost identical to the tetrahedral $FeCl_4$ one), similarly to the observed experimental feature (Fig. 8b). In Fig. 8b, it can also be seen that the asymmetrical shape of the white line is more accurately calculated in the case of the distorted tetrahedral $FeCl_4$ structure than with a regular tetrahedron. Furthermore, this distorted coordination structure for tetrahedral species has already been evoked by Hoffmann et al. (1999) for nickel-chloride association in hydrothermal aqueous conditions. Hence, in the case of the second end-member, the XANES calculations indicate that it is most probably a tetrahedral, Cl-rich complex, but cannot distinguish unequivocally between $[FeCl_3]^-$ and distorted $[FeCl_4]^{2-}$.

4. Thermodynamic analysis and comparison with solubility data

The spectroscopic analysis confirms the octahedral to tetrahedral transition of the Fe(II) chlorocomplexes upon increasing temperature and/or salinity. However, a surprising result is that a high-order tetrahedral complex containing 3 or more Cl ions becomes increasingly stable at high temperature: we observed that this complex was predominant in our experiments at 400 and 450 °C (Figs. 1 and 2). This result appears to contrast with solubility studies, which were interpreted using $FeCl_2(aq)$ as the major complex under these conditions (Table 1). For that reason, we investigated to see if it is possible to find a set of thermodynamic properties that reflects the speciation from our XAS study and is consistent with available experimental studies and in particular with the solubility data of Fein et al. (1992), which are high quality results conducted under *P*–*T* conditions overlapping those of our study, and which are the basis for the HKF parameters for Fe(II) chlorocomplexes proposed by Sverjensky et al. (1997).

The thermodynamic properties retrieved in this section are preliminary. Indeed, our XAS dataset is not large enough to provide high quality, i.e., low uncertainties, thermodynamic properties. Moreover, the *ab initio* XANES calculations show that XANES is not very sensitive to the replacement of a chloride by a water molecule (for a given geometry), and hence is not well suited for studying equilibria among chlorocomplexes with similar geometries (Section 3.3). XANES, however, is very sensitive to the octahedral to tetrahedral transition. Despite its limitations, the current analysis is valuable because it provides the first set of thermodynamic properties for $FeCl_4^{2-}$ at temperatures higher than 150 °C, and as such it will enable more accurate predictions than models based on erroneous speciation models. This analysis will also show that the spectroscopic results and Fein et al. (1992) solubility results are indeed compatible.

4.1. Thermodynamic analysis

The details of the fitting procedures have been described in Liu et al. (2007) and will not be repeated here. The approach relies on the validity of the Beer–Lambert law for each species over the temperature and composition range where this species contributes to the overall experimental spectra. Subtle changes in the geometry of the complex under different physico-chemical conditions (*T*, *P*, solvent composition) can result in a changing spectrum for a single species, breaking the assumption that each individual species possesses a unique spectrum. For example, Brugger et al. (2007) showed that the trigonal planar $CuCl_3^{2-}$ complex undergoes small distortions from trigonal geometry as salinity increases, resulting in small changes in the XANES spectra, but no visible change in EXAFS. In the case of the dataset of interest here, the validity of the Beer–Lambert law is well established, especially for the second end-member ($FeCl_4^{2-}$). The XANES spectra of solutions containing 0.932 to 5.055 m Cl at 450 °C are identical; these spectra are also identical to those measured at 400 °C at salt concentrations ≥2.092 m. This empirical confirmation of the validity of the Beer–Lambert law for the system under study is confirmed by the *ab initio* XANES calculations. Fig. 7 shows the small extent of changes caused by consideration of the water molecules in the second shell. The changes involved in the octahedral to tetrahedral transition are also much larger than any changes among octahedral species. Thus XANES spectroscopy is well suited for deriving thermodynamic properties for this type of coordination change, as noted by Liu et al. (2007).

The normalised XANES spectra between energies 7105 and 7209 eV were used in the BeerOz fitting. The combination of counting statistic errors and uncertainty arising from the normalisation procedure conducted with AUTOBK (Newville et al., 1993) results in an estimated

Table 4
Values for thermodynamic parameters from the literature used in the fitting of XANES spectra.

Property	25 °C	100 °C	200 °C	300 °C	400 °C	450 °C	References
$A_{\gamma,\ NaCl}$[a]	0.498	0.581	0.758	1.053	1.879	3.355	Helgeson and Kirkham (1974)
B_{γ}[a]	0.328	0.341	0.362	0.385	0.423	0.455	Helgeson and Kirkham (1974)
$b_{\gamma,NaCl}$[a]	0.072	0.080	0.058	0.008	−0.082	−0.204	Helgeson and Kirkham (1974)
$HCl_{(aq)} = Cl^- + H^+$	6.600	4.131	1.631	−0.488	−2.880	−5.315	Pokrovskii (1999)
$NaCl_{(aq)} = Cl^- + Na^+$	0.835	0.533	0.025	−0.668	−1.737	−3.054	Sverjensky et al. (1997)
$FeCl^+ = Fe^{2+} + Cl^-$	0.5	−0.1	−0.9	−1.5	−3.4	−4.3	This study
	0.2	0.1	−0.95	−2.0	−3.4	−4.3	Sverjensky et al. (1997)
	0.5	−0.3	−0.8[b]	−1.0 [b]	−1.11 [b]	−1.3 [b]	Zhao and Pan (2001)
				−2.06	−3.36		Fein et al. (1992)
$FeCl_{2(aq)} = Fe^{2+} + 2Cl^-$	4.2	0.2	−2.7	−3.9	−6.6	−9.6	This study
	8.3	4.4	0.3	−3.4	−7.1	−9.6	Sverjensky et al. (1997)
	1.9	0.7	−0.5[b]	−1.6[b]	−3.2[b]	−4.9[b]	Zhao and Pan (2001)
				−3.75	−7.04		Fein et al. (1992)
$FeCl_4^{2-} = Fe^{2+} + 4Cl^-$	6.2	4.8	−1.2	−4.0	−8.4	−13	This study
	>2.2	>1.5	+/−0.6	+/−0.6	<−8.1	<−11.1	Range (90% confidence level)

Values given for aqueous species are log(*K*) of dissociation. Log(*K*) of $FeCl^+$ and $FeCl_{2(aq)}$ used in this study is compared with values derived from Fein et al. (1992), Sverjensky et al. (1997), and Zhao and Pan (2001). All values are given at 500 bar.

[a] Used in the activity coefficient function, see Eq. (1).

[b] Extrapolated from Zhao and Pan's (2001) data of 25–100 °C.

"experimental" error of about 0.005 to 0.01 absorbance units at the 67% confidence level (1-σ). Activity coefficients were calculated using the extended Debye–Huckel formalism, which is used in most studies of metal transport and deposition under hydrothermal conditions:

$$\log(\overline{\gamma_n}) = \frac{-A_\gamma Z_n^2 \bar{I}^{1/2}}{1 + B_\gamma \mathring{a}_n \bar{I}^{1/2}} + b_{\gamma,\mathrm{NaCl}}\bar{I} + G_\gamma, \tag{1}$$

where A_γ and B_γ are the Debye–Huckel solvent parameters taken from Helgeson and Kirkham (1974) and $b_{\gamma,\mathrm{NaCl}}$ is the extended-term parameter (b-dot coefficient) for NaCl-dominated solutions (see Table 4), $\mathring{a}_n$ is the distance of closest approach of ion n, and is given a value of 5 Å for divalent and trivalent ions, and 4.0 Å for monovalent ions, except for H^+ and Fe^{2+} which are given a value of 9 Å and 6 Å, respectively (Kielland, 1937). $\bar{I}$ is the true ionic strength using the molal scale. G_γ is a mole fraction to molality conversion factor. The extended Debye–Huckel formalism is suitable for electrolyte solutions up to ionic strengths ~3 m (e.g., Helgeson and Kirkham, 1974; Heinrich and Seward, 1990), and this formalism has been used for many geological applications of reactive transport under hydrothermal conditions. The data in our study cover the salinity range from 0.547 to 5.055 m Cl_{tot} (solution G was not used in the thermodynamic analysis, because its ionic strength is well beyond the range of the extended Debye–Huckel formalism). As the most concentrated solution (5.055 m Cl_{tot}) is still beyond the usual safe range for using the extended Debye–Huckel formalism, we also performed the fitting on the 0.51–3.0 m Cl_{tot} range (only solutions A–D): as the results are equivalent within error, we chose to use the full salinity range.

The speciation model and equations of mass and charge balances are identical to those in Liu et al. (2007). The speciation model includes the following species: Cl^-, Na^+, HCl(aq), NaCl(aq), Fe^{2+}, $FeCl^+$, $FeCl_2$(aq), and $FeCl_4^{2-}$. Previous studies suggest that there can be at most 2 chloride ions in the octahedral species (i.e., $FeCl_2$(aq); Susak and Crerar, 1985; Zhao and Pan, 2001). Our spectroscopic XANES data exclude almost unequivocally the presence of the tetrahedral $[FeCl_3(H_2O)]^-$ complex but cannot exclude the trigonal $[FeCl_3]^-$ complex. However, the poorer fits and unrealistic deconvoluted spectra obtained by alternative models which include the complex $[FeCl_3]^-$ in the thermodynamic analysis do not support its existence. This is also consistent with the interpretations of the Ni(II) and Zn(II) similar systems (Mayanovic et al., 1997; Anderson et al., 1998; Mayanovic et al., 1999; Hoffmann et al., 1999; Mibe et al., 2009). Therefore it is not included in the final model. Because XANES is mainly sensitive to octahedral to tetrahedral transitions, the available XANES data only permit the fitting of the formation constants for the $[FeCl_4]^{2-}$ complex; even then, the complete spectral change of octahedral to tetrahedral transition as a function of salinity is observed only at 300 °C for the range of salinities investigated. Therefore, values of the formation constants for all species except $FeCl_4^{2-}$ are required. For practical reasons, we favour using properties derived using the Helgeson–Kirkham–Flowers (HKF) formalism (Helgeson et al., 1981), as this formalism covers the range of conditions investigated in our experiments, and is the most popular source of thermodynamic properties for aqueous species at elevated pressures and temperatures for geological applications (e.g., Johnson et al., 1992; Sverjensky et al., 1997). The Unitherm database (Shvarov and Bastrakov, 1999) was used to extrapolate log(K)s to the temperature and pressure of our experiments (see Table 4).

All thermodynamic parameters used in this study are listed in Table 4. Formation constants for NaCl(aq) are from Sverjensky et al. (1997) and for HCl(aq) from Pokrovskii (1999). The latter is the most recent HKF analysis of available experimental data. No attempt to integrate the results of Ho (2001) [100–410 °C, P to 305 bar] was made, because the latter author found good agreement with the previous study for densities >0.5 g/cm³, and the ligand exchange reactions studied in our study are not pH dependent.

Sverjensky et al. (1997) fitted HKF parameters for the $FeCl^+$ complex, using mainly the UV–Vis data of Heinrich and Seward (1990) and the electrochemical study of Palmer and Hyde (1993). Zhao and Pan (2001) conducted careful UV–Vis studies up to 100 °C; their value at 25 °C is preferred, because they use a similar speciation model as the one demonstrated by our XAS study (Fig. 9a; Table 4). For temperatures between 100 °C and 300 °C, the average value between Sverjensky et al.'s (1997) values and the polynomial extrapolation from Zhao and Pan (2001) was selected. At 100 °C and especially 200 °C, the values from both sources are close; however the discrepancy is larger at 300 °C (1 log unit; Table 4). Choosing Sverjensky et al.'s (1997) value resulted in unrealistic calculated XANES spectra for the $FeCl_2$(aq) species (very similar to the spectrum of $[FeCl_4]^{2-}$). The discrepancy may be explained by the fact that $[FeCl_4]^{2-}$ becomes stable at low salt concentration at 300 °C (e.g., ~50% at 1 m NaCl; Fig. 10), and yet this

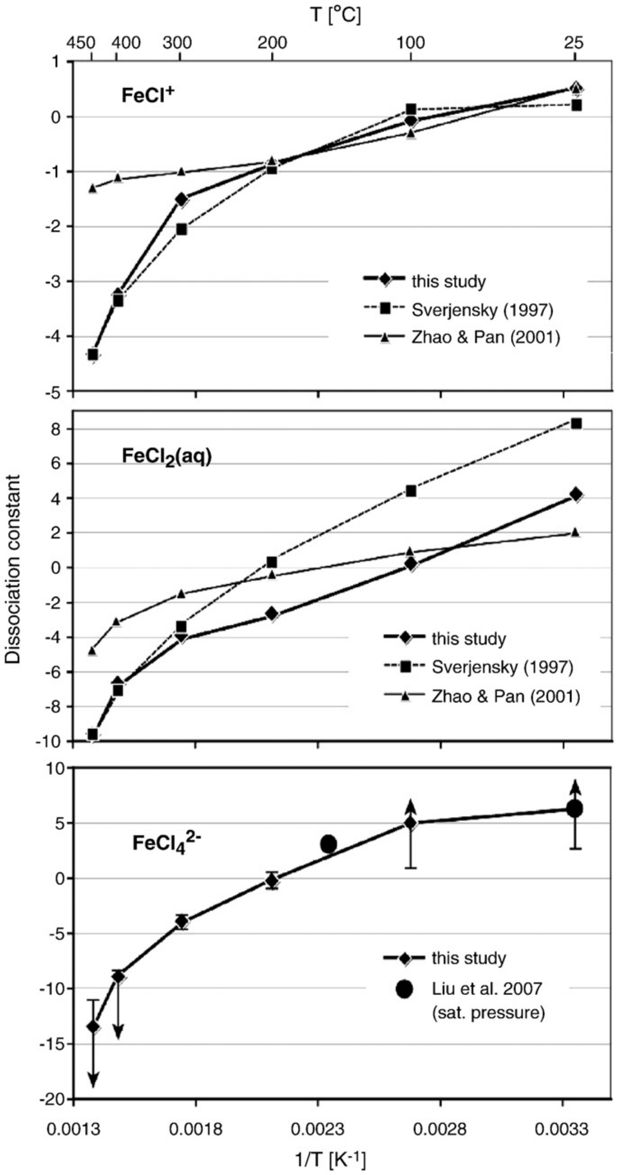

Fig. 9. Comparison of the log(K) of dissociation of $FeCl^+$, $FeCl_2$(aq), and $FeCl_4^{2-}$ derived in this study with those from the literature (data in Table 4). Data are calculated for a pressure of 500 bars, except for Liu et al. (2007) that are at vapour saturation. The error bars and arrows in the $[FeCl_4]^{2-}$ graph are the range of log(K)s corresponding to a 90% confidence level (see Table 4).

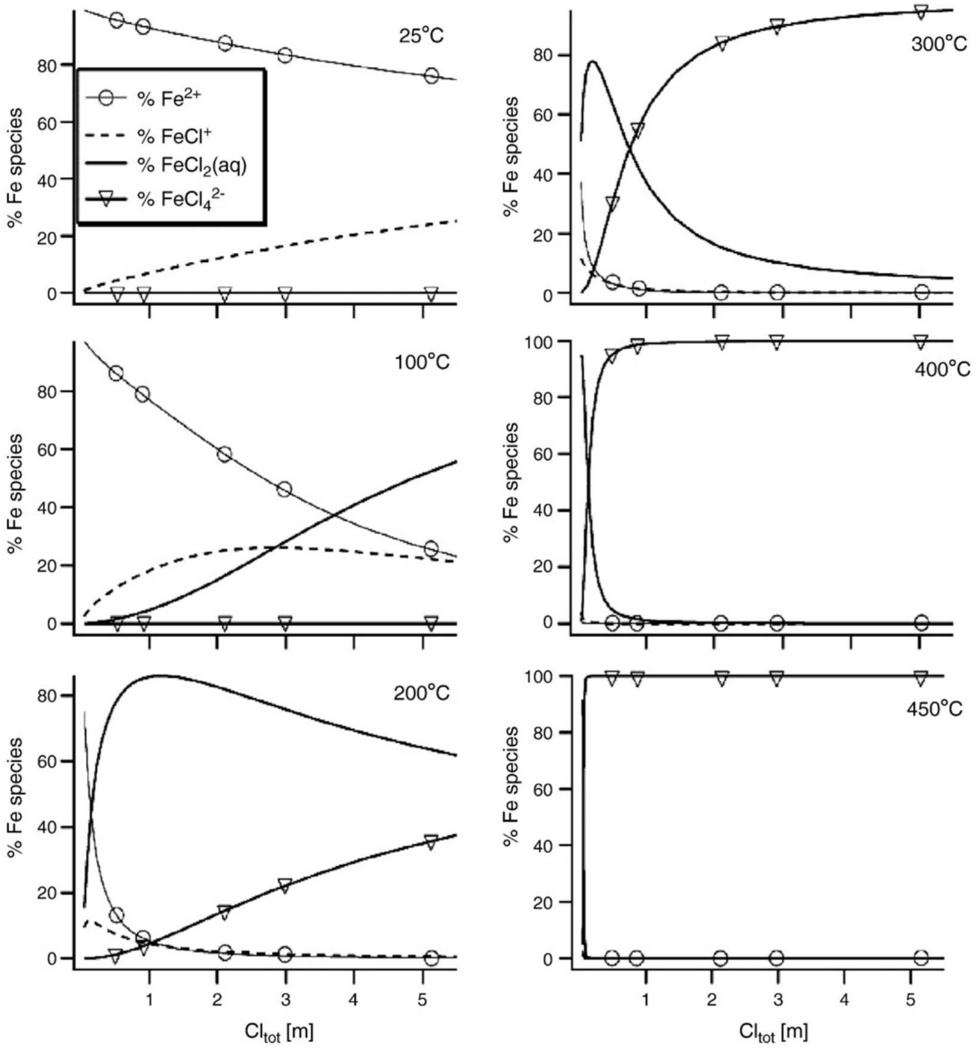

Fig. 10. Results of the speciation and thermodynamic analysis conducted with BeerOz: plots of the distribution of Fe species in our experiments with increasing salt concentration, for each experimental temperature. The symbols on the curves are located at the salinities for which XANES spectra are available.

species was not considered in the experimental studies underlying Sverjensky et al.'s (1997) extrapolation. At the temperatures of 400 °C and 450 °C no octahedral species are detected in solutions with ≥0.5 m chloride, so our data do not provide any information on equilibria among octahedral species at those temperatures; the values from Sverjensky et al. (1997) were retained.

For $FeCl_2(aq)$, the proposed values (Fig. 9b; Table 4) were derived using the following principles: favour the values of Zhao and Pan (2001) at $T \leq 150$ °C, as this study uses the correct speciation model; and use the extrapolations of Sverjensky et al. (1997) at $T \geq 400$ °C. At 200 °C and 300 °C, where the XANES dataset allows the most detailed study of the octahedral to tetrahedral transition from $FeCl_2(aq)$ to $[FeCl_4]^{2-}$, it was found that the literature values were too high. The fitting responded to this by predicting a XANES spectrum for $FeCl_2(aq)$ similar to that of $[FeCl_4]^{2-}$. Values of −2.7 (200 °C) and −3.9 (300 °C) were chosen, that result in realistic spectra for $FeCl_2(aq)$ (Fig. 11). The value at 300 °C is close to Sverjensky et al.'s (1997) value (−3.4, see Fig. 9). At 400 °C, only the first solution (0.547 m Cl) shows a small contribution from an octahedral species. In this case, the stability constants of $FeCl_2(aq)$ and $[FeCl_4]^{2-}$ were manually adjusted in order to be consistent with both the XANES data and the solubility data of Fein et al. (1992) (see below).

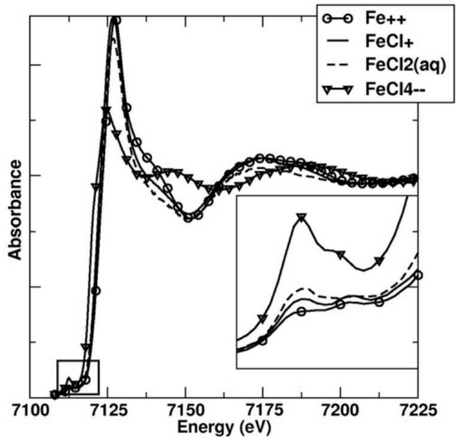

Fig. 11. Results of the speciation and thermodynamic analysis conducted with BeerOz: extracted spectra for the Fe^{2+}, $FeCl^{+}$, $FeCl_{2(aq)}$ and $FeCl_4^{2-}$ species. The inset corresponds to the pre-edge region.

Table 5
The sources of thermodynamic properties for mineral and aqueous species used in the calculations of the solubility of iron minerals.

Species	Data sources
$Fe(OH)^+$, $Fe(OH)_{2(aq)}$	Shock et al. (1997)
Magnetite	Berman (1988)
Pyrrhotite	Robie and Hemingway (1995)
Pyrite	Helgeson et al. (1978)
K-feldspar, muscovite and quartz	Berman (1988)
Dissociation constant of water	Marshall and Franck (1981)
K^+, Cl^-	Shock and Helgeson (1988)
$HCl_{(aq)}$	Pokrovskii (1999)
$KCl_{(aq)}$	Sverjensky et al. (1997)
HS^-	Shock and Helgeson (1988)
$H_2S_{(aq)}$	Shock et al. (1989)

The properties and sources of other species used in the calculations are listed in Table 4.

The results of the final fit are shown in Figs. 10 and 11. The final fit was performed on the whole dataset, excluding the highest chloride concentration 12.031 m (i.e., 0.547–5.055 m Cl_{tot}; T 25–450 °C; P 500 bar). The spectra of all the four Fe^{2+} complexes in the model were refined over all data, while individual log(K)s for the dissociation of $[FeCl_4]^{2-}$ were refined independently at each temperature. The residual (χ^2) for the chosen model is 0.41. It should be noted that a limitation with our approach is that because some species are not present at some temperatures, only a minimum or maximum in the dissociation constant for that absent species can be retrieved at these temperatures (shown by arrows in Fig. 9). For example, the log(K) value for $[FeCl_4]^{2-}$ at 25 °C is only constrained to be in excess of 2.4 by our experiments; this is consistent with the value of 6.2 determined by Liu et al. (2007) using the same approach on a wider range of Cl concentrations, so their value is retained here. Liu et al.'s (2007) value at 150 °C is 2.9, lying between our values at 100 °C and 200 °C (Table 4).

The retrieved spectra for the individual species (Fig. 11) indicate that Fe^{2+}, $FeCl^+$, and $FeCl_2$(aq) have octahedral structures. The main differences between the spectrum of Fe^{2+} and those of the chloro-complexes $FeCl^+$ and $FeCl_{2(aq)}$ is the decrease in intensity of the band around 7140 eV. $FeCl_{2(aq)}$ also shows a decrease in the intensity of the white line relative to the other octahedral complexes. Note that the spectrum for Fe^{2+} is strongly constrained by the 25 °C dataset, as this species dominates in these solutions (Fig. 10). $FeCl^+$ is important only at low temperature (<150 °C), and even then it is only a minor species (<30%, see Fig. 10). Consequently, its retrieved XANES spectrum suffers from the greatest uncertainty. The results at room temperature are in agreement with the EXAFS results, showing only a small amount of chlorine in the solvation shell (Fig. 10). Similarly, the spectrum of $[FeCl_4]^{2-}$ is determined by the high-temperature datasets (400 °C and 450 °C), where this complex is nearly the only one present. In contrast, $FeCl_{2(aq)}$ appears to be dominant at 200 °C, and is also an important complex at 100 °C and at low salinity at 300 °C.

It is interesting to compare the spectra of the octahedral species in Figs. 7 and 11. First, the main features of Fig. 11, i.e., the decrease of the shoulder at 7140 eV with increasing chloride coordination as well as the increase of the intensity at 7150 eV, follow the same trend in Fig. 7 (features A and B respectively). Finally, the intensity of the white line slightly decreases between Fe^{2+} and $FeCl_2$(aq), and the crest of the latter is shifted towards slightly lower energy in both figures. Note that in Fig. 11 Fe^{2+} and $FeCl^+$ have essentially identical spectra; indeed the calculated spectrum of $FeCl^+$ appears to be very sensitive to the choice of log(K) for the formation of $FeCl^+$ and $FeCl_2$(aq), and can vary from being similar to the spectrum of Fe^{2+} or to that of $FeCl_2$

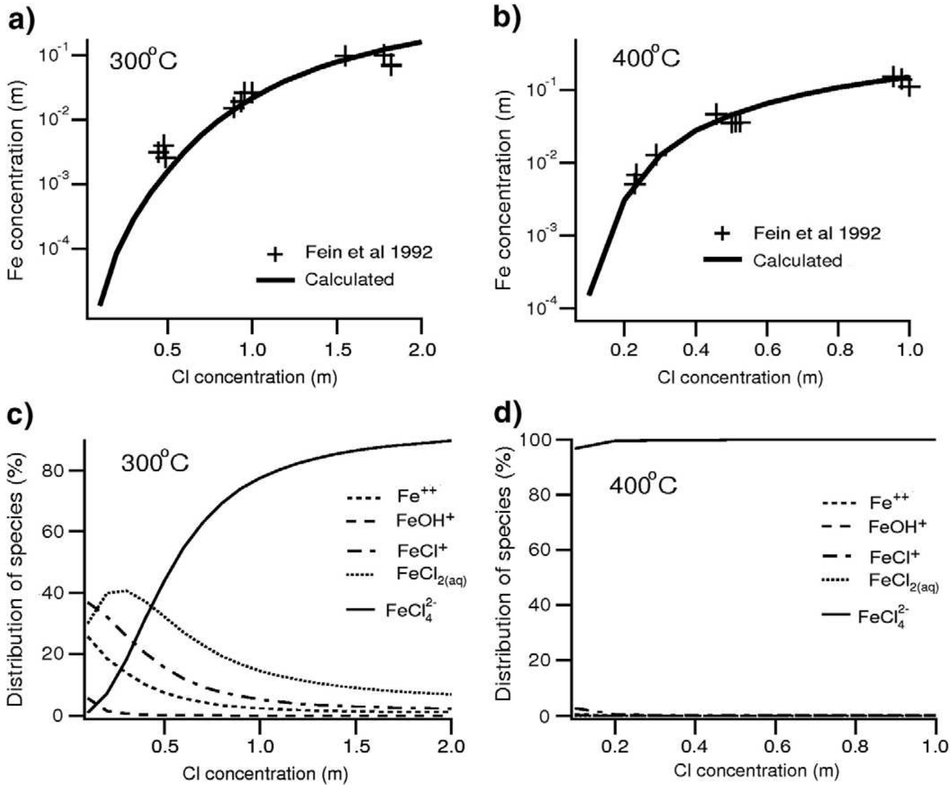

Fig. 12. Experimental and calculated solubilities of the mineral assemblage magnetite–pyrite–pyrrhotite–quartz–muscovite–K-feldspar in KCl solutions at 500 bars and 300 °C (a) and 400 °C (b). The solid crosses are experimental values by Fein et al. (1992), and the lines represent calculated values based on the log(K) data derived from this study. Bottom plots are the corresponding calculated distribution of species at 300 °C (c) and 400 °C (d).

(aq). This reflects the strong co-linearity among these three species. This overall agreement, for intermediate chlorinated species, between two independent methods gives support to our speciation model.

The octahedral–tetrahedral transition as a function of temperature and chloride concentration observed in this study is consistent with the general trend observed for the first-row transition metals as described in a qualitative UV study (Susak and Crerar, 1985). Our log (*K*) values for $FeCl_4^{2-}$ (Table 4) are comparable to the only available data for $ZnCl_4^{2-}$ (e.g., −9.01 at 300 °C and water-saturated pressures, Ruaya and Seward, 1986). Two XAS studies also show that $ZnCl_4^{2-}$ is predominant in saline fluid inclusions (Anderson et al., 1998) and 6 m chloride solutions at high temperature and pressure (Mayanovic et al., 1999).

4.2. Solubility of iron minerals in chloride solutions

In this section we calculate the solubility of iron minerals in chloride solutions using the data generated from this study (Table 4), and compare with existing experimental values. The solubility of the magnetite–pyrite–pyrrhotite–quartz–muscovite–K-feldspar assemblage in KCl solutions was calculated using the HCh program and the UNITHERM database (Shvarov and Bastrakov, 1999). The source of the thermodynamic properties for the mineral and aqueous species other than Fe(II) chloride species are listed in Table 5. The results are compared with the experimental values obtained by Fein et al. (1992) in Fig. 12a and c (300 °C, 500 bars) and b, d (400 °C, 500 bar). The calculated solubilities are within half an order of magnitude of the experimental measurements. It should be noted that the calculations rely on accurate estimation of the pH and redox conditions prevailing at the experimental conditions, and hence a ~half an order of magnitude discrepancy is well within uncertainty. This good agreement at 300 °C is a strong indicator of the validity of our approach. At this temperature, the formation constants of both $FeCl_2$(aq) and $[FeCl_4]^{2-}$ are well constrained by our XANES data. At 400 °C, the good agreement reflects the fact that the formation constants of both complexes were adjusted to fit Fein et al. (1992) solubility data, but it is also an important confirmation of our results, as it shows that this dataset can be interpreted satisfactorily using $FeCl_4^{2-}$ as a major species over most of the experimental conditions. The original interpretation stressed the dominance of the neutral $FeCl_2$(aq) species, but the latter hypothesis is not supported by our XANES or EXAFS spectra and calculations, and there is little doubt that the end-member species (450 °C, 5.055 m Cl^-) is indeed a high-order chlorocomplex, such as $FeCl_4^{2-}$; the exact nature of this complex, whether it is distorted, and its formal charge (possible presence of Na^+ in the second shell) still remain to be confirmed. In this context, experiments where both *in-situ* solubility and spectroscopy measurements are conducted in parallel are of high interest: see for example the works by Pokrovski et al. (2005, 2006) and Liu et al. (2008).

5. Conclusions

This study emphasises the importance of high-order chlorocomplexes (i.e., tetrahedral $[FeCl_4]^{2-}$) in iron transport and deposition in high-temperature hydrothermal fluids ($T \geq 300$ °C; Fig. 10). Several previous studies have revealed a similar trend for the first-row transition metal chlorocomplexes. Susak and Crerar (1985) first demonstrated by means of a qualitative UV–Vis study the occurrence of the octahedral–tetrahedral (Oh–Td) transition behaviour of Co(II), Ni(II), Cu(II) and Fe(II) chlorocomplexes under hydrothermal conditions. Hoffmann et al.'s (1999) study provided EXAFS evidence of this transition for Ni(II) chloride complexes, and Mayanovic et al. (1997, 1999) and Anderson et al. (1998) for the Zn(II) chlorocomplexes. Our study quantitatively describes such a change for Fe(II) chlorocomplexes. The driving force of the Oh–Td change has been attributed to the decrease of the dielectric constant of the solvent (water) and ligand-field energy stabilisation as a function of temperature (e.g. Susak and Crerar, 1985), but more work is needed to understand the mechanism at the molecular level.

The recognition of the stability of high-order chlorocomplexes at high *P*–*T*, and the mapping of the conditions under which this tetrahedral complex ($[FeCl_4]^{2-}$) is replaced by octahedral complexes ($[FeCl_x(H_2O)_{6-x}]^{2-x}$, $x = 0$–2), has first-order consequences for our understanding of the transport of Fe in hydrothermal systems. This Oh–Td transition means that the solubility of Fe minerals is strongly affected by the activity of the chloride ion, and hence that dilution is going to cause a strong decrease in the solubility of Fe minerals. A decrease in temperature will have a similar effect. The thermodynamic properties provided here significantly improve our ability to model accurately Fe mobility in important ore-forming environments, in particular Iron Oxide Copper Gold systems (e.g., Haynes et al., 1994; Pollard, 2006) and porphyry copper systems (e.g. Herzarkhani et al., 1999).

In such high-temperature conditions, the XAS techniques are not sensitive to the presence and nature of a second shell (poorer data quality due to absorption by the window materials; larger thermal disorder). More precisely, although the existence of a tetrahedral $[FeCl_4]^{2-}$ entity is ascertained, the possibility of having two Na^+ or H^+ ions bound to this complex to ensure a neutral charge is not ruled out. If such a species was indeed the dominant one, its thermodynamic properties would differ slightly from the ones derived in this study because of differences in calculated activity coefficients for species of different formal charges. Further experiments (i.e., comparing speciation at different ionic strengths, pH, and background electrolyte) coupled with molecular dynamic simulations are required to explore this question. Nonetheless, the excellent agreement between the experimental Fe concentrations in Fein et al.'s (1992) solubility experiments and those calculated using the thermodynamic properties derived independently in this study provides strong support for the validity of our XAS-based approach.

Acknowledgements

The authors are particularly grateful to Harald Müller for help with work in the chemistry laboratory at the ESRF. The research has been supported by the Australian Research Council (DP0208323 and DP0878903 to J.B.; LX0667264 to J.B. and D.T.), and by an Access to Major Research Facilities research grant administered by the Australian Nuclear Science and Technology Organisation. The authors acknowledge the European Synchrotron Radiation Facility for provision of synchrotron radiation beamtime and facilities and would like to thank the FAME team for assistance in using their beamline.

References

Anderko, A., Pitzer, K.S., 1993. Equation-of-state representation of phase equilibria and volumetric properties of the system NaCl–H_2O above 573 K. Geochim. Cosmochim. Acta 57, 1657–1680.

Anderson, G.M., 2005. Thermodynamics of Natural Systems, 2nd edition. Cambridge University Press. 662 pp.

Anderson, G.M., Castet, S., Schott, J., Mesmer, R.E., 1991. The density model for estimation of thermodynamic parameters of reactions at high temperatures and pressures. Geochim. Cosmochim. Acta 55, 1769–1779.

Anderson, A.J., Mayanovic, R.A., Bajt, S., 1998. A microbeam XAFS study of aqueous chlorozinc complexing to 430 °C in fluid inclusions from the Knaumühle granitic pegmatite, Saxonian granulite facies, Germany. Can. Mineral. 36, 511–524.

Apted, M.J., Waychunas, G.A., Brown, G.E., 1985. Structure and specification of iron complexes in aqueous solutions determined by X-ray absorption spectroscopy. Geochim. Cosmochim. Acta 49, 2081–2089.

Baes Jr., C.F., Mesmer, R.E., 1976. The Hydrolysis of Cations. Wiley, New York.

Bakker, R.J., 2003. Package FLUIDS 1. Computer programs for analysis of fluid inclusion data and for modelling bulk fluid properties. Chem. Geol. 194, 3–23.

Bassett, W.A., Anderson, A.J., Mayanovic, R.A., Chou, I.M., 2000. Hydrothermal diamond anvil cell for XAFS studies of first-row transition elements in aqueous solution up to supercritical conditions. Chem. Geol. 167, 3–10.

Benfatto, M., Della Longa, S., 2001. Geometrical fitting of experimental XANES spectra by a full multiple-scattering procedure. J. Synchrotron Radiat. 8, 1087–1094.

Benfatto, M., Solera, J.A., Chaboy, J., Proietti, M.G., García, J., 1997. Theoretical analysis of X-ray absorption near-edge structure of transition-metal aqueous complexes in solution at the metal K edge. Phys. Rev. B 56 (5), 2447–2452.

Benfatto, M., D'Angelo, P., Della Longa, S., Pavel, N.V., 2002. Evidence of distorted fivefold coordination of the Cu2+ aqua ion from an X-ray-absorption spectroscopy quantitative analysis. Phys. Rev. B 65, 174205.

Benfatto, M., Della Longa, S., Natoli, C.R., 2003. The MXAN procedure: a new method for analysing the XANES spectra of metallo-proteins to obtain structural quantitative information. J. Synchrotron Radiat. 10, 51–57.

Berman, R.G., 1988. Internally-consistent thermodynamic data for minerals in the system Na_2O–K_2O–CaO–MgO–FeO–Fe_2O_3–Al_2O_3–SiO_2–TiO_2–H_2O–CO. J. Petrol. 29, 445–522.

Bischoff, J.L., Pitzer, K.S., 1989. Liquid-vapor relations for the system NaCl–H_2O: summary of the P–T–x surface from 300 °C to 500 °C. Am. J. Sci. 289, 217–248.

Boctor, N.Z., Popp, R.K., Frantz, J.D., 1980. Mineral-solution equilibria; IV, solubilities and the thermodynamic properties of $FeCl^0_2$ in the system Fe_2O_3 –H_2 –H_2O–HCl. Geochim. Cosmochim. Acta 44, 1509–1518.

Booth, C.H., Bridges, F., 2005. Improved self-absorption correction for fluorescence measurements of extended X-ray absorption fine-structure. Phys. Scr. T115, 202–204.

Brugger, J., 2006. BeerOz, a suite of MATLAB routines for the quantitative thermodynamic interpretation of electronic spectra of aqueous complexes. Comput. Geosci. 33, 248–261.

Brugger, J., McPhail, D.C., Black, J., Spiccia, S., 2001. Complexation of metal ions in brines: applications of electronic spectroscopy in the study of the Cu(II)–LiCl–H_2O system between 25 and 90 °C. Geochim. Cosmochim. Acta 65, 2691–2708.

Brugger, J., Etschmann, B., Liu, W., Testemale, D., Hazemann, J.-L., Van Beek, W., Proux, O., 2007. An XAS study of the chloride complexing of Cu(I) in brines. Geochim. Cosmochim. Acta 71, 4920–4941.

Bruyère, R., Prat, A., Goujon, C., Hazemann, J.-L., 2008. A new pressure regulation device using high pressure isolation valves. J. Phys.: Conf. Ser. 121, 122003.

Bugaev, L.A., Ildefonse, P., Flank, A.-M., Sokolenko, A.P., Dmitrienko, H.V., 1998. Aluminum K-XANES spectra in minerals as a source of information on their local atomic structure. J. Phys.: Condens. Matter 10, 5463–5473.

Bunker, G., 1983. Application of the ratio method of EXAFS analysis to disordered systems. Nucl. Instrum. Methods Phys. Res. 207, 437.

Chaboy, J., Muñoz-Páez, A., Merkling, P.J., Sánchez Marcos, E., 2006. The hydration of Cu^{2+}: Can the Jahn-Teller effect be detected in liquid solution? J. Chem. Phys. 124, 064509.

Chou, I.M., Eugster, H.P., 1977. Solubility of magnetite in supercritical chloride solutions. Am. J. Sci. 277, 1296–1314.

Coulet, M.-V., Testemale, D., Hazemann, J.-L., Gaspard, J.-P., Bichara, C., 2005. Local order in liquid $Ge_{0.15}Te_{0.85}$ alloy studied by X-ray Absorption Spectroscopy and a reverse Monte Carlo analysis. Phys. Rev. B 72, 174209.

Crerar, D.A., Susak, N.J., Borcsik, M., Schwartz, S., 1978. Solubility of the buffer assemblage pyrite + pyrrhotite + magnetite in NaCl solutions from 200 to 350 °C. Geochim. Cosmochim. Acta 42, 1427–1438.

Crerar, D.A., Wood, S., Brantley, S., 1985. Chemical controls on solubility of ore-forming minerals in hydrothermal solutions. Can. Mineral. 23, 333–352.

D'Angelo, P., Benfatto, M., 2004. Effect of multielectronic configurations on the XAFS analysis at the Fe K edge. J. Phys. Chem. A 108, 4505–4514.

D'Angelo, P., Benfatto, M., Della Longa, S., Pavel, N.V., 2002. Combined XANES and EXAFS analysis of Co^{2+}, Ni^{2+}, and Zn^{2+} aqueous solutions. Phys. Rev. B 66, 064209.

D'Angelo, P., Roscioni, O.M., Chillemi, G., Della Longa, S., Benfatto, M., 2006. Detection of second hydration shells in ionic solutions by XANES: computed spectra for Ni^{2+} in water based on Molecular Dynamics. J. Am. Chem. Soc. 128, 1853–1858.

Ding, K., Seyfried Jr., W.E., 1992. Determination of iron-chlorine complexing in the low-pressure supercritical region (sodium chloride fluid): iron solubility constraints on pH subseafloor hydrothermal fluids. Geochim. Cosmochim. Acta 56, 3681–3692.

Fein, J.B., Hemley, J.J., D'Angelo, W.M., Komninou, A., Sverjensky, D.A., 1992. Experimental study of iron-chloride complexing in hydrothermal fluids. Geochim. Cosmochim. Acta 56, 3179–3190.

Ferlat, G., Soetens, J.-C., San Miguel, A., Bopp, P.A., 2005. Combining extended X-ray absorption fine structure with numerical simulations for disordered systems. J. Phys.: Condens. Matter 17, 145–157.

Galoisy, L., Calas, G., Arrio, M.A., 2001. High-resolution XANES spectra of iron in minerals and glasses: structural information from the pre-edge region. Chem. Geol. 174, 307–319.

Garcia, J., Bianconi, A., Benfatto, M., Natoli, C.R., 1986. Coordination geometry of transition metal ions in dilute solutions by XANES. J. Phys. 47 (C8), 49–54.

Gu, Y., Gammons, C.H., Bloom, M.S., 1994. A one-term extrapolation method for estimating equilibrium constants of aqueous reactions at elevated temperatures. Geochim. Cosmochim. Acta 58, 3545–3560.

Hayakawa, K., Hatada, K., D'Angelo, P., Della Longa, S., Natoli, C.R., Benfatto, M., 2004. Full quantitative multiple-scattering analysis of X-ray absorption spectra: application to potassium hexacyanoferrat(II) and -(III) complexes. J. Am. Chem. Soc. 126, 15618–15623.

Haynes, D.W., Bills, K.C., Redd, M.H., 1994. Olympic Dam ore genesis: a fluid mixing model. Econ. Geol. 90, 281–307.

Hazemann, J.-L., Nayouf, K., de Bergevin, F., 1995. Modelisation by finite elements of sagittal focusing. Nucl. Instrum. Methods Phys. Res., Sect. B 97, 547–550.

Heinrich, C.A., Seward, T.M., 1990. A spectrophotometric study of aqueous iron(II) chloride complexing from 25 to 200 °C. Geochim. Cosmochim. Acta 54, 2207–2221.

Heinrich, C.A., Walshe, J.L., Harrold, B.P., 1996. Chemical mass transfer modelling of ore-forming hydrothermal systems—current practice and problems [Review]. Ore Geol. Rev. 10, 319–338.

Helgeson, H., Kirkham, D.H., 1974. Theoretical prediction of the thermodynamic behavior of aqueous electrolytes at high pressures and temperatures: II. Debye–Hückel parameters for activity coefficients and relative partial molal properties. Am. J. Sci. 274, 1199–1261.

Helgeson, H.C., Delany, J.M., Nesbitt, H.W., Bird, D.K., 1978. Summary and critique of the thermodynamic properties of rock-forming minerals. Am. J. Sci. 278A, 229.

Helgeson, H., Kirkham, D.H., Flowers, G.C., 1981. Theoretical prediction of the thermodynamic behavior of aqueous electrolytes at high pressures and temperatures: IV. Calculation of activity coefficients, osmotic coefficients, and apparent molal and standard and relative partial molal properties to 600 °C and 5 kb. Am. J. Sci. 281, 1249–1516.

Herdman, G.J., Neilson, G.W., 1992. Ferrous Fe(II) hydration in a 1 molal heavy water solution of iron chloride. J. Phys.: Condens. Matter 4, 649–653.

Herzarkhani, A., Williams-Jones, A.E., Gammons, C.H., 1999. Factors controlling copper solubility and chalcopyrite deposition in the Sungun porphyry copper deposit, Iran. Miner. Depos. 34, 770–783.

Ho, P.C., 2001. Conductivity measurements of dilute aqueous HCl solutions to high temperatures and pressures using a flow-through cell. J. Phys. Chem. B105, 1260–1266.

Hoffmann, M.M., Darab, J.G., Palmer, B.J., Fulton, J.L., 1999. A transition in the Ni^{2+} complex structure from six- to four-coordinate upon formation of ion pair species in supercritical water: an X-ray absorption fine structure, Near-Infrared, and Molecular Dynamics study. J. Phys. Chem. 103, 8471–8482.

Hoffmann, M.M., Darab, J.G., Heald, S.M., Yonker, C.R., Fulton, J.L., 2000. New experimental developments for in situ XAFS studies of chemical reactions under hydrothermal conditions. Chem. Geol. 167, 89–103.

Inada, Y., Funahashi, S., 1999. Equilibrium and structural study of chloro-complexes of iron(III) ion in acidic aqueous solution by means of X-ray absorption spectroscopy. Z. Naturforsch., B: Chem. Sci. 54, 1517–1523.

Johnson, J.W., Oelkers, E.H., Helgeson, H.C., 1992. SUPCRT92: a software package for calculating the standard molal thermodynamic properties of minerals, gazes, aqueous species and reactions from 1 to 5000 bars and 0° to 1000 °C. Comput. Geosci. 18, 899–920.

Joly, Y., 2001. X-ray absorption near-edge structure calculations beyond the muffin-tin approximation. Phys. Rev. B 63, 125120.

Joly, Y., Cabaret, D., Renevier, H., Natoli, C.R., 1999. Electron population analysis by full-potential X-ray absorption simulations. Phys. Rev. Lett. 82, 2398–2401.

Kielland, J., 1937. Individual activity coefficients of ions in aqueous solutions. J. Amer. Chem. Soc. 59, 1675–1678.

Koplitz, L.V., McClure, D.S., Crerar, D.A., 1987. Spectroscopic study of chloroiron(II) complexes in LiCl–DCl–D_2O solutions. Inorg. Chem. 26, 308–313.

Krause, M.O., Oliver, J.H., 1979. Natural widths of atomic K and L levels, K alpha X-ray lines and several KLL Auger lines. J. Phys. Chem. Ref. Data 8, 329.

Kritzer, P., Boukis, N., Dinjus, E., 1999. Factors controlling corrosion in high-temperature aqueous solutions: a contribution to the dissociation and solubility data influencing corrosion processes. J. Supercrit. Fluids 15, 205–227.

Lauher, J.W., Ibers, J.A., 1975. Structure of Tetramethylammonium tetrachloroferrate(II), $[N(CH_3)_4]_2[FeCl_4]$. Comparison of iron(II) and iron(III) bond lengths in high-spin tetrahedral environments. Inorg. Chem. 14 (2), 348.

Liu, W., Brugger, J., McPhail, D.C., Spiccia, L., 2002. A spectrophotometric study of aqueous copper(I)-chloride complexes in LiCl solutions between 100 °C and 250 °C. Geochim. Cosmochim. Acta 66, 3615–3633.

Liu, W., Etschmann, B., Brugger, J., Foran, G., Spiccia, L., McInnes, B., 2006. UV–Vis spectrophotometric and XAFS studies of ferric chloride complexes in hyper-saline LiCl solutions at 25–90 °C. Chem. Geol. 231, 326–349.

Liu, W., Etschmann, B., Foran, G., Shelley, M., Brugger, J., 2007. Deriving formation constants for aqueous metal complexes from XANES spectra: Zn(II) and Fe(II) chloride complexes in hypersaline solutions. Am. Mineral. 92, 761–770.

Liu, W., Brugger, J., Etschmann, B., Testemale, D., Hazemann, J.-L., 2008. The solubility of nantokite (CuCl(s)) and Cu speciation in low density fluids near the critical isochore: an *in-situ* XAS study. Geochim. Cosmochim. Acta 72, 4094–4106.

Marshall, W.L., Franck, E.U., 1981. Ion product of water substance, 0–1000 degrees C, 1–10000 bars, new international formulation and its background. J. Phys. Chem. Ref. Data 10, 295–304.

Mayanovic, R.A., Anderson, A.J., Bajt, S., 1997. Microbeam XAFS studies on fluid inclusions at high temperatures. J. Phys. IV 7, 1029–1030.

Mayanovic, R.A., Anderson, A.J., Bassett, W.A., Chou, I.M., 1999. XAFS measurements on zinc chloride aqueous solutions from ambient to supercritical conditions using the diamond anvil cell. J. Synchrotron Radiat. 6, 195–197.

Mibe, K., Chou, I.-M., Anderson, A.J., Mayanovic, R.A., Bassett, W.A., 2009. The speciation of aqueous zinc(II) bromide solutions to 500 °C and 900 MPa determined using Raman spectroscopy. Chem. Geol. 259, 48–53.

Mustre de Leon, J., Rehr, J.J., Zabinsky, S.I., Albers, R.C., 1991. *Ab initio* curved-wave X-ray-absorption fine structure. Phys. Rev. B 44 (9), 4146–4156.

Newville, M., 2001. IFEFFIT: interactive XAFS analysis and FEFF fitting. J. Synchrotron Radiat. 8, 322–324.

Newville, M., Livins, P., Yacoby, Y., Rehr, J.J., Stern, E.A., 1993. Near-edge X-ray absorption fine structure of Pb: a comparison of theory and experiment. Phys. Rev. B 47, 14126–14131.

Newville, M., Ravel, B., Haskel, D., Rehr, J.J., Stern, E.A., Yacoby, Y., 1995. Analysis of multiple-scattering XAFS data using theoretical standards. Physica B 208–209, 154–156.

Ohmoto, H., Hayashi, K.-I., Kajisa, Y., 1994. Experimental study of the solubilities of pyrite in NaCl-bearing aqueous solutions at 250–350 °C. Geochim. Cosmochim. Acta 58, 2169–2185.

Palmer, D.A., Hyde, K.E., 1993. An experimental determination of ferrous chloride and acetate complexation in aqueous solutions to 300 °C. Geochim. Cosmochim. Acta 57, 1393–1408.

Parsons, J.G., Aldrich, M.V., Gardea-Torresdey, J.L., 2002. Environmental and biological applications of extended X-ray absorption fine structure (EXAFS) and X-ray absorption near edge structure (XANES) spectroscopies. Appl. Spectrosc. Rev. 37 (2), 187–222.

Poiarkova, A.V., 1999. X-ray absorption fine structure Debye–Wallor factors. Ph. D. thesis, University of Washington.

Pokrovskii, V.A., 1999. Calculation of the standard partial molal thermodynamic properties and dissociation constants of aqueous HCl^0 and HBr^0 at temperatures to 1000 °C and pressures to 5 kbar. Geochim. Cosmochim. Acta 63, 1107–1115.

Pokrovski, G.S., Zakirov, I.V., Roux, J., Testemale, D., Hazemann, J.-L., Bychkov, A.Y., Golikova, G.V., 2002. Experimental study of arsenic speciation in vapor phase to 500 °C: implications for As transport and fractionation in low-density crustal fluids and volcanic gases. Geochim. Cosmochim. Acta 66, 3453–3480.

Pokrovski, G.S., Schott, J., Farges, F., Hazemann, J.-L., 2003. Iron (III)–silica interactions in aqueous solution: insights from X-ray absorption fine structure spectroscopy. Geochim. Cosmochim. Acta 67, 3559–3573.

Pokrovski, G.S., Roux, J., Hazemann, J.-L., Testemale, D., 2005. An X-ray absorption spectroscopy study of argutite solubility and germanium aqueous speciation in hydrothermal fluids to 500 °C and 400 bar. Chem. Geol. 217, 127–145.

Pokrovski, G.S., Borisova, A.Y., Roux, J., Hazemann, J.-L., Petdang, A., Tella, M., Testemale, D., 2006. Antimony speciation in saline hydrothermal fluids: a combined X-ray absorption fine structure spectroscopy and solubility study. Geochim. Cosmochim. Acta 70, 4196–4214.

Pokrovski, G.S., Tagirov, B.R., Schott, J., Bazarkina, E.F., Hazemann, J.-L., Proux, O., 2009. An in situ x-ray absorption spectroscopy study of gold-chloride complexing in hydrothermal fluids. Chem. Geol. 259, 17–29.

Pollard, P.J., 2006. An intrusion-related origin for Cu–Au mineralization in iron oxide–copper–gold (IOGG) provinces. Miner. Depos. 41, 179–187.

Proux, O., Biquard, X., Lahera, E., Menthonnex, J.-J., Prat, A., Ulrich, O., Soldo, Y., Trevisson, P., Kapoujyan, G., Perroux, G., Taunier, P., Grand, D., Jeantet, P., Deleglise, M., Roux, J.-P., Hazemann, J.-L., 2005. FAME: a new beamline for X-ray absorption investigations of very diluted systems of environmental, material and biological interests. Phys. Scr. T115, 970–973.

Proux, O., Nassif, V., Prat, A., Ulrich, O., Lahera, E., Biquard, X., Menthonnex, J.-J., Hazemann, J.-L., 2006. Feedback system of a liquid-nitrogen-cooled double-crystal monochromator: design and performances. J. Synchrotron Radiat. 13, 59–68.

Ravel, B., Newville, M., 2005. ATHENA, ARTEMIS, HEPHAESTUS: data analysis for X-ray absorption spectroscopy using IFEFFIT. J. Synchrotron Radiat. 12, 537–541.

Remsungnen, T., Rode, B.M., 2003. QM/MM Molecular dynamics simulation of the structure of hydrated Fe(II) and Fe(III) ions. J. Phys. Chem. A 107, 2324–2328.

Robie, R.A., Hemingway, B.S., 1995. Thermodynamic Properties of Minerals and Related Substances at 298.15 K and 1 bar (10^5 Pascals) Pressure and at Higher Temperatures. U. S. Geological Survey, Reston.

Ruaya, I.R., Seward, T.M., 1986. The stability of chlorozinc(II) complexes in hydrothermal solutions up to 300 °C. Geochim. Cosmochim. Acta 50, 651–661.

Rueff, J.-P., Journel, L., Petit, P.-E., Farges, F., 2004. Fe K pre-edges as revealed by resonant X-ray emission. Phys. Rev. B 69, 235107.

Seward, T.M., Barnes, H.L., 1997. Metal transport by hydrothermal ore fluids. In: Barnes, H.L. (Ed.), Geochemistry of Hydrothermal Ore Deposits. Wiley, New York, pp. 435–486.

Seward, T.M., Driesner, T., 2004. Hydrothermal solution structure: experiments and computer simulations. In: Palmer, D.A., Fernández-Prini, R., Harvery, A.H. (Eds.), Aqueous Systems at Elevated Temperatures and Pressure. Elsevier Academic Press, pp. 149–182.

Seward, T.M., Henderson, C.M.B., Charnock, J.M., Dobson, B.R., 1996. An X-Ray Absorption (EXAFS) spectroscopic study of aquated Ag+ in hydrothermal solutions to 350 °C. Geochim. Cosmochim. Acta 60, 2273–2282.

Simonet, V., Calzavara, Y., Hazemann, J.-L., Argoud, R., Geaymond, O., Raoux, D., 2002. X-ray absorption spectroscopy studies of ionic association in aqueous solutions of zinc bromide from normal to critical conditions. J. Chem. Phys. 117, 2771–2781.

Shock, E.L., Helgeson, H.C., 1988. Calculation of the thermodynamic and transport properties of aqueous species at high pressures and temperatures; correlation algorithms for ionic species and equation of state predictions to 5 kb and 1000 °C. Geochim. Cosmochim. Acta 52, 2009–2036.

Shock, E.L., Helgeson, H.C., Sverjensky, D., 1989. Calculation of the thermodynamic and transport properties of aqueous species at high pressures and temperatures; standard partial molal properties of inorganic neutral species. Geochim. Cosmochim. Acta 53, 2157–2183.

Shock, E.L., Sassani, D.C., Willis, M., Sverjensky, D.A., 1997. Inorganic species in geologic fluids: correlations among standard molal thermodynamic properties of aqueous ions and hydroxide complexes. Geochim. Cosmochim. Acta 61, 907–950.

Shvarov, Y.V., Bastrakov, E.N., 1999. HCh, a Software Package for Geochemical Equilibrium Modeling: User's Guide. Australian Geological Survey Organisation. Record 1999/25.

Smolentsev, G., Soldatov, A.V., 2006. Quantitative local structure refinement from XANES: multi-dimensional interpolation approach. J. Synchrotron Radiat. 13, 19–29.

Smolentsev, G., Soldatov, A.V., Feiters, M.C., 2007. Three-dimensional local structure refinement using a full-potential XANES analysis. Phys. Rev. B 75, 144106.

Susak, N.J., Crerar, D.A., 1985. Spectra and coordination changes of transition metals in hydrothermal solutions: implications for ore genesis. Geochim. Cosmochim. Acta 49, 555–564.

Sverjensky, D.A., Shock, E.L., Helgeson, H.C., 1997. Prediction of the thermodynamic properties of aqueous metal complexes to 1000 °C and 5 kb. Geochim. Cosmochim. Acta 61, 1359–1412.

Testemale, D., Hazemann, J.-L., Pokrovski, G.S., Joly, Y., Roux, J., Argoud, R., Geaymond, O., 2004. Structural and electronic evolution of the $As(OH)_3$ molecule in high temperature aqueous solutions: an X-ray absorption investigation. J. Chem. Phys. 121, 8973–8982.

Testemale, D., Argoud, R., Geaymond, O., Hazemann, J.-L., 2005a. High pressure/high temperature cell for X-ray absorption and scattering techniques. Rev. Sci. Instrum. 76, 043905.

Testemale, D., Coulet, M.-V., Hazemann, J.-L., Simon, J.-P., Geaymond, O., Argoud, R., 2005b. Small angle X-ray scattering of a supercritical electrolyte solution: the effect of ions on local density inhomogeneities. J. Chem. Phys. 122, 194505.

Tooth, B.A., Brugger, J., Liu, W., Ciobanu, C., 2009. Melts in hydrothermal systems: gold scavenging in the liquid bismuth collector model. Geology 36, 815–818.

Tröger, L., Arvanitis, D., Baberschke, K., Michaelis, H., Grimm, U., Zschech, E., 1992. Full correction of the self-absorption in soft-fluorescence extended X-ray-absorption fine structure. Phys. Rev. B 46, 3283–3289.

Waychunas, G.A., Apted, M.J., Brown Jr., G.E., 1983. X-ray K-edge absorption spectra of Fe minerals and model compounds: near-edge structure. Phys. Chem. Miner. 10, 1–9.

Wernet, P., Testemale, D., Hazemann, J.-L., Argoud, R., Glatzel, P., Pettersson, L.G.M., Nilsson, A., Bergmann, U., 2005. Spectroscopic characterization of microscopic hydrogen bonding disparities in supercritical water. J. Chem. Phys. 123, 154503.

Westre, T.E., Kennepohl, P., De Witt, J.G., Hedman, B., Hodgson, K.O., Solomon, E.I., 1997. A multiplet analysis of Fe K-edge 1s–3d pre-edge features of iron complexes. J. Am. Chem. Soc. 119, 6297–6314.

Wilke, M., Farges, F., Petit, P.-E., Brown Jr., G.E., Martin, F., 2001. Oxidation state and coordination of Fe in minerals: an Fe K-XANES spectroscopic study. Am. Mineral. 86, 714–730.

Wood, S.A., Crerar, D.A., Borcsik, M.P., 1987. Solubility of the assemblage pyrite–pyrrhotite–magnetite–sphalerite–galena–gold–stibnite–bismuthinite–argentite–molybdenite in H_2O–NaCl–CO2 solutions from 200 °C to 350 °C. Econ. Geol. 82, 1864–1887.

Zhao, R., Pan, P., 2001. A spectrophotometric study of Fe(II)-chloride complexes in aqueous solutions from 10 to 100 °C. Can. J. Chem. 79, 131–144.

1.2.1.2 Fayalite (Fe_2SiO_4) dissolution kinetics determined by X-ray absorption spectroscopy

Key ideas of the publication:

- XAS measurements were used to determine **the solubility of fayalite, and the kinetics of its dissolution**, at hydrothermal conditions: such data help understanding the availability of iron from the dissolution of ferrous minerals. The equilibrium solubilities (50 mmol) calculated from transmission and fluorescence measurements are in agreement with thermodynamical calculations. Quantitative kinetics parameters (dependence on pH and temperature) were also derived (see figure 4). In parallel, the analysis of XANES spectra confirmed the speciation of Fe^{II} in the fluid. The set of data than were obtained in this study is a solid demonstration of the capabilities of **our setup as a micro-batch reactor**.

- The experimental setup, in particular the way the solid samples are loaded in the inner cell, is described in our siderite study (10), and visible in figure 1.2 (page 41). Its strengths are **1)** the relatively large samples that can be loaded, both solid and liquid (solids are large enough to be characterized *post mortem,* see figure 2 that shows SEM images of "before" and "after" fayalite samples; liquid volume is large enough that ICP-AES measurements can be done on the recovered fluids, see table 2), **2)** the quality of the collected data that are not contaminated by a contribution from the solid, and **3)** the controlled fluid sample volume (the value of the volume is necessary for kinetics normalization).

- This manuscript details **the complementarity of transmission and fluorescence measurements** to determine iron solubility, the difficulty of the latter (see section 3.1 of the publication), and their agreement (see figure 3 of the publication). It also exhaustively exposes the calculation of the error bars of those data, and the uncertainties associated to the presence of impurities in the beryllium (used on the beamline and the autoclave, see chapter 2).

- As it was the case for the earlier siderite study (10), **the interpretation of the spectroscopic data strongly benefited from the speciation study** presented above (7). In particular, since only XANES spectra were acquired during the kinetics runs (to save time) the interpretation of small modifications of XANES features were crucial to understand iron speciation. I wish to highlight the pertinence of this strategy: first determine metal speciation (as a function of temperature and salinity, typically) with experiments where the constituents of the samples are known and at concentrations optimized for spectroscopic measurements, and later use these results to interpret data acquired from more challenging samples (such as dissolution experiments like here, or natural samples[a]).

- This study also unveils one of the limitations of our setup, which is the **lack of *in situ* pH measurement**. This is certainly not a big hurdle for "simple" speciation studies, and is a common trait of all HP cells, but since so many characteristics of our technology make it suitable for thermodynamic studies, this lack is significant. The implementation of *in situ* pH measurements would be a very ambitious undertaking, though.

---

[a] One such example is our study of arsenic speciation in fluid inclusions (13) which deeply benefited from previous XAS studies conducted with our autoclaves in optimized conditions (14, 5).

Chemical Geology 275 (2010) 161–175

Contents lists available at ScienceDirect

Chemical Geology

journal homepage: www.elsevier.com/locate/chemgeo

Research papers

Fayalite (Fe_2SiO_4) dissolution kinetics determined by X-ray absorption spectroscopy

Damien Daval [a,b,*], Denis Testemale [c], Nadir Recham [d], Jean-Marie Tarascon [d], Julien Siebert [e], Isabelle Martinez [a], François Guyot [a,e]

[a] Institut de Physique du Globe de Paris, Centre de Recherches sur le Stockage Géologique du CO_2, 4 Place Jussieu, 75005 Paris, France
[b] Laboratoire de Géologie, UMR 8538 du CNRS, École Normale Supérieure, 24 Rue Lhomond, 75005 Paris, France
[c] Institut Néel, Département MCMF, 25 Avenue des Martyrs, 38042 Grenoble, France
[d] LRCS-UMR 6007-Université de Picardie Jules Verne, 33 rue Saint-Leu, 80039 Amiens, France
[e] Institut de Minéralogie et de Physique des Milieux Condensés, CNRS, Université Paris 6 et 7, 140 rue de Lourmel 75252, Paris, France

ARTICLE INFO

Article history:
Received 20 January 2010
Received in revised form 6 May 2010
Accepted 6 May 2010

Editor: J. Fein

Keywords:
Fayalite
Dissolution rate
In situ X-ray absorption spectroscopy
Hydrothermal fluids
Iron speciation
Acetate ligands

ABSTRACT

Dissolution of fayalite has been monitored in a small size batch reactor at a constant pressure of 30 MPa and temperatures of 50, 65, 80 and 100 °C, either in dilute HCl or in acetate buffered solutions. The technique, based on *in situ* X-ray absorption spectroscopy measurements, allowed simultaneous measurements of aqueous iron concentration and speciation as a function of time under high pressure and high temperature conditions. Far from equilibrium, dissolution rate normalised to geometric surface area (R_{net}) can be described in dilute HCl solutions by:

$$R_{net} = k_0 \exp(-E_a / RT) a^n_{H^+}$$

with $\log(k_0) = 0.17 \pm 0.63$ (k_0 being expressed in mol cm^{-2} s^{-1}); $E_a = 45{,}100 \pm 4200$ J mol^{-1}; $n = 0.74 \pm 0.15$, so that R_{net} is expressed in mol cm^{-2} s^{-1}. These results are found to be consistent with some previous fayalite dissolution studies. In acetate buffered solutions, the dissolution rate was found to be enhanced and positively correlated with the activity of acetate. Whereas speciation of Fe^{2+} in HCl solutions is dominated by hexahydrated octahedral species, the combination of *ab initio* XANES calculations, measurement of X-ray absorption spectra, and thermodynamic modelling allowed us to determine that aqueous Fe^{2+} was complexed octahedrally with two acetate ligands, each bonded to iron through one oxygen atom, the corresponding formula being $Fe(CH_3COO)_2 \cdot 4H_2O$. Supposing that surface complexes resemble the major complex species in solution, this solvation by acetate ions would explain the observed enhancement of the dissolution rate, because of the nucleophilic attack of acetate ligands at the silicate surface.

1. Introduction

Iron-bearing minerals are common phases of surface and subsurface environments. The relative dissolutions of Fe(II) and Fe(III) are important for determining the oxidation and reduction potentials of subsurface fluids. In the presence of aqueous fluids, ferrous-bearing minerals such as olivines are unstable, and thus provide Fe(II) to the fluid phase. This instability makes their dissolution of major importance for living organisms, providing essential nutrients, and more generally, for electron exchange with the environment. With respect to this latter point, the dissolution of Fe-bearing minerals is fundamental because it can be responsible for the generation of reactive reduced species, as is the case, for example, of deep-sea hydrothermal systems reactions: aqueous Fe(II) is oxidised by water to Fe(III), which quickly precipitates as Fe(III)-bearing minerals, while the hydrogen from water is released as H_2. The overall process can be schematically represented by the general reaction (McCollom and Seewald, 2007; see also Berndt et al., 1996 for the particular case of olivine serpentinisation):

$$2(FeO)_{min} + H_2O \rightarrow (Fe_2O_3)_{min} + H_2 \tag{1}$$

where $(FeO)_{min}$ and $(Fe_2O_3)_{min}$ stand for Fe(II)- and Fe(III)-oxides included in minerals of reactants and products. If CO (or CO_2) is also present in the system, the reaction above is crucial, as it represents the first necessary step for the abiotic production of organic compounds following Fischer–Tropsch type (FTT) synthesis, which can be represented in its simplest form by:

$$nCO + (2n+1)H_2 \rightarrow C_nH_{2n+2} + nH_2O, \forall n \in [1, N]. \tag{2}$$

---

[*] Corresponding author. Institut de Physique du Globe de Paris, Centre de Recherches sur le Stockage Géologique du CO_2, 4 place Jussieu, 75005 Paris, France. Tel.: +33 1 44 32 22 90; fax +33 1 44 32 22 00.
E-mail address: daval@ipgp.jussieu.fr (D. Daval).

0009-2541/$ – see front matter. Crown Copyright © 2010 Published by Elsevier B.V. All rights reserved.
doi:10.1016/j.chemgeo.2010.05.005

Besides, the occurrence of organic compounds associated with H_2O–CO_2–Fe(II)-bearing minerals reaction was frequently evidenced both in the field (see McCollom and Seewald, 2007 for a review) and in laboratory experiments (e.g. Berndt et al., 1996; McCollom and Seewald, 2001; McCollom and Seewald, 2006; Dufaud et al., 2009). This underlines the need to obtain accurate rate data for the dissolution step of Fe-bearing minerals, as it could (at least partly) control the production rate of H_2 and abiotic organic compounds.

Recently, the importance of ferrous-bearing amorphous (such as basaltic glass) and crystalline solids has also been highlighted because of their potential role in mineral carbonation, one of the various strategies envisaged in response to rising levels of anthropogenic CO_2 in the atmosphere (e.g. Lackner, 2003). Reaction of fayalite with CO_2, which can be written according to:

$$Fe_2SiO_4 + 2CO_2 \rightarrow 2FeCO_3 + SiO_2 \qquad (3)$$

is thermodynamically favoured ($\Delta G_r^\circ = -30.3$ kJ/mol according to calculations based on data provided in Holland and Powell, 1990). First note that this principle of carbonation scheme might be strongly affected if significant amounts of O_2 are co-injected with CO_2. If this is not the case, reaction (3) is spontaneous at typical pressure and temperature of CO_2 confined in geological reservoirs (up to ~100 °C and a few tens of bars, e.g. Bachu, 2000), but whether carbonation of ferrous phases is an efficient way to store large amounts of CO_2 is an open question since the reaction rates remain poorly constrained. Indeed, in aqueous medium, the overall carbonation reaction can be divided into two main steps: silicate (or oxide) dissolution followed by carbonate precipitation (e.g. Daval et al., 2009a). The release of dissolved ferrous iron may precipitate to form either pure siderite ($FeCO_3$) (see e.g. numerical simulations of CO_2 sequestration by Xu et al., 2004 and Palandri and Kharaka, 2005, and high temperature experiments by Kaszuba et al., 2005) or solid solution like ankerite ($Ca(Fe,Mg)(CO_3)_2$), if the ferrous minerals are, as in basalts, associated to pyroxenes or Ca-feldspars (Dufaud, 2006; McGrail et al., 2006). Studies are thus needed to constrain the dissolution rate of the primary silicates (which, in some cases, controls the overall carbonation rate of silicates, see Daval et al., 2009a for details), as well as the precipitation rate and/or the stability of the neo-formed carbonate minerals under a wide range of realistic conditions of CO_2 sequestration. With respect to siderite ($FeCO_3$), this latter point has received detailed attention in recent studies (Bénézeth et al., 2009; Golubev et al., 2009; Testemale et al., 2009b).

Even though fayalite is not a common mineral of the Earth's crust, it can be considered as a useful standard material for modelling complex processes occurring on Earth and involving Fe-rich olivine solid solutions (e.g. FTT synthesis, carbonation reactions). Moreover, Fe-rich olivines are more widespread in other planetary environments such as the Martian surface (e.g. Fo_{53-68} according to Koeppen and Hamilton, 2006). As a consequence, the accurate knowledge of the dissolution kinetics of the iron end-member olivine is necessary, in order to compute full dissolution rate laws for olivine solid solutions with various compositions, and evaluate for example the persistence of olivine and water on Mars (Olsen and Rimstidt, 2007).

To the best of our knowledge, the data on dissolution kinetics of fayalite are not extensive, and previous studies were restricted to ambient conditions (e.g. Wogelius and Walther, 1992; Casey and Westrich, 1992; Westrich et al., 1993; Santelli et al., 2001), whereas the conditions at which the processes described above (e.g. olivine serpentinisation and CO_2 sequestration) actually take place range from a few tens to a few hundreds of degrees. In addition, the effect of organic ligands, which was shown to promote the dissolution rate of forsteritic olivine (e.g. Grandstaff, 1986; Wogelius and Walther, 1991, 1992; Hänchen et al., 2006; Olsen and Rimstidt, 2008) is unknown for fayalitic olivine, and remains to be investigated. This lack of data thus motivated the present study which aimed at determining the acid pH and temperature dependence (between 50 °C and 100 °C) of fayalite dissolution kinetics, either in dilute HCl (0.05 and 0.1 molal) or in acetate buffered solutions. Because the fast oxidation of Fe(II) to Fe(III) could make the accurate determination of rate laws using classical flow-through reactors a challenging task (both because of the oxidation of fayalite surface, the passivating ability of Fe(III)-rich secondary coatings (e.g. Velbel, 1993) and of errors in Fe dosage), our methodology was based on *in situ* X-ray absorption spectroscopy (XAS) on synchrotron sources, at the iron K-edge. The set-up we used (see Section 2.2) allowed the simultaneous determination of iron concentrations in the fluid, speciation and oxidation state of the corresponding dissolved species, as a function of time: this is a crucial benefit of our method as aqueous Fe^{3+} species were identified to have strong inhibiting effects on fayalite dissolution rates (Santelli et al., 2001). The efficiency of this method for monitoring dissolution of geological materials under elevated pressures and temperatures was recently demonstrated (e.g. Pokrovski et al., 2005, 2006; Testemale et al., 2009b) using the same apparatus.

2. Materials and methods

2.1. Starting materials

2.1.1. Fayalite synthesis and sintering

Fayalite was synthesized under argon at 750 °C for 24 h in an arc-welded stainless steel tube, from Fe_2O_3, Fe metal and SiO_2 powders according to the following reaction:

$$(2/3)Fe_2O_3 + (2/3)Fe^0 + SiO_2 \rightarrow Fe_2SiO_4 \qquad (4)$$

To improve the reactivity, nanometric Fe_2O_3 powders were synthesized from commercial dehydrated Fe(II) oxalate ($FeC_2O_4 \cdot 2H_2O$) by calcination under air at 400 °C for 10 h. For the same reason, SiO_2 nano-powders were prepared via hydrolysis of tetraethoxysilane (TEOS) in water–ethanol (1–5) mixture, and one drop of ammoniac as catalyst to promote room temperature precipitation. Once recovered, the precipitate was heated to 400 °C for 2 h in order to remove the remaining water. Last, stoichiometric amounts of Fe_2O_3, SiO_2 and Fe powders were thoroughly ball-milled for half an hour, under Ar atmosphere and using a SPEX 8000 shock-miller, in a 10 ml cell with a ball/powder ratio of 4. Afterwards the powders were placed in a stainless steel tube sealed under argon; the tube was annealed at 750 °C for 24 h to produce pure fayalite (Fe_2SiO_4) powders, as checked by X-ray diffraction (XRD) (not shown).

Powder of fayalite was then sintered at high pressure and high temperature using a piston-cylinder press. A standard 3/4″ salt pressure cell assembly with MgO spacers and graphite furnace was used. Sample was loaded in a graphite capsule, pressurised to 1 GPa using the cold piston-in technique and sintered at 900 °C for at least 12 h. Temperature was monitored with a type C thermocouple ($W_{95}Re_5/W_{74}Re_{26}$) inserted axially in an alumina four bore thermocouple sleeve above the capsule. The charge was quenched by switching off the electrical power. It was verified by XRD that the sintering process did not affect the mineralogy of the material, which remains pure fayalite (Fig. 1).

As the sintering operation presumably affects the defect density of the grains, one could wonder whether this method impacted the dissolution rates. Based on previous studies which did not evidence any strong dependence of crystal dissolution rate upon defect density (e.g. Schott et al., 1989, see also discussion and additional references in Daval et al., 2009a), we suppose that the dissolution rates measured in the present study are not fundamentally different from what would have been obtained with "defect-free" samples.

2.1.2. Starting fluid and solid samples

The experiments were conducted on millimetric fragments recovered from the sintered starting material. The selected samples

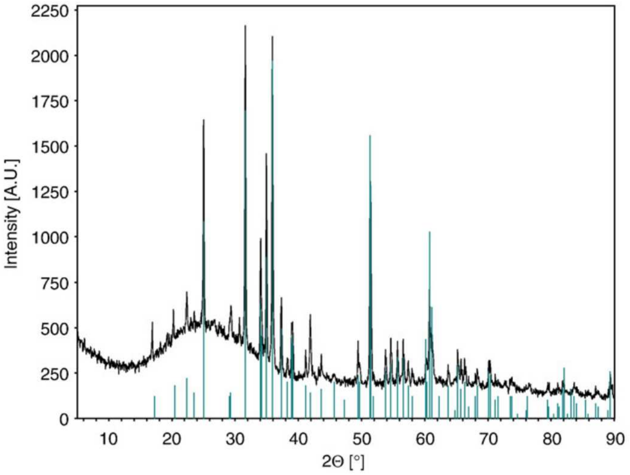

Fig. 1. X-ray diffraction pattern of sintered fayalite powders. The peaks identification is based on data from the National Bureau of Standards (1983). Note that the broad scattering intensity around 25° comes from the glass sample holder itself, because of the extremely small amount of materials used for XRD.

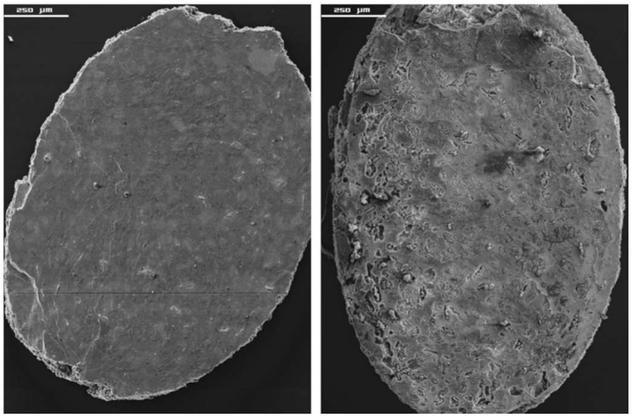

Fig. 2. SEM pictures of a typical fayalite fragment (left) before and (right) after reaction (experiment H-80). Note the absence of fine particles before the experiment and the presence of dissolution features such as deep and irregular etch pits after reaction.

were ultrasonically cleaned in absolute ethanol for ~5 min in order to take away possible fine particles; the supernatant was removed and the samples were then rinsed with deionised water (18 MΩ cm^{-1}) for ~5 min, before introduction in the batch micro-reactor. Imaging the fayalite fragments by scanning electron microscopy (SEM, Hitachi S-2500) operating at 15 kV revealed that this process was efficient (see Fig. 2a for a typical SEM picture). The characteristics of the fayalite fragments used in the different experiments are gathered in Table 1. As there was not enough material to determine the specific surface area (SSA) of fayalite by gas adsorption (the so-called Brunauer–Emmet–Teller (BET) method), the dissolution kinetics parameters determined hereafter were normalised to geometric surface areas. Attempts to compare the rates measured in the present study to previously reported rates normalised to BET surface areas will be discussed in Section 4.1.2.

The aqueous solutions were prepared with deionised water (18 MΩ cm^{-1}) and weighed amounts of HCl (Sigma-Aldrich™, ACS Reagent), acetic acid (Sigma-Aldrich™, ACS reagent), and sodium acetate (Sigma-Aldrich™, ACS reagent). The pH of the starting solutions was determined with a Hannah Instruments™ pH-meter electrode calibrated beforehand with commercial buffer solutions (pH 4.01, and 7.00 at 25 °C). Because of the small sample volume of aqueous solutions (~50 mm^3, see Section 2.2), the pH after experiment could only be monitored using pH testing paper. However, the pH evolution during fayalite dissolution experiments was accurately modelled using a geochemical code (see Section 2.5 for details).

2.2. Experimental apparatus

The fayalite fragment(s) and aqueous solution were loaded in a high-pressure vessel optimised for the study of supercritical fluids as described in details in Testemale et al. (2005). The experimental set-up for dissolution measurements is described in Pokrovski et al. (2006), and is briefly reported hereafter (see also further description and Fig. 1 in Testemale et al., 2009b).

The sample container consists of a glassy carbon tube (internal diameter = 4 mm) and two glassy carbon inner rods, which were placed in the tube in order to delimit a cell volume of ~50 mm^3. The fragments of fayalite were placed on top of the bottom inner rod and were immersed in the solution loaded in the tube. Heating was undertaken with a Mo resistive heater, and pressure was adjusted to 30 MPa by placing the cell in a stainless steel vessel, pressurised via high-purity grade helium gas. The high-pressure vessel was installed on beamline BM30b (FAME: French Absorption spectroscopy beam line in Material and Environmental sciences) at the European Synchrotron Radiation Facility (ESRF, Grenoble, France). X-ray absorption spectroscopy (XAS) data, including the X-ray absorption near edge structure region (XANES), were collected both in transmission and fluorescence modes at the Fe–K-edge (7112 eV in metal Fe). The beam size on the sample was about 280 × 100 µm FWHM (H × V) and the photons flux is typically around 10^{12} photons/s/200 mA on FAME beamline at this energy. The beam energy was selected using a Si(220) double crystal monochromator (Proux et al., 2006) and scanned between 7050 and 7300 eV, with a minimum step size of 0.25 eV in the XANES region, and a counting time of 1 s per point. For transmission mode studies, silicon diodes were used to measure the incident (I_0) and transmitted (I_1) X-ray beams. For detection of the fluorescence,

Table 1
Characteristics of fayalite fragments used in dissolution experiments.

Expt.	Solution	T (°C)	m (g)	Frags	$A_{\min}$ (cm²)	SSA_0 (cm²/g)
H-50	HCl 0.10 molal	50	3.3E−03	2	0.0757	22.9
H-65	HCl 0.10 molal	65	2.0E−03	1	0.0404	20.2
H-65b	HCl 0.05 molal	65	1.6E−03	1	0.0375	23.4
H-80	HCl 0.10 molal	80	3.3E−03	1	0.0497	15.1
H-100	HCl 0.10 molal	100	3.0E−03	1	0.0476	15.9
A-1	AcOH–AcONa (1:1 molal)	65	5.4E−03	3	0.1167	21.6
A-2	AcOH–AcONa (0.55:0.45 molal)	65	3.9E−03	2	0.0800	20.5
A-3	AcOH–AcONa (1.9:0.1 molal)	65	1.3E−03	1	0.0346	27.2

The crystals consist in elliptic cylinders (minor axis: $d_1 = 0.11$ cm and major axis: $d_2 = 0.15$ cm). The number of fragments introduced in each run is reported in the column labelled "frags". The height of each fragment is calculated knowing the mass (m, in grams) and the specific gravity ($\rho_0 = 4.39$ g cm^{-3}) of fayalite samples. The surface area ($A_{\min}$ in cm²) and specific surface area (SSA_0 in cm² g^{-1}) of each sample were calculated using this height (see text for details).

a 30-element solid-state germanium Canberra energy-resolved detector, placed at 90° to the X-ray beam, was used (Proux et al., 2005). Dissolution of fayalite, at given pressure and temperature, was followed by the determination of iron concentration and speciation in the aqueous solution in contact with the solid. The sample was scanned regularly to check the homogeneity within the solution. Our approach permits us to follow the dissolution under complex fluid evolution and is thus complementary to the 'classic' dissolution studies performed using flow-through reactors. Besides, our methodology uniquely allows us to avoid any sampling bias of iron measurements, as it could be the case, for example, if the concentration of iron had to be determined in weakly acidic solution exposed to air whose measurement would require careful and heavy protocols.

Except for a small loss of mass in agreement with the release of iron in solution and for the formation of etch pits onto the mineral surface (see SEM picture in Fig. 2b), no change of the solid samples occurred at a µm-scale (e.g. no secondary phases).

2.3. Ab initio XANES calculations

X-ray Absorption Near Edge Structure (XANES) is sensitive to the speciation of the metal aqueous complexes: redox state, three dimensional structure, ligand replacement. For that reason, it is very useful to have the possibility to measure such spectra during dissolution experiments, and thus to possibly correlate variations of dissolution rates with modifications of metal aqueous speciation (see details in Sections 4.1.4 and 4.2.1). In particular, the XANES signal is stronger than the Extended X-Ray Absorption Fine Structure (EXAFS) signal and can be detected in more challenging experimental conditions than EXAFS (low metal concentration, concentrated matrix, high-pressure setups, etc.). For that reason, efforts have been undertaken recently in hydrothermal geochemistry to interpret quantitatively the XANES spectra of aqueous iron (Testemale et al., 2009a), copper (Brugger et al., 2007) and gold (Pokrovski et al., 2009) in hydrothermal brines; XANES was then used to interpret aqueous speciation during dissolution experiments, of iron-bearing (Testemale et al., 2009b) and copper-bearing (Liu et al., 2008) minerals.

We applied the same methodology to the present case of fayalite dissolution. A detailed explanation of the method for *ab initio* XANES calculations of aqueous iron spectra was given by Testemale et al. (2009a). The same method was applied here: we used the FDMNES code (Joly, 2001) within the full potential Finite Difference Method to calculate final states and absorbing cross-sections. Convolution of the raw calculated spectra was done based on the iron core-hole lifetime broadening (1.25 eV at the iron K-edge, Krause and Oliver, 1979), plasmon inelastic interactions, and experimental resolution of the FAME beamline (0.8 eV FWHM at the iron K-edge, Proux et al., 2006). Calculations were done on input structures, using neutral atoms and without taking into consideration thermal disorder (Testemale et al., 2009a).

2.4. Complementary fluid analyses

When possible, the aqueous solution was retrieved at the end of each run, diluted ~50 times in ultrapure (18 MΩ cm^{-1}) water and acidified. The samples were then analysed by ICP-AES for iron and silicon. The analytical uncertainties in the measurements were ~5%, based on repeated analyses of standard solutions and blanks.

2.5. Thermodynamic calculations and kinetic modelling

During our experiments, the solution composition (and especially the pH) changes as a function of fayalite dissolution. Hence, fayalite dissolution rate changes as well, because it is pH-dependent (e.g. Wogelius and Walther, 1992). As a consequence, it could be risky to extrapolate kinetic parameters from the initial slopes of total iron released as a function of time. Instead, we chose to fully model the dissolution process using a geochemical code (CHESS, van der Lee and De Windt, 2002), in order to determine the rate constant, the pH and temperature dependences of fayalite dissolution kinetics.

The CHESS code consists of two interconnected thermodynamic and kinetic modules. The thermodynamic module allows to calculate the fluid speciation. It uses a self-consistent database (chess.tdb), derived from that of EQ3/6 code (Wolery, 1992). Activity coefficients for aqueous species are calculated using the Davies equation, and the electrical balance is ensured using pH as an adjustable parameter. The kinetic module uses the following equation to link the dissolution/precipitation rate of a mineral to the major rate-controlling parameters (adapted from van der Lee and De Windt, 2002):

$$r = \pm k_0 \exp(-E_a/RT) A_{\min} a_{H^+}^{n} \left(1 - \left(Q/K_{eq}\right)^{\mu}\right)^{\lambda}. \quad (5)$$

In this equation, r is the overall dissolution/precipitation rate (mol s^{-1}), negative values indicating dissolution, and positive values precipitation, k_0 is the rate constant that incorporates pre-exponential factors in the Arrhenius relation (mol cm^{-2} s^{-1}), E_a is the activation energy (J mol^{-1}) supposed to be pH-independent. This is a strong assumption which is debated with respect to forsteritic olivine dissolution kinetics (and recently addressed by Hänchen et al., 2006), and which remains to be verified with respect to fayalite dissolution kinetics. The terms R and T stand for the gas constant (J mol^{-1} K^{-1}) and temperature (K) respectively, $A_{\min}$ is the reactive surface area (cm²). The $a_{H^+}{}^{n}$ term expresses the dependence of the rate on H$^+$ activity. The last term of the equation $(1-(Q/K_{eq})^{\mu})^{\lambda}$, denotes the dependence of the dissolution/precipitation rate on the fluid saturation state (in other words, the Gibbs free energy ΔG_r of the reaction: $Fe_2SiO_4 + 4H^+ \rightarrow 2Fe^{2+} + 2H_2O + SiO_2(aq)$), Q being the activity product of the reaction and K_{eq}, the corresponding equilibrium constant. The exponents n, μ and λ are parameters generally determined experimentally. For fayalite dissolution, as for many minerals, μ and λ are actually unknown and are then assigned values of unity, as in most of modelling works (e.g. Xu et al., 2004; Knauss et al., 2005). In this case the term $(1-Q/K_{eq})$ describes the affinity-dependence of the reaction within the framework of transition state theory (TST) (e.g. Lasaga, 1981). Such an approximation can be the source of large overestimations of the "true" reaction rates (see Daval et al., 2010 for details), and as a consequence, the data closer to equilibrium were not considered to determine the unknown kinetic parameters k_0, E_a and n. Finally, note that the use of Eq. (5) precludes any dependence of the dissolution rate upon the hydrostatical pressure. Thus, any comparison of our data with others from the literature supposes that this dependence is negligible, or of second order compared to pH or T. The CHESS code linearly decreases the reactive surface area as a function of the amount of fayalite remaining ($n_{Fa}(t)$, expressed in mol) by the relation:

$$A_{\min}(t) = SSA_0 \cdot n_{Fa}(t) \quad (6)$$

where SSA_0 is the initial specific surface area (expressed in m²mol^{-1}) of the fayalite fragment(s) introduced in the batch micro-reactor. In practical terms, the amount of fayalite consumed is so low that $A_{\min}(t)$ is roughly constant through time.

3. Results

3.1. Iron and silicon concentrations

Both transmission X-ray absorption and fluorescence signals can be used to determine aqueous iron concentration. Whereas the first method is an absolute measurement, directly correlated to the iron molality, the second one first needs to be calibrated. In transmission mode, the iron concentration was obtained from the difference in absorption below and above Fe–K-edge energy (*eH*) according to:

$$eH = D\left(\frac{m}{\rho}\right)_{Fe} M_{Fe} m_{Fe} \rho x \quad (7)$$

where $D\left(\frac{m}{\rho}\right)_{Fe}$ is the difference in specific mass absorption ($cm^2 g^{-1}$) of iron below and above the Fe–K-edge, M_{Fe} is the atomic mass of Fe ($g\ mol^{-1}$), m_{Fe} is the molality of Fe in the solution ($mol\ kg^{-1}$), ρ is the density of solution ($g\ cm^{-3}$), approximated to that of pure water (Wagner and Pruss, 2002; the choice of the model for calculation of water density is not critical in the range of conditions of this study, since the density remains very close to 1, ranging from 1.001 at 50 °C to 0.972 at 100 °C), and x is the length of the X-ray path (cm). In the literature, Eq. (7) has been regularly used to derive the concentration of dissolved species (see e.g., Pokrovski et al., 2005, 2006; Testemale et al., 2009b). The pre-edge and post-edge parts of the transmitted spectra are fitted with spline curves, using the software Athena from the Horae package (Ravel and Newville, 2005), and the differences between the two lines at the Fe(II) K-edge are taken as the values of *eH*. The imprecision on this measurement, usually due to noise in spectra and/or to low signal intensity leading to imprecision in the fits of pre-edge and post-edge lines, is estimated to be 0.01 in absolute value. The two unknown parameters in Eq. (7) are the molality m_{Fe} and the path length of X-rays through the cell x. This parameter x does not vary between two different experiments if the same internal cell is used. It was measured precisely prior to the fayalite dissolution experiments using standard solutions of known iron molalities (see Testemale et al., 2009b for details). The value of x was determined to be 3.51 mm, in fair agreement with the one reported by Testemale et al., 2009b ($x = 3.25$ mm), who used a similar set-up. Taking into account the aforementioned imprecision of 0.01 in the measurement of *eH*, this translates into an error of about ±1.5 mmolal in the determination of iron molality in the investigated solutions. Finally, note that Fe impurities present in the beryllium high-pressure windows of the autoclave and protection of the solid-state detector used in the set-up limit the lowest Fe concentration that can be detected in transmission mode to 4 mmolal (Testemale et al., 2009b).

To use fluorescence measurements to determine iron molality, all other parameters (than the iron concentration) that impact the fluorescence intensity need to be kept constant between experiments: detector position and solid angle, counting time, absorbance of the matrix. Then the fluorescence intensity is proportional to the iron molality. Due to auto-absorption effects, this is not true for high values of concentrations, but typical values of 50 mmolal in our experiments are safe, as shown a posteriori by the linear correlation between absorption and fluorescence derived concentrations obtained. The fluorescence intensity measured at a given (post-edge) fixed energy was thus calibrated against the transmission signal by using experiment H-65 (equilibration of a fayalite sample with a 0.1 molal HCl solution at 65 °C; besides, note that a similar method to that described below was applied with experiment A-1 to calibrate the fluorescence signal in acetate buffered solutions). Since both the transmission and fluorescence signals are proportional to the iron molality, the calibration consisted in finding the best proportionality coefficient between the absolute value of transmission signal and the corresponding fluorescence intensity: this parameter was thus found by minimising the average differences between the molalities determined in transmission and fluorescence modes over the whole time range of experiment H-65. Fig. 3 shows the results of the calibration. As the regression coefficient is close to 1 ($r^2 = 0.983$), the determination of iron molality using the fluorescence technique is in good agreement with transmission data and is quite robust. From this regression, the standard deviation was calculated to be ~2.1 mmolal.

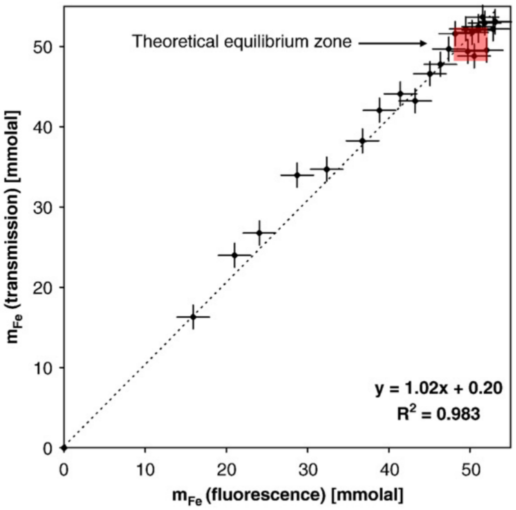

Fig. 3. Comparison of iron molalities determined by the transmission signal with those determined by the fluorescence signal calibrated using the experiment H-65. Note that the end of experiment data points corresponds closely to the expected equilibrium value (red square on the figure).

Finally, as can be seen on the figure, the data points at the end of experiment correspond closely to the expected equilibrium value (area delimited by the red square on the figure): under these conditions, this value was calculated to be 50 ± 2 mmolal, the uncertainties being based on the relative precision of the weighed mass of HCl and water used to prepare the solution. To summarise, two types of measurements were done:

(1) continuous measurement of fluorescence intensity (at a fixed post-edge energy) from which iron molality was derived with good time resolution;
(2) longer acquisition of spectra from which the molality was determined (transmission signal) and the speciation was derived (fluorescence signal, XANES signal in fluorescence mode).

Results of the evolution of iron molalities in 0.1 molal HCl aqueous solutions in contact with fayalite are shown as a function of temperature and time in Fig. 4. All these data were acquired under a confining pressure of 30 MPa. For each experiment conducted in 0.1 molal HCl, the iron molality levels up to a plateau, which corresponds closely to the theoretical equilibrium concentration value of 50 mmolal. On the other hand, experiments done in acetate buffers were stopped while the iron molality was still increasing (Fig. 5), indicating that thermodynamic equilibrium was not reached yet (see Section 4.2.2). Whatever the initial fluid composition is, there is a good agreement between the iron molalities determined either by XAS or by ICP-AES (see Table 2). Excluding the fluid sample from experiment A-3, the relative differences between the two measurements for a same sample are consistent within less than 10%, which is better than the uncertainties for each technique. The ratios of iron over silica aqueous concentrations are close but systematically above the stoichiometric ratio of fayalite (~2). Possible explanations for such trends are discussed below.

3.2. Iron speciation

Under all conditions investigated, the speciation of Fe in solution was studied by acquiring XANES spectra. This region is highly sensitive to the structure and composition of aqueous iron complexes. Fe(III) was never detected in any experiment neither as dissolved

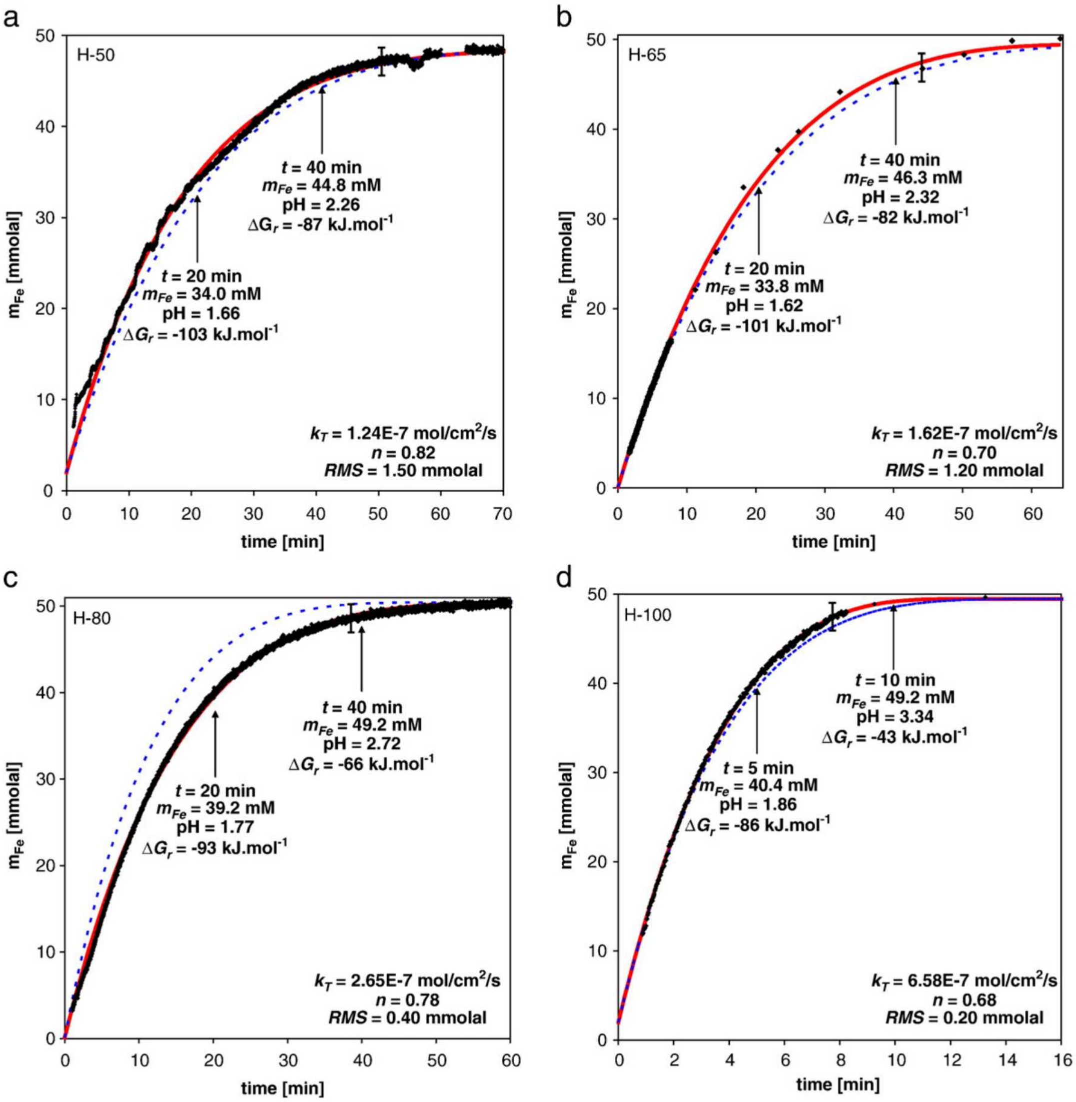

Fig. 4. Evolution of iron molality as a function of time at (a) 50 °C, (b) 65 °C, (c) 80 °C and (d) 100 °C for fayalite dissolution at 30 MPa and 0.1 molal HCl. The experimental data points are shown as black diamonds: isolated (respectively closed-packed) data points correspond to transmission (respectively fluorescence) data. The continuous red lines correspond to fits of the dataset at the corresponding temperature (from which parameters k_T and n are derived at this temperature) and the dashed blue lines, the evolution of iron molality calculated with the CHESS code using parameters (k_0, E_a and n) determined using the totality of the experiments (see text for details). The quantitative results of the least square procedure are indicated in the right lower corner. The modelled chemical characteristics of the fluids are given at some specific points of the fits.

species nor as possible colloids which, if present, would produce easily recognisable noisy signatures in the XAS signals (Da Silva et al., 2009). Although straightforward, this observation is of great importance and constitutes the major application of being able to record continuously XAS signals in the course of dissolution experiments. In Fig. 6 the XANES spectra of the solutions in contact with fayalite in 0.1 molal HCl at 50 °C (experiment H-50) and acetate buffered solutions at 65 °C (experiment A-1), are plotted. As can be seen, these spectra are almost indistinguishable. XANES spectra of a synthetic solution containing 50 mmolal of $FeCl_2$ in a 2 molal acetate buffer (1 molal acetic acid; 1 molal sodium acetate) were also acquired and are identical to the latter (experiment A-1). As it can be seen in Fig. 6, all these spectra are almost identical, and the small visible differences are within the experimental uncertainties. For clarity reasons, all XANES spectra from the other experiments are not shown, as they are indistinguishable from the ones already plotted in Fig. 6.

4. Discussion

4.1. Kinetic modelling of dissolution experiments performed in HCl solutions

4.1.1. Modelling strategy

As pointed out above, the fayalite samples introduced in the micro-reactor consisted of cylinders with elliptic sections, for which the major and minor axes are known, because they were shaped by the apparatus used to sinter the fayalite nanocrystals. The accurate lengths of these axes were determined by SEM analyses on one sample (see Fig. 2). The surface area of an ellipse-shaped face (A_e, in cm) is given by:

$$A_e = \frac{\pi \times d_1 \times d_2}{4} \tag{8}$$

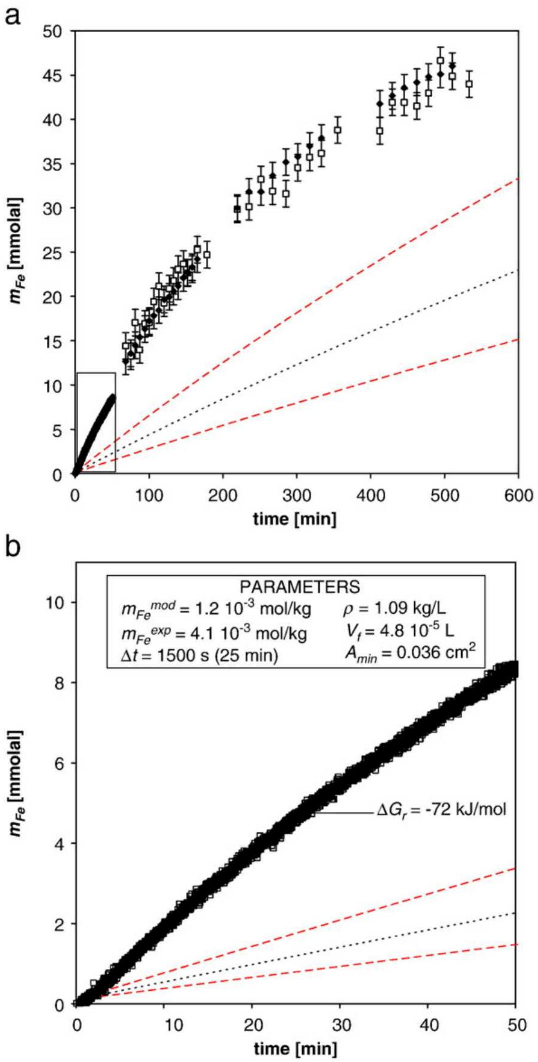

Fig. 5. Evolution of iron molality as a function of time at 65 °C and 30 MPa for fayalite dissolution in acetate buffer (experiment A3: acetic acid (1.9 molal) and sodium acetate (0.1 molal)). (a) Global evolution of iron over the total duration of the experiment (~8 h). Filled diamonds (respectively open squares) correspond to fluorescence (respectively transmission) data. The dotted black line corresponds to kinetic modelling using Eq. (5) and the parameters determined from experiments led in HCl; the dashed red lines indicate the confidence interval (see text for details). (b) Close up of the beginning of the experiments (delimited by the rectangle in panel a). The parameters mentioned in this figure were used to determine the acetate-dependence of fayalite dissolution rate (see text, Eq. (15)).

Table 2
Solution composition measured at the end of each run.

Expt.	m_{Fe} XAS	m_{Fe} ICP	m_{Si} ICP	Δm_{Fe} (%)	m_{Fe}/m_{Si}	$\Delta G_r(SiO_2)$
H-50	n.d.	n.d.	n.d.	n.d.	n.d.	n.d.
H-65	50.88	53.70	21.98	5.54	2.44	−4.66
H-65b	24.00	21.97	10.76	−8.44	2.04	−1.42
H-80	52.20	54.60	21.82	4.60	2.50	−4.19
H-100	50.31	47.16	19.82	−6.24	2.38	−3.43
A-1	102.1	n.d.	n.d.	n.d.	n.d.	n.d.
A-2	57.31	54.57	18.50	−4.76	2.95	−4.14
A-3	45.90	39.66	19.96	−13.59	2.34	−4.34

The first column indicates the name of the experiment. The iron molalities (mmolal) measured either by XAS or by ICP-AES are reported in the two following columns. The 4th column reports the molality of aqueous silica determined by ICP-AES (mmolal). The two following columns indicate the relative difference between iron molalities determined by ICP-AES and XAS, and the ratio of iron over silica aqueous concentrations (based on ICP-AES measurements). In the last column, the Gibbs free energy of amorphous silica precipitation (kJ mol^{-1}), calculated using the ICP-AES fluid composition and the CHESS code, is given.

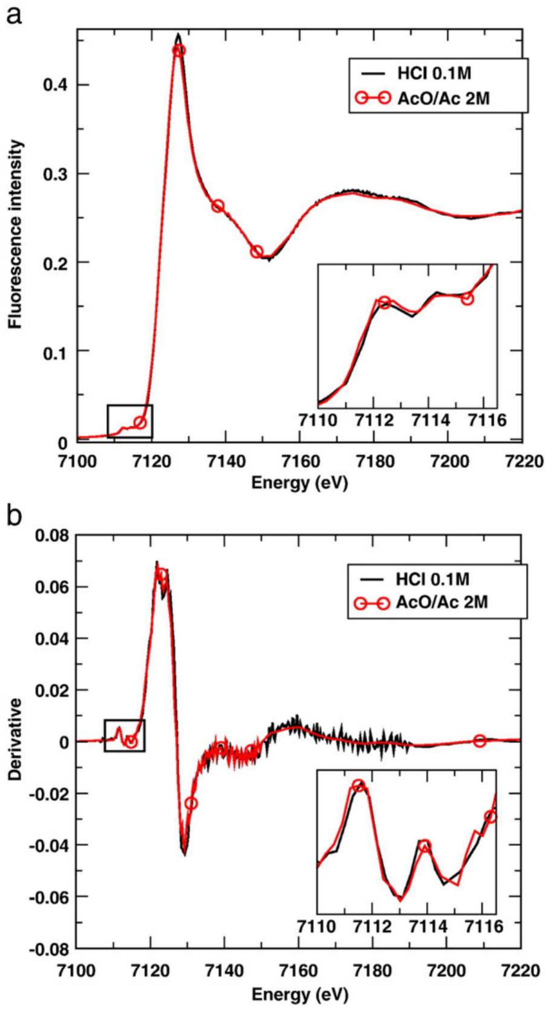

Fig. 6. Typical (a) XANES spectra and (b) corresponding derivatives obtained at the iron K-edge either in 0.1 molal HCl solution at 50 °C (black line, experiment H-50), or in acetate buffered solution at 65 °C (red line, experiment A-1). The two spectra and corresponding derivatives are very similar. Insets represent pre-edge-zooms of the areas delimited by the rectangles.

where $d_1 = 0.11$ cm and $d_2 = 0.15$ cm represent the lengths of minor and major axes, respectively. As the height of the cylinders (h) varies from one sample to another, it was more convenient to determine it by measuring the mass of each cylinder instead of analysing the grains one by one using SEM. The height of a cylinder with elliptic base section can be calculated according to:

$$h = \frac{4 \times m}{\pi \times \rho_0 \times d_1 \times d_2} \qquad (9)$$

where m is the mass of fayalite sample (Table 1) and ρ_0 is the specific gravity of fayalite ($\rho_0 = 4.39$ g cm^{-3}). Then, using Ramanujan's approximation for the circumference of an ellipse, the total surface area of fayalite for a given run is:

$$A_{\min} = 2N_{\mathrm{f}} \times A_{\mathrm{e}} + \frac{h}{2} \times \pi \times \left(3(d_1 + d_2) - \sqrt{(3d_1 + d_2)(d_1 + 3d_2)}\right) \tag{10}$$

where N_{f} is the number of fayalite fragments initially introduced into the micro-reactor (see Table 1). The initial specific surface area (SSA_0) is then simply obtained by dividing $A_{\min}$ by the initial amount of fayalite. An important assumption arises from the fact that this calculation, coupled together with the surface model used by CHESS (Eq. (6)), neglects the increase of surface area because of the etch pits formation, so that the strict use of Eqs. (6) and (10) is only valid at the start of the experiments. In common mineral dissolution kinetics studies, the effect of etch pits formation is frequently omitted, as the rates are often normalised by the initial surface area of the grains. In fact, as previously discussed in Daval et al. (2009a), whether the increase of SSA during dissolution could artificially cause an increase of the mineral dissolution rate is an open question. As an example, Gautier et al. (2001) proposed that the increase of SSA during quartz dissolution consisted of essentially unreactive etch pit walls which contribute negligibly to mineral dissolution. Although this statement would require more investigation for fayalite, we decided to follow this proposition, which seems reasonable. However, one has to keep in mind that it could be a source of shortcomings and thus, of errors in the determination of the kinetic parameters.

Referring back to Eq. (5), the following parameters are unknown: k_0, E_{a}, n, μ and λ. For a given experiment at constant temperature, the unknown parameters are reduced to k_{T}, n, μ and λ if we set $k_{\mathrm{T}} = k_0 \exp(-E_{\mathrm{a}}/RT)$. As previously discussed, because of the lack of experiments dedicated to rate–affinity relationships for fayalite, we decided to adopt the simplest TST formulation to model the dissolution kinetics of this mineral (i.e. $\mu = \lambda = 1$). Within this framework, the dependence of the dissolution kinetics of a solid phase on ΔG_r (often referred to as the $f(\Delta G_r)$ function, where ΔG_r stands for the Gibbs free energy of dissolution, see Section 2.5) becomes numerically negligible and experimentally impossible to measure over a wide range of free energies (e.g. at 50 °C, $f(\Delta G_r) > 0.99$ as long as $\Delta G_r < -13$ kJ mol^{-1} and at 100 °C, $f(\Delta G_r) > 0.99$ as long as $\Delta G_r < -15$ kJ mol^{-1}). However, recent experimental studies showed that, for some minerals, the actual ΔG_r-independent dissolution rate plateaus can actually be reached at far lower ΔG_r values (e.g. -50 kJ mol^{-1} for labradorite (Taylor et al., 2000); -70 kJ mol^{-1} for albite (Hellmann and Tisserand, 2006); -76 kJ mol^{-1} for diopside (Daval et al., 2010)). To the best of our knowledge, no mineral was found to exhibit a ΔG_r-dependent rate at $\Delta G_r < -76$ kJ mol^{-1}. This value was chosen as an upper bound up to which the dissolution rate of fayalite could reasonably be considered as to be ΔG_r-independent. For example, at 50 °C, using the CHESS thermodynamic module and considering the least favourable $m_{\mathrm{Fe}}/m_{\mathrm{Si}}$ ratio of ~3 (see Table 2), this ΔG_r value translates into an iron molality of 48.3 mmolal if the calculation is performed in 0.1 molal HCl (the equilibrium value being $m_{\mathrm{Fe}} = 50.2$ mmolal), and 23.6 mmolal for the one performed in 0.05 molal HCl (theoretical equilibrium value: $m_{\mathrm{Fe}} = 25.0$ mmolal). Consequently, nearly the full experimental dataset was used to determine the unknown parameters k_{T} and n, as ~95% of the total iron molality is released to the solution for $\Delta G_r < -76$ kJ mol^{-1}. Conversely, our experiments give no information about the rate–affinity relationships for fayalite.

Since the pH varies in the course of the experiments as a function of reaction extent in the batch micro-reactor, and given that it is not measured *in situ*, it has to be calculated at each step of the dissolution process. In order to perform the calculations of $a_{\mathrm{H^+}}$ and to retrieve the rate constant k_{T} and the pH-dependence coefficient n, we coupled the CHESS code to a least square fitting algorithm. Entry parameters for the CHESS code are the sample fluid volume of micro-reactor, initial concentration of HCl in solution, initial amount and specific surface area of the fayalite fragments loaded in each experiment, the temperature, the total simulation time, and *a priori* starting kinetic parameters $(k_{\mathrm{T}})_{i=1}$ and $n_{i=1}$ (the values of k_{T} and n for each iteration step i of our routine). The CHESS code then solves, at each incremental addition of iron and silica from fayalite to the solution (dissolution is supposed to be congruent, this assumption will be discussed in Section 4.1.3), mass balance equations, electroneutrality and chemical equilibria between the different species. Thus, for each routine iteration step i, with given values $(k_{\mathrm{T}})_i$ and n_i, the outputs of the model are, at each time step, the molalities of all the chemical species involved, and resulting parameters such as $a_{\mathrm{H^+}}$ and ΔG_r. The curve of iron molality as a function of time thus generated is then compared to the experimental one by a least square fitting procedure, the quantity to minimise being:

$$RMS_i = \sqrt{\frac{1}{N}\sum_{j=1}^{N}\left(m_{\mathrm{Fe}}^{\mathrm{exp}}\big|_{t=t_j} - m_{\mathrm{Fe}}^{\mathrm{mod}}\big|_{t=t_j}\right)^2}. \tag{11}$$

In the above equation, RMS_i stands for the root mean square of the simulation at step i (expressed in molal), N is the number of data points for which molality is <48.3 mmolal (or 23.6 mmolal for experiment H-65b realised in 0.05 molal HCl), $m_{\mathrm{Fe}}^{\mathrm{exp}}|_{t=t_j}$ and $m_{\mathrm{Fe}}^{\mathrm{mod}}|_{t=t_j}$ represent respectively the experimental and modelled iron molalities at time t_j. The values of k_{T} and n are then determined by dichotomy, and the refinement process is stopped when $\frac{RMS_{i+1}}{RMS_i} < 10^{-3}$, which corresponds approximately to $\frac{(k_{\mathrm{T}})_{i+1}}{(k_{\mathrm{T}})_i} < 10^{-2}$ and $\frac{n_{i+1}}{n_i} < 10^{-3}$.

The reliability of the final values of k_{T} and n was estimated by propagating the errors on the two parameters which have a major impact on the values of k_{T} and n, namely the starting concentration of H$^+$ and the iron experimental molality $m_{\mathrm{Fe}}^{\mathrm{exp}}$. The actual starting concentration of H$^+$ ($m_{\mathrm{H^+}}^0$) was found to be 99.8 ± 0.3 mmolal, and the error on $m_{\mathrm{Fe}}^{\mathrm{exp}}$ was previously reported to be ±2.1 mmolal (see Section 3.1). The fitting algorithm was then run five times for a given dataset:

- with $m_{\mathrm{H^+}}^0 = 99.5$ mmolal and either (1) $m_{\mathrm{Fe}}^{\min} = m_{\mathrm{Fe}}^{\mathrm{exp}} - 2.1$mmolal (i.e. corresponding to a negative shift of the entire dataset of 2.1 mmolal) or (2) $m_{\mathrm{Fe}}^{\max} = m_{\mathrm{Fe}}^{\mathrm{exp}} + 2.1$ mmolal (i.e. corresponding to a positive shift of the entire dataset of 2.1 mmolal);
- with $m_{\mathrm{H^+}}^0 = 100.1$ mmolal and either (3) $m_{\mathrm{Fe}}^{\min} = m_{\mathrm{Fe}}^{\mathrm{exp}} - 2.1$ mmolal or (4) $m_{\mathrm{Fe}}^{\max} = m_{\mathrm{Fe}}^{\mathrm{exp}} + 2.1$ mmolal;
- (5) using the actual measured values of $m_{\mathrm{H^+}} = 99.8$ mmolal and $m_{\mathrm{Fe}} = m_{\mathrm{Fe}}^{\mathrm{exp}}$.

Furthermore, to avoid an erroneous determination of k_{T} and n due to possible local *RMS* minima, the regression process was operated with different starting values of $(k_{\mathrm{T}})_{i=1}$ and $n_{i=1}$. On the whole, the method described above allowed us to determine the errors on the final values of n: ±0.07, ±0.05, ±0.04, ±0.04 and ±0.05 for experiments H-50, H-65, H-65b, H-80 and H-100 respectively. The larger uncertainties of the pH dependence in H-50 are likely due to the scattering of data points in this run. With respect to k_{T}, the errors were found to be better than ±13% (±20% for experiment H-50).

4.1.2. Determination of pH and temperature dependence

The fit of each one of the 5 datasets obtained in HCl solutions yields *RMS* values comprised between 0.2 (experiment H-100) and 1.5 mmolal (experiment H-50). The average difference between experimental and modelled curves is thus smaller than the estimated uncertainty on each datum point (±2.1 mmolal). The extrapolated values for k_T and n are mentioned in the bottom right corner of each graph of Fig. 4 (for experiment H-65b, which is not represented, the quantitative results are: $k_T = 1.32 \times 10^{-7}$ mol cm^{-2}s^{-1}, $n = 0.74$, $RMS = 0.3$ mmolal). Fig. 7 shows the pH dependence determined for all experiments performed in HCl solutions (note the presence of an additional point at 25 °C, taken from Wogelius and Walther, 1992). Considering the average values of n between 50 °C and 100 °C without taking into account the uncertainties on each data point, the pH dependence of the dissolution reaction seems to decrease with temperature, whereas most of the previous studies which reported temperature-dependent values of n showed that the pH dependence increased with T (e.g. Chen and Brantley, 1998; 2000), in agreement with the surface protonation model proposed by Casey and Sposito (1992). In fact, given the relative uncertainties on n calculated in Section 4.1.1 for each temperature, the pH dependence of fayalite should rather be considered to be temperature independent on the whole temperature range investigated (50–100 °C), with an average value of $n = 0.74$ and a maximum range of uncertainties of ± 0.15 within the temperature range 50–100 °C. Furthermore, this value is in good agreement with the one determined by Wogelius and Walther (1992) at 25 °C ($n = 0.69$), which could indicate that the pH dependence of fayalite is temperature independent between 25 °C and 100 °C. Finally, the validity pH range for n is limited by the starting and final pH values used for the fitting procedure. According to the CHESS code, this corresponds to pH comprised between ~1.11 and ~2.70 (this latter value corresponding to an iron molality of $m_{Fe} = 48.3$ mM for experiments initiated in 0.1 molal HCl solution).

The pH dependence found in the present study can be compared with a compilation of data for forsterite dissolution. As can be seen in Fig. 7 and unambiguously demonstrated by e.g. Hänchen et al. (2006), the pH dependence of forsterite dissolution is essentially temperature independent in the acidic range, with an average value close to 0.50 ($n = 0.46 \pm 0.03$). Different models were proposed to explain this value. On one hand, Rosso and Rimstidt (2000) noticed that a value of 0.5 usually indicates the dissociation of the aqueous reactant (i.e. H_3O^+) into two new species. They proposed that the activated complex for forsterite dissolution involves a hydronium ion adsorbed to the forsterite surface in such a way that two of the three hydrogen atoms are associated with two Si–O–Mg bridging oxygen atoms. Dissociation of this hydronium ion to form two H–O–Si groups on the forsterite surface would then lead to the observed reaction order upon hydrogen ions of 0.5. Note however that this model hardly explains the initial non-stoichiometry of dissolution frequently observed (e.g. Pokrovsky and Schott, 2000b; Chen and Brantley, 2000). On another hand, Pokrovsky and Schott (2000a,b) showed that the surface of forsterite actually consists in a silica-rich layer formed by the polymerisation of the initially isolated silicate tetrahedra. In agreement with the stoichiometry of surface titration analyses, they suggested that the adsorption of one proton on a silicate dimer (corresponding to a ratio of 0.5 H^+ per 1 forsterite surface site) was rate-controlling of the forsterite dissolution process, and thus accounted for the measured pH dependence of 0.5. The application of any of these two mechanistic models to fayalite dissolution is questionable, as n is noticeably different from 0.5. However, we must admit that the design of our experimental apparatus and our methodology based on Fe monitoring only are not suitable to unambiguously decipher a mechanism for the proton-promotion of dissolution rates. First, a more accurate value of n would have been obtained if the pH dependence had been determined on a larger pH range. Actually, this is not possible with our experimental apparatus, as running experiments at higher pH with iron molality of the order of tens of mmolal would correspond to ΔG_r higher than -76 kJ mol^{-1}. Secondly, further investigations such as surface titration should be done to better understand the measured pH dependence of fayalite. Without such complementary analyses, the reaction mechanism of proton-promoted dissolution of fayalite remains an open question.

To determine the temperature dependence of fayalite dissolution rate, the data were plotted in an Arrhenius-like diagram (Fig. 8) for the two pH values which bracket the relevant pH range previously mentioned (1.11; 2.70). In such a plot, the slope of a given regression corresponds to the activation energy of the reaction, and the intercept point, to $\ln(k_0 \times a^n_{H^+}$. As can be seen, the two regressions lines are roughly parallel, indicating that the activation energy of fayalite dissolution is pH-independent in the pH range 1.11–2.70. The regression yields $k_0 = 10^{0.17 \pm 0.63}$ mol cm^{-2}s^{-1} and $E_a = 45.1 \pm 4.2$ kJ mol^{-1}, respectively. Activation energies of this order of magnitude are consistent with a dissolution process that is controlled by chemical reaction at the solid surface (Lasaga, 1984), and not by

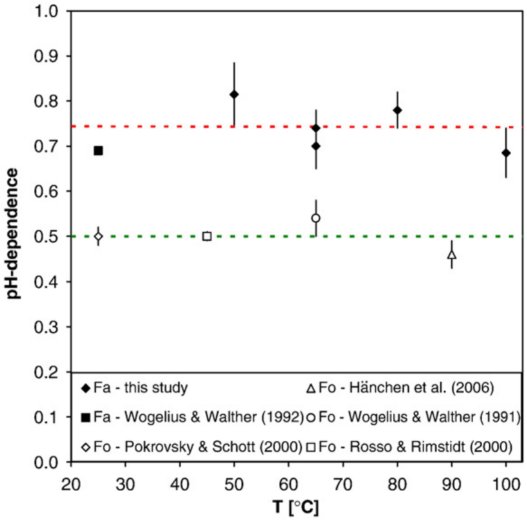

Fig. 7. Reaction order (n) with respect to a_{H^+} (i.e., pH dependence) as a function of temperature for fayalite (Fa) and forsterite (Fo) dissolution. The dashed red (respectively green) line represents the mean reaction order over the whole range of temperature for fayalite (respectively forsterite) dissolution. At 65 °C, two experiments were conducted in respectively 0.1 molal and 0.05 molal HCl.

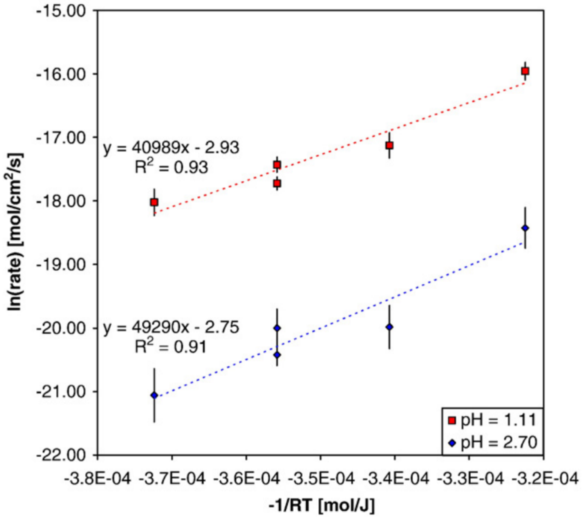

Fig. 8. Determination of the temperature dependence of fayalite dissolution kinetics using an Arrhenius-like plot, for the two pH values which bracket the relevant pH range of this study. The error bars were determined from the relative uncertainties on k_T and n.

diffusion processes in the fluid and/or the solid phases. The extent to which the overall rate law determined from the present study (i.e. Eq. (5), with $k_0 = 1.48$ mol cm^{-2}s^{-1}, $E_a = 45.1$ kJ mol^{-1}, $n = 0.74$, and $\mu = \lambda = 1$) accurately describes the data obtained in 0.1 molal HCl solutions can be evaluated by comparing the dashed lines in Fig. 4 with the data points (diamonds). As can be seen, the rate law based on averaged values for k_0, E_a and n reproduces quite well the experimental evolution of iron molalities as a function of time in all experiments.

Finally, it is interesting to assess the consistency of the dissolution rates derived from our overall rate law with those previously reported in the literature. The main difficulty consists in comparing rates which are normalised to surface areas determined with different techniques. An attempt was made using an empirical correlation proposed by Brantley and Mellot (2000), which links the mean grain diameter of a powder to its BET specific surface area (SSA_{BET}). For albite and olivine samples, Brantley and Mellot (2000) showed that SSA_{BET} can be estimated using the equation:

$$\log(SSA_{BET}) = a + b\log(d) \qquad (12)$$

where SSA_{BET} is expressed in cm^{2}g^{-1}, d in the mean grain diameter (µm), $a = 5.2 \pm 0.2$ and $b = -1.0 \pm 0.1$. For cylinders with base elliptic sections with $d_1 = 0.11$ cm, $d_2 = 0.15$ cm, and $h = 0.13$ cm (mean diameter: ~0.13 cm), the geometric SSA is 10.73 cm^{2}g^{-1}, whereas using Eq. (12), the corresponding SSA_{BET} is $10^{2.1 \pm 0.5}$ cm^{2}g^{-1} (that is, a mean value of ~125 cm^{2}g^{-1}). Thus, normalising the rates by this BET calculated surface area instead of a geometric surface area only changes the dissolution rate constant, which becomes $\log k'_0 = -0.9 \pm 0.5$ (with k'_0 in mol cm^{-2}s^{-1}). One should be aware that given the uncertainties on $\log(SSA_{BET})$ and thus, on $\log k'_0$, the extrapolation of our rate law, for purpose of comparison with other studies, is prone to large errors. More precisely, given the uncertainties on $\log k'_0$, discrepancies of up to 0.5 order of magnitude between rates could be considered as reasonable to state that the rate law determined in this study is quite consistent with previously measured fayalite dissolution rates. For the sake of simplicity, only the mean $\log k'_0$ are used in the following paragraph.

To the best of our knowledge, only four studies either were dedicated to the quantitative determination of kinetic parameters of fayalite dissolution, or reported fayalite dissolution rates far from equilibrium. Because of the limited pH range accessible in the present study, only the dissolution rates reported in the literature obtained between pH = 1.10 and pH = 2.70 will be considered for comparison. At pH ≈ 2.4 and $T = 25$ °C, Santelli et al. (2001) indicated that fayalite dissolution rate was $\sim 1 \times 10^{-11}$ mol cm^{2}s^{-1}, which is in fair agreement with an extrapolation based on the present study using k'_0 as the rate constant, $E_a = 45.1$ kJ mol^{-1}, $n = 0.74$ (2.7×10^{-11} mol cm^{2}s^{-1}). At pH = 2 and $T = 25$ °C, Casey and Westrich (1992) and Westrich et al. (1993) both reported that the dissolution rate of fayalite normalised to BET surface area is 3.0×10^{-11} mol cm^{2}s^{-1}. Under the same conditions, an extrapolation based on our parameters using k'_0 as the rate constant leads to a dissolution rate of 5.3×10^{-11} mol cm^{2}s^{-1}, which is again in good agreement with the two aforementioned studies. On the other hand, these values are ~1 order of magnitude greater than that calculated from the rate law determined by Wogelius and Walther (1992) (4.8×10^{-12} mol cm^{2}s^{-1}). Explanations for such discrepancies are not obvious though. Interestingly, one can note however that, as in our study, Wogelius and Walther (1992) did not measure directly the BET surface area of their fayalite samples, such that their mean rate value should be prone to similar large errors as well. This could (at least partly) account for the larger discrepancies existing between the dissolution rate reported in this study and the value extrapolated above. To conclude, our extrapolated experimental rates can be considered to be reasonably consistent with most of previously published studies.

4.1.3. Final fluid composition and dissolution stoichiometry

As pointed out in Section 3.1, the final fluid composition measured by ICP-AES revealed that the ratio of iron over silica molalities (m_{Fe}/m_{Si}) is slightly above the ratio of congruent fayalite dissolution, ranging from 2.04 (experiment H-65b) to 2.50 (experiment H-80). As the XAS technique did not allow the simultaneous determination of both aqueous silica and iron concentrations, it was not possible de decipher unambiguously whether the final ratios correspond to (1) a non-stoichiometric followed by a stoichiometric process; (2) a stoichiometric followed by a non-stoichiometric process; (3) a continuous non-stoichiometric dissolution; and (4) quenching effects. As a consequence, each of these alternatives is briefly discussed hereafter.

(1) The first proposition could likely explain the measured m_{Fe}/m_{Si} ratios. In fact, transient non-stoichiometric dissolution at acidic pH with preferential release of mono- or divalent metal cations is frequently reported in the literature (for instance, with respect to forsteritic olivine dissolution, the reader could refer to Pokrovsky and Schott, 2000b, Chen and Brantley, 2000) and could apply to fayalite as well. After the transient period, the metal cations leaving the mineral surface have to go through a silica-rich surface layer prior to reaching the bulk aqueous solution, the dissolution process becoming increasingly stoichiometric. Whether the silica-rich surface layer slows down the release rate of metal cations has been a source of lively debates for over 50 years (see Daval et al., 2009b for a brief summary and e.g. Béarat et al., 2006 for recent results on forsterite) whose answer could at least partly be provided by the determination of its mechanism of formation (e.g. Hellmann et al., 2003; Daval et al., 2009b) or, perhaps more importantly, by the determination of its restructuring dynamics (e.g. Cailleteau et al., 2008). However, our set-up was not designed to address this question, and does not provide any information on these points.

(2) When looking closely at Table 2, the second proposition has to be considered with attention. In fact, the final fluid composition is supersaturated with respect to all SiO_2 polymorphs, among which is amorphous silica (Table 2). Consequently, the measured m_{Fe}/m_{Si} could result from the precipitation of a silica phase, which could be amorphous silica (SiO_2(am)). A few studies (e.g. Giammar et al., 2005 and Daval et al., 2009a for olivine and wollastonite weathering respectively) reported that at moderately high temperature (90–95 °C), the release of SiO_2(aq) from the parent mineral was limited by the solubility of SiO_2(am). However in the present study, if one supposes congruent dissolution of fayalite, the extent of this hypothetical precipitation is relatively weak: indeed, according to thermodynamic calculations using CHESS, if the fluid was in equilibrium with respect to SiO_2(am), the final fluid composition would have the following m_{Fe}/m_{Si} ratios: 14.8; 11.7; 9.6 and 7.7 at 50 °C; 65 °C; 80 °C and 100 °C, respectively. As the measured ratios remain close to the stoichiometric ones, this suggests that only limited amounts of SiO_2(am) may have precipitated. In addition, at a µm-scale, SEM images on fayalite fragments collected after experiments revealed neither secondary phases and coatings, nor significant changes in the iron over silicon ratio of the weathered fayalite measured by X-ray energy dispersive spectroscopy analyses (note that XEDS analyses average the chemical composition of the first few µm of the solid surface, so that coatings smaller than a few µm would be roughly undetectable).

(3) Although not common, the assumption of a continuous non-stoichiometric dissolution process cannot be discarded, as it was already reported for other silicate minerals (e.g. wollastonite, Weissbart and Rimstidt, 2000). However, the structural difference between wollastonite (inosilicate) and fayalite

(orthosilicate), as well as the congruent dissolution process reported by Wogelius and Walther (1992) for fayalite at 25 °C does not make that possibility highly likely.

(4) The possibility that precipitation of silica occurred during quenching is also a good candidate (see similar observations in Daval et al., 2010), since the solubility of amorphous silica decreases with decreasing temperature. This explanation is supported by the fact that the m_{Fe}/m_{Si} ratio for experiment H-65b, whose equilibrium state with respect to fayalite implies a smaller concentration of $SiO_2(aq)$, is almost stoichiometric. In that case, the measured non-stoichiometry of the m_{Fe}/m_{Si} ratios would represent an artefact of the experiments.

To summarise, further investigations should be performed in order to determine unambiguously the stoichiometry of dissolution of fayalite at elevated temperature, and its evolution with time. Note also that a combination of the abovementioned processes cannot be discarded. Following this idea, the limited non-stoichiometry of the solution composition could be consistent with a combination of propositions (1) and (4). The relative contribution to the non-stoichiometry of each of these two processes would remain to be determined accurately, but based on experiment H-65b, one could expect that proposition (4) contributes mainly to the apparent non-congruent dissolution of fayalite.

4.1.4. Iron speciation in the liquid phase and insights on fayalite surface speciation

According to thermodynamic calculation using CHESS, the octahedral hexahydrated aqueous iron species $Fe(H_2O)_6^{2+}$ (noted hereafter Fe^{2+}) is dominant at the end of all experiments in HCl solutions, and all the chlorinated species are expected to represent less than 5% of dissolved Fe(II). This prediction is confirmed by the experimental spectra (Fig. 6) which is consistent with *ab initio* calculations of Fe^{2+} K-edge XANES shown in Fig. 9. If present, chlorinated species would have caused slight but recognisable differences in XANES, occurring in the 7130–7150 eV region and, to a smaller degree, in the 7170–7200 eV region (progressive reduction of the amplitude of the oscillations as the degree of chlorination increases; see e.g. Testemale et al., 2009a for theoretical XANES spectra, and Testemale et al., 2009b for an example based on siderite dissolution in 1 molal NaCl solution). In fact, with such total concentration of chloride ions in solution, Testemale et al. (2009a) proposed that Fe^{2+} would remain by far the dominant species as long as the temperature is below 200 °C, temperatures greater than 300 °C being necessary to stabilise the

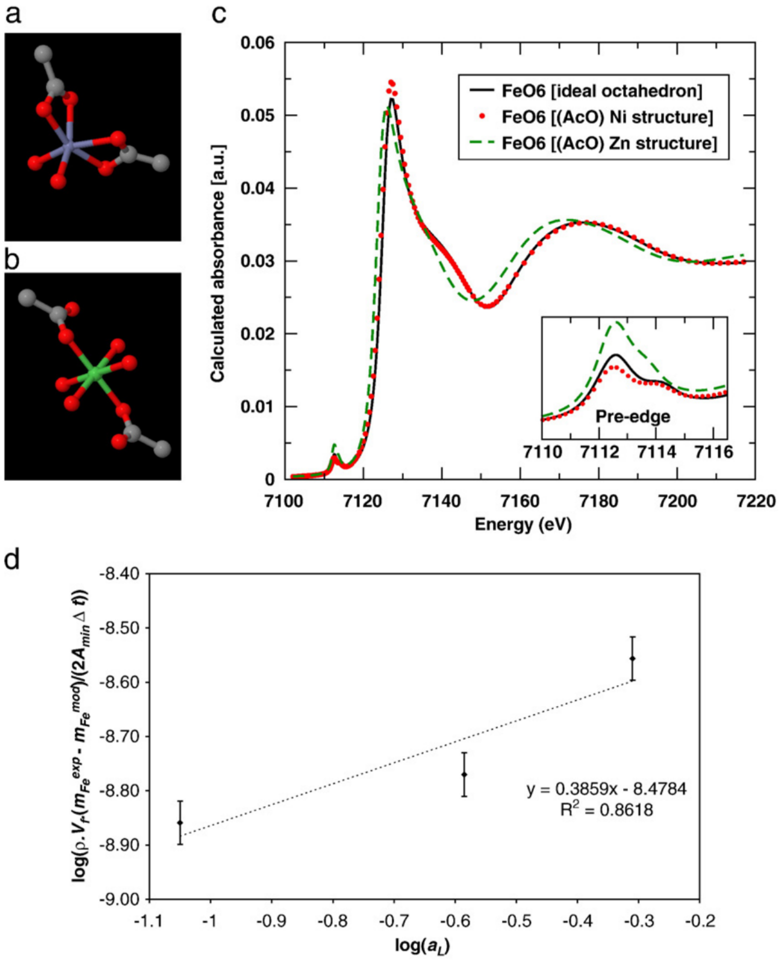

Fig. 9. Fayalite dissolution in acetate buffered solutions. (a) Metal cluster with a Zn-acetate structure (the acetate ligands are bidentate). (b) Metal cluster with an Ni-acetate structure (the acetate ligands are monodentate). (c) *Ab initio* calculations of XANES spectra for Fe^{2+} (black curve), $Fe(CH_3COO)_2 \cdot 4H_2O$ (i.e. the Ni acetate-like structure, red curve) and $Fe(CH_3COO)_2 \cdot 2H_2O$ (i.e. the Zn acetate-like structure, green curve). Whereas the two first structures are almost identical and yield spectra similar to the measured one (see Fig. 6), the last one is clearly different, and does not correspond to any measured spectrum. (d) Dependence of the dissolution rate of fayalite upon the activity of acetate ligands (see text for details).

formation of dominant $FeCl_2(aq)$ and $FeCl_4^{2-}$ species. Besides, it has been suggested for a few years that the activated surface complexes could resemble the corresponding dissolved complexes (e.g. Ludwig et al., 1995). Following this proposition, this would indicate that water molecules are predominantly bonded to Fe at the fayalite–solution interface, rather than Cl^-. If true, one can be confident that the rate constant determined in the present study does not incorporate any hidden term such as a possible dependence upon the concentration of Cl^- species. The conclusion could differ completely at higher temperature (or in more concentrated NaCl solutions for example), where Fe^{2+} is not the aqueous predominant species anymore (and, by extension, such would be the case at the fayalite-solution interface).

4.2. Kinetic modelling of dissolution experiments performed in acetate solutions

4.2.1. Iron speciation in the liquid phase and insights on fayalite surface speciation

Unlike the fluid speciation in HCl solutions, Fe^{2+} is not the dominant species in any of the 3 experiments in acetate solutions. Indeed, according to thermodynamic calculations using the CHESS code, the proportion of Fe^{2+} species at the end of each experiment ranges from ~4.8% (experiment A-1) to ~34.7% (experiment A-3) of the total molality of dissolved iron (Table 3), and the main proportion of aqueous iron is complexed by acetate ligands. As a consequence, following the reasoning of Ludwig et al. (1995) (see above), one can expect that the surface speciation of fayalite is modified accordingly, if the acetate ligands do form an inner-sphere complex.

To determine the geometry of the presumable dominant surface complexes, *ab initio* XANES calculations of aqueous iron spectra were performed. Unfortunately, it was not possible to find any crystallographic structure reference for solid $Fe(CH_3COO)_2$. However, structures of $Ni(CH_3COO)_2\cdot 4H_2O$, $Co(CH_3COO)_2\cdot 4H_2O$ (these two crystals being isostructural) and $Zn(CH_3COO)_2\cdot 2H_2O$ have been published (Van Niekerk and Schoening, 1953a,b). The corresponding metal clusters are shown in Fig. 9. Whereas the acetate ligands bind through two bridging oxygens with Zn (Fig. 9a), they bind through one oxygen only with Ni and Co, and the corresponding metal cluster is almost perfectly octahedral (Fig. 9b). The XANES spectra of the metal clusters $Fe(H_2O)_6^{2+}$ (octahedral structure, noted Fe^{2+} hereafter), $Fe(CH_3COO)_2\cdot 4H_2O$ (i.e. the Ni acetate-like structure) and $Fe(CH_3COO)_2\cdot 2H_2O$ (i.e. the Zn acetate-like structure) were calculated, and are shown in Fig. 9c. As it can be seen, the calculated spectra for Fe^{2+} and $Fe(CH_3COO)_2\cdot 4H_2O$ (Ni acetate-like structure) are almost indistinguishable. In both structures the first shell of metal atoms is made of 6 oxygen atoms, whereas complex structures (almost perfect octahedra) and second neighbours (lights elements) are similar, explaining in turn the similarity of XANES spectra. On the other hand, the calculated spectrum for $Fe(CH_3COO)_2\cdot 2H_2O$ (Zn acetate-like structure) is clearly different. In the latter, there are an increase of the pre-edge amplitude, a change in the frequency of the oscillations corresponding to different average Fe–O distances, and modifications in the 7125–7150 eV energy region. By comparing these theoretical XANES spectra to the experimental ones shown in Fig. 6, the occurrence of aqueous iron acetate with a distorted Zn acetate-like structure (i.e. with bidentate acetate ligands) can thus be discarded. In acetate solutions, based on thermodynamic calculations, Fe acetate aqueous species are predominant (see Table 3). It is thus likely that the corresponding aqueous complexes are formed by the binding of acetate ligands with Fe through one bridging oxygen only (Fig. 9b). Following the reasoning of Ludwig et al. (1995), we propose that monodentate complexation of iron at the fayalite/solution interface occurs as well. Finally, because acetate ions are more charged than water molecules, dissolution rates in the presence of acetate are expected to be higher (see e.g. similar conclusions for the role of oxalate with respect to forsterite in Olsen and Rimstidt, 2008). The next section aims at quantifying this effect.

Table 3
Calculated iron speciation (in mol%) for experiments led in acetate buffered solutions using the CHESS code.

Experiment	$Fe(CH_3COO)_2(aq)$	$FeCH_3COO^+$	Fe^{2+}
A-1	74.5	20.7	4.8
A-2	60.0	28.2	11.8
A-3	29.5	35.8	34.7

4.2.2. Dependence of fayalite dissolution rate upon acetate concentration

The typical evolution of iron molality as a function of time for one of the 3 experiments in acetate buffers (experiment A-3) is reported in Fig. 5. In this figure, the experimental data are compared with the expected evolution using Eq. (5) and the parameters k_0, n and E_a determined in the present study. Although the global shape of both the modelled and experimental curves needs more discussion (see below), a first striking point is that the actual dissolution rate of fayalite is far greater than the modelled one. Such is the case for the two other experiments A-1 and A-2 (data not shown). As explained above, these differences could result from the complexation at the fayalite–solution interface by acetate ligands, whose nucleophilic character is stronger than that of water molecules; this would in turn promote the enhancement of fayalite dissolution rate.

One possible way to take into account this effect consists in introducing a specific dependence upon the activity of acetate ligands in the overall kinetic rate law. Far from equilibrium, if the ligand-promoted and proton-promoted dissolution reactions are parallel, then the overall reaction rate (labelled R_{net} in the equation below) can be written as the sum of the ligand-free rate law and the ligand-promoted rate law (e.g. Grandstaff, 1986; Wogelius and Walther, 1992; Stillings et al., 1996; Golubev and Pokrovsky, 2006; Olsen and Rimstidt, 2008):

$$R_{net} = k_T \cdot a_{H^+}^{n} + k_L \cdot a_{L^-}^{p}. \qquad (13)$$

In the above equation, k_L represents the temperature-dependent ligand-promoted rate constant ($mol\,cm^{-2}\,s^{-1}$), a_{L^-} the activity of acetate ligands, and p the reaction order with respect to acetate. Note that some of the abovementioned studies expressed the ligand-promoted dissolution rate using concentrations of ligands instead of activities. Given the fact that our experiments in acetate buffers were carried out in solutions which cannot be considered as to be diluted (ionic strength >0.1 molal), activities were preferred. However, we verified that the use of concentrations or activities of acetate ligands in Eq. (13) did not significantly affect the numerical values of k_L and p.

From Eq. (13), one can calculate that after a given reaction time Δt, the total iron molality $m_{Fe}(t)$ is expected to be:

$$m_{Fe}(t) = k_T \cdot a_{H^+}(t)^n \cdot \left(\frac{2\Delta t \cdot A_{min}(t)}{\rho \times V_f}\right) + k_L \cdot a_{L^-}(t)^p \cdot \left(\frac{2\Delta t \cdot A_{min}(t)}{\rho \times V_f}\right) \qquad (14)$$

where V_f (expressed in L if ρ is in $kg\,L^{-1}$) stands for the volume of the fluid in the micro-reactor. The first term of the sum above can be retrieved by performing a kinetic simulation using the CHESS code, with $k_T = 1.48 \times \exp(-45{,}100/(8.314 \times 338))\ mol\,cm^{-2}\,s^{-1}$ at 65 °C and $n = 0.74$. This term will be noted hereafter $m_{Fe}^{mod}(t)$. Thus, for a given reaction time, Eq. (14) can be rewritten following:

$$\log\left(\frac{\rho \cdot V_f \cdot \left(m_{Fe}^{exp}(t) - m_{Fe}^{mod}(t)\right)}{2A_{min}(t) \cdot \Delta t}\right) = \log k_L + p \cdot \log\left(a_{L^-}(t)\right) \qquad (15)$$

where $m_{Fe}^{exp}(t)$ refers as to the actual iron molality measured after an experimental duration Δt. If the reaction time is chosen such that the amount of iron released to the fluid is not too large, then $A_{\min}(t)$ can simply be set equal to $A_{\min}(0)$, the dissolution rate is actually ΔG_r-independent (see below), and thus, the use of Eq. (14) is valid. A reaction time of 25 min was chosen, as it verifies the abovementioned conditions.

By plotting $\log\left(\frac{\rho \cdot V_{\mathrm{f}} \cdot \left(m_{\mathrm{Fe}}^{\exp}(t) - m_{\mathrm{Fe}}^{\mathrm{mod}}(t)\right)}{2A_{\min}(t)\cdot \Delta t}\right)$ as a function of $\log(a_{\mathrm{L^-}})$ (Fig. 9d), we determined that $k_{\mathrm{L}} = 10^{-8.48}$ mol cm^{-2} s^{-1}, and $p = 0.39$. The relatively good regression coefficient of the fit ($r^2 = 0.86$) presumably indicates that the mechanism responsible for the increase of fayalite dissolution rate was correctly singled out, even if more data are obviously required to determine a more accurate rate law. Moreover, one of the possible reasons why the regression coefficient is not even closer to unity is that the 3 experiments were not under exactly the same ionic strength (it was decided not to add an electrolyte such as NaCl to the aqueous solutions because it would have significantly complicated the experimental determination of iron molalities, because of the higher absorbance of the solution (see Section 3.1)). However, one must be aware that ionic strength could slightly influence the dissolution rates as well, such that the values of k_{L} and p above should rather be considered as indicative. On the whole, it should be kept in mind that the rate equation determined above is limited to acidic pH, moderate ionic strength (i.e. <1 molal) and $\mathrm{Fe^{3+}}$-free aqueous solutions.

A final remark can be made concerning the characteristics of the evolution of iron molality over long durations (Fig. 5a). Intriguingly, the experimental release of iron as a function of time is not linear. This is at odds with thermodynamic and kinetic modelling which predicts that both the pH and the concentration of acetate ligands remain roughly constant through time in all of the 3 experiments led in acetate buffers, resulting in an almost linear release of iron as function of time. A common explanation for such parabolic trends is that during the first stages of dissolution, the process is controlled by the rapid disappearance of fine surface particles present on the dissolving grains (e.g. Schott et al., 1981). But although this justification can be considered valid when working with natural, crushed and sieved materials (this procedure being inevitably the source of fine particles), it is more questionable when working with synthetic, uncrushed minerals, as it is the case here. Another explanation frequently proposed is that the dissolution process is limited by the diffusion of reactants in the fluid and/or the solid phases. We cannot discard that possibility for long-term experiments in acetate buffers, i.e. the rate-limiting step moves from a surface-controlled to a diffusion-controlled process, especially if the final measured $m_{\mathrm{Fe}}/m_{\mathrm{Si}}$ ratios are not only artefacts due to quenching effects. Another possibility is that the decrease of fayalite dissolution rate as a function of time could be due to the release of iron itself, either through an inhibition effect (such as proposed by e.g. Oelkers et al., 1994 for Al with respect to albite dissolution), or through an increase of ΔG_r, leading to a change in dissolution mechanism (e.g. Lasaga and Lüttge, 2001; Hellmann et al., 2010). For example, if we consider the particular case of experiment A-3, after 25 min, the Gibbs free energy with respect to fayalite dissolution was calculated to be $\Delta G_r = -72$ kJ mol^{-1}, and gradually increases until the end of the experiment (after ~8 h, $\Delta G_r = -54$ kJ mol^{-1}). As mentioned in Section 4.1.1, it was previously shown for other minerals that the dissolution rate could be affected by ΔG_r, even in a range of such low Gibbs free energies. Interestingly, similar conclusions were previously reached 30 years ago for the weathering of feldspars in batch reactors (Lagache, 1976). To test this assumption and determine precisely the presumable rate-determining elementary reaction, specific experiments dedicated to the rate–affinity relationships of fayalite dissolution should be carried.

5. Conclusions

In situ X-ray absorption spectroscopy measurements were conducted in a small batch reactor to characterise the kinetics of dissolution of fayalite in HCl solutions, between 50 °C and 100 °C, at a constant pressure of 30 MPa. From the iron molalities, far-from-equilibrium dissolution kinetics of fayalite can be expressed as: $r = k_0 \exp(-E_{\mathrm{a}}/RT)a_{\mathrm{H^+}}{}^{n}$, with $k_0 = 10^{0.17 \pm 0.63}$ mol cm^{-2} s^{-1}; $E_{\mathrm{a}} = 45.1 \pm 4.2$ kJ mol^{-1} and $n = 0.74 \pm 0.15$. In parallel with these dissolution measurements, the speciation of dissolved iron was monitored by qualitative interpretation of the XANES signal. Consistently with thermodynamic calculations, it was found that iron is hydrated in the conditions of our study. The XANES observations rule out the presence of ferric ions in the system. By using a previously published empirical correlation between geometric and BET surface areas, we showed that our renormalised rate data are in good agreement with some of the literature data, indicating faster far-from-equilibrium dissolution of fayalite than forsterite by about one order of magnitude. The type of dataset derived from such studies is useful to build more complex geochemical models, such as computing the full dissolution rate laws for olivine solid solutions with various compositions.

In situ X-ray absorption spectroscopy was also shown to be a powerful tool to monitor the role of acetate ligands on the reactivity of fayalite. Supposing that the surface complexes are related to the major complex species in solution, our method combined with *ab initio* XANES calculations allowed us to determine that water molecules are predominantly bonded to Fe at the fayalite–solution interface when the reaction was initiated in HCl solutions. On the other hand, in acetate buffers, acetate ligands are bonded to Fe through one bridging oxygen. In parallel, we showed that the dissolution rate is positively correlated with the logarithm of acetate activity. By combining these observations we propose that, as for many other minerals, organic ligands are able to promote the dissolution of fayalite via surface complexation. This finding is interesting, as living organisms which participate to $\mathrm{CO_2}$ biomineralisation in subsurface environments (see e.g. Dupraz et al., 2009 and references therein) can excrete that kind of organic ligands and thus increase Fe-rich olivine weathering and iron mobility. Finally, our methodology shows that good quality kinetic data can be obtained by full inversion of batch experiments which is particularly appropriate for studying dissolution of ferrous minerals. It opens promising perspectives for studying the effect of various ligands, including siderophores, on these dissolution processes.

Acknowledgements

The authors acknowledge the European Synchrotron Radiation Facility for provision of synchrotron radiation beamtime and facilities, and would like to thank the FAME staff for assistance in using their beamline. Fabrice Brunet (ENS Paris) is also warmly acknowledged for his help with the sintering of fayalite powders. The careful reading by an anonymous reviewer and Pr. John V. Walther was much appreciated, and considerably helped to improve this manuscript. This is IPGP contribution 3003.

References

Bachu, S., 2000. Sequestration of $\mathrm{CO_2}$ in geological media: criteria and approach for site selection in response to climate change. Energy Convers. Manage. 41 (9), 953–970.

Béarat, H.H., McKelvy, M., Chizmeshya, A., Gormley, D., Nunez, R., Carpenter, R.W., Squires, K., Wolf, G.H., 2006. Carbon sequestration via aqueous olivine mineral carbonation: role of passivating layer formation. Environ. Sci. Technol. 40 (15), 4802–4808.

Bénézeth, P., Dandurand, J.L., Harrichoury, J.C., 2009. Solubility product of siderite (FeCO3) as a function of temperature (25–250 degrees C). Chem. Geol. 265, 3–12.

Berndt, M.E., Allen, D.E., Seyfried, W.E., 1996. Reduction of $\mathrm{CO_2}$ during serpentinization of olivine at 300 °C and 500 bar. Geology 24 (4), 351–354.

Brantley, S.L., Mellot, N.P., 2000. Surface area and porosity of primary silicate minerals. Am. Mineralog. 85, 1767–1783.

Brugger, J., Etschmann, B., Liu, W., Testemale, D., Hazemann, J.-L., Emerich, H., van Beek, W., Proux, O., 2007. An XAS study of the structure and thermodynamics of Cu(I) chloride complexes in brines up to high temperature (400 °C, 600 bar). Geochim. Cosmochim. Acta 71, 4920–4941.

Cailleteau, C., Angeli, F., Devreux, F., Gin, S., Jestin, J., Jollivet, P., Spalla, O., 2008. Insight into silicate–glass corrosion mechanisms. Nat. Mater. 7 (12), 978–983.

Casey, W.H., Sposito, G., 1992. On the temperature dependence of mineral dissolution rates. Geochim. Cosmochim. Acta 56, 3825–3830.

Casey, W.H., Westrich, H.R., 1992. Control of dissolution rates of orthosilicate minerals by divalent metal oxygen bonds. Nature 355 (6356), 157–159.

Chen, Y., Brantley, S.L., 1998. Diopside and anthophyllite dissolution at 25° and 90 °C and acid pH. Chem. Geol. 147, 233–248.

Chen, Y., Brantley, S.L., 2000. Dissolution of forsteritic olivine at 65 °C and $2<\mathrm{pH}<5$. Chem. Geol. 165, 267–281.

Da Silva, C., Proux, O., Hazemann, J.-L., James-Smith, J., Testemale, D., Yamaguchi, T., 2009. X-ray absorption spectroscopy study of salvation and ion-pairing in aqueous gallium bromide solutions at supercritical conditions. J. Mol. Liq. 147, 83–95.

Daval, D., Martinez, I., Corvisier, J., Findling, N., Goffé, B., Guyot, F., 2009a. Carbonation of Ca-bearing silicates, the case of wollastonite: experimental investigations and kinetic modelling. Chem. Geol. 265, 63–78.

Daval, D., Martinez, I., Guigner, J.-M., Hellmann, R., Corvisier, J., Findling, N., Dominici, C., Goffé, B., Guyot, F., 2009b. Mechanism of wollastonite carbonation deduced from observations at a micro- to nanometre scale-length study. Am. Mineralog. 94, 1707–1726.

Daval, D., Hellmann, R., Corvisier, J., Tisserand, D., Martinez, I., Guyot, F., 2010. Dissolution kinetics of diopside as a function of solution saturation state: macroscopic measurements and implications for modeling of geological storage of CO_2. Geochim. Cosmochim. Acta 74, 2615–2633.

Dufaud, F., 2006. Etude expérimentale des réactions de carbonatation minérale du CO_2 dans les roches basiques et ultrabasiques. Institut de Physique du Globe de Paris, Paris. 261 pp.

Dufaud, F., Martinez, I., Shilobreeva, S., 2009. Experimental study of Mg-rich silicates carbonation at 400 and 500 °C and 1 kbar. Chem. Geol. 265 (1–2), 54–62.

Dupraz, S., Ménez, B., Gouze, P., Leprovost, R., Bénézeth, P., Pokrovsky, O.S., Guyot, F., 2009. Experimental approach of CO_2 biomineralization in deep saline aquifers. Chem. Geol. 265 (1–2), 54–62.

Gautier, J.M., Oelkers, E.H., Schott, J., 2001. Are quartz dissolution rates proportional to BET surface areas? Geochim. Cosmochim. Acta 65 (7), 1059–1070.

Giammar, D.E., Bruant Jr, R.G., Peters, C.A., 2005. Forsterite dissolution and magnesite precipitation at conditions relevant for deep saline aquifer storage and sequestration of carbon dioxide. Chem. Geol. 217, 257–276.

Golubev, S.V., Pokrovsky, O.S., 2006. Experimental study of the effect of organic ligands on diopside dissolution kinetics. Chem. Geol. 235, 377–389.

Golubev, S.V., Benezeth, P., Schott, J., Dandurand, J.L., Castillo, A., 2009. Siderite dissolution kinetics in acidic aqueous solutions from 25 to 100 °C and 0 to 50 atm pCO_2. Chem. Geol. 265 (1–2), 13–19.

Grandstaff, D.E., 1986. The dissolution rate of forsteritic olivine from Hawaiian beach sand. In: Colman, S.M., Dethier, D.P. (Eds.), Rates of Chemical Weathering of Rocks and Minerals. Academic Press, Orlando, FL, pp. 41–57.

Hänchen, M., Prigiobbe, V., Storti, G., Seward, T.M., M., M., 2006. Dissolution kinetics of fosteritic olivine at 90–150 °C. Geochim. Cosmochim. Acta 70, 4403–4416.

Hellmann, R., Tisserand, D., 2006. Dissolution kinetics as a function of the Gibbs free energy of reaction: an experimental study based on albite feldspar. Geochim. Cosmochim. Acta 70, 364–383.

Hellmann, R., Penisson, J.-M., Hervig, R.L., Thomassin, J.-H., Abrioux, M.-F., 2003. An EFTEM/HRTEM high-resolution study of the near surface of labradorite feldspar altered at acid pH: evidence for interfacial dissolution–reprecipitation. Phys. Chem. Miner. 30 (4), 192–197.

Hellmann, R., Daval, D., Tisserand, D., 2010. The dependence of albite feldspar dissolution kinetics on fluid saturation state at acid and basic pH: progress towards a universal relation. C. R. Geosci. 342 (7–8), 676–684.

Holland, T.J.B., Powell, R., 1990. An enlarged and updated thermodynamic dataset with uncertainties and correlations. J. Metamorph. Geol. 8, 89–124.

Joly, Y., 2001. X-ray absorption near-edge structure calculations beyond the muffin-tin approximation. Phys. Rev. B 63, 125120.

Kaszuba, J.P., Janecky, D.R., Snow, M.G., 2005. Experimental evaluation of mixed fluid reactions between supercritical carbon dioxide and NaCl brine: relevance to the integrity of a geologic carbon repository. Chem. Geol. 217 (3–4), 277–293.

Knauss, K.G., Johnson, J.W., Steefel, C.I., 2005. Evaluation of the impact of CO_2, co-contaminant gas, aqueous fluid and reservoir rock interactions on the geologic sequestration of CO_2. Chem. Geol. 217, 339–350.

Koeppen, W.C., Hamilton, V.E., 2006. The distribution and composition of olivine on Mars. Lunar and Planetary Science Conference XXXVII, abstract 1964.

Krause, M.O., Oliver, J.H., 1979. Natural widths of atomic K and L levels, K alpha X-ray lines and several KLL Auger lines. J. Phys. Chem. Ref. Data 8, 329.

Lackner, K.S., 2003. A guide to CO_2 sequestration. Science 300, 1677–1678.

Lagache, M., 1976. New data on the kinetics of the dissolution of alkali feldspars at 200 °C in CO_2 charged water. Geochim. Cosmochim. Acta 40 (2), 157–161.

Lasaga, A.C., 1981. Transition state theory. In: Lasaga, A.C., Kirkpatrick, R.J. (Eds.), Kinetics of Geochemical Process. Mineralogical Society of America, pp. 135–169.

Lasaga, A.C., 1984. Chemical kinetics of water–rocks interactions. J. Geophys. Res. 89 (NB6), 4009–4025.

Lasaga, A.C., Luttge, A., 2001. Variation of crystal dissolution rate based on a dissolution stepwave model. Science 291, 2400–2404.

Liu, W., Brugger, J., Etschmann, B., Testemale, D., Hazemann, J.-L., 2008. The solubility of nantokite (CuCl(s)) and Cu speciation in low-density fluids near the critical isochore: an in-situ XAS study. Geochim. Cosmochim. Acta 72, 4094–4106.

Ludwig, C., Casey, W.H., Rock, P.A., 1995. Prediction of ligand-promoted dissolution rates from the reactivities of aqueous complexes. Nature 375 (6526), 44–47.

McCollom, T.M., Seewald, J.S., 2001. A reassessment of the potential for reduction of dissolved CO_2 to hydrocarbons during serpentinization of olivine. Geochim. Cosmochim. Acta 65 (21), 3769–3778.

McCollom, T.M., Seewald, J.S., 2006. Carbon isotope composition of organic compounds produced by abiotic synthesis under hydrothermal conditions. Earth and Planetary Science Letters 243 (1–2), 74–84.

McCollom, T.M., Seewald, J.S., 2007. Abiotic synthesis of organic compounds in deep-sea hydrothermal environments. Chem. Rev. 107 (2), 382–401.

McGrail, P.B., Schaef, T.H., Ho, A.M., Chien, Y.-J., Dooley, J.J., 2006. Potential for carbon dioxide sequestration in flood basalts. J. Geophys. Res. 111, B12201.

National Bureau of Standards, 1983. Joint Committee on Powder Diffraction Standards. Monograph, reference 34-0178. 25, 20–59.

Oelkers, E.H., Schott, J., Devidal, J.-L., 1994. The effect of aluminum, pH, and chemical affinity on the rates of aluminosilicate dissolution reactions. Geochim. Cosmochim. Acta 58, 2011–2024.

Olsen, A.A., Rimstidt, J.D., 2007. Using a mineral lifetime diagram to evaluate the persistence of olivine on Mars. Am. Mineralog. 92 (4), 598–602.

Olsen, A.A., Rimstidt, J.D., 2008. Oxalate-promoted forsterite dissolution at low pH. Geochim. Cosmochim. Acta 72 (7), 1758–1766.

Palandri, J.L., Kharaka, Y.K., 2005. Ferric iron-bearing sediments as a mineral trap for CO_2 sequestration: Iron reduction using sulfur-bearing waste gas. Chem. Geol. 217 (3–4), 351–364.

Pokrovski, G.S., Roux, J., Hazemann, J.L., Testemale, D., 2005. An X-ray absorption spectroscopy study of argutite solubility and aqueous Ge(IV) speciation in hydrothennal fluids to 500 degrees C and 400 bar. Chem. Geol. 217 (1–2), 127–145.

Pokrovski, G.S., Borisova, A.Y., Roux, J., Hazemann, J.-L., Petdang, A., Tella, M., Testemale, D., 2006. Antimony speciation in saline hydrothermal fluids: a combined X-ray absorption fine structure spectroscopy and solubility study. Geochim. Cosmochim. Acta 70 (16), 4196–4214.

Pokrovski, G.S., Tagirov, B.R., Schott, J., Bazarkina, E.F., Hazemann, J.-L., Proux, O., 2009. An *in situ* X-ray absorption spectroscopy study of gold-chloride complexing in hydrothermal fluids. Chem. Geol. 259, 17–29.

Pokrovsky, O.S., Schott, J., 2000a. Forsterite surface composition in aqueous solutions: a combined potentiometric, electrokinetic, and spectroscopic approach. Geochim. Cosmochim. Acta 64 (19), 3299–3312.

Pokrovsky, O.S., Schott, J., 2000b. Kinetics and mechanism of forsterite dissolution at 25 °C and pH from 1 to 12. Geochim. Cosmochim. Acta 64 (19), 3313–3325.

Proux, O., Biquard, X., Lahera, E., Menthonnex, J.-J., Prat, A., Ulrich, O., Soldo, Y., Trevisson, P., Kapoujyan, G., Perroux, G., Taunier, P., Grand, D., Jeantet, P., Deleglise, M., Roux, J.-P., Hazemann, J.-L., 2005. FAME: A new beamline for X-ray absorption investigations of very-diluted systems of environmental, material and biological interests. Phys. Scr. T115, 970–973.

Proux, O., Nassif, V., Prat, A., Ulrich, O., Lahera, E., Biquard, X., Menthonnex, J.-J., Hazemann, J.-L., 2006. Feedback system of a liquid-nitrogen-cooled double-crystal monochromator: design and performances. J.Synchrotron Radiat. 13, 59–68.

Ravel, B., Newville, M., 2005. ATHENA, ARTEMIS, HEPHAESTUS: data analysis for X-ray absorption spectroscopy using IFEFFIT. J. Synchrotron Radiat. 12, 537–541.

Rosso, J.J., Rimstidt, D.J., 2000. A high resolution study of forsterite dissolution rates. Geochim. Cosmochim. Acta 64 (5), 797–811.

Santelli, C.M., Welch, S.A., Westrich, H.R., Banlfied, J.F., 2001. The effect of Fe-oxidizing bacteria on Fe-silicate mineral dissolution. Chem. Geol. 180, 99–115.

Schott, J., Berner, R.A., Lennart Sjöberg, E., 1981. Mechanism of pyroxene and amphibole weathering—I. Experimental studies of iron-free minerals. Geochim. Cosmochim. Acta 45 (11), 2123–2135.

Schott, J., Brantley, S.L., Crerar, D., Guy, C., Borcsik, M., Willaime, C., 1989. Dissolution kinetics of strained calcite. Geochim. Cosmochim. Acta 53 (2), 373–382.

Taylor, A.S., Blum, J.D., Lasaga, A.S., 2000. The dependence of labradorite dissolution and Sr isotope release rates on solution saturation state. Geochim. Cosmochim. Acta 64 (14), 2389–2400.

Stillings, L.L., Drever, J.I., Brantley, S.L., Sun, Y.T., Oxburgh, R., 1996. Rates of feldspar dissolution at pH 3–7 with 0–8 mM oxalic acid. Chem. Geol. 132 (1–4), 79–89.

Testemale, D., Argoud, R., Geaymond, O., Hazemann, J.-L., 2005. High pressure/high temperature cell for X-ray absorption and scattering techniques. Rev. Sci. Instrum. 76, 043905.

Testemale, D., Brugger, J., Liu, W., Etschmann, B., Hazemann, J.-L., 2009a. In-situ X-ray absorption study of Iron(II) speciation in brines up to supercritical conditions. Chem. Geol. 264, 295–310.

Testemale, D., Dufaud, F., Martinez, I., Bénézeth, P., Hazemann, J.-L., Schott, J., Guyot, F., 2009b. An X-ray absorption study of the dissolution of siderite at 300 bar between 50 °C and 100 °C. Chem. Geol. 259, 8–16.

van der Lee, J., De Windt, L., 2002. CHESS Tutorial and Cookbook. Updated for version 3.0., Manual Nr. LHM/RD/02/13, Paris, 116 pp.

Van Niekerk, J.N., Schoening, F.R.L., 1953a. The crystal structures of nickel acetate, Ni $(CH3COO)_2.4H_2O$, and cobalt acetate, $Co(CH3COO)_2.4H_2O$. Acta Cryst. 6, 609.

Van Niekerk, J.N., Schoening, F.R.L., 1953b. The crystal structures of zinc acetate dihydrate, $Zn(CH3COO)_2.2H_2O$. Acta Cryst. 6, 720.

Velbel, M.A., 1993. Formation of protective surface layers during silicate-mineral weathering under well-leached, oxidizing conditions. Am. Mineralog. 78 (3–4), 405–414.

Wagner, W., Pruss, A., 2002. The IAPWS formulation 1995 for the thermodynamic properties of ordinary water substance for general and scientific use. J. Phys. Chem. Ref. Data 31 (2), 387–535.

Weissbart, E.J., Rimstidt, D.J., 2000. Wollastonite: incongruent dissolution and leached layer formation. Geochim. Cosmochim. Acta 64 (23), 4007–4016.

Westrich, H.R., Cygan, R.T., Casey, W.H., Zemitis, C., Arnold, G.W., 1993. The dissolution kinetics of mixed-cation orthosilicate minerals. Am. J. Sci. 293 (9), 869–893.

Wogelius, R.A., Walther, J.V., 1991. Olivine dissolution at 25 °C: effects of pH, CO_2, and organic acids. Geochim. Cosmochim. Acta 55, 943–954.

Wogelius, R.A., Walther, J.V., 1992. Olivine dissolution kinetics at near-surface conditions. Chem. Geol. 97 (1–2), 101–112.

Wolery, T.J., 1992. EQ3NR, A computer program for geochemical aqueous speciation-solubility calculations: theoretical manual, user's guide, and related documentation (Version 7.0). pp. 262. Lawrence Livermore Natl. Lab. UCRL-MA-110662 PT III.

Xu, T., Apps, J.A., Pruess, K., 2004. Numerical simulation of CO_2 disposal by mineral trapping in deep aquifers. Appl. Geochem. 19, 917–936.

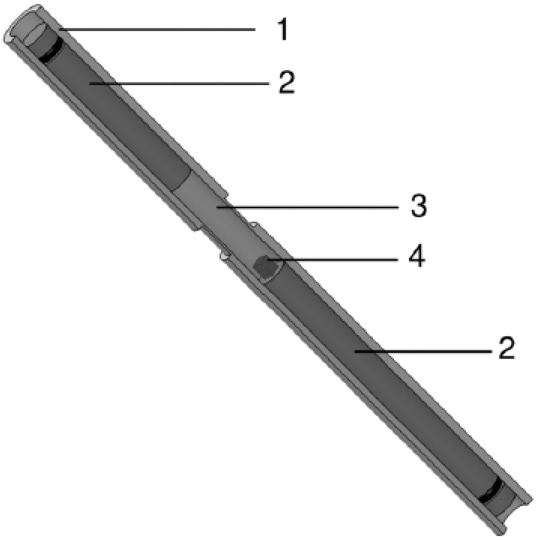

Fig. 1. Sample container used in the experiments. 1) Glassy carbon tube, internal diameter of 4 mm, total length is 85 mm; 2) alumina internal rods, pistons with viton rings; 3) aqueous sample volume; the glassy carbon can be thinner (100 μm in this experiment) in this area; 4) siderite single crystal placed on top of the bottom inner rod. This experimental configuration provided a sample volume of about 75 mm^3.

Figure 1.2: Figure from reference (10), which shows the inner cell loaded with a solid sample and an aqueous solution.

1.2.2 Iron(III) at hydrothermal conditions.

Note: This is still an advanced work in progress with no publication (yet), but a detailed summary of the main results is given in the following, which constitutes a solid basis for a future manuscript.

Collaborations:

- *Münster University (C. Sanchez-Valle)*
- *IMPMC and IPGP (F. Guyot)*
- *GET (G. Pokrovski)*
- *Local: Néel Institute (Y. Joly) + FAME staff*

Key ideas of the study:

- **The speciation results are similar to Fe^{II}**: the temperature and chloride concentration drive the transition from hydrated octahedral species to tetrahedral chlorinated species. In particular, EXAFS and XANES analyses demonstrate the likely predominance of the $FeCl_4^-$ species at high temperature and high chloride concentration. In that way, Fe^{3+} behaves like most 3d transition metals.
- One striking difference is **the redox behaviour at high temperatures**: the reduction to Fe^{2+} is systematically observed above 200°C, even in buffered HMQ conditions. Given the exhaustive experimental efforts provided to evaluate this redox stability, it is firmly believed that it is not an experimental side effect. This stability of the reduced form of aqueous iron has strong consequences for the geochemical cycle of iron.
- From a technological point of view, in addition to what was shown above in Fe^{II} studies (transmission/fluorescence methodology, solubility/speciation coordinated study, micro-batch reactor), this Fe^{III} study demonstrates **the redox capabilities of our autoclave/XAS set-up**: in situ determination of redox ratios; work in controlled redox conditions by loading mineral buffer assemblages; very large sample/beam volume ratio which is favorable to limit beam damage.

The usual strategy has been used to tackle the case of Fe^{III}. Fe^{III}-bearing minerals are major controlling phases of iron. In shallow P and T conditions Fe^{III} oxides and hydroxides play a critical role in industrial and environmental processes (chemical weathering, water purification, soil evolution, etc.) (15). In more elevated P and T conditions, Fe^{III} importance holds: still in an industrial environment (supercritical water oxidation and power generation processes), but also in the context of arc-magmas generation and subduction zones where the redox processes are not fully understood, yet. In this specific case, the oxidized state of subduction zone magmas, coupled with the isotopic evidence of fluid-rock interactions in the corresponding zenoliths (16), makes water and the oxydized components of aqueous solutions (generated by the melting of the subducted oceanic crust) possible candidates to explain this redox situation (17). Consequently, this study investigates both Fe^{III} speciation, but also its redox behaviour at experimental conditions typical of subduction zones.

This study about Fe^{III} at hydrothermal conditions is an ongoing project of mine since (too) many years, focussed mainly on the chloride complexation. In this chapter I chose to expose the main elements of this work, collected along the last 10 years, in collaboration with several persons: F. Guyot (IMPMC, Paris), Y. Joly and I. Gautier-Luneau (Néel Institute, Grenoble), C. Sanchez-Valle (Münster University), G. Pokrovski (GET, Toulouse). A related study conducted in collaboration with J. Brugger and his team, and dedicated to Fe^{II}/Fe^{III} fluoride complexation, was published recently (18). As in the rest of this manuscript I won't go into all the details but instead provide the main results in order to depict a more global picture.

1.2.2.1 Speciation of Fe^{III} at hydrothermal conditions

The first axis of investigation was to study the speciation of Fe^{III} at hydrothermal conditions, in particular the nature and structure of iron chloride species. Two methods were used to put Fe^{III} in solution: dissolution of the $FeCl_3$ salt, in controlled quantities; and dissolution of Fe-bearing oxide minerals (see the corresponding solubility results below). Basically, the speciation results are similar with both methods, with a few differences which makes the grouping of all data relevant:

- at ambient conditions, the solubility method doesn't put enough iron in solution to acquire spectra (the kinetics of mineral dissolution at room temperature don't play well with the timescale of a synchrotron experiment!).
- the solubility method doesn't enable the control of iron concentration in solution because the solubility varies with temperature; this is less than ideal to optimize the data quality (signal-to-noise) and to control the Fe/Cl ratio.

Solution	Cl molality (mol/kg)	Pressure (bar)	Temperature range (°C)
Dissolved $FeCl_3$ salt (0.05 m) in 0.1 m HCl	0.25	300	25
Dissolution of hematite in 0.3 m HCl	0.3	300	25-350
Dissolution of hematite in 1 m HCl	1	300	25-350
Dissolution of hematite in 3 m HCl	3	300	25-350
Dissolved $FeCl_3$ salt (0.13 m) in 0.2 m HCl/5.3 m LiCl	5.9	300	25-350

Table 1.1: Experimental conditions for the study of Fe^{III} speciation.

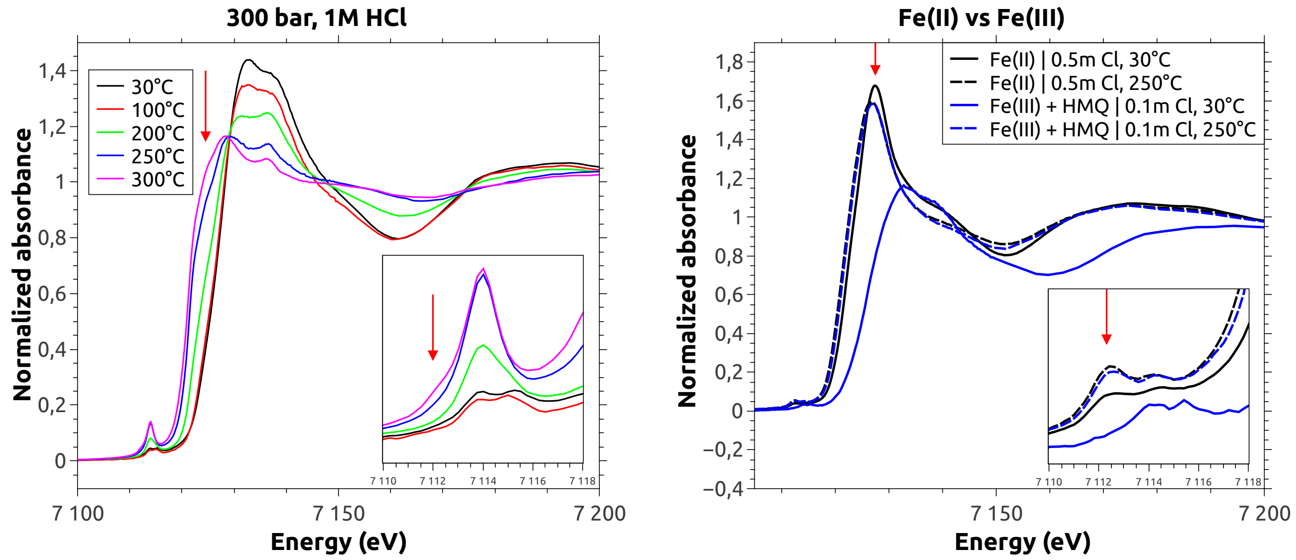

Figure 1.3: Left: XANES spectra of a 300 bar Fe^{III} (1 m HCl) solution, as a function of temperature from 30 to 300°C; the growing of Fe^{II} XANES features from 250°C are indicated with the red arrows both in the white line and the pre-edge area. Right: XANES spectra of a Fe^{II} chloride solution (from reference (7)) and a Fe^{III} chloride solution equilibrated with a HMQ mineral assemblage, at 30 and 250°C: the complete similarity of the spectra at 250°C demonstrate the complete reduction of iron.

- the solubility method is more relevant from a geologic point of view, in particular the use of buffer minerals assemblage (see below).

The different experimental conditions investigated are listed in table 1.1.

Qualitative analysis: Figure 1.4 shows the typical spectral changes of Fe^{III} spectra with temperature for a given chloride concentration, the latter obtained through addition of HCl (or LiCl for the 6M solution). All spectra are normalized fluorescence measurements, either from a solution equilibrated with hematite (dissolution of hematite as a way to release Fe^{III}) or from a starting solution of dissolved $FeCl_3$. Before going further, there is one important conclusion of this study that has to be highlighted already here: Fe^{III} is reduced to Fe^{II} for temperatures above 200°C (the possible reasons and the issues at stake are detailed below in a dedicated section of the manuscript, page 47). This result was observed in multiple experimental runs covering a broad range of conditions (HCl and Cl concentrations, either dissolved $FeCl_3$ or hematite, measurement durations, etc.), over many years. Figure 1.3 summarizes these observations and demonstrate clearly this iron reduction occurring with temperature.

With that result in mind, the trend visible in figure 1.4 is very similar to what was observed for Fe^{II}, like it is summarized in Fig. 1 of reference (7) (see manuscript above), with a characteristic evolution of the XANES features: shift of the white line to lower energies, decrease of its amplitude, growing of an oscillation around 7150 eV. Based on this qualitative comparison, it can already be established that Fe^{III}

speciation undergoes an octahedral-to-tetrahedral transition, along with a chlorination. More quantitative information is needed in order to establish reliably the speciation: in particular, the same strategy as in Fe^{II} study has been used with the objective to determine the nature of the end-members, i.e. the species that are predominent at both "ends" of the experimental conditions, at low temperature/low chlorinity and high temperature/high chlorinity (or more exactly *highest* temperature before iron reduction, about 200°C).

The two candidate end-members are the lowest temperature/lowest chloride concentration and highest temperature/highest chloride concentration, which are respectively 30°C/0.25 m and 200°C/6M. Before determining their structure, it has to be evaluated if they really are unique species. As a complement to figure 1.4, figure 1.5shows the spectra at the lowest (30°C) and highest (200°C) temperature, as a function of Cl concentration. Based on the observation of these figures, it can be seen that in low temperature/low chlorinity conditions the spectral variations are small (a good indication for the predominence of a species), which doesn't come as a surprise since it is known that $Fe(H_2O)_6$ prevails in these conditions. At high temperature/high chlorinity conditions, the XANES spectra keep on changing with the chloride concentrations, but the spectral evolution at 6M chloride concentration seems to slow down noticeably above 200°C, and stops above 300°C, a good indication that one species mostly predominates above 200°C. Unfortunately, the reduction $Fe^{III} \rightarrow Fe^{II}$ in this temperature range is a limitation to conclude unambiguously. But the comparison with the case of Fe^{II} is helpful: indeed in reference (7), figures 2 and 10 show that at 5M chloride concentration, the end-member $FeCl_4^{2-}$ becomes predominant between 200 and 300°C. So qualitatively, it seems that Fe^{III}speciation follows a similar trend as Fe^{II}.

EXAFS results: For this analysis, the number of neighbours is an important parameter to determine. Not much for the low temperature and chlorinity end-member whose speciation is known (octahedral $M(H_2O)_6$) due to the easy experimental conditions, but critically for the high temperature and chlorinity end-member where the experimental evidence are scarce or non-existant. In this case, there are several candidates, all with a tetrahedral geometry (as it was inferred from the qualitative assessment of the data above), but the number of chloride is to be determined. Indeed, to put things in perspective, in our previous studies about divalent transition metal speciation at hydrothermal conditions, several species/end-members have been identified at high temperature and chlorinity conditions: either fully chlorinated $FeCl_4^{2-}$ for Fe(II) (7), $CoCl_4^{2-}$ for Co(II) (19), $ZnCl_4^{2-}$ for Zn(II) (20), $CdCl_4^{2-}$ for Cd(II) (21); or partially chlorinated $MnCl_3(H_2O)^-$ for Mn(II) (22), and $NiCl_3(H_2O)^-$ for Ni(II) (23). And in the case of Fe(III) we're interested in here, Liu et al. (8) used UV-Vis and XAS measurements to conclude about the predominance of $FeCl_3$ (tetrahedral or dipyramidal) and $FeCl_4^-$ (tetrahedral) species. In that study, the experimental measurements were conducted up to very high chlorinities (15 m) but limited to 90°C; for higher temperatures data were extrapolated. In short, we expect 6 oxygen neighbours at low temperature/chlorinity, and want to arbitrate between 3 and 4 chloride neighbours at high temperature/chlorinity.

Since we need a reliable number of neighbours N, the S_O^2 EXAFS parameter has to be handled with care because it is 100% correlated with N. For this reason, we decided to use dedicated FEFF calculations and S_O^2 parameters for each end-member fit, based on crystal structures close to the expected aqueous speciation. Thus, for the 30°C/0.25 m end-member we did FEFF calculations in the siderite structure (octahedral Fe-O coordination), refined S_O^2 with siderite experimental data and used this value to fit the solution. For the 200°C/6 m end-member we did the same with the inorganic crystal structure $(HPy)_2FeCl_4(NO_3)$ that contains $Fe^{III}Cl_4$ tetrahedral moieties. Such a compound was synthesized and characterized at Néel Institute in collaboration with Pr. Isabelle Gautier-Luneau.

The EXAFS results are gathered in table 1.2. The numbers clearly point towards the $Fe(H2O)_6^{3+}$ and $FeCl_4^-$ species. It is interesting to observe that these results compare very favorably with the Fe^{2+} results from our previous studies (see table 3 in reference (7)): the speciation is identical, but also the MSRD values, the energy misfit, the uncertainties, etc. are all similar. Also, for the two species, the small deviations from what would be a 'perfect' agreement (i.e., 6 and 4 neighbours, and smaller MSRD parameters) can be explained by the expected presence of secondary species: based on the example of Fe^{2+}, in the case of the octahedral $Fe(H2O)_6^{3+}$ one can expect a small chlorination in the first shell ($FeCl(H2O)_5^{2+}$), and in the case of $FeCl_4^-$ there can be small quantities of less chlorinated species (octahedral or tetrahedral $FeCl_2(H2O)_2^+$ for example). The problem is that it is very difficult to assess reliably this option: first because most of the measurements were not optimized for EXAFS analysis (dissolution experiments not

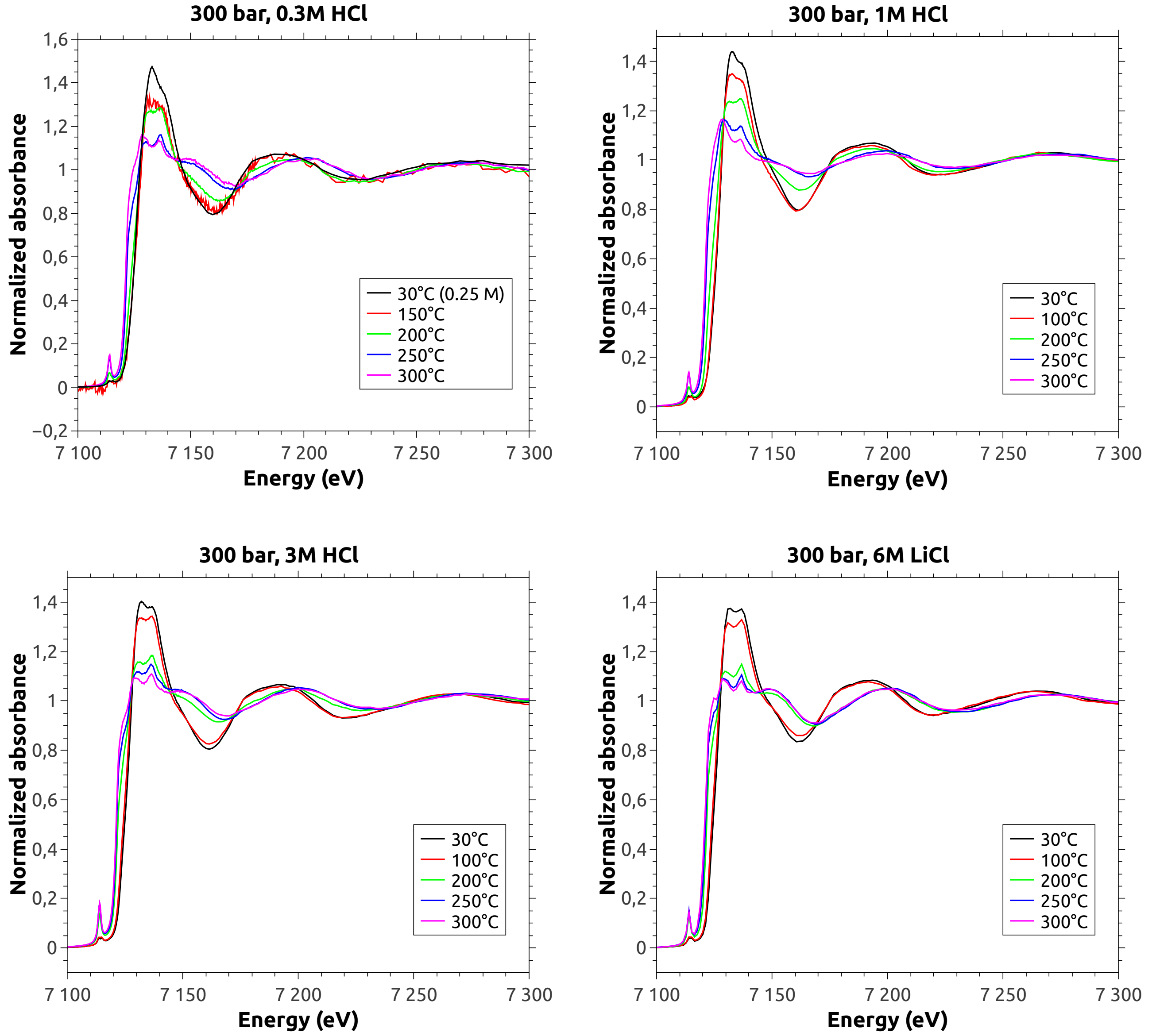

Figure 1.4: XANES spectra of Fe^{III} solutions, as a function of temperature, at 300 bar, for different chloride concentrations. The dissolved iron was obtained either through dissolution of hematite with temperature (0.3, 1 and 3M solutions for T>150°C) or through dissolution at room temperature of $FeCl3$ salt (6M solution and 1 and 3M solution for T<150°C). The reason the 0.3M/150°C data is very noisy is the very low iron dissolved (from hematite) in such conditions: about 4 mmol/200 ppm.

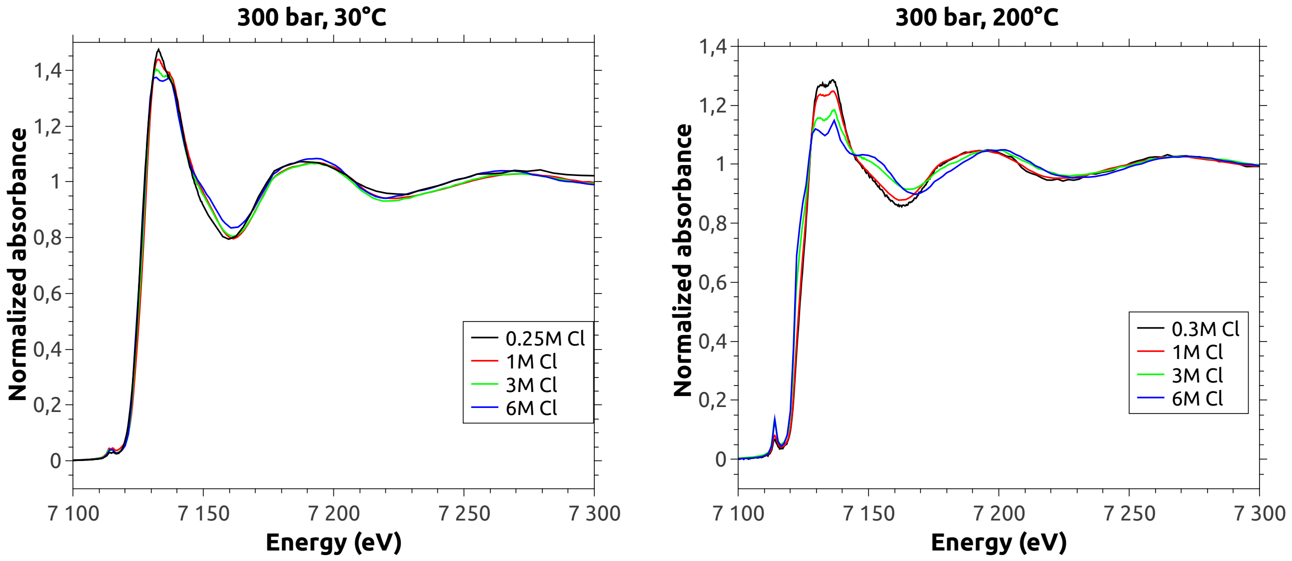

Figure 1.5: XANES spectra of 300 bar Fe^{III} solutions, as in figure 1.4, as a function of Cl concentration, at 30 and 200°C.

providing an optimal iron concentration; desire not to expose the solution too much to the beam because of redox problems; large chloride concentrations; etc.), and then mainly because of the (very) limited data ranges. Indeed, there are simply not enough data in a single shell Fourier transform to set up an elaborate multi-shell EXAFS model: in terms of EXAFS statistics, 5 to 6 independent points are available in a typical dataset, which means that even a simple single shell model with 5 variables is delicate, let alone with a second shell!

Which brings me to the next EXAFS item, the opportunity to determine the iron speciation between the end-member conditions, i.e. in the ranges (30-200°C) and (0.3-6 m) chloride molalities where more than one iron species exist. The short answer is: it is very complex and delicate, and the results must be manipulated carefully. As hinted above, this type of dataset suffers from parameter under-determination: there are not enough independent points in the data to use the number of fit variables needed for a robust 2 shells coordination model, whether it is one species containing both O and Cl neighbours, or a mixture of several species involving both O and Cl. Some constraints need to be applied on the parameters, such as fixing the energy misfit, equaling the MSRD of both shells, etc. But they can quickly result in fit divergence. In recent years we used such a method on more complete datasets (more Cl concentrations and temperatures), in the case of Ni (23) and Mn (22) speciation. I quote one excerpt from our reference (22) which explains the methods:

> "Based on the XANES data, most chloride solutions contain mixtures of octahedral and tetrahedral complexes at intermediate temperatures (200–450 °C). As each complex has different Mn–O and Mn–Cl distances, Cl/O ratio, and Debye–Waller factors, parameter under-determination is a problem. To reduce the number of fit parameters, EXAFS data at intermediate temperatures for each solution were analyzed assuming that they consist of a mixture of the species that exist at low (100 °C; octahedral coordination) and high temperatures (500 °C; tetrahedral coordination). For each solution, the fraction of tetrahedral and octahedral species was derived from XANES data via LCF (Linear Combination Fit). These fractions were fixed in the EXAFS refinements and the Mn–Cl and Mn–O bond lengths and corresponding Debye–Waller factors were fitted, and represent average values of octahedral and tetrahedral complexes in each solution."

If this method is applied here, it will only give an indication of the relative quantity of octahedral and tetrahedral species (through the LCF of XANES data), but due to the absence of low temperature spectra

End-member	N	R (Å)	σ^2 (Å$^2 x 10^{-3}$)	ΔE_0 (eV)	R factor
30°C/0.25 m	5.6±0.7	2.02±0.01	0.004±0.002	-1.0±1.6	0.011
200°C/6 m	3.6±0.5	2.21±0.01	0.005±0.001	2.0±1.6	0.005

Table 1.2: Local structure of the 2 end-members as determined by fitting the EXAFS fluorescence spectra. The parameters are the coordination numbers (N), the distance to the scattering shell (R), the mean square relative displacement (MSRD, σ^2), the energy misfit (ΔE_0), and the goodness-of-fit R-factor. The k and R data range over which the fit was conducted are (3.5-10) Å^{-1} and (1-3) Å respectively. All the analysis work was conducted with the Horae package, based on FEFF calculations and IFEFFIT analysis routines (24).

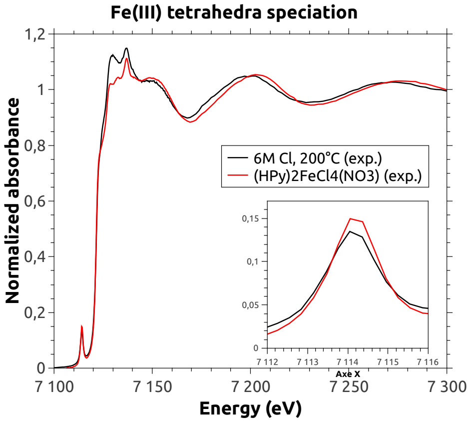

Figure 1.6: XANES spectra of the 200°C/6 m end-member and the $(HPy)_2FeCl_4(NO_3)$ standard. The inset shows the pre-edge peak area.

(no dissolution of hematite at 30°C) and the limitation to 200°C it does not seem reliable to conduct such a guided EXAFS fit.

XANES results: The XANES quantitative analysis is still a work in progress, because it is more demanding than expected: inded, preliminary results show that the *ab initio* calculated spectra of Fe^{3+} species are more sensitive to the electronic parameters (orbital population, high-level parameters of the FDMNES code, etc.) than in the case of previous Fe^{2+} calculations (7).

A qualitative analysis was conducted nevertheless. In particular, regarding the high temperature and chlorinity end-member, figure 1.6 shows the agreement between its XANES spectrum and the one of the $(HPy)_2FeCl_4(NO_3)$ standard which contains $Fe^{III}Cl_4$ tetrahedral moieties. In this figure, the notable features are: the very good agreement of the pre-edge (in the inset), which is a very good indication of a similar number of neighbours and asymetry; the very good agreement in the rise of the white line where the shoulder characteristic of tetrahedral species is identical; the very good agreement above 7150 eV, aside from the difference of frequency that is due to the different Fe-O interatomic distances (2.21 Å in the fluid vs 2.18 Å in the solid standard). After the EXAFS results, that is an additional hint towards the presence of $FeCl_4^-$ species as an end-member.

1.2.2.2 Solubility and redox of Fe^{III}-bearing minerals at hydrothermal conditions

Fe^{III}-bearing magnetite and hematite solubility have been investigated, following the same methods already exposed for Fe^{II}, based on transmission/fluorescence absorption measurements. The results and experimental details are summarized in figure 1.7 and its legend.

The iron solubilities exposed in these graphs cover a broad range of values, from 1 to 1500 mmol. The magnetite solubility was explored early (2007) when the methodology was being developed: for this reason we made the choice to work in highly acidic conditions to optimize the signal, even though these

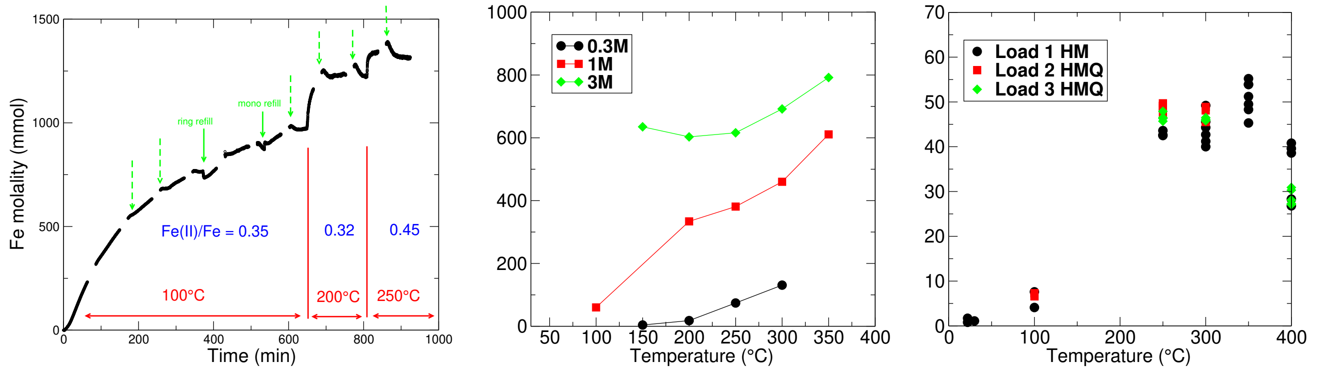

Figure 1.7: Fe^{III}-bearing minerals solubility determined by XAS measurements. Left: iron molality as a function of time for magnetite dissolution in a 3 m HCl aqueous solution. The molality is derived from the fluorescence intensity which is calibrated against standard iron solutions (not shown), following the same method exposed above (reference (11)). The irregularities in the measurement are correlated with reinjection of the ESRF ring and with FAME monochromator nitrogen refills. The ratio Fe^{II}/Fe is determined by fitting the XANES features with a linear combination of the spectra of Fe^{II} and Fe^{III} standards. Center: iron molality as a function of temperature at 300 bar for hematite dissolution in HCl aqueous solutions (0.3, 1 and 3 m HCl concentrations). The molality is derived from transmission measurements. Right: iron molality as a function of temperature at 1000 bar for Hematite-Magnetite-Quartz mineral assemblages dissolution in 0.1 m HCl aqueous solutions. Several loads were repeated, the first one without quartz.

experimental conditions were definitely not relevant for iron transport in natural hydrothermal conditions. Nevertheless, the ratio Fe^{II}/Fe could be determined by linear combination of XANES spectra: below 250°C, the dissolution of magnetite can be considered congruent, where the Fe^{II}/Fe ratio remains the same (around 0.33) in the solution as in the mineral. But above 250°C, we observed a clear change and a strong reduction of iron. This point is discussed below. As evoked earlier in this chapter, the dissolution of Fe^{III}-bearing hematite (figure 1.7, center) was investigated mainly with the objective to determine Fe^{3+} aqueous speciation. In this context, the solubility values were useful to determine the Fe/Cl ratio, relevant for the speciation. They show a dependance with pH, as expected for the acidic dissolution of an oxide:

$$Fe_2O_3 + 6H^+ \rightarrow 2Fe^{3+} + 3H_2O$$

In collaboration with C. Sanchez-Valle (Münster University), the dissolution of hematite-magnetite-quartz (HMQ) mineral assemblages was investigated. This study is the most recent and the logical continuation of all the previous ones: first, given the previous solubility measurements and their limits, the solubility of iron in more relevant conditions (i.e. less acidic) needed to be measured; then, since the previous Fe^{III} XAS measurements clearly showed iron reduction above 200°C, the Fe^{III} stability needed to be investigated in more controlled redox conditions. Figure 1.7 shows the measured solubility of HMQ in 0.1 m HCl aqueous solutions. The results can be compared to the work of Liu et al. where they determined the speciation and formation constants of ferric chloride complexes, based on UV-Vis and XAFS measurements in hydrothermal conditions up to 15 m chloride but only up to 90°C (8). For higher temperatures, the thermodynamic data are extrapolated. The results of interest are in their figure 13 which is reproduced here in figure 1.8: in 0.1 m HCl conditions, their modelization of hematite solubility show a decrease followed by an increase of iron solubility up to a value of ~0.032 m at 250°C. This value is in agreement with our results (figure 1.7, center and right, ~0.045 m iron). It is worth pointing that the most chlorinated species in their model is $FeCl_3$, with almost no $FeCl_4^-$: since we demonstrated that the $FeCl_4^-$ species does exist when sufficient amounts of chloride are available, the iron molality seems to be mostly limited by the availability of chloride, the ratio Cl/Fe being exactly 3 (100/32 mmol). It is highly likely that our data could help to optimize the thermodynamic data from Liu et al. (work in progress).

Regarding the reduction of iron at high temperatures, apart from being problematic when studying Fe^{III} speciation because it limits the temperature range (see above), it is an important research topic

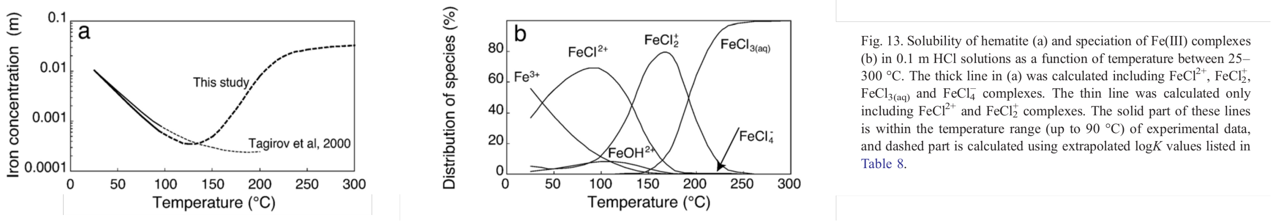

Fig. 13. Solubility of hematite (a) and speciation of Fe(III) complexes (b) in 0.1 m HCl solutions as a function of temperature between 25–300 °C. The thick line in (a) was calculated including $FeCl^{2+}$, $FeCl_2^+$, $FeCl_{3(aq)}$ and $FeCl_4^-$ complexes. The thin line was calculated only including $FeCl^{2+}$ and $FeCl_2^+$ complexes. The solid part of these lines is within the temperature range (up to 90 °C) of experimental data, and dashed part is calculated using extrapolated log$K$ values listed in Table 8.

Figure 1.8: Figure 13 (modified) from reference (8). Our experimental conditions match their solubility

in the geochemistry of subduction zones. Indeed, it is still questioned what is the oxidizing agent from the hydrated subducted crust that controls the redox state of the slab-mantle interface: it could be the released water itself, or some of the components of the aqueous fluids, Fe^{3+} being a likely candidate. Conceptually, there are many factors that can impact the redox state of an hydrothermal solution when it is experimentally measured, and we had to take all of them into consideration (and under control) before coming to the conclusion that Fe^{II} is indeed favored at high temperatures:

- beam reactivity and/or damage: the intense synchrotron radiation creates radiolysis species, in particular in aqueous samples, that are highly reactive and can either result in unnatural redox reactions or kinetically accelerate the reach of the 'natural' thermodynamic equilibrium. We discussed quite exhaustively this effect in our recent review (25), which is included in section 1.4 (page 51 of this manuscript): the discussion about beam damage can be found page 223 of this publication. This is also addressed in the chapter dedicated to the HP technology.

- oxygen fugacity: the environment of the sample can impose an oxygen fugacity value which is irrelevant if very different from natural conditions. For this reason we studied the dissolution of the HMQ mineral assemblage, which is a redox buffer. Another player is the sample container: if it is chemically reactive, it may impose its own redox conditions. But, the post mortem detailed observation (visual and SEM image) of the glass-like carbon cells that we routinely use showed no sign of chemical reactivity, which is a good indication that the HMQ buffer is dominant. Another argument has been building over the last 15 years: in this period, we observed regularly the same reduction of metals at hydrothermal conditions measured in sample containers made of different materials (sapphire, Ti and quartz).

- specificity of iron: as indicated just above, the same reduction has been observed for other metals, many times in our own experiments: arsenic (14), copper (26, 27), europium, bismuth (28), gold (29), etc.

In conclusion, the higher thermodynamic stability of the lower oxidation state element in aqueous solutions at FAME-type conditions (300-600°C, <2 kbar) seems to be a fairly general rule: the thermodynamics behind is that a lower charge and/or smaller ionic radius, associated with reduced metallic aqueous species, result in a lower coordination number and a big entropy gain. This is also discussed in our 2016 review (25), and further down in section 1.4.

1.3 The contribution of XANES in hydrothermal geochemistry

Collaborations:

- *Néel Institute (Y. Joly)*

This section is an overview of the use of quantitative XANES spectroscopy in hydrothermal geochemistry studies, and its evolution from 'barely used' 20 years ago to 'widely used' today. Indeed, XANES qualitative analysis (the so-called fingerprinting method, i.e., comparing XANES spectra of unknown with spectra of references) has been a common tool for more than 30 years, mainly associated with classical

EXAFS, but the quantitative analysis (based on the modelisation of spectra) is much more recent. This situation is due to a more complex theoretical framework for XANES than for EXAFS, and the much larger computing power required.

The first quantitative XANES calculations were conducted around the nineties in solid state physics: because the spectroscopy software programmers usually have a background in physics, and also because the solid state samples often are highly symmetric, which is very helpful to reduce computing requirements. About 10 years later (around 2000), the first XANES calculations in aqueous solutions appeared, mostly driven by M. Benfatto and his collaborators (30, 31, 32). Technically, those calculations were based on a full multiple scattering scheme within the code MXAN (33). At the same period, Y. Joly at the Laboratoire de Cristallographie was developing the FDMNES program (34), based on the Finite Difference Method scheme to solve the Schrödinger equation. During my PhD in the same laboratory (2000-2003) I made use of this program to calculate arsenic (6) and uranium (35) speciation in aqueous solutions. Aside from being novel XANES calculations in fluids, they were applied to high temperature and pressure conditions for the first time (to my knowledge). These FDMNES calculations were perfected by our group in the following years (14, 36, 7, 37). Today such XANES calculations are not routine yet (the analysis is still challenging), but are considered a logical complement to EXAFS analysis, and among the research groups that collaborate with us, they are almost systematically conducted and beneficial to the studies. Lastly, to illustrate anecdotally this point, I quote a recent review for a paper which is under revision:

> "Lastly, moving on to the XANES data presented in this manuscript, I was very disappointed to see that no real attempt was made to extract information about the geometrical character of the local ion environment from these spectra. Plenty of widely accessible analysis tools are now available to tackle this issue e.g. MXAN or FDMNES , and such analyses can prove critical in systems such as the one tackled here."

Indeed such analyses can be critically useful. The allusion to the existence of "plenty of" programs is a bit far-fetched though, and he/she forgot to mention the program FEFF which is probably the most used for this purpose.

There is another methodological evolution that arose in hydrothermal geochemistry in recent years, and which is gaining momentum: the growing occurence of molecular dynamics (MD) simulations. Similarly to XANES quantitative analysis (mentioned above), the improvement of theoretical schemes and the constantly growing computing power both make it possible to determine speciation and (sometimes) thermodynamics of metal complexation. A summary of this evolution, with technical details and some examples, is given in our recent review (25), which is included in section 1.4 (page 51 of this manuscript): the discussion about molecular simulations can be found page 224 of the publication. It might seem odd to mention MD in this section, dedicated to XANES spectroscopy, since they are independent methods. But they share the capability to provide very detailed local structure information, and MD can significantly help to extract more reliably structural information from XANES data. Two situations come to mind to illustrate this added value:

- the study of asymmetric/distorted metal complexes: when one wants to explore the impact on the XANES spectra from distorsion of the geometry, it is indeed inefficient to browse through different possibilities by trial-and-error. Here, numerically MD calculated geometries (or DFT optimized geometries, by the way) are a good starting point, and are more relevant since they are justified by the theory of physical interactions and/or energy minimization.
- the study of the influence of the solvation shell on the XANES spectra of the metal complexes: even if the geometry of the metal complexes (octahedral, or tetrahedra; interatomic distance) defines primarily the XANES spectra, the influence of the more distant solvation shells cannot be ruled out. This is especially true in the case where the XANES calculations of the metal complexes are robust and reliable (like for octahedral species), which enables to explore second order smaller XANES features. Without MD input, the solvation shells investigated were very symetrical: it was still interesting to evaluate their influence on the XANES spectra, but it was undeniably over-estimated. This point is discussed in my 2009 paper dedicated to Fe^{2+} speciation (7) (the paper is included in this manuscript, above, page 8, and the discussion is to be found in section 3.3.1 of the publication). D'Angelo and collaborators used MD to determine solvation shells structures and did calculate the resulting XANES spectra (38). I followed the same method by using very rough MOLDY (39)

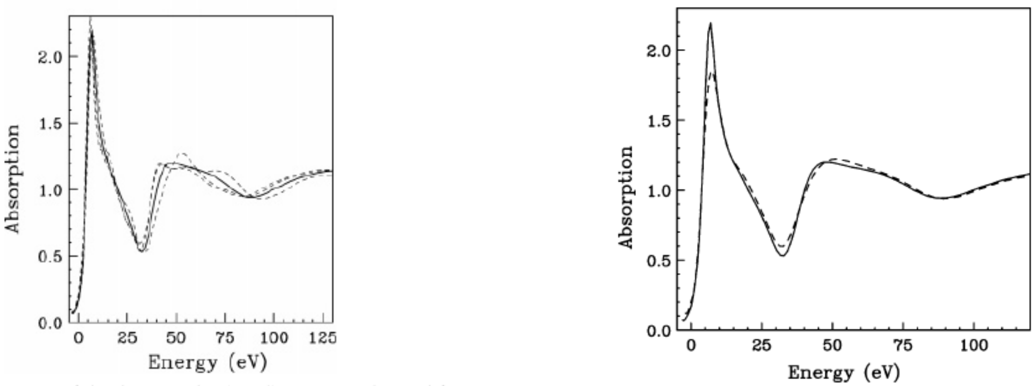

Figure 4. Comparison of the theoretical XANES spectrum obtained from the MD average including the first and second hydration shells (solid line) and three spectra associated with individual MD configurations (dashed line). Upper panel: typical first and second-shell hydration cluster.

Figure 5. Comparison of the theoretical XANES spectrum obtained from the MD average including the first hydration shell (dashed line) and the averaged theoretical XANES spectrum including the first and second shells (solid line).

Figure 1.9: Figures extracted from the study by D'Angelo et al. on the solvation of Ni^{2+} (38): these figures show the influence of MD calculated second solvation shells on the XANES spectra. I obtained similar results for MD calculations conducted for Fe^{2+} and Fe^{3+} solvation structures.

calculations (they were rough because I'm not an expert and had to learn by myself). I chose not to show the results here: basically, the influence of the second shell that I found for Fe^{2+} and Fe^{3+} solvation is on par with what D'Angelo et al. obtained in their study on Ni^{2+} (38). Their results are summarized in figure 1.9: the impact is limited to the first 50 eV above the edge, is somehow weak but still of the same amplitude as other weak XANES features that one might want to interpret to obtain geometrical information (such as distorsion of octahedral or tetrahedral structures).

On a side note, I find this use of MD (to optimize the XAS analysis of hydrothermal metal speciation) a missed opportunity by me. I either tried very rough MD by myself with limited success, or I collaborate with people who collaborate with theoricians. I can cite two reasons for this lack of direct and efficient collaborations: iron is hard to include in MD, and here (at Néel Institute) theoricians study nano or magnetic structures. Too bad.

1.4 15 years of using autoclaves at FAME: the progress of knowledge in hydrothermal metal transport.

This HDR manuscript is a good opportunity to critically review what has been done (and later think about what can be done, in the 'Perspectives' chapter). Thus, while the previous sections were specific scientific examples holding many details, the present section is more a global summary of our contribution to the progress that was made, in the last 15 years, in the research field of hydrothermal metal transport.

Main collaborations:

- *Adelaide and Melbourne University (J. Brugger, B. Etschmann), Melbourne CSIRO (W. Liu)*
- *GET (G. Pokrovski)*

Supervision:

- *Y. Mei, co-supervisor PhD (Adelaide University 2010-2013)*
- *J. James-Smith, co-supervisor PhD (Adelaide University 2006-2010)*

1.4.1 Methodological advances

Above, we have seen that our autoclave set-up allows:

- the collection of *in situ* high-quality XAS data at hydrothermal conditions for the determination of metal speciation;
- the collection of *in situ* solubility data: given that the thermodynamical equilibrium is reached (high temperatures), it can be considered a micro-batch reactor, providing data in agreement with more traditional laboratory long-term solubility measurements (see G. Pokrovski's numerous studies which combine both techniques);
- the collection of these speciation and solubility data in very challenging experimental conditons, relevant for metal transport: *i)* down to very low aqueous densities (e.g. 0.1 $g.cm^{-3}$), *ii)* down to very low metal concentrations (typically <100 ppm in ideal conditions), *iii)* down to low X-ray energies, in particular below 10 keV where the HP materials that were used to reach hydrothermal conditions historically rendered the experiments very challenging.

Taken individually each method listed here is not new, but their combination and the fact that they can be routinely implemented in our autoclave set-up constitute a unique and very efficient installation, available to the international earth sciences community at the FAME and FAME-UHD beamlines[1].

1.4.2 Scientific advances

The list above refers to methods and technical details, but it is worth evaluating what are the resulting scientific advances. The most distinctive results are:

- access to the speciation of transition 3d metals (their absorption K-edges correspond to energies in the range (5-10) keV), and more recently to the lanthanides (lanthanum L3-edge is at 5.483 keV!);
- retrieval of thermodynamical data from XAS spectra: either through a 'classical' method that uses solubility numbers obtained in our autoclave (G. Pokrovski is an expert user, the first one to make use of our micro-batch reactor, during my PhD, see reference (40) for a characteristic example of the method applied on Ge speciation and argutite solubility), or a more original method that uses a PCA-based analysis of the XAS spectra to derive formation constants of aqueous species (method developped by J. Brugger, see the example of iron speciation, reference (7), included above in the manuscript page 8);
- access to both liquid and vapor speciation, and the corresponding vapor-liquid partitioning data: 2 characteristic examples are G. Pokrovski et al.'s work on antimony speciation (41), and J. Brugger et al.'s study on copper hydrosulfide complexation (36). In both cases the experiment covered density ranges from 1 down to 0.15 $g.cm^{-3}$.

The reference (25), that I co-authored with my australian collaborators (J. Brugger, B. Etschmann, W. Liu and Y. Mei), is a comprehensive review that tackles the coordination chemistry in hydrothermal systems, and its role on the formation of ore deposits, from existing publications. Consequently, it also includes all the data obtained in more than 10 years of successful collaboration with Adelaide and Monash (Melbourne) Universities, and CSIRO (Melbourne). I decided to include it in this manuscript because it carefully develops many ideas that I touched upon here, and it is very relevant to expose in this section the scientific advances made recently. It is composed of (an introduction and) 3 mains parts: *i)* a discussion about the recent molecular information available through *in situ* spectroscopic measurements and molecular simulations (pages 221-224), *ii)* a very exhaustive updated review of the speciation of all the metals at hydrothermal conditions (pages 224-238), *iii)* a discussion about the interpretation of speciation data and the role of the different experimental variables (pages 238-245).

---

[1] Both the technological details and the strategy of autoclave integration on our beamlines are later discussed in dedicated chapters.

Key ideas of the study:

This paper is very dense. But I highlighted (yellow) some interesting ideas (already touched upon in the manuscript). In particular, what I consider the very distinctive features of this manuscript are:

- The original discussion about **beam damage** and the importance of sample vs beam **volume ratio**.
- The **customized periodic table** that summarizes a lot of speciation data at hydrothermal conditions.
- The discussion about **the role of entropy** as a driver for metal complexation in hydrothermal fluids.

Chemical Geology 447 (2016) 219–253

Contents lists available at ScienceDirect

Chemical Geology

journal homepage: www.elsevier.com/locate/chemgeo

A review of the coordination chemistry of hydrothermal systems, or do coordination changes make ore deposits?

Joël Brugger [a,*], Weihua Liu [b], Barbara Etschmann [a], Yuan Mei [a,b], David M. Sherman [c], Denis Testemale [d]

[a] *School of Earth, Atmosphere and the Environment, Monash University, Clayton, 3800, VIC, Australia*
[b] *CSIRO Mineral Resources, Clayton, VIC 3168, Australia*
[c] *School of Earth Sciences, University of Bristol, Bristol BS8 1RJ, UK*
[d] *CNRS, Université Grenoble Alpes, Institut NEEL, F-38000 Grenoble, France*

ARTICLE INFO

Article history:
Received 12 June 2016
Received in revised form 11 October 2016
Accepted 13 October 2016
Available online 18 October 2016

Keywords:
Coordination chemistry
Hydrothermal fluids
In situ spectroscopy
Geochemical cycling
Ore deposits
Mineral solubility
Molecular dynamics

ABSTRACT

The hydration and complexation of metals in hydrothermal fluids are key processes controlling the mobility of elements in the Earth's crust, leading to the formation of ore deposits from which the World's supply of Fe, Mn, Ag, Au, Pd, Cu, Zn, Co, Pb, U, and Mo is mined. In the past 20 years a large amount of in situ spectroscopic data, complemented by increasingly accurate ab initio molecular dynamic simulations, have dramatically improved our understanding of the nature and geometry of the metal complexes that are responsible for metal transport in the upper crust. This new information underpins a "Coordination Chemistry" approach to ore transport and deposition.

In order to highlight the unifying principles brought about by the concepts of coordination chemistry, we present a *periodic table of metal coordination chemistry in hydrothermal fluids* based on a review of the literature and new XAS data on the hydration of the uranyl ion in hydrothermal fluids, and the pressure dependence of Ni(II) and Zn(II) complexing. The different coordination geometries of metal complexes control some of the first order behaviours of these metals in hydrothermal systems. In particular, (i) complexes with low coordination number and open structures (i.e., linear and trigonal pyramidal) have an enhanced affinity for low-density, vapour-like fluids, relative for example to tetrahedral and octahedral complexes; and (ii) fractionation and changes in solubility are associated with changes in coordination geometry caused by changes in pressure, temperature, and ligand availability. For example, first row divalent transition metals as well as Cd(II) all occur as chloride-poor, octahedral complexes at low T, low salinity, and tetrahedral-like chloride-richer complexes at high T, high salinity in chloride brines. However, the octahedral–tetrahedral transition occurs at different conditions for different metals, and this can drive fractionation between geochemical pairs such as Zn/Cd, Fe/Mn and Co/Ni.

This review highlights the central role of entropy in driving the formation of metal complexes and changes in coordination geometry as a function of temperature and, to a lesser extent, pressure. Changes in coordination geometry are associated with large changes in entropy. Hence, coordination changes usually occur rapidly as a function of temperature (few 10's of °C), and can result in rapid changes in mineral solubility. These effects need to be taken into account when extrapolating the thermodynamic properties of metal complexes to high temperature and high pressure. A molecular-level understanding of metal speciation hence underpins the development of more accurate models of reactive-transport over wide ranges in pressure, temperature, fluid composition and physical states.

Contents

1. Introduction . . . 220
2. A wealth of new information: towards a *molecular level* understanding of metal transport in hydrothermal fluids . . . 221
    2.1. Spectroscopic studies of complexes and complex-forming reactions under hydrothermal conditions . . . 221
        2.1.1. In situ spectroscopy . . . 221
        2.1.2. A note on beam damage . . . 223

---

[*] Corresponding author.
E-mail address: joel.brugger@monash.edu (J. Brugger).

http://dx.doi.org/10.1016/j.chemgeo.2016.10.021
0009-2541/

2.2. Molecular simulations . . . 224
3. Review of coordination of metals in hydrothermal fluids . . . 224
3.1. Titanium, zirconium and hafnium . . . 224
3.2. Vanadium . . . 225
3.3. Niobium and tantalum . . . 226
3.4. Chromium, molybdenum and tungsten . . . 226
3.5. Iron and manganese, nickel and cobalt, zinc and cadmium: transition metals existing mainly as octahedral and tetrahedral aqua- and chloro-complexes . . . 227
3.6. Copper, silver and gold . . . 230
3.7. Mercury . . . 232
3.8. Platinum group elements (PGE) . . . 232
3.9. Gallium . . . 232
3.10. Indium . . . 233
3.11. Thallium . . . 233
3.12. Germanium . . . 233
3.13. Tin . . . 233
3.14. Lead . . . 234
3.15. Arsenic, antimony and bismuth . . . 234
3.16. Selenium, tellurium (and polonium) . . . 235
3.17. Rare earth elements, yttrium and scandium . . . 235
3.18. Uranium and thorium . . . 237
4. Discussion . . . 238
4.1. Metal transport in hydrothermal systems – a view from coordination chemistry . . . 238
4.1.1. A periodic table for hydrothermal geochemistry . . . 238
4.1.2. Effects of temperature and salinity . . . 239
4.1.3. Effects of pH and redox state . . . 241
4.1.4. Effect of pressure . . . 241
4.1.5. Coordination chemistry controlled by ligands . . . 242
4.2. Driver for metal complexation in hydrothermal systems: key role of translational entropy . . . 242
4.3. A few key issues in hydrothermal geochemistry . . . 244
4.3.1. Sulfur versus chloride complexing . . . 244
4.3.2. Liquids and vapours . . . 244
4.3.3. Charged versus neutral complexes – the dielectric diktat? . . . 245
5. Conclusions and perspectives . . . 245
Acknowledgements . . . 245
Appendix A. Supplementary data . . . 245
References . . . 245

1. Introduction

Most of the World's metals (Fe, Mn, Ag, Au, Pd, Cu, Zn, Co, Pb, U, Mo, …) are mined from hydrothermal ore deposits. These ore deposits either form as a result of the flow of aqueous fluids within the Earth's crust and the ability of these fluids to carry metals in soluble form (Heinrich et al., 1996), or are often modified by geofluids (Altree-Williams et al., 2015). Ore-forming fluids cover wide ranges in temperature (25 to >600 °C), pressure (0.1 to >500 MPa) and compositions ranging from nearly pure water, to low density 'vapours' rich in volatiles such as CO_2, CH_4, H_2O or SO_2, or to complex 'hydrated melts' with >50 mol% salt (NaCl, KCl, $CaCl_2$, $FeCl_2$). Aqueous fluids play a key role in controlling the composition of the Earth's crust by redistributing metals as a result of dehydration reactions during regional metamorphism or subduction (Bebout and Penniston-Dorland, 2016; Zhong et al., 2015b), or during exsolution from rising magmas (Heinrich et al., 2004).

A quantitative understanding of metal transport and deposition under geological conditions (e.g., via reactive-transport modelling) is important for our understanding of crustal geochemistry, and is key to sustaining mineral exploration (predictive mineral discovery). This quantitative understanding underpins the optimisation and development of environmentally sustainable hydrometallurgical methods for processing ores of ever increasing complexity and decreasing concentration (Brugger et al., 2010; Seward and Driesner, 2004). Hydrothermal fluids also are important in a number of physical chemistry and engineering applications (e.g., corrosion in power plants, geothermal energy, use of supercritical water as a green solvent for material synthesis, catalysis; Grunwaldt et al., 2003).

At a fundamental level, mineral solubility is controlled by (i) the crystal chemistry and stability of the minerals (lattice energy); (ii) the physicochemical properties of aqueous electrolyte solutions; and (iii) the thermodynamic and molecular properties of the aqueous species of metals (Crerar et al., 1985). At the birth of thermodynamics in the late 19th century (Gibbs, 1873), little information was available about the structures of metals in solution, and Alfred Werner (1866–1919) won the 1913 Nobel Prize in Chemistry for proposing the correct octahedral configuration of some transition metal complexes (Werner, 1893). However, it was well known at that time that metals react with ligands to form complexes, because of the effect of these complexes on mineral solubility. As illustrated in Fig. 1a, the activity of a complex increases in a linear fashion with respect to the activity of the ligand on a log-log plot, with the slope of the line equal to the ligand:metal ratio. In thermodynamic models of aqueous solutions, the role of water as a ligand is often ignored; in other words, the thermodynamic models assume that the activity of water ($a$$H_2O$) is equal to one when it comes to complex-forming reactions. This is reflected by the fact that dissolved ions or metal complexes are written for example as Co^{2+} and $CoCl_2$(aq), ignoring the coordinated water molecules. This convention is still overwhelmingly used today by hydrothermal geochemists – and by many inorganic chemists, geochemists, and engineers alike (Bethke, 2008).

In their seminal study, Susak and Crerar (1985) observed a change in coordination geometry from octahedral to tetrahedral in the aqueous complexes of divalent transition metals (Fe, Co, Ni, Cu) upon heating and upon increasing chloride concentration, based on semi-quantitative in situ spectroscopic UV–vis measurements. This

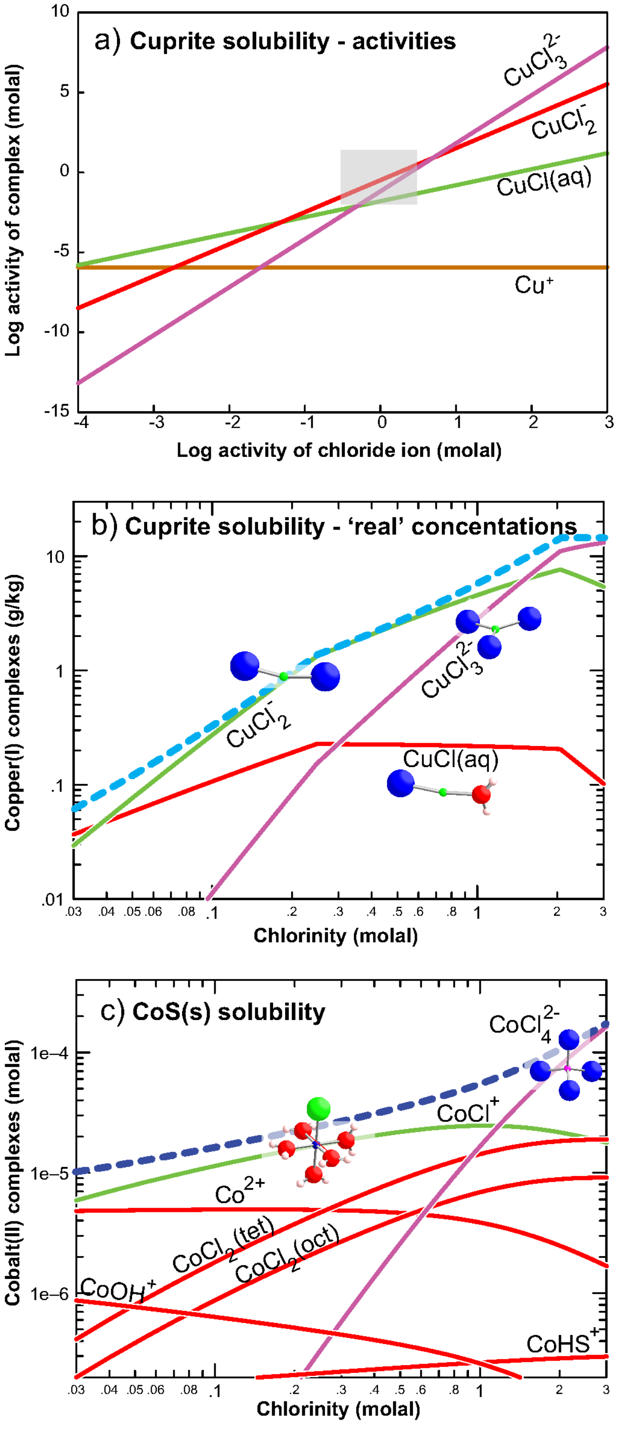

Fig. 1. Effect of ligand (Cl^-) activity and concentation on mineral solubility for metals with different coordination chemistry. (a,b) Solubility of cuprite ($Cu_2O(s)$) in NaCl solutions at 25 °C at $pH_{25\,°C} = 5$, shown both on an activity-activity digram (a) and as concentrations, i.e., including corrections for activity coefficients and mass balance (data from Liu et al., 2001); and (c) solubility of CoS(s) in NaCl at 250 °C (data from Liu et al. 2011a; Migdisov et al. 2011b). The rectangle on (a) indicates the approximate location of the region plotted in (b). The dashed lines represent the total solubility.
Calculations performed using the Geochemist's Workbench software (Bethke, 2008).

change in coordination geometry was also associated with a change in the number of coordinated chloride ligands. Hence, Susak and Crerar (1985) first proposed that the solubility changes associated with the coordination changes could play an important role in controlling metal transport and deposition in the Earth's crust.

Here we review the large amount of new experimental information about the coordination chemistry of metals and metalloids in hydrothermal fluids accumulated over the past 20 years, thanks mainly to the rapid development of in situ X-ray absorption spectroscopy methods at 3rd generation synchrotron sources (Brugger et al., 2010; Seward and Driesner, 2004). We use this information to build a *periodic table of coordination chemistry of metals* in upper crustal hydrothermal fluids, and to explain some of the processes that lead to fractionation among the metals, and the formation of fluids with distinct geochemical characteristics. Finally, we present an up-to-date view of the controls on coordination geometry and coordination changes in hydrothermal systems.

2. A wealth of new information: towards a *molecular level* understanding of metal transport in hydrothermal fluids

The structure of the solvation sphere and the formation of complexes with geologically relevant ligands (e.g., Cl^-, HS^-, OH^-, acetate) of metals and metalloids in aqueous electrolyte solutions have been extensively studied at room temperature by many different methods. Under hydrothermal conditions, until ~1995 the bulk of the knowledge of metal complexation was based on solubility studies. Solubility data provide information on the ligand to metal molar ratios (Fig. 1a), but no direct information about the geometry of the complex(es). It is also difficult to use solubility experiments to measure the number of coordinated waters, since it is not possible to change the activity of water without affecting the solvation properties of the solvent (e.g., hydrogen bond network). The reliance on solubility data for deriving thermodynamic models of element transport and deposition at elevated P, T is the main reason justifying the common neglect of water as a ligand in thermodynamic models.

The characterisation of ion solvation and coordination complexes requires information about properties such as the coordination number and geometrical arrangement of ligands (including water) in the first coordination shell; the distance between ion and the coordinated ligands; and the residence times of ligands in the coordination environment (Persson, 2010; Seward and Driesner, 2004). Some of these parameters can be obtained directly using Ultraviolet–visible (UV–vis) and vibrational spectroscopy, Nuclear Magnetic Resonance (NMR) spectroscopy, neutron diffraction and scattering methods, X-ray diffraction, and X-ray absorption (XAS) spectroscopy (e.g., Grunwaldt et al., 2003; Table 1). These parameters can also be directly determined using molecular simulations.

2.1. Spectroscopic studies of complexes and complex-forming reactions under hydrothermal conditions

2.1.1. In situ spectroscopy

Different in situ spectroscopic methods have various strengths and limitations in the study of metal complexes in hydrothermal fluids. NMR studies can probe the dynamics of ligand exchange and complex-forming reactions; however, the application of NMR to hydrothermal conditions is challenging and limited to relatively low temperatures (≤150 °C; Cusanelli et al., 1996; Grundler et al., 2013), as the magnet must be maintained at cryogenic temperatures. Neutron- and X-ray scattering provide information on the radial distribution function of solutions and solutes (Neilson et al., 2001). Relatively few studies have been conducted under hydrothermal conditions, due to the inherent difficulty in collecting large scattering angles using high pressure and high temperature cells. Furthermore, the method requires high concentrations of the solutes, which are not relevant when compared to concentrations in natural samples. Vibrational spectroscopy also has been used to study aqueous complexes at elevated P and T. Raman requires high concentrations and intense active Raman nodes in the complex,

Table 1
Summary of experimental methods most commonly applied in hydrothermal geochemistry and the main information derived for metal complexes.

Method	Main advantages	Main limitations	Formation constants[a]
Solubility experiment	Measurement of a key parameter of direct relevance for reactive-transport (how much material is dissolved in a fluid under given conditions). Precise determination of metal:ligand molar ratios.	Requires a suitable mineral; need to control many physico-chemical parameters precisely. No information about coordination geometry. Artefact due to solution sampling/quenching.	***
Electrochemistry	In situ. Well suited to study redox processes.	Complex interface chemistry at electrode surface.	**
UV–vis spectroscopy	In situ. Simple instrumentation. Sensitive to coordination changes. In situ spectroscopy.	Deviations from Beer-Lambert law can affect quantitative interpretation. Not all complexes have useful spectral features.	**
Vibrational spectroscopy (IR-NIR & Raman)	In situ. Sensitive to coordination changes. In situ spectroscopy; Raman is suitable to high pressure (small excitation volume, suitable for diamond anvil cells studies).	Raman: high concentrations required. Not all complexes have useful features.	**
NMR	In situ. Highly sensitive to ligand exchange kinetics.	Limited to relatively low temperature as the sample need to be placed in a superconducting magnet. Sensitive to many but not all nuclei.	*
Neutron/X-ray diffraction and scattering	In situ. Neutron-based methods are highly sensitive to hydrogen.	Need concentrated solutions; higher atomic number elements are more sensitive to X-ray diffraction.	–
XANES & EXAFS	In situ. Direct information on the geometry of the complex (e.g., coordination number; bond distances via EXAFS). Spectra can be calculated accurately from *first principles*.	Some elements are difficult to access because of lower edge energy (e.g., Cr, Ti). Some ligands can be difficult to distinguish (e.g., O/F, Cl/S).	*/**

[a] This column estimates the importance of the method in providing information about the formation constants of complexes under hydrothermal conditions, from (***) for methods that provide the bulk of high quality data, to (*) for those that delivered quantitative (or semi-quantitative) data in a few examples.

so that application has been limited to a few ions, e.g. Au(III) (Murphy et al., 2000; Pan and Wood, 1991), Fe(II)–sulfate (Rudolph et al., 1997); Zn(II)–bromide and –sulfate (Mibe et al., 2009; Rudolph et al., 1999a, b), and As(III) (Pokrovski et al., 1999). Only a few studies have used in situ IR or NIR spectroscopy for the characterisation of aqueous complexes under hydrothermal conditions (Hoffmann et al., 2000, 2001a, b). UV–vis electronic spectroscopy is a key tool for investigating the coordination chemistry of transition metals, as many of these complexes absorb light in the UV–vis region due to electronic transitions among d-orbitals. However, d-d transitions are very weak and cannot be exploited to identify species at low concentrations. Ligand-to-metal charge-transfer transitions (where an electron is excited from an orbital localised on a ligand to an empty orbital localised on the metal atom) are very intense and can be used to measure speciation even when metal concentrations are at the ppm level. However, such transitions are in the ultraviolet (Suleimenov and Seward, 2000). Using UV–vis transparent windows (e.g., sapphire, diamond), it is possible to investigate complexing in aqueous solutions up to supercritical conditions. Most UV–vis hydrothermal studies assume a qualitative understanding of the structure of the complexes (often limited by attributing specific electronic transitions to absorbance bands), and use the Beer-Lambert law to derive quantitative information about ligand-exchange reactions (e.g., Brugger, 2007; Heinrich and Seward, 1990; Liu et al., 2012b).

X-ray absorption spectroscopy (XAS) probes excitations of the core-level electrons (Bunker, 2010). XAS is sensitive to the short-range structure about a specific atom, and hence is ideally suited for studying coordination chemistry in aqueous solutions. XAS data are divided into two regions depending on the distance from the absorption edge: the XANES (X-ray Absorption Near Edge Structure; typically within 30 eV, up to 50–60 eV of the main absorption edge) and EXAFS (Extended X-ray Absorption Fine Structure; up to several 100's to 1000's of eV above the edge) regions. EXAFS reflects the radial electronic distribution around the central atom, from which the nature, bond distance and number of scattering ligand can be determined. In contrast, XANES is mainly sensitive to the oxidation state (i.e., charge distribution) of the investigated atom and to the local coordination (nature of ligands, geometry of the complex). Similar to UV–vis spectroscopy, XANES data have also been used to determine the stability constants of aqueous metal complexes (e.g., Liu et al., 2007, 2011a).

Advantages of XAS over UV–vis–NIR spectrophotometry include element specificity and broader applicability, as not all aqueous complexes absorb in the UV–vis–NIR wavelength range. Quantitative *first principles* modelling is well established for EXAFS (e.g., Rehr et al., 2010), and the capacity of this technique to provide direct information about metal-ligand distance in dilute solutions up to high P and T motivated much of the early work (Pfund et al., 1994; Seward et al., 1993, 1995, 1996; Wallen et al., 1996). Modelling XANES spectra is more challenging as it requires accurate density of state calculations (based for example on density functional theory), but is coming of age (Benfatto et al., 1997; Joly, 2001; Joly et al., 2009; Bourke et al., 2016). XANES complements EXAFS data, and is of great value for understanding the coordination geometry of metals (Benfatto et al., 2002; Testemale et al., 2004).

The penetrative nature of X-rays makes it possible to obtain measurements on hydrothermal solutions in situ at high pressure and temperature. However, the relatively low energy of the K-edge lines of transition metals requires relatively thin windows; while the high-temperature and often corrosive nature of hydrothermal solutions place some additional constraints on the design of X-ray spectroscopic cells for XAS measurements of solutions up to supercritical conditions. Testemale et al. (2005) (improved version described by Testemale et al., 2016a) designed a highly successful 'large volume' (~40–1000 μl) cell (Fig. 2) for medium pressure applications (T to ~1000 °C; P to ~1000 bar). The cell allows precise, independent controls of pressure and temperature (Bruyère et al., 2008); high quality EXAFS and XANES data can be collected concurrently in transmission and fluorescence modes, and the setup has been used extensively to study the speciation of metals in solutions up to supercritical solutions (Ferlat et al., 2002; Testemale et al., 2004), even in near-critical conditions that are difficult to investigate experimentally (Liu et al., 2008). Mineral solubility (Pokrovski et al., 2005b, 2006), mineral dissolution kinetics (Testemale et al., 2009b), metal oxidation kinetics (Picard et al., 2012), and liquid-vapour partitioning coefficients (Pokrovski et al., 2006; Etschmann et al., 2010) have also be measured using this setup.

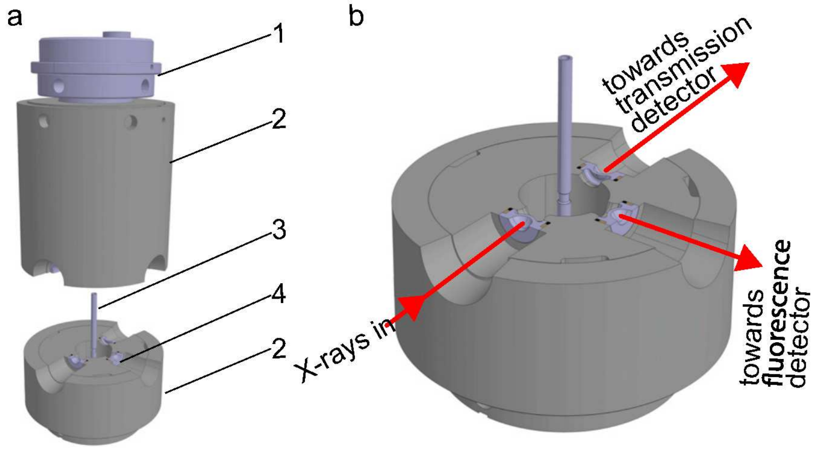

Fig. 2. Rendering of a spectroscopy cell used for in situ mineral solubility and solution XAS studies up to supercritical conditions at the FAME beamline, European Synchrotron Research Facility, Grenoble, France (Testemale et al., 2005, 2016a). (a) Overview and (b) cross-section of the autoclave at X-ray beam level (1: autoclave head, integrated power and thermocouple feedthroughs and helium pressure line; 2: autoclave body; 3: glassy carbon cell; 4: X-ray windows (beryllium or glassy carbon)).

The hydrothermal diamond anvil cell (HDAC) is the method of choice for measurements at higher pressures (up to 9 kbar; Mibe et al., 2009). Here, a tiny volume of solution (~50 nl) is trapped within a gasket between two diamonds (Mayanovic et al., 1999, 2009a). Another interesting application of XAS is the direct measurement of the speciation of metals in natural fluid inclusions (Anderson et al., 1995, 1998; Berry et al., 2006, 2009; Cauzid et al., 2007; James-Smith et al., 2010; Mavrogenes et al., 2002), which can be directly compared with that in synthetic fluids inclusions (Hack and Mavrogenes, 2006; Ulrich and Mavrogenes, 2008) and the predictions from models derived from autoclave/HDAC experiments.

2.1.2. A note on beam damage

X-rays (e.g., Jayanetti et al., 2001; Saffré et al., 2011) and other ionizing radiation (e.g., 193 nm excimer laser radiation; Lambrecht et al., 2008) induce radiolysis of water, thus producing radiolytic species such as H^+, H, OH, OH^- and hydrated electron, e^-_{aq}, which upon reaction with one another produce redox-active species such as hydrogen peroxide, dissolved hydrogen ($H_2(aq)$) and oxygen ($O_2(aq)$). Similarly, in CO_2–bearing fluids, radiolysis leads to the production of carbon monoxide (CO(aq)) and oxygen ($O_2(aq)$).

In the case of synchrotron X-ray spectroscopy, the effects of radiolytic species on the oxidation states of metal ions are well established, if not well understood. In the case of Cu(II), reduction to Cu(I) occurs already at room temperature, with further reduction to metallic Cu(0) occurring at much higher flux density in a HDAC (Jayanetti et al., 2001). Mesu et al. (2005) showed that at room temperature, the rate of reduction of Cu(II) to Cu(I) was dependant upon solution composition, the effect being particularly fast in chloride-rich solutions. As noted initially by Fulton et al. (2000b), reduction of Cu(II) to Cu(I) is expected to occur spontaneously at hydrothermal conditions, since Cu(I) becomes increasingly stable relative to Cu(II) at elevated T (300 °C).

In the case of As, synthetic $As(V)_2O_5$–H_2O–NaOH solutions started to reduce to As(III) above 250 °C in alumina cells, which is in-line with the increasing stability of As(III) with increasing temperature (Testemale et al., 2011). However, the opposite effect was observed in measurements of As in natural fluid inclusions, As(III) oxidizing rapidly to As(V) under the X-ray beam above 150–200 °C (James-Smith et al., 2010). This difference can be related to the different conditions of beam irradiation in these two As studies: the sample volume was approximately 0.1 ml and the beam size $300 * 150\ \mu m^2$ in the former (autoclave) and the sample volume was approx. 0.1 nl and the beam size $20 * 20\ \mu m^2$ in the latter (fluid inclusions). The consequence is that the large sample volume of the autoclave experiments and the convective movements in the heated fluid ensure a continuous dilution of radical species, whereas many more radical species are available to the As atoms in the fluid inclusions. This further illustrates the importance of solution composition and sample to beam volume ratio in determining the effect of beam damage on speciation. A similar situation was observed for W(IV), with no photochemistry observed in the autoclave (Borg et al., 2012), and reduction to W(IV) observed in diamond anvil cell experiments (Mayanovic et al., 2012).

The case of Fe(III/II) is of particular interest, and similar to the As situation discussed above. Mayanovic et al. (2012) showed using time-dependent energy-dispersive XAS measurements in a diamond anvil cell that X-ray-induced radiolysis leads to rapid oxidation of the Fe(II) ions at 300 °C in aqueous solutions of $Fe(II)Cl_2$; however, upon further heating up to 500 °C, rapid reduction of the Fe(III) ions –and of Fe(II) ions at the highest temperatures– was observed. In contrast, Testemale et al. (2016b) also observed the reduction of Fe(III) in solutions at high temperatures (above 300 °C) but saw no trace of Fe(II) oxidation under the beam (Testemale et al., 2009a) in their autoclave experiments (sample volume ~0.1 ml). The difference with Mayanovic et al. (2012)'s results can be explained again by the much larger sample volume in autoclaves compared to the very small sample volume of diamond anvil cells (~3 nl).

In summary: (**i**) beam damage effects, if not carefully considered, can skew the interpretation of spectroscopic data. (**ii**) An important parameter is the volume of the fluid compared to the volume affected by the beam. When this ratio is small (e.g., diamond anvil micro-beam experiments), extreme photochemistry is observed (e.g., reduction of Cu(I) to Cu(0); W(VI) to W(IV); oxidation of Fe(II) to Fe(III); As(III) to As(V)). If the ratio is relatively large, the beam often simply increases the kinetics of conversion of the ion in solution to the thermodynamically stable species. For example in the case of Fe(III), XAS studies confirm that Fe(III) is not stable at high temperatures in hydrothermal fluids (Testemale et al., 2016b). (**iii**) It is possible to take advantage of the effect of the beam in designing experiments. In the case of Cu, Cu(I) is the stable form of Cu in hydrothermal fluids, and Fulton et al. (2000a,b) and subsequent in situ EXAFS studies used the beam-induced reduction to help remove traces of Cu(II) from their experimental solutions (i.e., the beam increases the kinetics of an expected, beneficial reaction). This beneficial effect is of course detrimental for studying the speciation of Cu(II) under hydrothermal conditions using XAS. The presence of highly reactive radiolytic species can also improve the kinetics of dissolution for in situ solubility experiments.

2.2. Molecular simulations

It is now fairly straightforward to predict the structures and energetics of metal complexes using quantum mechanical calculations based on density functional theory (e.g., Asthagiri et al., 2004; Butterworth et al., 1992; Feller et al., 1999; Sherman, 2007; Tossell, 1991; Tossell and Vaughan, 1993; Zajacz et al., 2011). Predicted geometries can be compared with bond lengths and coordination geometries determined by EXAFS and XANES, and these comparisons can help to identify species in solution, and resolve ambiguities in the interpretation of 'classical' solubility and spectroscopic measurements (e.g., Mei et al., 2015b). However, predicting the thermodynamics of complexation reactions is a much greater challenge as it is necessary to evaluate the entropic terms that contribute to the free energies of each species. If only the reactions that occur in an ideal gas phase are considered, the prediction of reaction free energies is easy. We can first determine the absolute static change in internal energy of the reaction by the difference in the energies of the product and reactant species. The vibrational/rotational energies of each species can then be calculated to determine the zero-point energies and the heat capacities. From those, the enthalpies and entropies can be predicted. Note that it is also necessary to evaluate the ideal gas translational entropy for each species using the Sackur-Tetrode equation.

To go beyond the ideal gas phase, the solvation free energies of each species by the aqueous solution need to be included. In the spirit of the Born theory (Born, 1920), we might estimate the solvation free energy by modelling the aqueous solvent as a dielectric continuum with a dielectric constant (which, in turn, is a function of P, T). The effect of the dielectric continuum on each solute species is modelled by surrounding each solute species with a surface defined by spheres of a fixed radius. Such models have been incorporated into most quantum chemistry codes and are widely used in simulations of proteins in aqueous solutions. However, predicting the solvation effect on the thermodynamics of metal-complexation reactions in aqueous solutions using continuum models has not been very successful (e.g., Sherman, 2007); the problem is that the solute radius and local dielectric constant are not well defined. A better approach would be to treat the solvent molecules explicitly and determine the free energy of solvation by integrating over all the solvent configurations. This is impossible, but can be approximated using molecular dynamics. First, we start with an assemblage of atoms that is large enough to define the composition of the system of interest. For example, to model a 1 m CuCl solution, a cell containing 1 Cu, 1 Cl and 55 H_2O molecules can be a suitable starting point. Periodic boundary conditions are applied to the cell, so that if one atom leaves the cell, an equivalent atom enters the cell from the other side. The periodic boundary conditions remove any surface artifacts and allow the solvent molecules to adopt the structures they might have in a bulk solution. Next, the forces on each atom due to the presence of all the other atoms are calculated. These forces could be calculated using empirical pair potentials, or they may be calculated quantum mechanically using density functional theory (ab initio MD). With knowledge of the forces on each atom, the classical equations of motion can be solved to predict the velocities and positions of each atom after a suitably small timestep (on the order of <1 fs). This process is repeated many (10^6) times. The fundamental motivation of molecular dynamics is that the time average of any quantity will approach its thermodynamic average (this is the "Ergodic Hypothesis"). Hence, if the system is closed, it should evolve towards an equilibrium state provided that the simulation is run for a long enough interval compared to the lifetime of the species/processes of interest. The fraction of time that each species (e.g., Cu^+, CuCl(aq)) exists will be equal to the relative concentration of that species at chemical equilibrium. In practice, evaluating equilibrium concentrations this way may require running long simulations since some species can have very long lifetimes (μs scale) compared to the computational timesteps (fs scale); this may be unrealistic with current computational capabilities. An alternative approach is to directly evaluate the free energy of a reaction by using constraints. For example, the free energy of the reaction,

$$Cu^+ + Cl^- = CuCl(aq), \tag{1}$$

can be evaluated by constraining the Cu–Cl distance to some fixed value r. We then run a simulation and evaluate the time-average of the force required to maintain that constraint. The simulation is repeated over a number of Cu–Cl distances to obtain $F(r)$. The integral of $F(r)$ with respect to the Cu–Cl distance corresponds to the work required to form CuCl from Cu^+ and Cl^- in solution. That work, if done at constant volume, is the Helmholtz free energy.

Molecular dynamics simulations have traditionally used classical analytical functions to describe the potential energy of an atom as a function of the other atomic positions. The simplistic approach is to assume that interaction between any two atoms is independent of the position of the other atoms. This means that the total potential energy is the sum of two-body interatomic potentials. Such potentials can be derived by fits to empirical data or by fits to potential surfaces calculated quantum mechanically. For systems containing only H_2O, CO_2, Na^+ and Cl^-, two-body potential models can yield remarkably accurate predictions of the fluid's equation of state and ion speciation (Driesner et al., 1998; Raiteri et al., 2010; Sherman and Collings, 2002; Smith and Dang, 1994). However, the speciation of transition metals and metalloids in aqueous fluids cannot be reliably predicted using simple two-body potentials. Instead, the interatomic interactions need to be explicitly evaluated quantum mechanically at each timestep in the simulations. This a formidable computational challenge, but has become practical using the method of Car and Parrinello (1985). In recent years, such ab initio molecular dynamics simulations have been applied to predict the speciation of Cu(I) (Mei et al., 2013a, 2014; Sherman, 2007), Au(I) (Liu et al., 2011b; Mei et al., 2013b, 2014), Ag(I) (Liu et al., 2012d; Pokrovski et al., 2013), Zn(II) (Liu et al., 2011c; Mei et al., 2015b), Pd(II) (Mei et al., 2015a), and Y(III) (Haigis et al., 2013; Liu et al., 2012c). These studies report excellent agreement with experiment and XAS data in particular.

Some of these simulations have employed thermodynamic integration along a constrained reaction coordinate to evaluate free energies and formation constants of metal complexes at high pressure and temperature. These calculations are most reliable for simulations at high temperature (T ≥ 200 °C) where, due to faster particle motions, it becomes easier to sample sufficient configurations to yield an accurate time-average of the constraint force along the constrained coordinate. The speciation and stability constants derived from ab initio MD studies of Cu(I) (Mei et al., 2013a), Zn(II) (Mei et al., 2015b), and Pd(II) (Mei et al., 2015a) also predict the changes in solubility brought about by changes in P, T, and solution composition; in general, there also is good agreement (within one order of magnitude) in calculating metal solubilities in ore-forming fluids. This indicates that these computational methods will play an increasingly significant role in understanding energetic properties of metals and their behaviour in hydrothermal fluids.

3. Review of coordination of metals in hydrothermal fluids

In this section we review the coordination chemistry of metals and metalloids (columns 3 to 16) in geothermal fluids. We focus on the main oxidation states and complexes that are likely to account for metal transport in crustal fluids, from near-surface environments to high temperatures (mostly to 600 °C). The vast majority of available data is at vapour-saturated pressures (T ≤ 350 °C), with comparatively few studies at higher pressures and temperatures (mostly ≤2 kbar) (Seward and Driesner, 2004).

3.1. Titanium, zirconium and hafnium

High Field Strength elements (HFSE: Ti, Zr, Hf, as well as Nb and Ta) are often assumed to be sparingly soluble in crustal fluids; however, numerous examples show that these metals can be mobile in aqueous fluids at least at local scale, e.g., the occurrence of rutile or zircon-rich veins in ultra-high pressure metamorphic rocks (Gao et al., 2007; Rubatto and Hermann, 2003) and some contact aureoles (Gieré, 1986). In a few examples, magmatic-hydrothermal processes led to the formation of economic concentrations of these metals (e.g., Strange Lake and Thor Lake Nechalacho deposit, Canada; Galineiro complex, Spain; Gysi et al., 2016; Salvi and Williams-Jones, 1996; Sheard et al., 2012).

Titanium exists mainly in the tetravalent state in crustal environments. The predominant coordination number in solid Ti(IV)-containing compounds is six-fold (e.g., in the three TiO_2 polymorphs rutile, anatase and brookite), or, when Ti substitutes in the silicate framework, four-fold (Roberts et al., 1996). As an HFSE, Ti is regarded as immobile in most crustal fluids, although Ti mobility is well documented in specific environments from room-temperature (e.g., Cabral et al., 2012) to metamorphic conditions (Van Baalen, 1993). Organic ligands are most likely responsible for Ti mobility at low temperature (Cabral et al., 2012). Information on Ti(IV) complexing in aqueous solutions is scarce. Van Sijl et al. (2010, 2011) conducted ab initio molecular dynamic simulations on the Ti^{4+} aqua complex, and found that a five-fold coordination of Ti to water was predominant at low T; this coordination increases to six-fold at 1000 K in high density fluids (1021 to 1260 kg m^{-3}), decreasing at the same temperature but lower pressures/densities. However, hydroxide complexes are likely to account for Ti transport in most hydrothermal systems, as Ti(IV) is a very strong Lewis acid. Knauss et al. (2001) deduced on the basis of solubility experiments that the neutral complex $Ti(OH)_4(aq)$ was most stable at acidic to neutral pH over the T range 25–300 °C, although its predominance range appears to decrease with increasing temperature in favour of charged hydroxyl-complexes. A tetrahedral geometry is usually assigned to $Ti(OH)_4(aq)$ (Vogel and Kilin, 2014), although the theoretical study of van Sijl et al. (2010) suggests a high stability of octahedral inner- and outer-sphere hydroxy complexes at elevated temperature in high density fluids.

Recent solubility data show that at high temperature (700–1100 °C; 5 kbar), rutile solubility was 2–4 times higher in chloride brines, and 20–100 times higher in fluoride brines, than in pure water (Borisenko et al., 2011). This suggests the formation of chloride and fluoride complexes of unknown coordination geometry. Further mobility of Ti(IV) in high temperature metamorphic and magmatic hydrothermal systems could be achieved by the formation of Ti–Si–(Na) clusters (Antignano and Manning, 2008) (see zirconium as well).

Zirconium. Zr^{4+} speciation in acidic, dilute chloride solutions (2.5 wt% HCl) is dominated by the 8-fold-coordinated $[Zr(H_2O)_8]^{4+}$ aqua complex from room temperature up to 420 °C (Louvel et al., 2013). In silica-alkali-rich aqueous supercritical fluids/melts (i.e., 3–60 wt% dissolved $Na_2Si_2O_5$; 600–650 °C; Louvel et al., 2013, 2014; Wilke et al., 2012), high Zr solubility is attributed to the formation of alkali-zirconosilicate clusters, in which Zr in coordinated octahedrally to six oxygen atoms (Fig. 3).

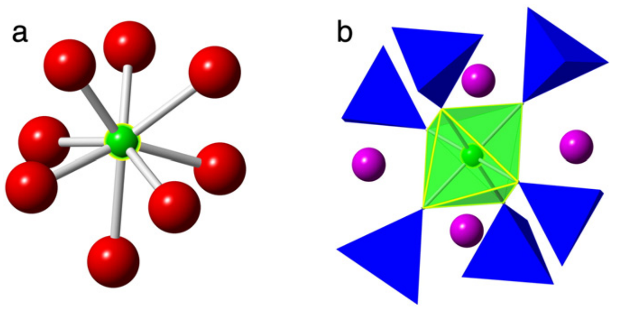

Fig. 3. Coordination change of Zr^{4+} in (a) dilute, F-free aqueous fluids and (b) supercritical $H_2O–Na_2Si_2O_5$ fluids (i.e., hydrated melts) (modified after Louvel et al., 2013), showing a change in coordination from 8-fold to 6-fold.

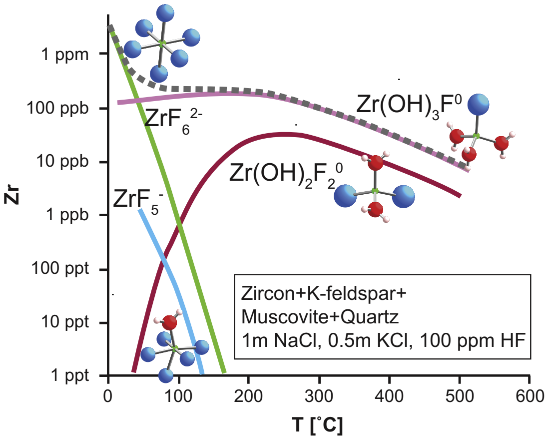

Fig. 4. Speciation and solubility of zircon in a model solution after Migdisov et al. (2011a). The sharp change in solubility at low temperature is due to a change in coordination from octahedral to tetrahedral complexes. Zirconium atoms are shown as green spheres, chloride ions in blue, oxygen in red, and hydrogen in pink. The dashed line represents the total solubility.

Based on measurement of baddeleyite (ZrO_2) solubility (T to 400 °C; P to 700 bar) in HF-bearing aqueous solutions, Migdisov et al. (2011a) showed that Zr is transported mainly in the form of the hydroxyfluoride species $ZrF(OH)_3(aq)$ and $ZrF_2(OH)_2(aq)$ at T > ~100 °C (Fig. 4). Although no direct evidence for the coordination geometry of these species is available yet, the proposed speciation suggests a change in coordination from 8- or 6-coordinated fluoro-aqua complexes at low temperature, to tetrahedral hydroxyl-fluoro-complexes at high temperature. This transition is associated with a decrease in F coordination and a decrease in solubility. Although the solubility of $ZrO_2(s)$ is retrograde with respect to temperature, the measured concentrations of Zr are orders of magnitude higher than those predicted from theoretical extrapolations based on simple fluoro-aqua complexes (ZrF_3^+–ZrF_6^{2-}; Fig. 4).

Hafnium. The fundamental inorganic chemistry of Hf has not been studied as intensively as the other Group 4 elements (Underwood et al., 2013). Hf^{4+} is mobile in F-alkali-rich aqueous solutions at T 400–575 °C, and compounds containing Hf^{4+} in 6- to 8-coordination with fluoride ions (and sometimes one oxygen) form under these conditions (e.g., octahedral HfF_6^{2-}; square face monocapped trigonal prismatic HfF_7^{3-}). In nature Zr/Hf fractionation seems to be associated with magmatic processes rather than hydrothermal processes (Yin et al., 2013).

3.2. Vanadium

Most vanadium is mined from V- and Ti-rich magmatic magnetite and steel-making slags. Some fossil fuel deposits such as crude oil, coal and tar sands also contain elevated V (Pohl, 2011), and V is enriched in some supergene environments due to the low solubility of V minerals (Evans and Garrels, 1958; Kamona and Gunzel, 2007) or via scavenging by Fe- and Mn-oxyhydroxides in oceans (Brugger and Gieré, 2000; Trefry and Metz, 1989). Hydrothermal mobility of V is characteristic of many epithermal systems (Cooke and McPhail, 2001; Spry and Scherbarth, 2006) and a few orogenic and shear-hosted Au systems (e.g., Golden Mile, Western Australia; Hemlo, Ontatio; Harris, 1989; Nickel, 1977; Tomkins et al., 2004). Yet, little is known about the hydrothermal geochemistry of V, and to our knowledge no experimental study of V under hydrothermal conditions is available. Thermodynamic modelling of V-mobility is based on extrapolation from room-T data (Shock et al., 1997b).

Vanadium exists mainly in three oxidation states in crustal minerals (Wong et al., 1984), melts (Sutton et al., 2005) and fluids (Fig. 5).

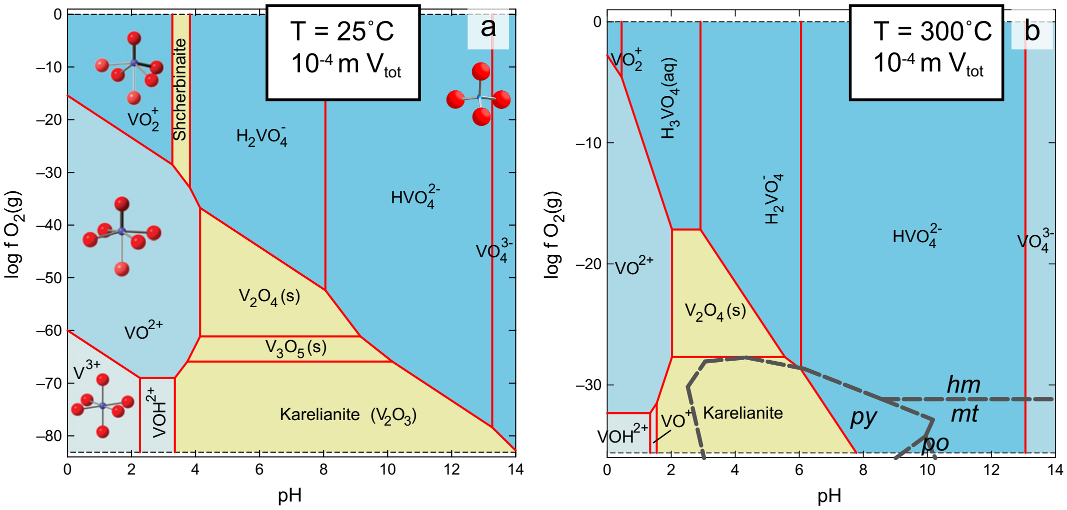

Fig. 5. Speciation of vanadium at room temperature (a) and 300 °C (b) in dilute solutions.
Activity diagram drawn with Geochemist's Workbench (Bethke, 2008), using thermodynamic properties from Shock et al. (1997b) for aqueous species, and Wagman et al. (1982) for solids.

Vanadium(III), V(IV) and V(V) form oxy-hydroxy complexes. Under acidic conditions, the aqua complexes have increasingly distorted octahedral geometries with increasing oxidation state at room temperature ($[V(III)(H_2O)_6]^{3+}$; $[V(IV)O(H_2O)_5]^{2+}$; $[V(V)O_2(H_2O)_4]^{+}$; Krakowiak et al., 2012). Vanadium(III) complexes are predicted to predominate at highly reducing conditions at acidic pH (Fig. 5), but V(III) is the main oxidation state of V in hydrothermal V-minerals (e.g. roscoelite, Wong et al., 1984). Vanadium(V) complexes predominate in oxidizing conditions; with increasing pH, the distorted octahedral complexes cede to tetrahedral complexes based on the $[VO_4^{3-}]$ vanadate ion. Concentrated oxidised V solutions at room T are dominated by polynuclear vanadate complexes; in acidic solutions (pH range 3–6), the orange colored decavanadates ($H_nV_{10}O_{28}^{(6-n)-}$, where n = 0–3), in which each V(V) is octahedrally coordinated, are prevalent. At neutral and basic pH (<12), a number of clusters (V_2 to V_6) exist, depending on pH and V concentration; V(V) is present in tetrahedral coordination in these complexes. In the absence of experimental data under hydrothermal conditions, the geometry of V-complexes in hydrothermal systems remains unconstrained; extrapolations from room-temperature suggest that tetrahedral vanadate monomer complexes are the most important V-complexes in hydrothermal systems at 300 °C (Fig. 5).

3.3. Niobium and tantalum

There are several well-documented minerals containing Nb^0, Nb^{2+}, Nb^{4+} and Nb^{5+}, and Ta follows a similar pattern (Martin and Wulser, 2014), but Nb^{5+} and Ta^{5+} are assumed to be the only important oxidation states of these HFSE in natural fluids. This was confirmed by Burnham et al. (2012), who showed experimentally that only Nb^{5+} and Ta^{5+} exist in silicate glasses quenched from melts equilibrated at 1400–1650 °C, atmospheric pressure to 1.5 GPa, at oxygen fugacities ranging from +6.7 to −4.3 log units relative to the iron–wüstite buffer. According to Mackay and Simandl (2014), Nb mineralization associated with carbonatite complexes is commonly interpreted as magmatic, whereas economic enrichment of Ta (and REEs) may be related to magmatic hydrothermal fluids or to the redistribution of primary magmatic concentrations by hydrothermal fluids.

Reliable data on the solubility and coordination chemistry of Nb and Ta in hydrothermal solutions are scarce. Nb^{5+} and Ta^{5+} form octahedral complexes with O and F ligands, but both are poorly soluble in aqueous solutions at low temperature, with the exception of the $Nb(OH)_6^-$ complex at high pH (>11; Schweitzer and Pesterfield, 2010). Zaraisky et al. (2010) investigated the solubility of Ta_2O_5 and columbite–tantalite in fluoride solutions from 300 to 550 °C at 1 kbar, and concluded that hydrothermal transport of Ta(V) and Nb(V) is possible only in concentrated fluoride solutions, conditions found for example in some alkaline igneous settings (Sheard et al., 2012). Based on a study of Nb_2O_5 solubility to 250 °C, Timofeev et al. (2015) showed that $Nb(OH)_4^+$ is the main Nb complex at low F-concentration even under acidic conditions (pH 2), whereas $NbF_2(OH)_3^0$ predominates in F-rich solutions. The importance of F^- as well as Cl–Nb(V) complexes was further demonstrated by Tanis et al. (2015), who obtained ppm-level Nb concentrations in NaCl (6–150 ppm) and NaF (180–910 ppm)-rich solutions at 300–800 °C, 10–65 kbar. The in situ Ta L_3-edge XAS measurements of Mayanovic et al. (2013) show that Ta(V) exists in distorted octahedral geometry in Ta-bearing peraluminous silicate glass + H_2O system to 960 °C and ~0.6 GPa.

3.4. Chromium, molybdenum and tungsten

These three Group VIB elements occur in nature in two oxidation states with contrasting coordination chemistry.

Chromium^{3+} is assumed to be the predominant oxidation state of Cr in hydrothermal fluids under crustal conditions. Chromium^{2+} is mainly reported to play a role in reduced, Fe^{3+}-free melts, such as lunar basalts (fO_2 below metallic Fe-wüstite), and is not considered important for aqueous geochemistry (Bell et al., 2014; Cardelli et al., 2003; Hanson and Jones, 1998). Chromium^{6+} (mainly as chromate ion and its protonated forms, $[H_n(CrO_4)]^{(2-n)-}$, n = 0, 1, 2) exists in the weathering environment, resulting in the formation of colourful chromate minerals (e.g., stichtite replacing chromite; Melchiorre et al., 2014). The chromate ion (n = 0) has a rigid tetrahedral structure, with Cr–O distances ranging from 1.65 Å to 1.66 Å, which displays little change to 400 °C (Hoffmann et al., 2001b). Protonation (i.e. bichromate ion, n = 1) involves a distortion of the geometry (short distance at 1.62 Å), again with little temperature effect (Hoffmann et al., 2001b). In salty solutions, the chloride complex $[CrO_3Cl]^-$ becomes important at elevated temperature and acidic pH (Palmer et al., 1987).

At ambient conditions, Cr^{3+} complexes exist in an octahedral geometry. The hexaaqua $Cr(H_2O)_6^{3+}$ complex is stable under acidic conditions ($pK_a^I \sim pK_a^{II} \sim 4.3$; Stünzi and Marty, 1983); at higher pH, octahedral hydroxide and chloride species (Ottonello and Zuccolini, 2005) are expected to be stable in geological fluids (e.g., $CrCl^{2+}$, $CrCl_2^+$, $CrCl_3(aq)$, Dellien et al., 1976; Diaz-Moreno et al., 1996; Magini, 1980; $Cr(OH)^{2+}$,

$Cr(OH)_2^+$, $Cr(OH)_3$(aq), $Cr(OH)_4^-$; Shock et al., 1997b). The EXAFS study of Diaz-Moreno et al. (1996) confirms that the stepwise substitution of up to three innersphere oxygen atoms by chloride ligands with increasing salt concentrations preserves the octahedral geometry of the complex at room temperature. As anticipated by Bjerrum (1908), Cr(III) is seldom present only in the monomeric form, and a vast number of polynuclear species form in sufficiently concentrated Cr(III) solutions; the importance of these species at high P, T remains untested. Watenphul et al. (2014) conducted the only study of hydrothermal transport of Cr(III), combining in situ solubility and Raman spectroscopy measurements and ab initio MD simulations in 1.6–4.2 m aqueous HCl solutions at 400–700 °C and pressures to 10 kbar. They concluded that Cr(III) shows a predominantly tetrahedral coordination environment ($CrCl_4^-$ or $Cr(OH)Cl_3$(aq)) in concentrated HCl solutions at a fluid density of 0.80 g/cm^3, and that this complex becomes more aquated at higher density (0.97 g/cm^3), with coordination number increasing to 5 and 6. At low Cl^- activity, mixed $CrCl_x(H_2O)_y(OH)_z^{3-x-z}$ complexes ($x < 3$; coordination of ≤6) are likely predominant.

Molybdenum. Although Mo is mostly mined from hydrothermal molybdenite (MoS_2) in which the oxidation state of Mo is +4, Mo is assumed to be transported as Mo^{6+} in natural fluids (Hurtig and Williams-Jones, 2014a; Minubayeva and Seward, 2010). Minubayeva and Seward (2010) determined thermodynamic properties for the ionization of molybdic acid (H_2MoO_4(aq)) from 30 to 300 °C and vapour-saturated pressures via UV–vis spectrophotometry, and proposed that $HMoO_4^-$ and MoO_4^{2-} are important species in low-sulfur hydrothermal fluids. Based on solubility and XANES studies of synthetic fluid inclusions, Ulrich and Mavrogenes (2008) suggested that oxychloride complexes, Mo–O ion pairs and molybdic acid are important in high salinity, low salinity solutions, and pure water, respectively. Using in situ XAS techniques, Borg et al. (2012) further identified the predominant Mo(VI) chloride species and characterised their geometries. They showed that the molybdate species (e.g., $HMoO_4^-$ or MoO_4^{2-}) share a tetrahedral geometry, and suggested that these tetrahedral complexes predominate in basic to near-neutral natural hydrothermal fluids. Liu et al. (2013) confirmed the tetrahedral geometry of molybdic acid and its deprotonated forms using ab initio MD. Borg et al. (2012) found no evidence for polynuclear Mo complexes. In contrast, chloride complexes with an octahedral structure (e.g., $MoO_mCl_n^{6-2m-n}$, $n + m = 6$) become predominant in acidic, chloride-rich solutions. The stability of these octahedral chloride complexes increases with temperature, but will only play a significant role in highly acidic fluids. In low density water vapours, exponential increase in Mo solubility with increasing water activity has been linked to the formation of second-shell Mo(VI) clusters with water, such as $MoO_3{\cdot}nH_2O$(g) in pure water vapour, and $MoO_2Cl_2{\cdot}nH_2O$(g) in HCl-bearing water vapour (T to 500 °C, P up to 160 bar; Hurtig and Williams-Jones, 2014a; Rempel et al., 2006, 2008, 2009). The detailed coordination geometry of these vapour species remains unknown. At higher temperatures and pressures (600–800 °C and 200 MPa), Zhang et al. (2012) suggested that an oxysulfide complex, $NaHMoO_2S_2$(aq), is the main species responsible for the solubility of MoS_2(s) in mineral-buffered fO_2-fS_2 fluids, based on solubility experiments.

Tungsten. Similarly to Mo, W is found in both tetravalent (e.g., tungstenite, WS_2(s)) and hexavalent (e.g., scheelite, $CaWO_4$(s), and ferberite, $FeWO_4$(s)) oxidation states in minerals; contrary to Mo, W is mined mainly from hydrothermal tungstate minerals. Consequently, W is assumed to be carried as a tetrahedral tungstate complex in crustal fluids. Compared to Mo, few experimental studies on W solubility and speciation in hydrothermal fluids have been done since the early works by Wesolowski et al. (1984), Wood (1992), and Wood and Vlassopoulos (1989). These solubility studies are consistent with the predominance of tungstate acid (H_2WO_4(aq)) or a cation-tungstate ion pair (e.g. $NaHWO_4$(aq)) in fluids up to 600 °C and 1 kbar, even at highly saline and acidic conditions (5 m NaCl or 5 m HCl; Wood and Samson, 2000). This conclusion was confirmed qualitatively by the recent solubility studies of Bali et al. (2012) and Redkin and Kostromin (2010). The behaviour of W hence is in contrast with that of Mo, since Mo-oxychloro complexes predominant in the acidic saline fluids (Borg et al., 2012).

3.5. Iron and manganese, nickel and cobalt, zinc and cadmium: transition metals existing mainly as octahedral and tetrahedral aqua- and chloro-complexes

The aqueous geochemistry of many first-row transition metals as well as Cd is characterised by the predominance of the divalent state, the importance of halide complexes, and coordination geometries that change from octahedral at low T to predominantly tetrahedral at high T, especially in chloride brines.

Iron and manganese are abundant in natural hydrothermal fluids, such as seafloor hydrothermal systems (Pester et al., 2011; Von Damm, 1995).

Iron is transported as Fe(II) and Fe(III) species in natural aqueous fluids. Liu et al. (2006) used UV–vis and XAS data to show that Fe(III) forms the chloro-complexes $FeCl^{2+}$, $FeCl_2^+$, $FeCl_3$(aq) and $FeCl_4^-$ in chloride solutions at P_{sat} to 300 °C. The predominance fields of $FeCl_3$(aq) and $FeCl_4^-$ expand to lower Cl concentrations with increasing T, which is related to a change in the geometry of the complex between $FeCl_2^+$ and $FeCl_3$(aq): Fe^{3+}, $FeCl^{2+}$ and $FeCl_2^+$ share an octahedral geometry; $FeCl_3$(aq) could be either tetrahedral or trigonal dipyramidal; and $FeCl_4^-$ is tetrahedral. Liu et al. (2006) predicted that the abrupt change in predominant coordination geometry with temperature will result in a large change in solubility upon cooling (Fig. 6a).

Iron(II) is considered to be the main oxidation state of Fe in hydrothermal fluids, and the solubility of Fe minerals and Fe(II) speciation has been studied extensively using various experimental methods (See Table 1 in Testemale et al., 2009a for a review). However until recently there has been considerable discrepancy between different experimental studies. Most solubility studies favour $FeCl_2$(aq) as the highest chloride complexes at temperature up to 650 °C and 2 kbar (Boctor et al., 1980; Chou and Eugster, 1977; Crerar et al., 1978; Ding and Seyfried, 1992; Fein et al., 1992; Ohmoto et al., 1994). This is consistent with the UV–vis study of Heinrich and Seward (1990) (25–200 °C). However, two UV–vis studies at lower temperatures and more saline solutions have identified the $FeCl_4^{2-}$ complex (10–100 °C, Cl ≤ 6 m, Zhao and Pan, 2001; 25–82 °C, Cl ≤ 6 m; Koplitz et al., 1987). Similarly, Liu et al. (2007) showed using XAS that tetrahedral $FeCl_4^{2-}$ is the predominant Fe(II) species in saline solutions (>10 m at 25 °C, and ≥7.5 m at 150 °C). More recently, Testemale et al. (2009a) mapped Fe(II) speciation in acidic chloride solutions over a wide range of temperatures and salinities (25–450 °C at 500 bar, 0.5–12 m chloride). They confirmed that octahedral species (e.g., $FeCl_x(H_2O)_{6-x}$) predominate in lower temperature and salinity fluids, and found that tetrahedral $FeCl_4^{2-}$ predominates at higher temperature and high salinity (T > 300 °C, Cl > 2 m). They estimated the formation constants of the predominant Fe(II) chloride species on the basis of XANES data, and showed that the change in the solubility of Fe minerals as a function of temperature and chloride concentration can be attributed to the tetrahedral–octahedral transition of Fe(II) chloride complexes. That is, replacement of tetrahedral $FeCl_4^{2-}$ by octahedral $FeCl_x(H_2O)_{6-x}$ species due to a temperature drop or dilution would cause a drop in solubility. Unpublished Ab initio MD calculations of Fe(II) in chloride-rich (10 m Cl^-) fluids at 350 °C (Fig. 6c) also show the breakdown of the $FeCl_2$(aq) complex to form a 4-fold $FeCl_4^{2-}$ species with a distorted tetrahedral structure, consistent with the model of Testemale et al. (2009a). Testemale et al. (2009a) used a new speciation model and log K data derived from their XAS data to reinterpret successfully the magnetite-pyrite-pyrrhotite solubility results of Fein et al. (1992). The changes of solubility of Fe-bearing mineral assemblages are controlled by the octahedral–tetrahedral transition (Fig. 6b).

Manganese. Mn^{4+}, Mn^{3+} and Mn^{2+} all occur in minerals, but only Mn^{2+} is considered to play a significant role for Mn transport in crustal

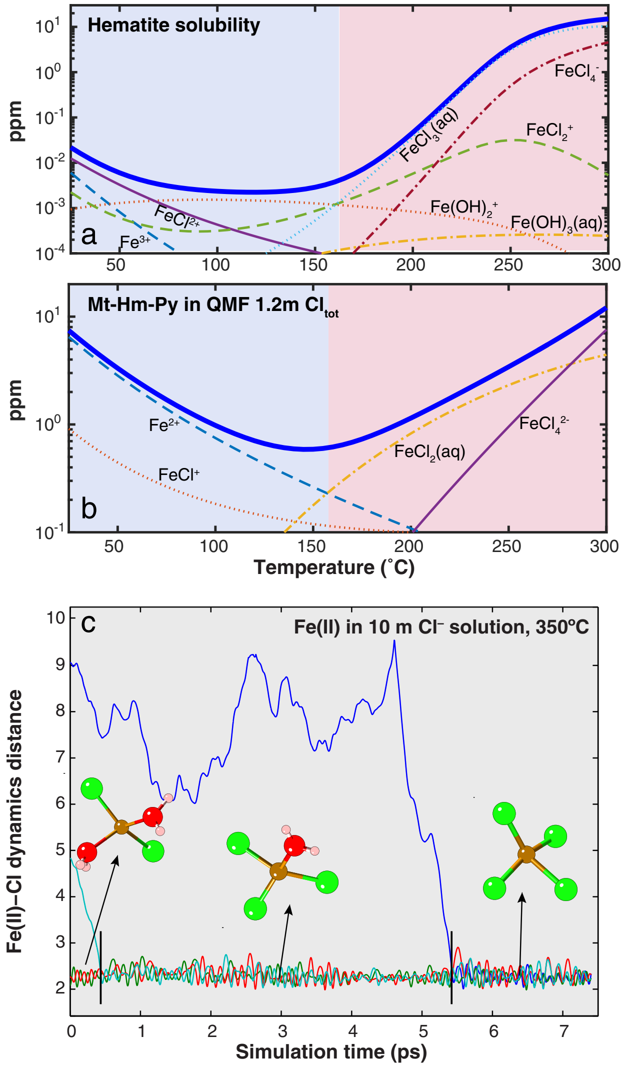

Fig. 6. Iron speciation in hydrothermal fluids. (a) Solubility of hematite in oxidised fluids (1 m NaCl, 0.001 m HCl). (b) Iron solubility in for the assemblage of pyrite, hematite, and magnetite, with fluid pH buffered by quartz-muscovite-K-feldspar (1 m NaCl, 0.01 m KCl). (c) Unpublished Dynamic Fe(II)–Cl distances during a simulation with 10 m Cl^- at 350 °C, 500 bar. The initial $[FeCl_2(H_2O)_2](aq)$ configuration evolves rapidly (~5 ps) into a stable $[FeCl_4]^{2-}$ configuration. The simulation was preformed using CPMD with PBE exchange correlation-functional and Vanderbilt ultrasoft pseudo-potentials. The bold solid (blue) line in (a) and (b) represents the total solubility.

fluids. Early solubility studies Gammons and Seward (1996) and Boctor (1985) provided formation constants for $MnCl^+$ and $MnCl_2(aq)$. Suleimenov and Seward (2000)'s in situ UV–vis study also identified these two species in 0.022–0.8 m NaCl solutions and provided their formation constants at 25–300 °C (P_{sat}). None of these studies have identified higher order chloride complexes, possibly due to the limited Cl concentration in their experimental solutions. Recently, based on XAS data, ab initio XANES simulations, and DFT calculations, Tian et al. (2014) obtained speciation and thermodynamic properties for Mn(II) chloride complexes at 30–550 °C and 600 bar, at Cl concentrations ranging from 0.1 to 10.34 m. This study showed that octahedral species predominate at ambient temperature, and tetrahedral species become important with increasing temperature and chloride concentrations. In contrast to Fe(II), Tian et al. (2014) found no evidence for the $MnCl_4^{2-}$ complex, with tetrahedral $MnCl_3(H_2O)^-$ being the limiting species at high salinity (Fig. 7c).

Cobalt and nickel. Most of the World's Co deposits are hydrothermal in origin (Smith, 2001), whereas Ni is gained primarily from magmatic deposits, where concentration occurs mainly via immiscibility of Ni-rich sulfide melts from silicate melts. In addition, the weathering of Ni-rich magmatic silicates leads to economically important 'Ni-laterites' (Fan and Gerson, 2011). Nickel is the main economic metal in only a few hydrothermal deposits, most often resulting from the remobilisation of magmatic Ni-sulfides (e.g., Gonzalez-Alvarez et al., 2013; Keays and Jowitt, 2013). This dichotomy reflects the fact that Ni is less mobile in hydrothermal fluids than Co.

Both Ni and Co exist in divalent form in natural waters and are transported in chloride-rich brines to form hydrothermal ore deposits (e.g., EnNaciri et al., 1997). Recent detailed in situ XAS studies combined with in situ UV–vis studies and solubility experiments provide an accurate picture of the coordination chemistry of Ni(II) and Co(II) (Liu et al., 2011a, 2012b; Migdisov et al., 2011b; Tian et al., 2012; Zhang et al., 2015a,b). At room temperature, both Ni(II) and Co(II) are coordinated by six water molecules in an octahedral configuration in dilute aqueous solutions. With increasing temperature and salt concentrations, both metals show an increased affinity for chlorine (Fig. 7d,e). Tian et al. (2012) determined that the $NiCl_2(aq)$ species exists in both octahedral ($[NiCl_2(H_2O)_4](aq)$) and tetrahedral ($[NiCl_2(H_2O)_2](aq)$) forms, with the ratio of octahedral to tetrahedral decreasing at elevated temperature (>200 °C). In contrast, octahedral $CoCl_2(aq)$ is only a minor species (if present at all) under all conditions, whereas tetrahedral $CoCl_2(aq)$ becomes an important species at high temperature in low- to moderately salty solutions (Fig. 7d). The new XAS data show that the octahedral to tetrahedral transition in Ni(II) chloride complexes occurs at higher temperature and higher salinity than the corresponding Co(II) complexes (Fig. 7d,e; Liu et al., 2011a). Since tetrahedral complexes display a higher affinity for chlorine than the octahedral complexes, Co solubility displays a stronger sensitivity to salinity than Ni, which exerts a major control on the contrasting mobility of Ni and Co in hydrothermal fluids.

Zinc and cadmium are usually associated in Zn-bearing minerals (e.g., sphalerite), as a result of their similar chemical and crystallographic properties. Bazarkina et al. (2010) noted that there is little variation in Cd/Zn mass ratios in crustal rocks (Cd/Zn = 0.001–0.003) and yet many hydrothermal Zn minerals have high Cd/Zn ratios; therefore, hydrothermal processes are key to controlling the fractionation of the these two metals. Both metals exist in just one oxidation state (divalent) in nature.

Zinc(II) chloride complexes (up to $ZnCl_4^{2-}$) are assumed to account for Zn transport in most crustal fluids (e.g., Anderson et al., 1995, 1998; Mayanovic et al., 1999; Brugger et al., 2003), although thermodynamic calculations by Zhong et al. (2015a) suggest that Zn bisulfide complexes (e.g., $Zn(HS)_2(aq)$) may become important at high temperatures (>500 °C). Zinc bisulfide complexing is constrained at elevated temperature to 250 °C by a single solubility study (Tagirov and Seward, 2010). Mei et al. (2016) used ab initio MD simulations, complemented by in situ XAS measurements, to demonstrate the high stability of the trigonal planar $Zn(HS)_3^-$ species at high temperature (≥500 °C), and provide estimates of log K values for the 4-fold tetrahedral $[Zn(HS)_n(H_2O)_{4-n}]^{2-n}$ complexes to 600 °C.

Zinc solubility and speciation in chloride brines are constrained by a number of quality experiments over a wide range in pressure and temperature up to 600 °C and 2 kbar (Bourcier and Barnes, 1987; Cygan et al., 1994; Plyasunov and Ivanov, 1991; Ruaya and Seward, 1986). Mei et al. (2015b) refitted these experimental data in light of ab initio molecular dynamic simulations and new in situ XAS measurements, and provided a robust model of Zn chloride complexing over a wide P, T range, which is consistent with most of these experimental studies. A unique feature of Zn(II) complexing, highlighted by the ab initio MD simulations, is that the octahedral aqua complex, $Zn(H_2O)_6^{2+}$, is destabilised by the addition of chloride ions; over a few ps of simulation time, the $ZnCl(H_2O)_5^+$ complex loses two waters to form tetrahedral $ZnCl(H_2O)_3^+$ even at room temperature. At high temperature, ab initio

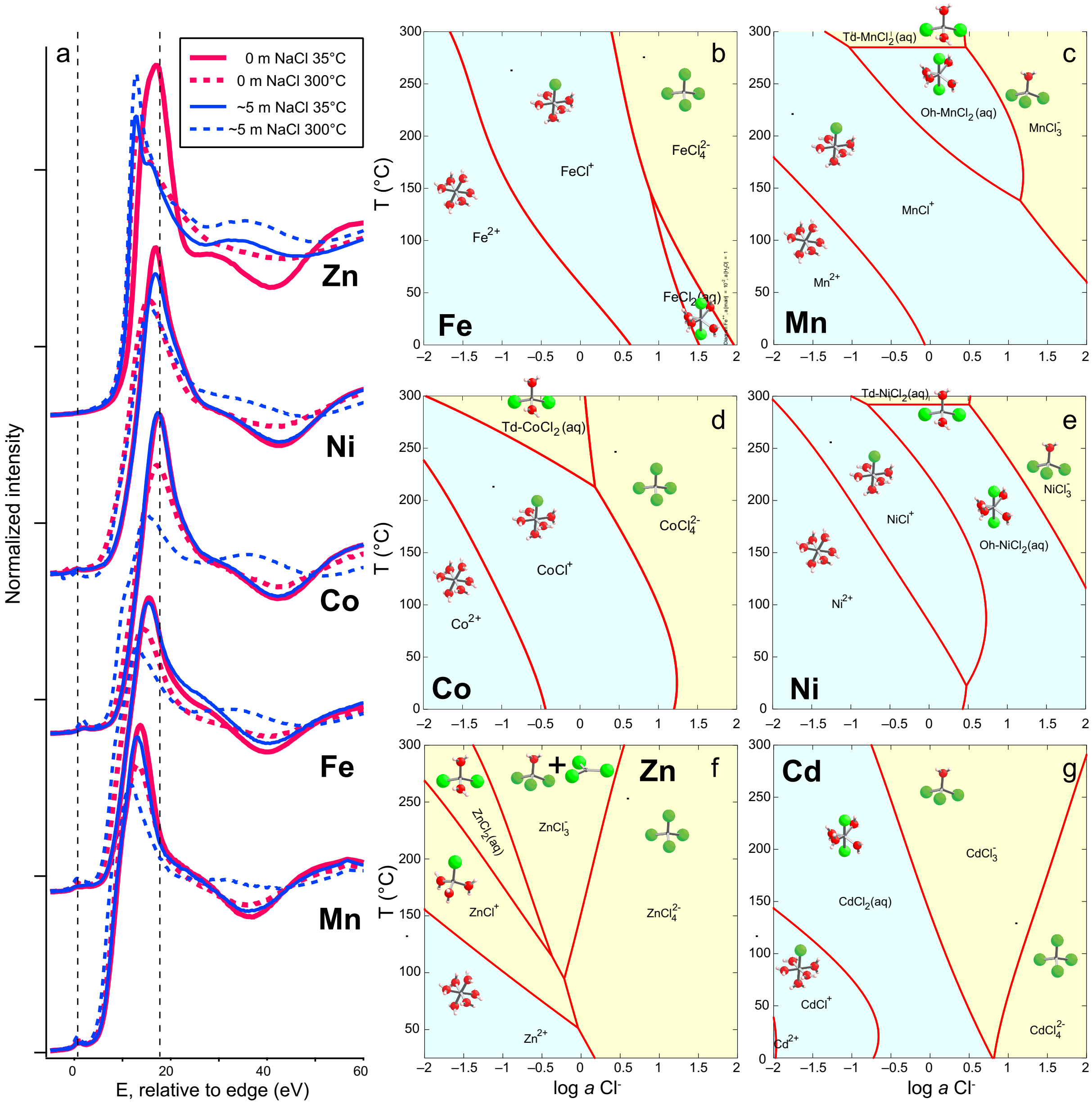

Fig. 7. Complexing and predominant coordination geometry of some divalent transition metals in chloride brines as a function of temperature and composition. (a) In situ XANES spectroscopy is a key source of information about the coordination geometry of transition metals under hydrothermal conditions. These data illustrate the coordination changes of Zn(II), Ni(II), Co(II), Fe(II) and Mn(II) in chloride solutions as a function of temperature and salinity. (b–g) Predictions of predominant species as a function of chloride ion activity and temperature. The activity-temperature diagrams were drawn using Geochemist's Workbench (Bethke, 2008), with thermodynamic data selected by Testemale et al. (2009a) (Fe); Tian et al. (2014) (Mn); Liu et al. (2011a) (Co); Tian et al. (2012) (Ni); Mei et al. (2015b) (Zn); and Bazarkina et al. (2010) (Cd). In the molecular models, chloride ions are shown in green, oxygen atoms in red, and hydrogen atoms in pink.

MD simulations reveal that the $Zn(H_2O)_6^{2+}$ complex becomes unstable, and rapidly loses two waters to form $Zn(H_2O)_4^{2+}$; in the simulation shown in Fig. 8, two waters are then displaced to form tetrahedral $ZnCl_2(H_2O)_2(aq)$, which remains stable for the remaining time of the simulation. Tetrahedral $ZnCl_4^{2-}$ is stable in saline solutions up to high temperature (Fig. 7f); however, with increasing temperature, $ZnCl_3^-$ and $ZnCl_2(aq)$ become increasingly stable. This is especially true for $ZnCl_3^-$, which also shows a change in geometry, from predominantly tetrahedral $[ZnCl_3(H_2O)]^-$ at lower temperature, to predominantly trigonal planar $[ZnCl_3]^-$ above ~600 °C (Fig. 7f).

Zinc bromide complexes have similar structures as Zn chloride complexes, with a high stability of the tetrahedral $ZnBr_4^{2-}$ complex to high temperature (Mayanovic et al., 2001; Liu et al., 2012a). Zinc bromide complexes most likely are only important in low temperature basional brines (Liu et al., 2012a). Mayanovic et al. (2001) also were able to characterise the outer hydration shell of the $ZnBr_4^{2-}$ complex, finding a 63% reduction in the number of waters in the outer hydration shell at 500 °C versus under ambient conditions.

Cadmium. The stoichiometry and geometry of Cd(II) in chlorine brines has recently been explored on the basis of in situ XAS measurements (20–450 °C and 1–600 bar) by Bazarkina et al. (2010). In contrast to Zn(II), octahedral Cd(II) chloride complexes display a significant stability over a wide range of chloride activity and temperatures (Fig. 7g). Tetrahedral $CdCl_4^{2-}$ is stable only at low temperature in highly saline

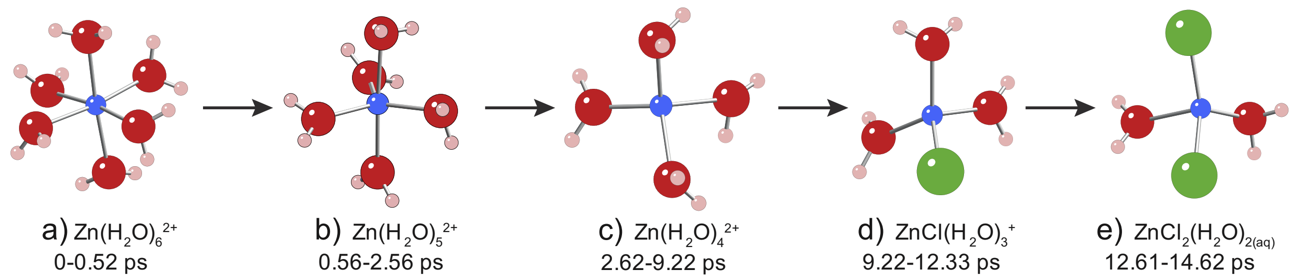
a) $Zn(H_2O)_6^{2+}$ 0-0.52 ps

b) $Zn(H_2O)_5^{2+}$ 0.56-2.56 ps

c) $Zn(H_2O)_4^{2+}$ 2.62-9.22 ps

d) $ZnCl(H_2O)_3^{+}$ 9.22-12.33 ps

e) $ZnCl_2(H_2O)_{2(aq)}$ 12.61-14.62 ps

Fig. 8. Transformation of a metastable octahedral Zn^{2+}(aq) molecule into the tetrahedral $ZnCl_2$(aq) complex, based on ab initio molecular dynamics simulations at 600 °C, 2 kbar. The octahedral aqua complex (set initial configuration, stable for 0.52 ps in (a)) first transforms via stepwise loss of two waters into a metastable tetrahedral aqua complex which remains stable for ~6 ps (c). Subsequently two chloride ions replace two water molecules in a stepwise fashion, to form the final $ZnCl_2$(aq) complex, which is predicted to be the predominant Zn complex under these conditions. See Mei et al. (2015b) for details on the simulations. Oxygen atoms are shown in red, hydrogen in pink, and chloride ions in green.

brines, and is of little importance in natural fluids. Tetrahedral $[Cd(H_2O)Cl_3^-]$ becomes increasingly stable with increasing temperature, and $[Cd(H_2O)_2Cl_2]$(aq) and $[Cd(H_2O)Cl_3^-]$ are the main Cd(II) species in hydrothermal fluids at 300 °C (Fig. 7g).

3.6. Copper, silver and gold

In geological fluids, Cu, Ag and Au all exist predominantly as linear complexes of the monovalent ion; indeed, Cu, Ag and Au are closely associated in many ore deposits. Aside from mineral solubility, fractionation among these metals is driven mainly by the relative strengths of chloride and bisulfide complexes, with Cu(I) having a higher affinity for chlorine and Au(I) for bisulfide. This can be readily explained by Soft-Hard Acid-Base theory (Pearson, 1963). Although the three monovalent ions are classified as soft acids, Au(I) is softest and Cu(I) hardest, thus Au(I) has the greatest affinity for the HS^- ligand, which is softer than Cl^-.

Copper exists in two oxidation states in nature, Cu(I) and Cu(II). *Cu(II)* requires highly oxidizing conditions found in near-surface environments (e.g. Sverjensky, 1987; Fig. 9). The Cu(II) aqua ion is soluble, with chloride complexing occurring at high salinity (Brugger et al., 2001; Fulton et al., 2000b). The coordination chemistry of Cu(II) is dominated by a strong Jahn-Teller effect, which results in a plethora of geometric arrangements of the ligands around the central atom (e.g., Smith, 1976 for Cu(II) chloride complexes). The structure of the Cu(II) aqua ion has been the topic of strong controversies, with the latest results suggesting a dynamic equilibrium between five-fold square pyramidal and distorted tetrahedral and octahedral geometries (Blumberger, 2008; Bowron et al., 2013; Chaboy et al., 2006; Liu et al., 2010). The five-fold coordination in the first solvation shell of the Cu(II) aqua ion has also been observed using neutron diffraction and ab initio molecular dynamics (Pasquarello et al., 2001). Copper(II) chloride complexes (Brugger et al., 2001; Collings et al., 2000) form in salty solutions, with $CuCl_4^{2-}$ (probably square planar) the highest order well-established complex. On the basis of in situ EXAFS measurements, Collings et al. (2000) deducted a maximum of stability of $CuCl_4^{2-}$ at ~125 °C, whereas only $CuCl^+$ and $CuCl_2$(aq) remained at 175 °C in a 5 M NaCl solution. However, the results at 175 °C need further verification, as it was not possible to reverse the experiment or recover the solution.

Copper(I) is the most common oxidation state of Cu in crustal hydrothermal fluids. Copper(I) chloride complexes are possibly the best studied aqueous metal complexes under hydrothermal conditions, and the predominant species have been characterised by various techniques (solubility, UV–vis, XAS, and molecular simulations; reviews in Brugger et al., 2007a; Liu et al., 2001). The aqua Cu(I) has a linear structure ($[H_2O–Cu–OH_2]^+$; Blumberger et al., 2004), although it is not stable in water and disproportionates rapidly to Cu(II) and native copper. At room temperature, Cu(I) forms stable complexes with a variety of ligands; these complexes display different geometries depending on ligand type and concentrations. In dilute chloride solutions, Cu(I) retains linear structures (e.g., $[H_2O–Cu–Cl]$(aq); $[Cl–Cu–Cl]^-$); however in concentrated chloride solutions, $CuCl_3^{2-}$ with a trigonal planar structure becomes stable (Brugger et al., 2007a; Liu et al., 2001; Sherman, 2007). Similarly, Cu(I) thiosulfate and mixed thiosulfate-chloride are

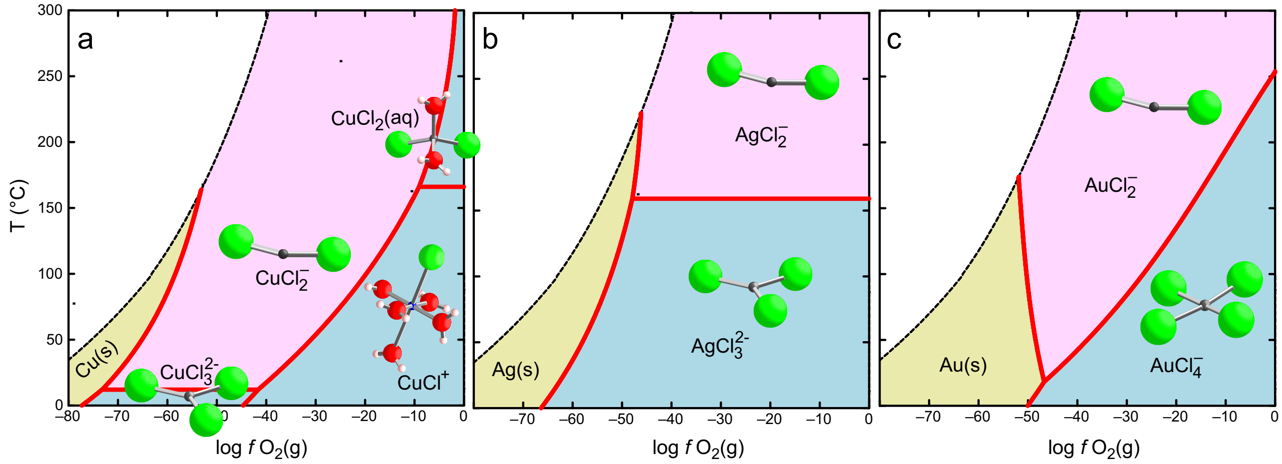

Fig. 9. Speciation and coordination of Cu, Ag and Cu in chloride brines ($a_{Cl} = 3$ m, pH = 3) as a function of temperature and redox state ($a_{Cu} = 10$ mmol, $a_{Ag} = 0.01$ mmol, $a_{Au} = 1 \times 10^{-12}$ m). Thermodynamic properties for Cu(I) chloride species are from Brugger et al. (2007a); for Au(I) chlorides from Stefánsson and Seward (2003c); for Cu(II) and Au(III) chlorides from Sverjensky et al. (2014a); and for Ag(I) chlorides from Akinfiev and Zotov (2001). In the molecular models, chloride ions are shown in green, oxygen atoms in red, and hydrogen atoms in pink.

trigonal planar (Etschmann et al., 2011). With increasing temperature, linear $CuCl_2^-$ becomes predominant even at high chloride concentrations, as demonstrated by XAS studies (Brugger et al., 2007a; Fulton et al., 2000a) and ab initio molecular simulations (Sherman, 2007). These studies also demonstrate that the tetrahedral $CuCl_4^{3-}$ moiety, which is very common in solids, does not exist in aqueous solutions.

Based on the available thermodynamic data, Zhong et al. (2015a) predicted Cu(I) bisulfide complexes to predominate Cu transport in S-bearing, high temperature fluids (e.g., magmatic hydrothermal or metamorphic fluids). Similarly to chloride complexes, Cu(I) hydrosulfide complexes have a linear geometry over the full experimental P-T range (up to 600 °C, 600 bar; Etschmann et al., 2010). The MD study of Mei et al. (2013a) found that linear mixed ligand species (e.g., $[Cl–Cu–HS]^-$) may be important in mixed Cl–HS solutions, consistent with the NaClCuHS(aq) species in the vapour phase suggested by Zajacz et al. (2011) on the basis of solubility experiments. The neutral complex $CuNaCl_2(aq)$ was also observed in ab initio MD of low-density fluids at high temperature (1000 °C; Mei et al., 2014). In this complex, the Na^+ ion is very weakly bonded in the outer coordination sphere with highly distorted structures and a very fast (ps) exchange rate in and out of the coordination sphere (Fig. 10).

Silver. Unlike Au (Au(I)/Au(III)) and Cu (Cu(I)/Cu(II)), Ag(I) is the only oxidation state of Ag in crustal fluids. Also in contrast to Cu(I) and Au(I), the Ag(I) aqua ion is stable at room temperature in aqueous solutions; however, there is some controversy about its geometry and in particular the number of water molecules in the first shell: the EXAFS studies of Yamaguchi et al. (1984) and Seward et al. (1996), and the MD simulations of Blumberger et al. (2004) and Liu et al. (2012d) suggest a four-coordinate tetrahedral structure, but Fulton et al. (2009; EXAFS) and Armunanto et al. (2003; MD) indicate 5–6 waters in the first shell of the Ag(I) ion at room temperature. With increasing temperature the hydration number appears to decrease to ~3 (Liu et al., 2012d; Seward et al., 1996).

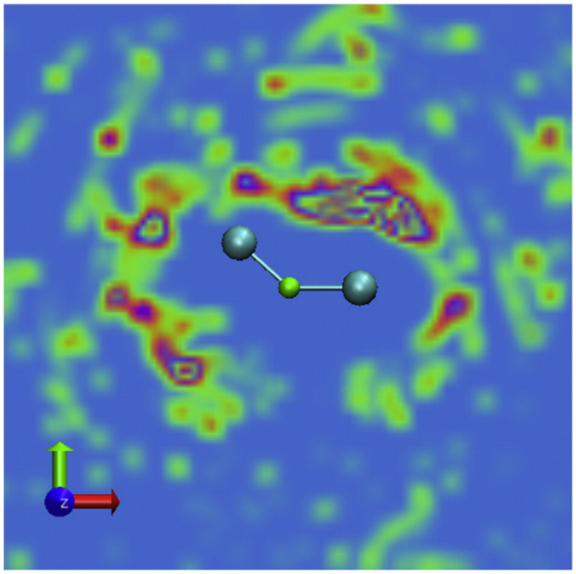

Fig. 10. Spatial distribution of the Na^+ ion around the $CuCl_2^-$ complex at 1000 °C, 1.5 kbar, showing Na^+ weakly bonded in the second shell of the $CuCl_2^-$ molecule. Details on simulations in Mei et al. (2014). The figure was created using the "TRAVIS" software (Brehm and Kirchner, 2011), by calculating the statistical spatial distribution of Na^+ around the reference molecule $CuCl_2^-$ over a 30 ps calculation time. The color maps represent the propability (warmer colour indicates higher probability) of Na^+ appearing at a certain position in the plane defined by the $CuCl_2^-$ molecule. The copper(I) ion is shown in green, and the chloride ion in blue.

Similar to the Au–Cl and Cu–Cl systems, solubility (e.g., Seward, 1976; Zotov et al., 1995), in situ XAS and MD simulations (Liu et al., 2012d; Pokrovski et al., 2013) all agree that $AgCl_2^-$ with a distorted linear structure is the predominant complex in hydrothermal solutions over a wide range of temperatures and salinity, with higher order species such as $AgCl_3^{2-}$ only present at lower temperatures (Fig. 9). Stefánsson and Seward (2003a)'s solubility study suggests that Ag(HS)(aq) and $Ag(HS)_2^-$ predominate at acid and neutral pH, and $Ag_2S(HS)_2^{2-}$ at alkaline conditions in S-bearing solutions at 25–400 °C (P_{sat} and 500 bar); however there is still a lack of in situ spectroscopic data to confirm the identity and geometry of these species. We speculate that Ag(HS)(aq) and $Ag(HS)_2^-$ should have linear structures similar to Au(I) and Cu(I) hydrosulfide complexes.

Gold. The Au atom is much larger than Cu and Ag, and the sum of the first, second and third ionization energies are the lowest among Cu, Ag and Au (Greenwood and Earnshaw, 1984). As a result, Au(III) complexes can be present at ambient conditions, but Au(I) is the main form of Au in geological fluids. *Au(III)* is thermodynamically stable in oxygenated waters at low pH, forming square planar complexes with H_2O, OH^-, and halide ions, e.g. $AuCl_4^-$ (Fig. 9; Chen et al., 2009; Sherman, 2010; Usher et al., 2009). Recently, Au(III) halide and/or hydroxide complexes have been shown to be present, in metastable form, in near-neutral to basic surface waters (Ta et al., 2014, 2015).

Similar to Cu(I), the *Au(I)* aqua ion is unstable in water; Au(I) is stabilised by the formation of coordination complexes, and these species also become important relative to the higher oxidation state cation with increasing temperature. Recent XAS studies (Liu et al., 2014; Pokrovski et al., 2009a,b) and MD simulations (Liu et al., 2011b) indicate that both Au–Cl (AuCl(aq), $AuCl_2^-$) and Au-bisulfide complexes (AuHS(aq), $Au(HS)_2^-$) possess distorted linear structures. This is also consistent with the predictions of predominant species based on the thermodynamic properties generated from solubility studies (e.g., Benning and Seward, 1996; Stefánsson and Seward, 2003b,c, 2004). Liu et al. (2014)'s XAS study compared the complexation of different ligands (Cl^-, Br^-, HS^- and NH_3) with Au(I) and concluded that Au–HS^- complexes outcompete other species in S-bearing fluids under shallow crustal conditions. This is consistent with the thermodynamic calculations showing that $AuCl_2^-$ is the predominant species under acidic conditions, and $Au(HS)_2^-$ under neutral to alkaline solutions (Williams-Jones et al., 2009).

Recently, renewed attention has been devoted to the speciation of sulfur at elevated pressure and temperature. Giggenbach (1971) first suggested that polysulfide species become stable relative to HS^-/$H_2S(aq)$ with increasing temperature and pressure. Based on in situ Raman spectroscopy, Pokrovski and Dubrovinsky (2011) and Pokrovski and Dubessy (2015a) showed that the blue-colored, linear trisulfur ion (S_3^-) can dominate speciation in S-rich solutions at P > 0.5 GPa and T > 250 °C. This difference in sulfur speciation is expected to affect the nature of metal complexes at high pressure, in particular Au(I) and Cu(I). The ab initio MD study of Mei et al. (2013b) concluded that Au(I)–S_3^- species, and mixed S_3^-/hydroxide/bisulfide complexes, display a distorted linear structure, and that the strength of the Au(I)–S_3^- bond is similar to that of the Au(I)–HS^- bond. These theoretical results have recently been confirmed by Pokrovski et al. (2015b), who also highlight the potential importance of Au(I) polysulfide complexes for metal transport at high pressure (≥0.5 GPa).

Neutral ions pairs such as $NaAuCl_2(aq)$ become important in low-density fluids at high temperature (Zajacz et al., 2010). Similarly to $NaCuCl_2(aq)$, $NaAuCl_2(aq)$ has a linear [Cl–Au–Cl] structure, with the Na^+ ion loosely bonded, i.e. highly disordered and with ps-scale exchange rate (Mei et al., 2014).

Comparing the coordination change of the Au, Ag and Cu chloride complexes as a function of temperature in a moderate salinity solution (3 m NaCl, pH = 3, P_{sat}; Fig. 9) shows that, despite the different predominant valence states and coordination numbers at ambient temperatures, $Me(I)Cl_2^-$ (Me refers to Cu, Au or Ag) complexes predominate at elevated temperatures over wide ranges of log $fO_2(g)$. This implies that increasing temperature favours the lower oxidation state and associated lower coordination numbers.

3.7. Mercury

Cinnabar, HgS, is the main Hg ore mineral and one of the most insoluble substances known. Mercury can be transported either as $Hg^0(g)$, $Hg^0(aq)$, or Hg(II)-complexes in crustal fluids (Bell et al., 2007; Krupp, 1988a; Lennie et al., 2003; Varekamp and Buseck, 1984). Varekamp and Buseck (1984) noted that $Hg^0(aq)$ is favoured by relatively high temperatures and pH, and relatively low total S, ionic strength, and $fO_2(g)$. Thus the $Hg^0(aq)$ – coordinated to six waters of solvation, and with little evidence for polymerisation (Paquette and Helz, 1995) – or $Hg^0(g)$ are important for geothermal transport. Hg(II) forms coordination compounds with bisulfide; these complexes are the dominant form of Hg in hot (~> 200 °C) solutions that contain hydrogen sulfide at neutral to alkaline pH (Krupp, 1988a). Lennie et al. (2003) and Bell et al. (2007) determined that Hg(II)–HS^- complexes exist as linear complexes (0.5 to 0.003 M $NaHS^-$, 2.8 to 0.28 mM Hg(II)/4 to 370 ppm Hg(II) at 25, 75 and 150 °C). Åkesson et al. (1994) used EXAFS and theoretical calculations to demonstrate that the Hg(II) complexes $HgCl_2(aq)$, $HgBr_2(aq)$ and $Hg(CN)_2(aq)$, which may exist in specific geochemical environments, all have a linear geometry.

3.8. Platinum group elements (PGE)

Palladium is the most mobile PGE element in geofluids (Barnes and Liu, 2012; Cabral et al., 2012; Reith et al., 2014), and consequently it is the best studied PGE in terms of hydrothermal geochemistry. H_2O, Cl^-, and HS^- are the most likely ligands for Pd in crustal fluids. Palladium exists in divalent form in aqueous fluids, and Pd(II) has a strong tendency to form square planar complexes. At room temperature, the aqua Pd(II) ion has 4 H_2O in square planar geometry at 2.0 Å, with a further two axial oxygen atoms at 2.7–2.8 Å forming a disordered 'meso shell' (Bowron et al., 2012; Hofer et al., 2007). It is notable that at elevated temperature this axial hydration shell no longer exists, and at 125 °C the Pd(II) aqua ion has the square planar structure ($Pd(H_2O)_4^{2+}$, Mei et al., 2015a), in accordance with the dehydration trend with increasing temperatures for the aqua ions of transition metals. Available XANES, EXAFS and ab initio MD simulations confirm that the complexes likely to account for Pd mobility in geofluids share a square planar geometry (e.g., $Pd(H_2O)_4^{2+}$; $PdCl_3(H_2O)^+$; $PdCl_4^{2-}$; and $Pd(HS)_4^{2-}$; Bazarkina et al., 2014; Boily and Seward, 2002; Boily et al., 2007; Mei et al., 2015a; Seward and Driesner, 2004).

The formation constants ($\log\beta_n$) for Pd(II) chloride complexes ($PdCl_n^{2-n}$) up to 300 °C and the Pd solubilities in chloride brines predicted by different groups are in reasonable agreement (predicted solubilities within one order of magnitude; Tagirov et al., 2013; Wood et al., 1992). The situation is much worse for Pd(II)-bisulfide complexes. Different groups proposed different predominant Pd–HS species ($Pd(HS)_2(aq)$, $Pd(HS)_3^-$; Gammons and Bloom, 1993; Pan and Wood, 1994; Tagirov et al., 2013), and consequently, calculated Pd solubilities in sulfur-rich solutions vary by several orders of magnitudes. Mei et al. (2015a) recently conducted ab initio MD simulations to predict the speciation of Pd–Cl and Pd–HS complexes at 300 °C. This study confirmed the square planar geometry and provided formation constants for major Pd(II)–Cl and Pd(II)–HS complexes. The predicted formation constants of Pd(II)–Cl complexes are within 0.1–1 order of magnitude of the recent experimental study of Tagirov et al. (2013). The MD simulations also strongly indicate that the square planar $Pd(HS)_4^{2-}$ complex predominates in HS^--rich hydrothermal fluids, whereas previous experimental studies neglected this species. Indeed, the absence of $Pd(HS)_4^{2-}$ in the interpretation of experimental data (Tagirov et al., 2013; Wood et al., 1992) posed an interesting (geo)chemical conundrum, since the $PdCl_4^{2-}$ complex is acknowledged by all studies to be the most important complex in chloride brines (review in Bazarkina et al., 2014). Modelling of Pd solubility in chloride- and sulfur-rich hydrothermal fluids based on the thermodynamic properties from MD simulations demonstrated that Pd is mainly carried as the $Pd(HS)_4^{2-}$ hydrosulfide complex at neutral-alkaline and reduced (pyrite/pyrrhotite stable) conditions, and as the $PdCl_4^{2-}$ chloride complex at acidic and oxidised conditions (Mei et al., 2015a).

Platinum. Pt(II) and Pt(IV) are the two oxidation states of Pt in crustal fluids. Pt(IV) species (e.g., octahedral $PtCl_6^{2-}$ and $PtCl_5(OH)^{2-}$, Spieker et al., 2002) are considered only important in oxygenated Cl-rich brines at low temperatures (Gammons, 1996), and Pt(II) chloride and bisulfide complexes are very similar to those of Pd(II), except that the Pt solubility is substantially lower than Pd (Gammons, 1996, Wood et al., 1994, Barnes and Liu, 2012). Hydrosulfide complexes are predicted to be responsible for Pt transport in typical hydrothermal fluids. Room temperature EXAFS data show that the hydrated Pt(II) ion has four water molecules at a Pt–O distance of 2.01(2) Å, and one or two weakly bonded axial waters at a Pt–O distance of 2.39(2) Å (Jalilehvand and Laffin, 2008). Since $PtCl_2(s)$ contains square planar $[PtCl_4]^{2-}$ moieties, in hydrothermal fluids Pt species should have a similar square planar structure as Pd, and differences among the solubilities of both metals are related to the energetics of the respective minerals.

Other PGE elements. Compared to Pd and Pt, hydrothermal experimental studies for other PGE elements are scarce and mainly done by one research group in KCl solutions. Xiong and Wood (1998) measured Os solubility in KCl solutions at 400 and 500 °C and 800 bar, and found that Os(II) chloride complexes are responsible for the observed Os solubility. Most Os(II) coordination compounds have a distorted octahedral geometry. The preliminary experimental studies of Xiong and Wood (1999, 2001) suggest that tetravalent Re(IV) is the main oxidation of Re in hydrothermal fluids, and that the predominant Re species are $Re(IV)Cl_4^0$ at 400 °C in 0.5–1 m KCl, and $ReCl_3^+$ at 500 °C in 0.5–1.5 m KCl brines. Structural data are not yet available for these species; in solids, the $ReCl_4$ moiety exists in square planar coordination (e.g., in $Cs_2Re_2Cl_8(H_2O)(s)$; Cotton and Hall, 1977) or square pyramidal $[ReCl_4O]$ (e.g., in $ReOCl_4(s)$; Edwards, 1972), although the octahedral $[ReCl_6]$ moiety is most common.

3.9. Gallium

Gallium exists predominantly in the trivalent oxidation state. The low solubility of Ga(III)-oxyhydroxide phases such as α-GaOOH(s) at $pH_{25\,^\circ C}$ 3–8 results in the enrichment of Ga in the weathering environment, for example in bauxites. The $Ga(H_2O)_6^{3+}$ aqua ion is octahedrally coordinated (Da Silva et al., 2009; Lindqvist-Reis et al., 1998; Wood and Samson, 2006), while in solutions with $pH_{25\,^\circ C} \geq 5$ there is one dominant complex: tetrahedral $Ga(OH)_4^-$ (Diakonov et al., 1997; Radnai et al., 2014). Radnai et al. (2014) found no experimental evidence for octahedral $Ga(OH)_6^{3-}$. It is generally agreed that hydroxide is the predominant ligand responsible for Ga hydrothermal transport; $Ga(OH)_4^-$ has a substantial field of predominance over the 25–400 °C range, and $Ga(OH)_4^-$ is still predominant at $pH_{300\,^\circ C}$ values greater than ~5 (Benezeth et al., 1997; Diakonov et al., 1997; Tarnopolskaia et al., 2016; Wood and Samson, 2006). Using in situ XAS spectroscopy (25 to ~400 °C, 300 bar), Da Silva et al. (2009) showed that Ga solubility increases at elevated temperature (from ~300 °C) due to the formation of tetrahedral $Ga(III)Br_n^{3-n}$ complexes ($n = 2$–4) in acidic solutions with Br:Ga ratios of 3 (0.017 and 0.17 mol/l $GaBr_3$). Gallium(III) also forms comparatively strong complexes with fluoride (Wood and Samson, 2006). Woodward and Nord (1956) report Raman spectroscopic evidence for the existence of the tetrahedral $GaCl_4^-$ complex in a 6.3 M HCl solution at room temperature. Recently, Tarnopolskaia et al. (2016) showed that $GaCl_4^-$, probably with tetrahedral geometry, can predominate in mildly acidic solutions at 300–400 °C and a_{Cl^-} as low as 0.1; the only other Ga(III) chloride complex detectable in their solubility experiments at 350 °C was $GaCl_3(aq)$. Nekrasov et al. (2013) show experimentally that appreciable Ga concentrations can be transported in HCl-bearing water vapour, and that this transport occurs as a result of the formation of the $GaOHCl_{2(g)}$ and $Ga(OH)_{3(g)}$ gas species.

3.10. Indium

Indium is recovered from hydrothermal ore deposits, where it occurs as In-minerals and as traces in base metal sulfides such as sphalerite (Cook et al., 2011, 2012; Schwarz-Schampera and Herzig, 2002). In chloride-free hydrothermal solutions, In(III) is soluble as an octahedral aqua-complex, with a constant In–O distance of 2.14(1) Å. The in situ XAS studies of Narita et al. (2014) (room temperature) and Seward et al. (2000) (25–250 °C) show that octahedrally coordinated complexes ($[InCl_n(H_2O)^{6-n}]^{3-n}$, $n \geq 4$) are present in HCl-solutions at room temperature, with In–Cl and In–O distances of 2.40 and 2.13 Å, respectively. The octahedral $[InCl_6]^{3-}$ complex is dominant at 10 M HCl. With increasing temperature to 350 °C (saturated vapour pressure), the complex geometry becomes predominantly tetrahedral with the formation of $InCl_4^-$ having an In–Cl distance of 2.37 Å (Seward et al., 2000).

3.11. Thallium

Thallium exhibits both lithophile and chalcophile behaviours; for example it can substitute for K and Rb in potassium feldspar, but also forms numerous hydrothermal sulfide and sulfosalt minerals. Thallium is recovered primarily as a by-product of Zn smelting (Xiong, 2007), but large concentrations can form in volcanogenic hydrothermal deposits (e.g., Allchar, Macedonia; Amthauer et al., 2012). The structure of the hydrated Tl(I) aqua ion, which is present in acidic solutions, is difficult to define, as it is strongly affected by the lone electron pair ($d^{10}s^2$ electronic structure; Persson, 2010). EXAFS and ab initio MD studies indicate a 2 + 2 coordination for the aqua ion, with two H_2O at ~2.73(2) Å and about two more at 3.18(6) Å (Persson et al., 2002; Vchirawongkwin et al., 2007). Bebie et al. (1998)'s UV–vis study of the Tl(I)–NaCl–HCl system to 200 °C provides the only experimental data of Tl complexing at elevated temperature, and concludes that TlCl(aq) is the main Tl species in ore fluids; they find evidence for $TlCl_2^-$, $TlCl_3^{2-}$, and with lower confidence, $TlCl_4^{3-}$. Based on extrapolations from room-temperature data, Xiong (2007) suggest that Tl(HS)(aq) could be an important species in near-neutral, reduced-sulfur bearing fluids.

3.12. Germanium

Germanium is extracted commercially from coal seams and Zn (i.e., sphalerite) concentrates; in both cases Ge is enriched via hydrothermal processes (Cook et al., 2015; Dai et al., 2015). Germanium is an element of low crustal abundance; most Ge is found at sub-ppm-level in silicate minerals, where tetrahedral $[Ge(IV)O_4]^{4-}$ substitutes for $[Si(IV)O_4]^{4-}$ tetrahedra. Ge can also behave as a chalcogenide element, forming discrete Ge-sulfide minerals or in solid-solution in sulfides such as sphalerite (Cook et al., 2015; Dutrizac et al., 1986; Melcher, 2003).

The two stable oxidation states for Ge in aqueous solutions are Ge^{2+} and Ge^{4+}. Ge^{4+} is present in all known minerals where the Ge oxidation state can be established unambiguously (Belissont et al., 2016; Cempirek and Groat, 2013; Cook et al., 2015), although Bonnet et al. (2014) recently provided the first XANES spectroscopic evidence for the presence of some Ge^{2+} in Ge-rich sphalerite from a MVT deposit. Divalent Ge typically occurs in triangular pyramidal coordination in oxide and halogenide compounds, with a stereochemically active lone electron pair oriented opposite to the triangle of anions, similar to As^{3+} (Cempirek and Groat, 2013). Ge^{2+} is stable in aqueous solutions at room temperature (Vanýsek, 2011), and complexing and high temperatures may increase the relative stability of the Ge^{2+} oxidation state in hydrothermal solutions (e.g., compare with Te; Grundler et al., 2013), but its geological relevance remains to be assessed.

Currently, Ge is assumed to be transported in the tetravalent state in hydrothermal fluids; the main species is germanic acid, $Ge(OH)_4$(aq), and its dissociation products. Pokrovski et al. (2005b) characterised the coordination of Ge(IV) in a 0.04 m Ge(IV) solution at 400 bar from 20 to 450 °C, and found that a complex with 4 ± 0.3 oxygen atoms at 1.75(1) Å, consistent with a tetrahedral structure for the $Ge(OH)_4$(aq) complex, was present over the whole temperature range. The constancy of the $Ge(OH)_4$(aq) structural parameters over the wide temperature and fluid-density range is consistent with the strong covalent character of the Ge–(OH) bonds (Pokrovski et al., 2005b), and with $Ge(OH)_4$(aq) being analogous to $Si(OH)_4$(aq). Halide complexes, and in particular fluoride complexes may also play a role (Wood and Samson, 2006). These halide complexes display octahedral structures at room temperature (e.g., $GeF_4(H_2O)_2$(aq); Buslaev et al., 1969), but their stability and geometry under hydrothermal conditions are yet to be determined.

3.13. Tin

Tin is mainly mined from cassiterite ($Sn(IV)O_2$) deposited from granite-related, high-temperature magmatic hydrothermal fluids (e.g., skarn and greisen). Sn(II) and Sn(IV) are considered to be the major oxidation states of Sn in natural fluids. Speciation calculations suggest that Sn(IV) complexes have limited importance for geochemistry: solubility of Sn(IV) complexes is low at low temperature, whereas at high temperature (≥300 °C) Sn(II) complexes are predicted to predominate under most geologically relevant conditions (Jackson and Helgeson, 1985; Pabalan, 1986; based on theoretical extrapolation from room temperature data).

At room temperature, Sn(IV) forms octahedral complexes with water and halide ions ($[SnX_n(H_2O)_{6-n}]^{(4-n)}$; x = Cl, Br; n = 0–6; Taylor and Coddington, 1992) in dilute acidic aqueous solutions. In alkaline solutions, $[Sn(OH)_6]^{2-}$ appears to be predominant. The in situ EXAFS study of Sherman et al. (2000b) indicated that octahedral $SnCl_6^{2-}$ (Sn–Cl distance of 2.39 Å) is the only Sn(IV) complex present in solutions containing 0.11 M HCl and 2.0 M NaCl between 25 and 250 °C.

X-ray scattering and EXAFS measurements supported by ab initio MD show that the Sn(II) aqua ion possesses a stereochemically active electron lone pair, and displays a highly asymmetric hydration sphere consisting of three, or possibly four, water ligands at a distance of 2.33–2.34 Å in a distorted trigonal pyramidal arrangement with the lone electron pair occupying the remaining position (Yamaguchi et al., 1982; Lim et al., 2009). The aqua ion is stable only in highly acidic, halide-free solutions; chloride, fluoride and hydroxyl species are expected to be the key species in hydrothermal solutions (Jackson and Helgeson, 1985; Kovalenko and Ryzhenko, 1997; Kovalenko et al., 1992). In most acidic hydrothermal brines, the chloride complexes of Sn(II) are expected to predominate (Jackson and Helgeson, 1985). Mössbauer spectroscopic studies conducted on frozen aqueous solutions of Sn(II) suggest the presence of SnX_3^- (X = F, Cl, Br) with a pyramidal geometry due to the presence of a sterically active electron pair (Cheng et al., 1981, 1984; Hsu et al., 1984). However later experimental studies reported conflicting information about the predominant Sn(II) species in hydrothermal brines. Wilson and Eugster (1990)'s solubility experiments found $SnCl^+$ and $SnCl_2$(aq) to be important at 400–700 °C; in contrast, Taylor and Wall (1993) interpreted their cassiterite solubility in NaCl and KCl solutions at 700–800 °C and 2 kbar using $SnCl_2$(aq), as well as a suite of mixed ligand complexes charge-balanced with K^+ and Na^+, such as $NaSnOHCl_2$(aq) and $NaSnCl_3$(aq). At lower temperatures (T < 400 °C), the cassiterite solubility study by Pabalan (1986) suggests that the chloride complexes $SnCl^+$, $SnCl_2$(aq), $SnCl_3^-$ and $SnCl_4^{2-}$ predominate in acid and moderately oxidised brines. Sherman et al. (2000b)'s in situ EXAFS study shows that in solutions with 0.5 and 2.5 m Cl_{tot}, the average Cl number around Sn(II) increases from 3.4 to 3.9 as temperature increases from 25 to 350 °C, indicating that $SnCl_4^{2-}$ (Sn–Cl distance ~2.47 Å) becomes important at higher temperature. Muller and Seward (2001)'s UV–vis study also found that Sn^{2+}, $SnCl^+$,

$SnCl_2(aq)$, $SnCl_3^-$ and $SnCl_4^{2-}$ are present at room temperature, but $SnCl_3^-$ was the highest order species at 300 °C. Using ab initio MD simulations, we found that the $SnCl_4^{2-}$ complex is unstable to dissociation, and that the dominant complex in 6 m NaCl and 350 °C is $SnCl_3^-$ (Sherman, unpublished data). There is a strong correlation between the Debye-Waller factor and coordination number when modelling EXAFS; consequently, it can be very difficult to distinguish between 3 and 4-fold coordination.

3.14. Lead

Lead displays the oxidation states II and IV as expected for p block elements; in nature, Pb(IV) is limited to rare microenvironments (e.g. radiogenic Pb; Kramers et al., 2009). Lead is mobile in hydrothermal systems, and is mined from hydrothermal deposits, where it is present mainly as galena, PbS. With a large atomic radius, Pb(II) is a weak Lewis acid with an electron lone pair. EXAFS data show that the Pb(II) aqua complex is 6-coordinated in a hemidirected fashion at room temperature (Persson et al., 2011), with Pb–O bond lengths between 2.54(1) and 2.908(4) Å.

In low temperature fluids (25–170 °C), Pb predominately complexes with chlorine (e.g., Lukanin et al., 2013; Sverjensky, 1986; Yardley, 2005). Yet, there are not many experimental measurements on the Pb(II)-chloride system. The most pertinent is the study by Seward (1984), which provides formation constants for Pb(II)-chloride complexes up to 300 °C based on in situ UV–vis measurements of $PbCl_2$–NaCl–HCl solutions containing 0.0012 to 3.223 m Cl_{tot}. This study identified five predominant Pb species at 25 °C: $PbCl_n^{2-n}$ (n = 0–4). Based on a sudden decrease in ΔH^0 for the stepwise formation of $PbCl_3^-$ at 25 °C, Seward (1984) suggest that $PbCl_3^-$ and $PbCl_4^{2-}$ share a tetrahedral geometry, while $PbCl^+$ and $PbCl_2(aq)$ are octahedral. At 300 °C the predominant species were $PbCl^+$, $PbCl_2^0$, and $PbCl_3^-$, and all species were assumed to be tetrahedral-like. Recent work by our team Rae et al. (2015) suggests that $PbCl_2(H_2O)(aq)$ is the limiting species at high T (400 °C) in a salty solution (10 m LiCl), consistent with ab initio MD calculations that suggest a highly disordered trigonal pyramidal geometry affected by a stereochemically active electron lone pair (see e.g., Bi(III) below) rather than tetrahedral geometry for these Pb(II) chloride complexes.

3.15. Arsenic, antimony and bismuth

The Group V elements As, Sb and Bi have mixed characteristics from metalloid (As) to mainly metallic (Bi). All occur predominantly in trivalent form in crustal fluids, and their coordination chemistry is influenced by the presence of a lone electron pair in this oxidation state. For all three elements, the neutral $M(OH)_3(aq)$ species, where the three oxygen atoms are located on the corners of a triangle with the metal above the plane, is an important complex in natural fluids. All three elements form abundant hydrothermal deposits and also have close relationship with the formation of hydrothermal Au deposits (pathfinder elements).

Arsenic exists in +5 and +3 oxidation states in geofluids; As(II) and anionic forms are found in solids (Deditius et al., 2008; Qian et al., 2013). As(V) is mostly present in the surface/near surface environment, forming tetrahedral hydroxyl complexes with a very rigid geometry (Brugger et al., 2007b; James-Smith et al., 2010; Testemale et al., 2011). Under hydrothermal conditions, As(III) is the predominant form of As in crustal fluids (James-Smith et al., 2010; Pokrovski et al., 2002; Testemale et al., 2004). Thermodynamic calculations (Ballantyne and Moore, 1988) and solubility and spectroscopic experiments (Pokrovski et al., 2002; Testemale et al., 2004; Zakaznova-Herzog et al., 2006) suggest that $As(OH)_3(aq)$ is the dominant aqueous species over a wide range in pH (0–8) and temperature (20–300 °C) in low- and high-density hydrothermal fluids. XAS data for the $As(OH)_3(aq)$ complex show a trigonal pyramidal geometry (Fig. 11), with a nearly constant geometry over the temperature range 30 to 500 °C at pressures of 250 and 600 bar, confirming the strong covalent bonding of As–O (Testemale et al., 2004).

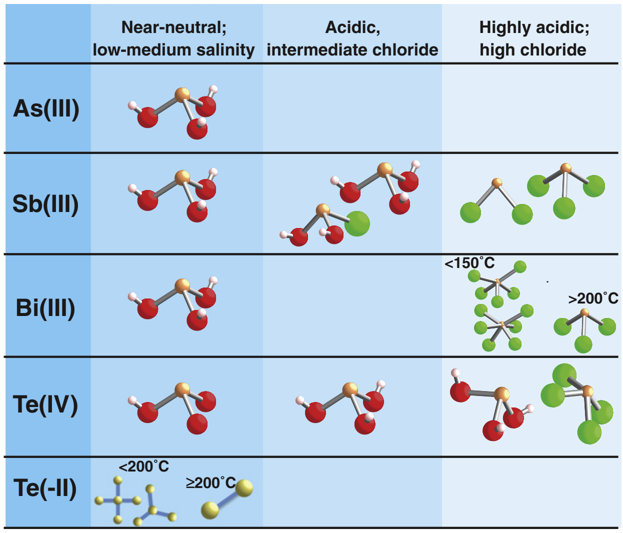

Fig. 11. Coordination chemistry of As(III), Sb(III), Bi(III), Te(IV) and Te(−II) in S-poor hydrothermal fluids.
Data sources: Brugger et al. (2012); Etschmann et al. (2016); Pokrovski et al. (2006); Testemale et al. (2004); Tooth et al. (2013). Metals are in yellow/orange, oxygen atoms in red, hydrogen atoms in pink, and chloride ions in green.

As reviewed in James-Smith et al. (2010), As(III) chloride and bisulfide complexes may be important in some hydrothermal systems, but these complexes remain poorly constrained and their coordination chemistry is unknown. Mironova et al. (1983) concluded that the dimeric species $As_2S_4^{2-}$ and $HAs_2S_4^-$ are the predominant As species in equilibrium with orpiment to 150 °C, in what appears to be the only study of As(III) bisulfide complexing at elevated temperature. Simon et al. (2007) observed an increase by a factor of 2.5 of the partitioning of As into the vapour for a melt-vapour assemblage at high temperature (800 °C) and pressure (120 MPa) in S-bearing systems relative to the S-free system, and concluded that As is transported as arsenious acid in S-free, low-salinity magmatic vapour, but that As–S species probably formed in the vapour phase in the S-bearing experiments. Surprisingly, there are no thermodynamic properties available for any As(III) chlorocomplex, and Pokrovski et al. (2002) found As chloride gaseous complexes to be negligible in the presence of HCl (up to 0.5 mol kg^{-1} of vapour) up to 500 °C.

Antimony is highly mobile in hydrothermal fluids (Tooth et al., 2013); this leads to the formation of hydrothermal Sb deposits (mainly antimonite, Sb_2S_3) at relatively low temperatures (Pavlova and Borovikov, 2010; Wilson et al., 2007). Similarly to As, Sb exists mainly as Sb(III) and Sb(V) in geochemical environments (Filella et al., 2002). While Sb(V) species are present under ambient conditions, Sb(III) is the prevalent form of Sb in hydrothermal fluids at elevated temperatures (e.g., Oelkers et al., 1998).

At ambient temperature, Sb(V) mainly exists as hydroxide ($Sb(OH)_5(aq)$ and $Sb(OH)_6^-$; Accornero et al., 2008) and organic complexes (Tella and Pokrovski, 2008), with all these species having an octahedral geometry (Tella and Pokrovski, 2008). Sherman et al. (2000a) conducted an EXAFS study for Sb(V) in sulfide solutions at 25–300 °C, and suggested that tetrahedral $Sb(HS)_4^+$ is stable below 150 °C; tetrahedral mixed-ligand hydroxide-bisulfide complexes predominate above 150 °C; and polyatomic clusters become significant above 250 °C. These authors also found no Sb(V) chloride complexation in 0.2 m NaHS + 0.06 m NaOH + 1 m NaCl solutions.

Experimental studies have investigated the solubility of Sb(III) minerals and speciation of Sb(III) in hydrothermal fluids, focusing on the

Sb–Cl, Sb–S and Sb–OH systems. In chloride solutions, $SbCl_n^{n-3}$ complexes (n up to 5–6) may form in highly acidic solutions (review by Filella et al., 2002). Oelkers et al. (1998)'s EXAFS study shows that for a 0.1 M $SbCl_3$ + 2.29 M HCl solution, the average number of Cl ligands increases from 2.6 to 2.9, and bond distances decrease from 2.42 to 2.38 Å with increasing temperatures from 25 to 250 °C. Pokrovski et al. (2006)'s more detailed EXAFS study suggested that $SbCl_2^-$ and $SbCl_3(aq)$ exist in strong acidic solutions (~3.5 m HCl), with the former having a distorted linear structure, and the latter being pyramidal (Fig. 11). Mixed hydroxyl-chloride complexes (such as pyramidal $Sb(OH)_2Cl(aq)$ and $Sb(OH)_3Cl^-$) predominate in less acidic (pH > 2–3) Cl-bearing solutions. Pokrovski et al. (2006) concluded that these species play only a minor role in natural hydrothermal fluids relative to hydroxide and sulfide species. Pokrovski et al. (2008) measured the partitioning of Sb(III) between liquid and vapour in H_2O–NaCl–HCl solutions, and suggested that $Sb(OH)_2Cl(aq)$ predominates in both vapour and liquid phases.

Antimony sulfide complexes are thought to be important in natural waters (Mosselmans et al., 2000). There are some studies at room temperature (reviewed by Filella et al., 2002), but few in situ studies are available on the speciation of Sb in S-bearing solutions at elevated temperature, and they are not conclusive due to the complexity of the speciation. The thermodynamic properties for Sb(III) sulfide species are mainly based on the early solubility studies (Krupp, 1988b; Spycher and Reed, 1989). An ab initio study (Tossell, 1994) calculated the structures and vibrational spectra of Sb(III) sulfide species, and found $SbS_2(SH)^{2-}$, $SbS(SH)_2^-$, and $Sb_2S_2(SH)_2(aq)$ at lower temperature, consistent with the Raman study of Wood (1989); mixed ligand species such as $Sb_2S_2(OH)_2$ become stable at elevated temperatures. Mosselmans et al. (2000) conducted an EXAFS study of Sb in bisulfide solutions up to 200 °C. They found oxidation of Sb(III) to Sb(V) during dissolution of stibnite in some solutions, which made data interpretation challenging. In summary, available data indicate that Sb is mainly transported as Sb(III) sulfide and hydroxide complexes in natural hydrothermal fluids typical for ore formation (200–350 °C, weak acid to weak alkaline fluids); however the exact stoichiometry and structures of the species remain to be determined.

Bismuth. Many reasons have been invoked for explaining the common association among Bi and Au in hydrothermal deposits, including Au-scavenging by Bi–(Te)-rich metallic melts (Cockerton and Tomkins, 2012; Tomkins and Mavrogenes, 2002; Tooth et al., 2011, 2013; Tormanen and Koski, 2005); co-enrichment in low-density magmatic fluids and vapours (Henley et al., 2012); and similar geochemical behaviour and precipitation mechanisms (Ciobanu et al., 2009; Grundler et al., 2013; Skirrow and Walshe, 2002). As demonstrated by Tooth et al. (2011), in some cases modelling gold grades can be achieved by modelling the precipitation of specific Bi-phases (e.g., Bi-melt versus bismuthinite).

Hydroxy complexes (mainly $Bi(OH)_2^+$ and $Bi(OH)_3(aq)$) with trigonal pyramidal structures are the most important Bi-complexes in geofluids. Polynuclear oxy-hydroxy-complexes exist in concentrated Bi-solutions at room-T, but have low thermal stability (Brugger et al., 2014). Bi(III) chloride and Bi(III) bisulfide complexes may be important in some settings, but their nature and stability remain poorly constrained (Kolonin and Laptev, 1982; Skirrow and Walshe, 2002). Bi(III) chloride complexes are expected to account for Bi mobility in acidic brines, and Etschmann et al. (2016) recently showed that Bi(III) most likely exists as a mixture of $BiCl_5^{2-}$ and $BiCl_6^{3-}$ (Fig. 11). The number of Cl coordinated to Bi(III) decreases with increasing temperature; at around 200 °C and above, Bi(III) is coordinated to three Cl atoms, most probably in trigonal pyramidal fashion (Fig. 11).

3.16. Selenium, tellurium (and polonium)

The Group 16 metalloids Se and Te are primarily recovered from anode slimes generated in the electrolytic refining of Cu. Selenium and Te can be enriched in hydrothermal deposits, where they can form selenide and telluride minerals (Se^{2-}/Te^{2-}), or substitute for S in major sulfide minerals (Simon and Essene, 1996). Selenium minerals are abundant in some epithermal deposits, skarns, uranium deposits, and black shales (Xiong, 2003), and Te minerals are most prominently associated with Au in epithermal deposits. Both Se and Te display a range of oxidation states in aqueous fluids, from anionic forms (selenide and telluride; polyselenide and polytelluride, e.g. Te_2^{2-}) to cationic forms, most prominently selenite/tellurite(IV) and selenite/tellurate(VI) (Grundler et al., 2008). Polonium is chemically similar to tellurium, and it occurs as a product of the ^{238}U, ^{235}U and ^{232}Th decay chains (longest half life of 138.4 days for ^{210}Po, resulting in ~0.8 ppb Po per wt% ^{238}U). To our knowledge, no specific study of Po geochemistry in hydrothermal fluids is available.

Selenium. In the absence of an experimental study of Se speciation in hydrothermal fluids, our understanding of Se transport in geofluids up to 300 °C is based on extrapolations from room temperature using the isocoulombic approach (Akinfiev and Tagirov, 2006; McPhail, 1995; Xiong, 2003; Fig. 12b). The predominance field of HSe^- is bigger than that of HS^-, covering a large portion of the hematite stable area, which implies that selenide (Se^{2-}) species are more important than selenite (SeO_3^{3-}) species in most hydrothermal ore fluids. Based on large angle X-ray scattering, EXAFS and double difference infrared spectroscopy, the selenite and selenate (SeO_4^{3-}) ions have similar structures as the sulfite and sulfate ions at room-temperature (Eklund and Persson, 2014); both have tetrahedral structures, with 4 oxygens in the first shell for selenate, and 3 oxygens for selenite, the fourth position being occupied by a lone electron pair.

Tellurium. Similarly to Se, the bulk of our understanding of Te transport in hydrothermal fluids is based on isocoulombic extrapolations (McPhail, 1995). Tellurium is generally poorly soluble under reducing conditions (sulfide field; Fig. 12). Tellurite complexes are stable close to the hematite/magnetite buffer, leading Grundler et al. (2013) to propose that tellurite complexes ($H_2TeO_3(aq)$, $HTeO_3^-$, and TeO_3^{2-}) account for Te transport in some Te-rich systems (e.g., porphyry-epithermal systems). In situ XAS measurements (Grundler et al., 2013) show that these tellurite complexes share a trigonal [TeO_3] geometry, with the electron lone pair above the pyramid (Fig. 11). In contrast to sulfur, Te can form complexes with halides (metal-like behaviour). The EXAFS study of Etschmann et al. (2016) shows that the square pyramidal [$TeCl_4(aq)$] complex (Fig. 11) occurs in very acidic brines, but this complex is likely to play a minor role in nature.

Reduced Te species such as $H_2Te(aq/g)$ are volatile, partitioning strongly into the vapour upon phase separation; they probably play an important role in the formation of bonanza Au–Te ores in epithermal systems (Cooke and McPhail, 2001; Grundler et al., 2013). Polytelluride species (e.g., Te_2^{2-}) are expected to be an important form of Te in basic fluids at high temperatures (e.g., CO_2-rich fluids; Fig. 12). Brugger et al. (2012) showed that polytellurides are indeed stable to high temperatures (599 °C; 800 bar); branched species are stable at low temperature, and only the Te_2^{2-} dimer remains at high temperature (Fig. 11).

3.17. Rare earth elements, yttrium and scandium

The rare earth elements are well established as petrogenetic indicators for understanding various geological processes, because these 14 elements (La to Lu, often grouped with Y and Sc in geochemistry) have similar electronic structures. All occur in trivalent form in fluids and rocks and behave in a coherent manner through geochemical processes (Lipin and McKay, 1989). Fractionation among REE is mainly a result of their ionic radii, which decreases smoothly from La (1.18 Å for CN = 8; Shannon, 1976) to Lu (0.97 Å), following the so-called 'lanthanide contraction'. The exceptions are Eu and Ce, which can occur as Eu(II) and Ce(IV) under some conditions, and consequently can be used as tracers of redox processes. This approach is particularly successful for magmatic processes. REE and the so-called Eu and Ce anomalies are also commonly used in tracking fluid sources and chemistry in

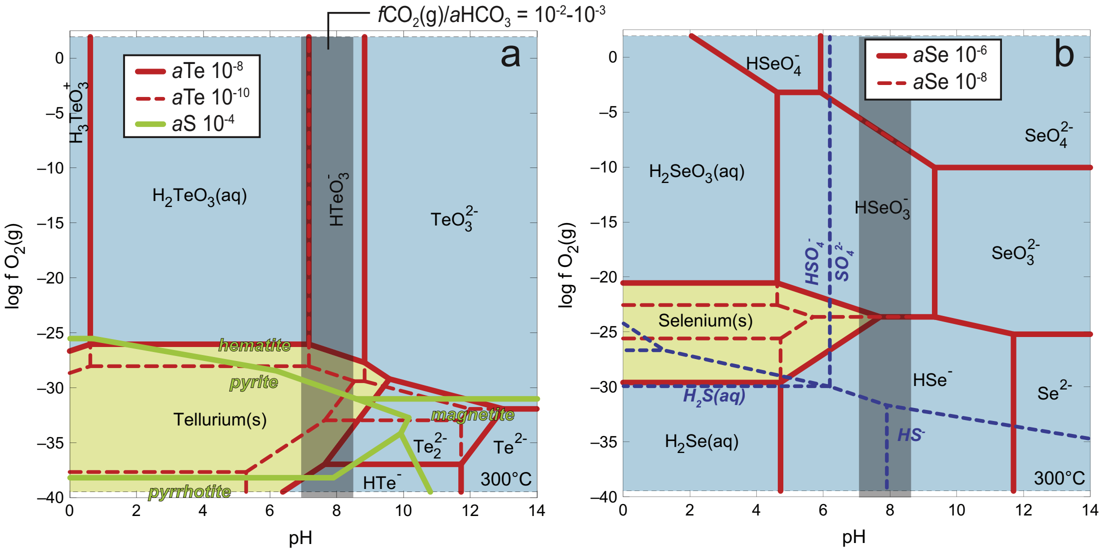

Fig. 12. Mineral solubility and speciation of Te (a) and Se (b) as a function of log $fO_2(g)$ versus pH at 300 °C. Data from Grundler et al. (2013) and McPhail (1995) for Xiong (2003) for Se.

hydrothermal systems, although the controls on the REE composition of hydrothermal minerals are complex (e.g., Brugger et al., 2000, 2008; Migdisov et al., 2016).

Ce(IV) is insoluble at low temperature, and oxidation mediated by surface catalysis (e.g., Mn(IV) minerals such as birnessite) or microbes (Moffett, 1990) results in Ce scavenging from fluids. Ce(IV) is not expected to play a role in hydrothermal transport.

At room temperature, the aqua ions of the light and medium REE^{3+} (La to Dy) display mainly nine-fold coordination (tri-capped trigonal prism; Lundberg et al., 2010; Persson, 2010; Persson et al., 2008; Fig. 13). The decrease in ionic radius of the HREE causes a weakening of the bonding of the capping waters, and a progressive decrease in coordination number to eight for Lu^{3+} at room temperature.

The hydrothermal geochemistry of REE has recently been reviewed by Migdisov et al. (2016). REE(III) fluoride complexes are particularly strong (Migdisov et al., 2009), but due to the low solubility of REE(III) fluoride minerals, the weaker REE(III) chloride complexes are expected to dominate in many hydrothermal environments (Migdisov and Williams-Jones, 2014). REE(III) hydroxide (Pourtier et al., 2010) and sulfate complexes, and possibly carbonate complexes, may also be important although their properties under hydrothermal conditions remain poorly constrained. Until recently, most of our understanding regarding REE hydrothermal geochemistry was based on the semi-empirical extrapolations of Haas et al. (1995). In situ XAS studies of REECl$_3$ solutions (REE = La, Nd, Gd, Yb) as a function of temperature (25–500 °C, P to 2 kbar) confirmed that chloride complexes become more stable with increasing temperatures, but contrary to theoretical predictions the light REE-chlorides are uniformly more stable than the heavy REE counterparts from low to higher temperatures (Anderson et al., 2002; Mayanovic et al., 2002, 2007, 2009a, 2009b). These studies also demonstrate a general decrease in coordination number with increasing temperature, from ~8 to 9 at 25 °C, to 7 at 500 °C. At 500 °C, REECl$_2^+$ and REECl$_3$(aq) are predicted to be predominant in these solutions based on the EXAFS data. These XAS studies are consistent with thermodynamic studies based on UV–vis and solubility experiments (Migdisov and Williams-Jones, 2002, 2006, 2007, 2008, 2014; Migdisov et al., 2008, 2009; Williams-Jones et al., 2012), which confirmed that fluoro- and chloro-REE complexes become more stable with increasing temperatures, with LREE(III) chloride complexes exhibiting uniformly greater stability than HREE(III) chloride complexes from low to high temperatures. These studies also showed that HREE(III) fluoride complexes are more stable than LREE(III) fluoride complexes to ~200 °C, but become less stable than the LREE at higher temperatures. A molecular dynamic study of La(III) in 14 M LiCl solution at room-temperature suggests the predominance of an 8-coordinated LaCl$_2^+$ complex, consisting of two Cl$^-$ and six water molecules arranged in a square antiprism geometry (Fig. 13b) (Petit et al., 2008b). The DFT study of van Sijl et al. (2009) confirmed that fluoride- and chloride-complexes of REE^{3+} are stronger with eight-fold than with nine-fold coordinated lanthanide complexes.

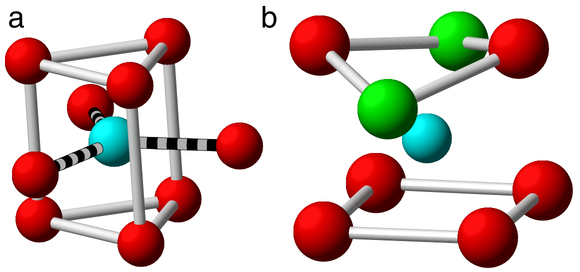

Fig. 13. Coordination chemistry of (a) REE^{3+} aqua ions (Persson et al., 2008) and (b) LaCl$_2^+$ (Petit et al., 2008b). Oxygens (from water molecules) are in red, chloride ions in green, and REE^{3+} in blue.

Yttrium(III) has an ionic radius close to that of Ho(III). The in situ EXAFS study of Ragnarsdottir et al. (1998) showed a decrease in hydration from 9 to 10 to ~8 upon heating from 25 to 340 °C, and did not reveal any chloride complexing (total chloride to 2.53 m). These results are at odds with the room-temperature Raman study of Rudolph and Irmer (2015), which found evidence for an 8-fold, square antiprismatic Y(III) aqua complex, as well as formation of chloride complexes (YCl^{2+}, YCl$_2^+$) at chloride concentrations >0.2 m. The solubility study of Loges et al. (2013) suggests that Y(III) forms higher order fluoride complexes than Ho(III) under similar conditions (dominance of YF$_2^+$ versus HoF^{2+}); such differences can account for the contrasts in the mobility of Y and REE in hydrothermal systems (Bau and Dulski, 1995; Loges et al., 2013).

Wood and Samson (2006) reviewed the hydrothermal geochemistry of *scandium*. Compared to REE^{3+} and Y^{3+}, Sc^{3+} is substantially smaller and appears to form much stronger complexes with ligands such as F$^-$ and OH$^-$ (Gramaccioli et al., 2000). Furthermore, the hydrated Sc^{3+} ion displays an octahedral coordination (Rudolph and Pye,

2000) rather than 8-fold coordination for $HREE^{3+}$. There are no experimental data on Sc geochemistry under hydrothermal conditions, but based on room-T extrapolations, hydroxy complexes and fluoride complexes (e.g., ScF_2^+), probably with octahedral coordination at low-T, are expected to dominate Sc transport in crustal fluids.

The thermodynamical stability of *Europium(II)* is limited in aqueous solution at room temperature (only in neutral to basic solutions, and near $fH_2(g) = 1$ bar). Theoretical extrapolations from room-temperature suggest that the stability of Eu(II) and its chloride complexes increases with temperature, so that Eu(II) is predicted to be the main oxidation state of Eu in aqueous fluids at 300 °C (Sverjensky, 1984). Little is known about the coordination chemistry of Eu(II) in hydrothermal fluids. The room-T EXAFS study of Moreau et al. (2002) concluded that Eu^{2+} occurs as an equilibrium between a predominant $[Eu(H_2O)_7]^{2+}$ and a minor $[Eu(H_2O)_8]^{2+}$ species. Until recently, there was no experimental data on Eu(II) chloride complexing. Based on comparison with transition metals, Haas et al. (1995) predicted that the $EuCl_4^{2-}$ complex is dominant in hydrothermal fluids even at moderate salinities. In solids, Eu(II) forms octahedral $[EuCl_6]$ (Villafuerte-Castrejon et al., 1997) as well as seven-coordinate $[EuCl_7]$ moieties (Masselmann and Meyer, 1998). The recent in situ (T to 400 °C; P 600 bar) XAS experiments by Liu et al. (2016) confirmed both the increasing stability of Eu(II) and the decrease in the total number of ligands coordinated to Eu(II/III) with increasing temperature. However, previous theoretical extrapolations appear to have over-estimated Eu(II)-halide bonding. Liu et al. (2016) found little evidence for complexation between Eu(II) and chloride, even in a 5 m NaCl solution, and could observe Eu(II) halide complexing only in an hypersaline bromide solution (10 m LiBr), with up to 1.3(7) Br bonded to Eu(II) at 400 °C. This may not be unexpected, given the similarity of Eu(II) with the Sr(II) and Ca(II) ions, with respect to ionic radius, charge, and general chemistry; for these ions the limiting Cl complexes are $SrCl_2(aq)$ and $CaCl_2(aq)$, respectively (Liu et al., 2016).

3.18. Uranium and thorium

Uranium. There have been numerous studies on the speciation of U in aqueous solutions at room temperature as a result of the intensive fundamental research related to nuclear waste disposal and remediation of nuclear sites (Burns et al., 2012). Thermodynamic data for many U minerals and aqueous species have been compiled in the Nuclear Energy Agency data bank (Grenthe et al., 1992; Guillaumont et al., 2003; http://www.oecd-nea.org/dbtdb/info/publications/). Yet, data about the speciation and solubility of U in hydrothermal fluids at elevated temperatures relevant for ore deposition and fluid-coolant interactions are scarce, and reactive-transport thermodynamic modelling of U in hydrothermal fluids is mostly based on theoretical extrapolations from room temperature data (Bastrakov et al., 2010; Shock et al., 1997a).

In nature, U exists mainly in the (IV) and (VI) oxidation states (Natrajan et al., 2014). Uranium(VI) complexes are soluble and predominate at moderate to oxidised conditions. Richard et al. (2012) showed that acid brines (pH 2.5–4.5, T to 150 °C) involved in the formation of giant unconformity-type U-deposits contained extremely high U concentrations in the form of uranyl complexes. In contrast, U(IV) compounds display very low solubilities at relatively low temperatures (<300 °C; Fig. 14). A few compounds with U(V) have been described (Burns and Finch, 1999) and U(V) is an important transition state in bio-mediated U reduction (Renshaw et al., 2005), but the role of U(V) in hydrothermal U transport remains unknown. As a result of the strong contrast in solubility between U(IV) and U(VI) minerals, U deposits are associated with redox barriers, and the most abundant U minerals are the U(IV) oxide (UO_{2-x}, uraninite) and U(IV) silicate ($USiO_4$, coffinite). Deposits of U as U(VI) are related to the low solubility of vanadate and phosphate U(VI) minerals (e.g., U in calcrete, Mann and Deutscher, 1978). According to the Hard and Soft Acid Base (HSAB) theory (Pearson, 1963), both U(IV) and U(VI) ions are hard acids and therefore tend to form complexes with hard bases such as fluoride, carbonate, sulfate and phosphate, as well as chloride which is classified as a borderline base; however the predominant species are affected by the availability of these ligands, which is limited by the solubility of minerals such as anhydrite and apatite.

In acidic solutions at room-temperature, U(IV) exists as a spherical cation surrounded by 9–10 water molecules in the first coordination sphere (Frick et al., 2009b; Hennig et al., 2005; Ikeda-Ohno et al., 2009; Moll et al., 1999; Fig. 14). Molecular dynamic simulations suggest that formation of hydroxide complexes results in a decrease in coordination number, although the low solubility of complexes such as $U(OH)_4(aq)$ has so far precluded direct experimental confirmation (Leung and Nenoff, 2012). Hennig et al. (2005)'s EXAFS data show the formation of chloride complexes with up to three Cl^- and a total of 8–9 ligands ($Cl^- + H_2O$). In dilute sulfate solutions, U(IV) forms the USO_4^{2+} complex, which exists both in monodendate and bidentate configurations (Fig. 14b) (Hennig et al., 2007). $U(SO_4)_2(aq)$ predominates in high sulfate solutions, but the number of oxygen around these sulfate complexes cannot be reliably resolved by EXAFS (Hennig et al., 2007), and no data are available at elevated temperature.

In most U(VI)-bearing compounds and solutions, U exists as the linear uranyl oxycation, UO_2^{2+}, in which U is strongly bonded to two oxygen atoms in a linear coordination at an average distance of 1.79(4) Å in solids (Burns, 1999; Burns et al., 1997). The uranyl ion is highly stable, and its reactivity is dominated by ligand exchange at the equatorial sites. At room temperature, EXAFS and theoretical studies indicate that the UO_2^{2+} aqua ion is surrounded by five equatorial waters, forming a pentagonal $UO_2(H_2O)_5^{2+}$ dipyramidal structure (Hennig et al., 2005; Frick et al., 2009a; Ikeda-Ohno et al., 2009; Fig. 15). The original XAS data presented in Fig. 15 show that the linear structure of the uranyl ion (UO_2^{2+}) is maintained in a 0.1 m $UO_2(NO_3)_2$ solution upon heating, but the number of equatorial oxygens decreased to 3–4 at 350 °C due to the replacement of water molecules by two bidentate nitrate ions.

The pentagonal dipyramidal geometry is retained by the uranyl chloride complexes $UO_2(H_2O)_4Cl^+$, $UO_2(H_2O)_3Cl_2(aq)$, and $UO_2(H_2O)_2Cl_3^-$ as well as in fluoride complexes ($UO_2F_n(H_2O)_{5-n}^{2-n}$, n = 3–5; Hennig et al., 2005; Nguyen et al., 2015; Vallet et al., 2001). On the other hand the hydroxide complex $UO_2(OH)_4^{2-}$ has a square bipyramid geometry both in the solid state and in solution (Vallet et al., 2001). Using Raman techniques, Dargent et al. (2013) found that uranyl chloride complexes ($UO_2Cl_n^{2-n}$, n = 0 to 5) exist in 0.3–12 m LiCl solutions over the temperature range 21–350 °C, and provided formation constants for these uranyl-chloro complexes. They also attribute the Raman band at 841 cm^{-1} to an un-identified polyuranyl chloride complex.

Similarly to U(IV), uranyl binds with one or two sulfate groups ($UO_2(SO_4)(aq)$ and $UO_2(SO_4)_2^{2-}$), both complexes occurring as a mixture of mono- and bidentate forms (Hennig et al., 2007; Fig. 14a,b). In carbonate solutions, Ikeda et al. (2007) found that $UO_2(CO_3)_3^{4-}$ predominates in 1.4 m Na_2CO_3 solutions; the carbonate groups form bidentate links to 6 planar oxygens (Fig. 14c). Bailey et al. (2005)'s EXAFS study found that U(VI) monomer species ($UO_2(cit)^-$) form in lower citrate/U ratio (<2) and dimer ($[(UO_2)_2(cit)_2]^{2-}$) in high citrate/U ratio solutions, and there was no detectable coordination change with increasing temperature to 200 °C; beyond this temperature the decomposition of the citrate was observed. Bailey et al. (2004)'s XAS study on uranyl acetate complexes at 25–250 °C identified the UO_2Ac^+, $UO_2(Ac)_2(aq)$ and $UO_2(Ac)_3^-$ complexes, in which acetate most likely forms bidentate links to planar O (Fig. 14d).

At much higher temperatures, Peiffert et al. (1994, 1996) reported U solubility in NaF, NaCl and $NaCO_3$ solutions and fluid-melt partitioning coefficients at 770 °C and 2 kbar. Uranium(IV) carbonate species predominate in reduced fluids (Ni–NiO buffer) and U(VI) carbonate species in oxidised fluids (Fe_3O_4–Fe_2O_3, Cu_2O–CuO buffers). The importance of fluoride complexes is illustrated by the fact that U solubilities were up to 20 times higher in NaF solutions than in NaCl solutions at the same

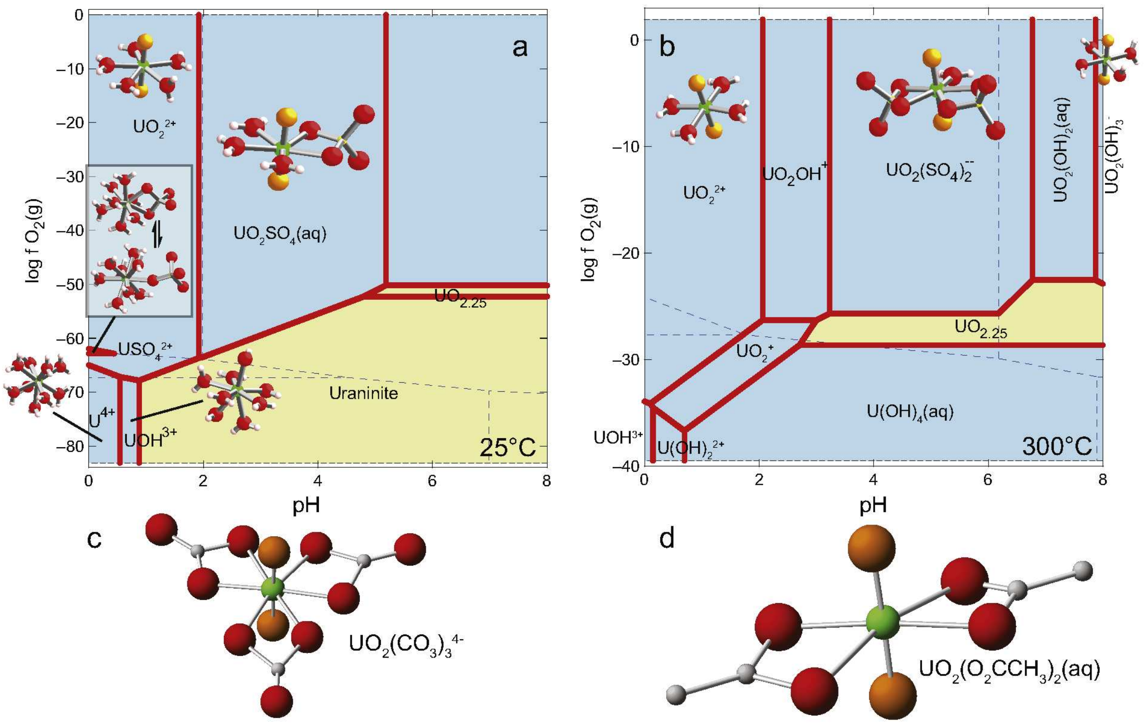

Fig. 14. Mineral solubility and predominant aqueous complexes in the U–O–S system at 25 and 300 °C (a,b), drawn using Geochemist's Workbench (Bethke, 2008). The geometries of the complexes are shown when known. $aSO_4^{2-} = 1$ mmol; $a(\text{U species}) = 10^{-8}$ (~2.4 ppb U). Uranyl oxygens are shown in orange, other oxygens in red, sulfur in yellow, uranium in green. Note that structures shown at 300 °C are based on 25 °C data, except for the UO_2^{2+} ion, which is based on the data presented in Fig. 15. (c,d) Proposed structures of bidentate carbonate and acetate uranyl complexes; atom colors as in (a,b), carbon in grey.
Source of thermodynamic data: Grenthe et al. (1992) and Schock et al. (1997a).

salt concentrations (Peiffert et al., 1996). Recently, Bali et al. (2011) measured the solubility of U and Th under conditions typical of subduction zone fluids (800 °C, 26.1 kbar); similarly they found that U solubility increases with increasing oxygen fugacity and chloride concentrations, and concluded that U exists predominantly as uranyl chloride complexes such as UO_2Cl^+ and $UO_2Cl_2(aq)$ in their experimental solutions, with U^{4+} chloride complexes predicted to be important only below the Fe–FeO redox buffer.

Thorium exists in the tetravalent valence state in rocks and fluids. In general, the coordination chemistry of Th(IV) is similar to that of U(IV). Yang et al. (2002)'s MD simulations found that similarly to U(IV), the Th(IV) aqua ion is surrounded by 9–10 water molecules in the first shell, and around 20 in the second shell, consistent with Moll et al. (1999)'s room temperature EXAFS data (10 ± 1 water molecules at 2.45 Å). Water molecules are replaced by chloride ligands with increasing chloride concentrations (Yang et al., 2002), and the EXAFS data of Moll et al. (1999) show that the ThF^{3+} complex has 1 fluoride and 9 water molecules in the first coordination shell at room temperature. Similarly to U(IV), Th(IV) forms mono- and bi-sulfate complexes at low and high sulfate concentrations, respectively (Hennig et al., 2007). Bali et al. (2011) found that the solubility of Th changes very little with fluid salinity and seems to be also less dependent than U on oxygen fugacity at conditions relevant for subduction zones (800 °C, 26.1 kbar), consistent with a single oxidation state of Th compared to U.

4. Discussion

Coordination chemistry is one of the pillars of inorganic and organometallic chemistry. Yet, the applications of these concepts to geochemistry, and to hydrothermal geochemistry in particular, remain limited. This section discusses the value of this approach to hydrothermal geochemistry in light of the literature review above.

4.1. Metal transport in hydrothermal systems – a view from coordination chemistry

4.1.1. A periodic table for hydrothermal geochemistry

A summary of the main complexes and their coordination geometry relevant for the transport of metals and metalloids in crustal fluids is presented in the form of a Periodic Table in Fig. 16. This Periodic Table highlights some of the key elemental associations typical of hydrothermal environments:

1. The base metals Mn, Fe, Co, Ni, Zn and Cd are characterised by the predominance of octahedral and tetrahedral aqua- and chloride complexes, with tetrahedral species becoming more prominent at high temperatures. Minor elements such as Ga, In and Tl, which often are associated with base-metal sulfide deposits, share a similar trend. Transitions among coordination geometries brought upon changes in temperature and fluid composition (e.g., salinity) can result in fast changes in solubility for these metals (Fig. 6). Fractionation among the metals occurs as the structural transitions take place at different temperatures and salinities. In nature, the geochemical couples Fe/Mn, Co/Ni, and Zn/Cd are often closely associated, due to similar ionic radii and chemistry. The differences in the stability of high order tetrahedral complexes explains some of the fractionation of these elements via hydrothermal transport; i.e. Fe, Co and Zn transition to tetrahedral, Cl-rich complexes at a lower temperature/salinity than their counterparts (Fig. 7).
2. Complexes with low coordination numbers (2- or 3-fold) have a high affinity to low-density vapours and supercritical fluids. The capacity of low-density fluids to carry significant amounts of metals has been recognised over the past decade (e.g., Pokrovski et al., 2005a; Williams-Jones and Heinrich, 2005). The Periodic Table in Fig. 16 shows that metals that have a relatively high affinity for the low-

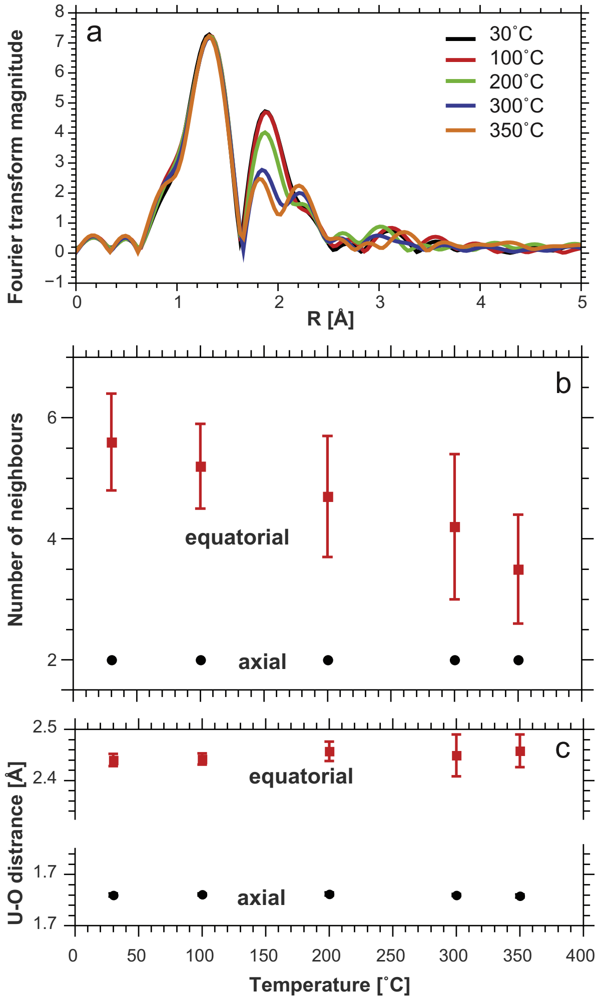

Fig. 15. Dehydration of uranyl aqua complex as a function of temperature. Results of EXAFS fitting on data collected at the FAME beamline, ESRF, on a 0.1 m uranyl nitrate solution (prepared by dissolving $UO_2(NO_3)_2 \cdot 6H_2O$ in deionized water), using the FAME autoclave (Testemale et al. 2005), at a pressure of 250 bar. The data were analysed using the HORAE package (Ravel and Newville, 2005). The decrease of the number of equatorial oxygen neighbors (figure b) corresponds to the progressive replacement of water molecules by 2 bidentate nitrate ions.

density phase, i.e. Cu, Ag, Au and Hg, exist in brines and low-density supercritical fluids as linear complexes with ligands such as water, bisulfide, and chloride. Since low density fluids have a low dielectric constant, neutral complexes are favoured; as a result, water-bearing 'vapours' show a much higher capacity to carry these metals than dry (e.g. CO_2 fluids) systems, due to the formation of first-shell coordination complexes such as $[H_2O–Cu–Cl](aq/g)$ or $[H_2O–Au–HS](aq/g)$. The second-shell hydration of these complexes also plays a critical role in controlling their stability in low-density fluids (Hurtig and Williams-Jones, 2014b, 2015; Liu et al., 2008; Migdisov et al., 2014), and this is related to the open geometry of linear complexes.

3. The metalloids As and Sb together with the metal Bi (and possibly Pb) share a similar coordination geometry characterised by a stereochemically active lone electron pair and the high stability of the neutral $M(OH)_3(aq/g)$ complex. As a result these metals are also soluble in low-density 'vapours' and are often associated with Cu/Au.

Understanding the coordination chemistry of metal complexes under hydrothermal conditions is key to improving the reliability of predictions of reactive-transport models. For example, Etschmann et al. (2011) showed how coordination chemistry constrains the stoichiometry of possible Cu(I) species with ligand such as chloride and thiosulfate, enabling distinction among several different interpretations of the experiments. Mei et al. (2015b) resolved a long-standing controversy about the nature and stoichiometry of Zn(II) chlorocomplexes using a coordination chemistry approach to reinterpret existing, apparently contradictory, solubility data. Mei et al. (2015b) also illustrate the value of ab initio molecular dynamic simulations for understanding hydrothermal reactions; combined with in situ XAS data, these new technologies underpin a paradigm change in hydrothermal geochemistry by enabling the development of sound speciation models for the (re)interpretation of experimental data using an integrated approach. Such sound speciation models also support the creation of more accurate semi-empirical models to predict the stability of aqueous and vapour species over wide ranges in P and T (e.g., Helgeson et al., 1981).

Changes in coordination of metal complexes are driven by changes in physico-chemical parameters of hydrothermal fluids as a result of various geological processes such as fluid mixing, cooling, and mineral–water interactions. In the following sections we will discuss the effects of temperature, pressure, ligand concentration, pH and redox on the coordination change of metal complexes, which in turn can cause rapid changes in mineral solubility, possibly driving phenomena such as ore deposition.

4.1.2. Effects of temperature and salinity

Temperature (e.g., via cooling) and salinity (e.g., via fluid mixing, phase separation) are two key parameters that can result in rapid changes in the coordination of metal complexes. Increasing temperature changes the structure of water and the hydrogen bond network (e.g., Seward and Driesner, 2004), and thus changes the solvation properties of metal ions and the geometry of complexes. For example, Fig. 4 shows a rapid decrease in zircon solubility upon heating to 100 °C, due to the destabilisation of octahedral F-complexes in favour of tetrahedral F–OH-complexes. This phenomenon also is a key driver of the hydrothermal geochemistry of transition metals (Fig. 16). In general, higher temperatures and higher salinities favour tetrahedral over octahedral coordination of ions such as Mn(II), Fe(II/III), Co(II), Ni(II), Cu(II), Zn(II), and Cd(II), as first emphasized by Susak and Crerar (1985). In addition, the tetrahedral complexes show a higher affinity for chloride ligands than the octahedral complexes. In detail, the relative stabilities of the octahedral versus tetrahedral complexes, as well as the affinity for chloride, varies from metal to metal. The element pairs Fe/Mn, Co/Ni, and Zn/Cd are closely associated, due to similar ionic radii and chemistry. However, in these examples, Fe(II), Co(II) and Zn(II) display a greater affinity for the tetrahedral coordination and for chloride, with the fully chlorinated MCl_4^{2-} being a predominant complex over a relatively wide range in temperature and salinity (Fig. 7); in contrast, Mn(II), Ni(II) and Cd(II) usually require higher temperatures/salinities to become fully tetrahedral, and in these cases the fully chlorinated MCl_4^{2-} complex never/rarely become important in crustal fluids.

Fig. 17 illustrates how these differences in coordination chemistry cause fractionation among transition metals in shallow hydrothermal fluids, by looking at the effect on the Ni/Co ratio in pyrite precipitated from a fluid containing 1000 ppm of each of the metals (see figure caption for details). Under the conditions of the simulation, Ni and Co both undergo an octahedral to tetrahedral transition at ~200 °C, which results in sharp changes in the Ni/Fe and Co/Fe ratios. These ratios are also relatively sensitive to the fluid salinity, because of the different affinities of the Ni(II) and Co(II) chlorocomplexes for chloride ions.

Temperature also has a significant impact on the oxidation state of some metals in the fluids. Increasing in situ experimental evidence has shown that for many transition metals with variable oxidation states, lower oxidation states become stable with increasing temperature: for example, Au(III) species are stable at room temperature but are replaced by Au(I) complexes at elevated temperature (Liu et al., 2014; Pokrovski et al., 2014). Cu(II) is predominant in many natural fluid inclusions at room temperature, but reverts to Cu(I) when the fluid inclusions are reheated

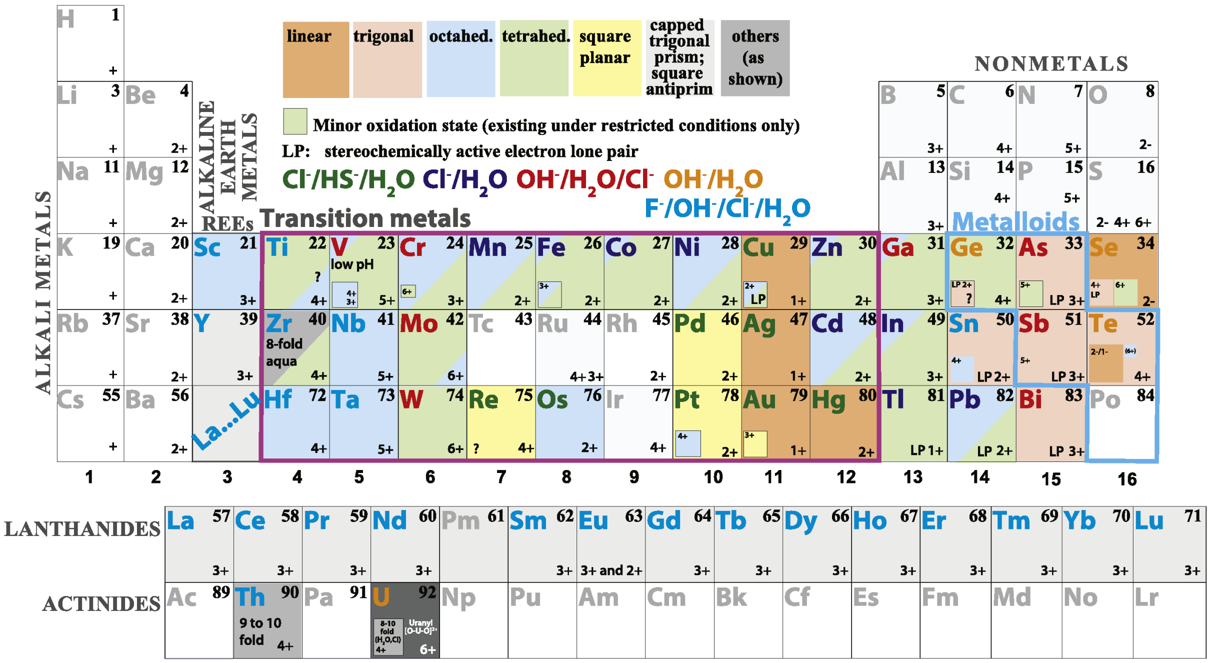

Fig. 16. Coordination chemistry of metals in upper crustal geological fluids derived from the literature review in this study.

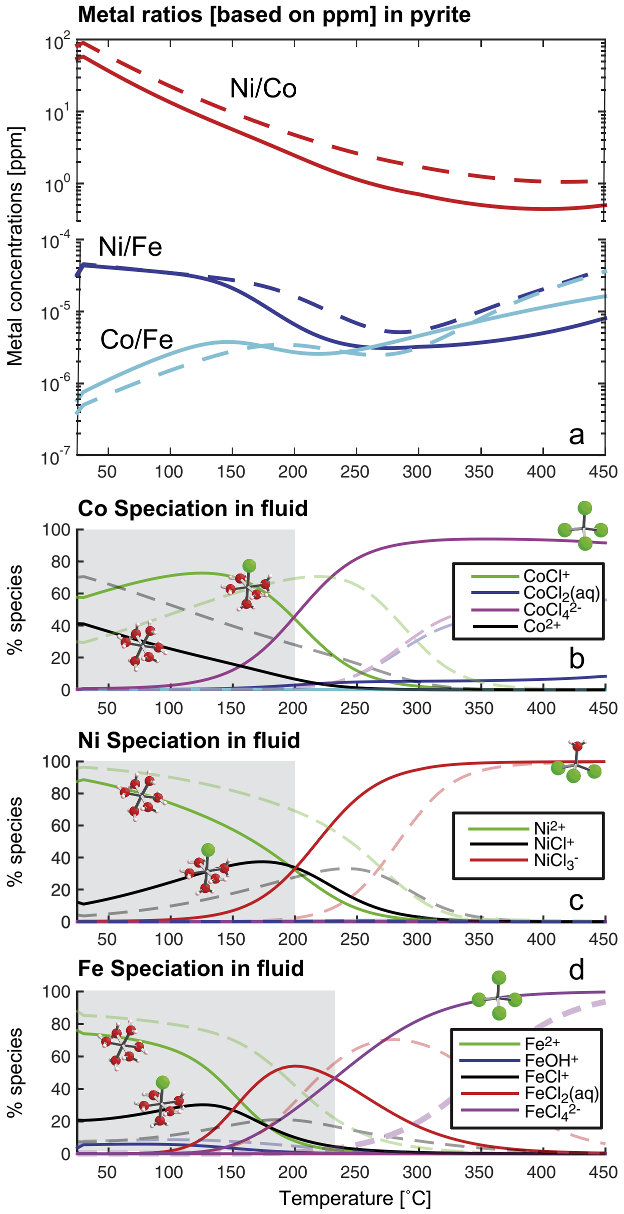

Fig. 17. Calculations of Ni, Co and Fe speciation and solubility in a pyrite-hematite-magnetite assemblage, in solutions with 0.6 m NaCl (~seawater; dashed lines) and 3 m NaCl (solid lines). The pyrite is set to contain 1000 ppm Co and 1000 ppm Ni (Clark et al., 2004). Pyrite, cattierite and vaesite are assumed to form an ideal solid solution. Calculations were conducted using the HCh software (Shvarov and Bastrakov, 1999), assuming ideal solid solution behaviour among pyrite, vaesite, and cattierite.
Sources of thermodynamic properties: cattierite, Robie and Hemingway (1995); vaesite, Gibbs free energy and entropy from Klein and Bach (2009), and heat capacity from Chase (1998).

(Mavrogenes et al., 2002). Synthetic Cu(II) chloride solutions exhibit a similar behaviour upon heating (Brugger et al., 2007a; Fulton et al., 2000a). Europium(II) becomes increasingly stable at high T, whereas Eu(III) predominates at room T (Liu et al., 2016); similarly the stability of Fe(III) in aqueous fluids appears to decrease in favour of Fe(II) with increasing temperature (Testemale et al., 2009a, 2016b).

4.1.3. Effects of pH and redox state

pH is a fundamental parameter that has significant impact on the predominant ligand type and therefore the coordination of metal complexes and mineral solubilities. By controlling the activity of the hydroxide anion (reaction (2)), pH is the key parameter defining the stability of hydroxide complexes.

$$H_2O = OH^- + H^+ \quad (2)$$

A classic example is the 'V' shaped pH-dependence of ZnO solubility in water (Benezeth et al., 2002), with high ZnO solubility in low pH (Zn^{2+} predominant) and high pH ($Zn(OH)_3^-$ predominant) ranges.

For metals such as Au, Ag, Zn, Cu, Pb or Pd, chloride complexes are the predominant species in acidic solutions, and bisulfide complexes more stable in neutral-alkaline solutions (Mei et al., 2013a, 2015a, 2016); in acidic solutions, less HS^- is available for complexing with metal ions:

$$HS^- + H^+ = H_2S(aq) \quad (3)$$

Therefore, in more alkaline solutions, chloride ions have to compete with bisulfide and hydroxide species, and for soft metal ions such as Au^+, Au–HS complexes predominate in such mixed-ligand solutions (Liu et al., 2014). Phillips and Evans (2004) suggested that the high CO_2-contents of ore fluids in many orogenic-type Au deposits reflect buffering of pH in a range optimal for Au transport as bisulfide complexes.

Solution pH also impacts the structure of metal-oxyanion acids. For example, the coordination structure of Mo(VI) complexes changes from tetrahedral molybdate (MoO_4^{2-}) to a series of octahedral species (e.g., molybdic acid, $MoO_3(H_2O)(aq)$) when pH decreases:

$$MoO_4{}^{2-}{}_{\text{tetrahedral}} + 2H^+ + 2H_2O = MoO_3(H_2O)_3(aq)_{\text{octahedral}}, \quad (4)$$

and chloride ligands can replace water in these octahedral species in HCl solutions (Borg et al., 2012). As a result of the large difference in ligand number associated with the change in coordination geometry, reaction (4) results in large changes in mineral solubility.

Redox reactions affect the oxidation state of metals and the nature of some ligands. Since elements with different oxidation states can have very different coordination chemistry (e.g., square planar Au(III) versus linear Au(I); complex Jahn-Teller distorted 4- to 6-fold geometries for Cu(II) compared to linear complexes for Cu(I)), the reactive-transport properties of the different ions can be rather different, and contribute to differences in mineral stability by generating strong changes in solubility across redox interfaces in geological systems (e.g., formation boundaries; fluid mixing). The redox state of the fluid also indirectly affects the coordination chemistry of hydrothermal systems by controlling the nature of the predominant aqueous ligands. Since chloride and sulfur are the major ligands in natural fluids, for many transition metals in more reduced fluids the competition is chloride versus bisulfide species; in contrast, in oxidised fluids the competition is chloride versus sulfate, where chloride species are stronger for 'soft' metals (Au, Cu, Zn…), and sulfate species are stronger for some 'hard' metals such as REE (Migdisov et al., 2016).

4.1.4. Effect of pressure

Seward et al. (1981) reviewed the effect of pressure on metal complexation in aqueous fluids, mainly based upon room temperature experimental data. In the last two decades the accumulation of new experimental and simulation data allow us to better understand the pressure factor. The definition of the Gibbs Free Energy is

$$G(P,T) = U + PV - TS = H - TS; \quad (5a)$$

$$dG = VdP - SdT + \sum_{i=1}^{k} \mu_i dN_i \ (\text{closed system}) \quad (5b)$$

where U is the internal energy, H the enthalpy, S the entropy, and μ_i is the chemical potential of species I with concentration N_i. So the first order effect of pressure is

$$\left(\frac{dG}{dP}\right)_T = V \tag{5c}$$

Increasing the system pressure emphasizes the PV term, and favours smaller total volumes, which affects the geometry of aqueous complexes via several mechanisms:

1) For coordination complexes with a fixed coordination, increased pressure causes a contraction of the bond distances. These effects however are small under crustal conditions; a recent XAS study has shown that for the Zn^{2+} aqua ion ($[Zn(H_2O)_6]^{2+}$), the Zn–O bond distance decreases from 2.078(2) Å to 1.992(7) Å as pressure increases from 1 bar (300 K) to 63.7 kbar (~520 K) (near the liquid-ice coexistence line; Migliorati et al., 2013).
2) Increasing pressure can cause coordination changes, with higher coordination resulting in a lower overall reaction volume. For example:

$$\left[Ni(H_2O)_4\right]^{2+} + 2H_2O = \left[Ni(H_2O)_6\right]^{2+}; \tag{6}$$

$$V_{\left[Ni(H_2O)_6\right]^{2+}} - V_{\left[Ni(H_2O)_4\right]^{2+}} - 2V_{H_2O} < 0$$

In general increasing pressure favours the transition from a tetrahedral to an octahedral structure, as observed using UV–vis spectroscopy for Co(II) chloride complexes up to 6 kbar and 500 °C (Lüdemann and Franck, 1967) and for Ni(II) chloride complexes up to 900 bar and 400 °C (Suleimenov, 2004). Recently, we conducted synchrotron XAS measurements to investigate the pressure effect on Ni(II) chloride and bromide complexes, as well as Zn(II) bromide complexes. We found that increasing pressure (1–1500 bar) causes an increase in the proportion of the 6-fold complexes (octahedral) at the expense of the 4-fold complexes (tetrahedral-like) (Fig. 18a,d). This was particularly well expressed for the XANES spectra of the Zn–Br solutions (Fig. 18d); interestingly, the corresponding EXAFS data show only a very small systematic difference at 200 °C as pressure increases from 200 to 1000 bar (Fig. 18e,f). In contrast, the $NiBr_2$ in 5 m NaBr solution shows a significant difference in the EXAFS data at 350 °C as pressure is increased from 300 to 1500 bar (Fig. 18b,c), which is explained by an increase in the number of octahedral oxygen atoms in the first coordiantion shell (supplementary data).

In general, the effect of pressure is not as significant as that of temperature and salinity on the octahedral–tetrahedral transition (Fig. 7). However, the situation is different for compressible vapours and low-density supercritical fluids, where pressure can cause large changes in solution density, and consequently large changes in the hydration number of metals complexes (e.g., CuCl(aq,g) and AuCl(aq,g); Fig. 19), leading to large changes in mineral solubility over relatively small pressure changes (Hurtig and Williams-Jones, 2014b, 2015; Liu et al., 2008; Migdisov et al., 2014). This effect can control mineral formation in shallow hydrothermal systems (e.g., epithermal-porphyry transition; seafloor exhalative deposits).

3) Increasing pressure enhances the dissociation of metal complexes into ionic species (Seward, 1981). For example, for the reaction

$$CuCl_2{}^- + 2H_2O = Cu(H_2O)_2{}^+ + 2Cl^-, \tag{7}$$

the logarithm of the dissociation constant increases from −5.91 to −3.91 as pressure increases from 0.5 to 5 kbar (Liu and McPhail, 2005). Plots of the dissociation constants for many metal complexes as a function of pressure and temperature compiled in Sverjensky et al. (1997) demonstrate this general trend. Seward (1981) and Seward and Barnes (1997) attribute this to the electrostriction of solvent dipole around the ions. Filipponi et al. (2003) showed using EXAFS that the structure of a RbBr aqueous solution undergoes a dramatic transformation in the 0.5–1 GPa pressure range, involving an increased orientational disorder in the hydration shells around the Rb^+ and, in particular, the Br^- ion. These changes favour the formation of the aqua ion versus complexes at high pressure.

4) In recent years experimental (Pokrovski and Dubessy, 2015a) and theoretical (Sverjensky et al., 2014b) studies have suggested that pressure may have a large effect on the coordination chemistry of metals and metalloids by affecting the speciation of S and C ligands. For example, at high pressure (≥5 kbar), polysulfide ions appear to dominate over the bisulfide and sulfate species over a wide range in Eh and pH:

$$HS^- + 2SO_2(aq) = S_3{}^- + ½H_2O + 1.75O_2(aq). \tag{8}$$

Similarly, organic carbon species such as acetate, which can complex a wide range of metals under hydrothermal conditions (e.g., Bailey et al., 2004; Liu et al., 2001), are predicted to become important at P > 20 kbar (Sverjensky et al., 2014b). As discussed in Section 4.1.5, some of these ligands (in particular organic ones) exert a strong influence on the coordination geometry of metal complexes.

4.1.5. Coordination chemistry controlled by ligands

In coordination chemistry, the geometry, and hence the physicochemical properties of a complex, can be manipulated by designing ligands that impose their own geometrical constraints. In hydrothermal geochemistry, carbonate and sulfate ligands can act in such a fashion, by forming for example bidentate complexes with uranyl (Fig. 14) or REE^{3+} ions (Liu et al., 2016). The proposed increased stability of organic carbon species such as acetate at high pressure (Sverjensky et al., 2014b) could have important implications for the coordination chemistry of metals in deep geofluids (Bailey et al., 2004, 2005; Borg and Liu, 2010). Similarly, in many cases, chloride has a strong impact on the coordination geometry of complexes compared to water/hydroxide ligands (e.g., Fig. 11).

4.2. Driver for metal complexation in hydrothermal systems: key role of translational entropy

Fundamental thermodynamics indicates that enthalpy (which includes volume changes) and entropy terms (Eqs. (5a), (5b), and (5c)) drive changes in coordination chemistry of metals in hydrothermal fluids. A traditional view emphasizes the role of binding energy (an enthalpy term) in defining the geometry of complexes. For some transition metals, octahedral complexes will be favoured over tetrahedral ones because of the extra ligand field stabilization energy (Crerar et al., 1985). This would be absent for d^5 and d^{10} metals such as Mn^{2+}, Cu^+ and Zn^{2+}, but significant for metals such as Ni^{2+} and Co^{2+} where the octahedral site preference energy can be on the order of 100–200 kJ/mol.

However, with increasing temperature, entropy can overcome the enthalpy contribution to the free energy and yield changes in coordination (e.g., Crerar et al., 1985; Susak and Crerar, 1985; Sherman 2007, 2010). This, for example, drives the octahedral to tetrahedral transition of many transition metals, explaining the predominance of the tetrahedral form of many transition metals at elevated temperature (Fig. 16):

$$\left[Zn(H_2O)_6\right]^{2+} + Cl^- = \left[Zn(H_2O)_3Cl\right]^+ + 3H_2O \tag{9}$$

Reaction (9) yields a large positive change in translational entropy, since the reactants consist of two molecules, whereas the products consist of four. Recent molecular dynamics simulations show that, with increasing temperature, translational entropy further drives the change in predominant geometry of the $ZnCl_3^-$ complex to a mixture of pseudo-tetrahedral $[ZnCl_3(H_2O)]^-$ and trigonal $[ZnCl_3]^-$ at high temperature

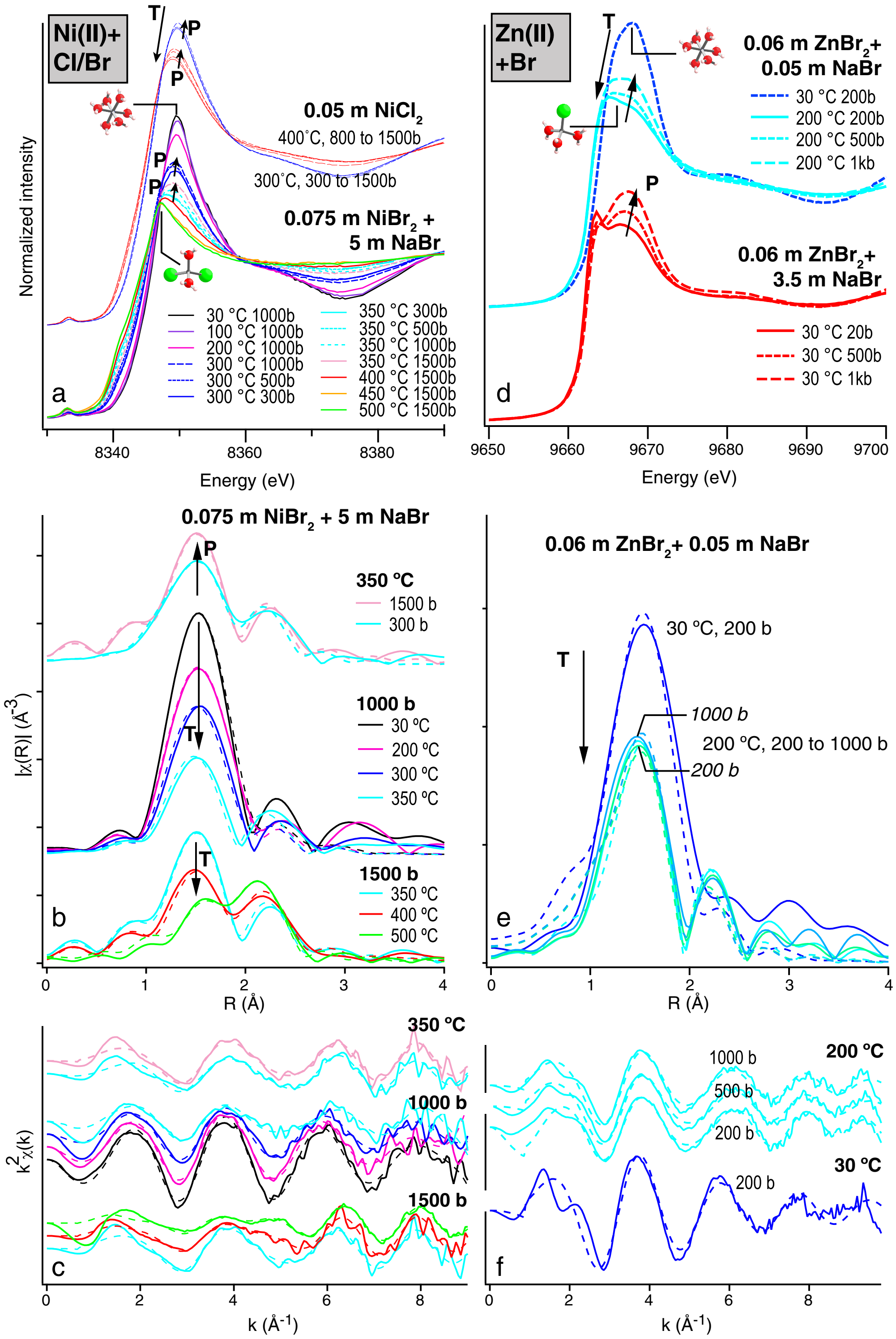

Fig. 18. Effect of pressure on the coordination geometry of Ni(II) (a–c) and Zn(II) complexes (d–f) in chloride and bromide solutions, illustrated by XANES (a,d) and EXAFS data. Fits to the EXAFS data are shown by dashed lines in (b,c,e,f); fit parameters are given in the supplementary materials. Note the opposite effects of temperature and pressure. Unpublished data collected at the FAME beamline, European Synchrotron Research Facility (ESRF), in fluorescence mode using the autoclave illustrated in Fig. 2.
Data collection and data analysis as in Mei et al. (2015b).

(Mei et al., 2015b):

$$[\mathrm{ZnCl_3(H_2O)}]^- = [\mathrm{ZnCl_3}]^- + [\mathrm{H_2O}] \qquad (10)$$

In reaction (10), the entropy term favours the right side, explaining the increasing fraction of the trigonal planar species compared to the four-fold complex with increasing temperature (Fig. 7f).

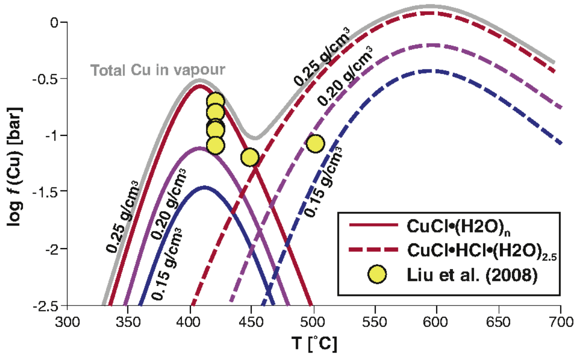

Fig. 19. The fugacity of Cu in fluids containing 0.1 vol% HCl and having densities between 0.15 and 0.25 g/cm^3 calculated using the thermodynamic model of Migdisov et al. (2014), compared to the experimental data of Liu et al. (2008).
Figure modified from Migdisov et al. (2014).

In general, it is necessary to take into account the full hydration of all the complexes involved in the reaction in order to gain a significant understanding of the change in translational entropy of a reaction (Mei et al., 2013a; Sherman, 2007). For example, the reaction between trigonal $[MCl_3]^-$ and tetrahedral MCl_4^{2-} displays only a small change in translational entropy (Eq. 11b) rather than a large positive one if the ion hydration is ignored (11a):

$$[ZnCl_3]^- + [Cl]^- = [ZnCl_4]^- \tag{11a}$$

$$\left[Zn(Cl(H_2O)_5)_3\right]^- + \left[Cl(H_2O)_6\right]^- = \left[Zn(Cl(H_2O)_5)_4\right]^- + H_2O \tag{11b}$$

Due to the hydration of the ligand, translational entropy can drive complexing in hydrothermal fluids even in the absence of coordination change (Mei et al., 2015b). For example, the high temperature reaction "$(T_d)Zn^{2+} + Cl^- = (T_d)ZnCl^+$" can be written as:

$$Zn(H_2O)_4{}^{2+} + \left[Cl(H_2O)_6\right]^- = \left[Zn(H_2O)_3(Cl(H_2O)_5)\right]^+ + 2H_2O \tag{12}$$

This is an important effect explaining the common increase in stability of chloride complexes with increasing temperature (e.g., Fig. 7).

The importance of entropy for determining metal speciation in hydrothermal fluids – and especially how the speciation changes with temperature – is well illustrated by Fig. 1. For Cu(I), the poor stability of the high order chloride complexes at elevated temperature versus CuCl(aq) and $CuCl_2^-$ was initially controversial (e.g., Liu et al., 2002). However, once the linear nature of CuCl(aq) and $CuCl_2^-$ had been recognised, this low stability could easily have been predicted, since the entropy of the reactants is about twice that of the products in this complex-forming reaction:

$$CuCl_2{}^- + Cl^- = CuCl_3{}^{2-} \tag{13}$$

In contrast, for Co, the higher order tetrahedral complex is favoured with increasing temperature due to a large increase in entropy:

$$CoCl(H_2O)_5{}^+ + 3Cl^- = CoCl_4{}^{2-} + 5H_2O \tag{14}$$

This is in spite of the large octahedral site preference energy for Co^{2+}. Changes in translational entropy are also important drivers for the general dehydration of aqua-complexes (i.e., decrease in coordination number) with increasing temperature (e.g., Fig. 15 for the uranyl aqua ion; rare earth elements). Entropy may also be responsible for the increased importance of hydroxide complexes with temperature. Although the data on this problem remain scarce, molecular dynamics simulations suggest that at room-temperature the hydroxyl complexes of U(IV) (Leung and Nenoff, 2012) and Y^{3+} (Liu et al., 2012c) have lower coordination numbers than the aqua complexes.

With increasing temperature, reactions that increase the translational entropy will be favoured. This effect will be mediated by pressure: as pressure increases, the volume of the system decreases; this, in turn, decreases the entropy of the system since

$$dS = \left(\frac{\partial S}{\partial T}\right)_P dT + \left(\frac{\partial S}{\partial P}\right)_T dP = \frac{C_P}{T} dT - \alpha V dP \tag{15}$$

where S is entropy, T is temperature, P is pressure, C_P is heat capacity, and α is the coefficient of isobaric expansion. However, the effect of pressure is much smaller than that of temperature in the liquid phase, because the pressure-induced volume change (and thus entropy change) is small in the incompressible liquid phase. In the highly compressible vapour phase, however, the pressure effect is more pronounced.

The importance of entropy in driving ion association has also been highlighted for example by Raiteri and Gale (2010) as a fundamental parameter in controlling the thermodynamic stability of prenucleation nanoparticles of amorphous materials. Overall, coordination changes with temperature are mostly driven by changes in entropy in hydrothermal systems. These coordination changes will strongly affect the mineral solubilities. Without knowledge of these coordination changes, extrapolations of mineral solubilities via semi-empirical methods (e.g., Helgeson et al., 1981) will result in potentially large errors.

4.3. A few key issues in hydrothermal geochemistry

4.3.1. Sulfur versus chloride complexing

Zhong et al. (2015a) suggest that for rock-buffered fluids (e.g. magmatic hydrothermal and metamorphic fluids), base metal bisulfide complexes may become important at high temperatures (>400 °C) due to the increase in reduced sulfur solubility. Combined with recent evidence for the increasing stability of polysulfide species at high pressures (P > 5 kbar; Pokrovski and Dubessy, 2015a), this highlights a need for a better understanding of metal complexing with S-ligands, which is a formidable task given the complexity of S chemistry. An understanding of coordination chemistry, obtained by a combination of experimental (solubility and in situ spectroscopy) and theoretical (ab initio MD) approaches is key to the success of this endeavour.

For example, Cu(I) forms trigonal planar complexes with thiosulfate ($S_2O_3^-$), but linear complexes with the bisulfide (HS^-) as well as S_3^- ions (Etschmann et al., 2011; Mei et al., 2013b; Pokrovski and Dubessy, 2015a). In the case of the trisulfur radical, molecular dynamics simulations, later confirmed by experiments, showed that Cu(I) and Au(I) complexes form linear monodentate complexes analogous to bisulfide complexes, rather than bidentate complexes. Another example is the relative stability of the Zn(II) chloride and bisulfide complexes (Mei et al., 2015b, 2016). Trigonal planar $Zn(HS)_3^-$ becomes increasingly stable compared to $ZnCl_3^-/ZnCl_3(H_2O)^-$ at high temperature, possibly as a result of hydrogen bonding involving the bisulfide groups.

4.3.2. Liquids and vapours

As mentioned in Section 4.1.1, complexes of the d^{10} M^+ ions (Cu^+, Ag^+, Au^+) as well as Hg^{2+} have a high affinity for water vapour and low density supercritical fluids, compared to neighbouring metals in the Periodic Table (Fig. 16). In dry (i.e., water-free), Cl-bearing vapours, these metals are sparsely soluble as ions pairs (e.g., CuCl(g)) and linear clusters (e.g., Cu_2Cl_2(g)). Over the past decade, it has emerged that solubility in wet vapours are many orders of magnitude higher than in dry vapours, due to the formation of hydrated clusters around electrically neutral, linear first shell moieties (e.g., $[H_2O\text{-}Cu\text{-}Cl]\cdot nH_2O(g)$; $[H_2O\text{-}Au\text{-}HS]\cdot nH_2O(g)$; Etschmann et al., 2010; Migdisov et al., 2014; Williams-Jones and Heinrich, 2005). As temperature increases, the increase in the entropy term eventually results in the destabilisation of these clusters; as a consequence, metal solubility in vapours displays two maxima as a function of temperature (Fig. 19).

In detail, our understanding of the nature and stability of these hydrated metal clusters in low density fluids remains poor, not least because of the experimental difficulties associated with the study of these fluids. Migdisov et al. (2014) show that, for Cu(I) at temperatures >450 °C, the $CuCl\cdot nH_2O(g)$ species give way to a species with 2 chloride ligands ($CuCl\cdot HCl\cdot(H_2O)_{2.5}$, or possibly $CuCl_2\cdot 3H_2O(g)$; Fig. 19). Clearly, it is critical to understand the nature of the high temperature species in term of their coordination chemistry in order to predict with more certainty Cu transport in low- to medium-density hydrothermal fluids, and explore possible similar processes for other metals (e.g., Ag, Mo, Au).

4.3.3. Charged versus neutral complexes – the dielectric diktat?

A common assumption in the interpretation of experimental data on metal complexing in hydrothermal fluids is that neutral complexes become predominant at high temperature (≥300 °C). Recent data show that some charged complexes can remain stable to high temperatures, and shed light on the transient nature of neutral ion pairs forming for example with alkali ions (Na^+).

In the Born theory, the solvation free energy of a metal ion with radius R and charge q is

$$\Delta G = \frac{-q^2e^2}{2R}\left[1-\frac{1}{\varepsilon}\right], \qquad (16)$$

where ε is the dielectric constant of the solvent, e the charge on one electron and R is the Born radius of the ion. The solvation energy can be calculated as a function of pressure and temperature if we know the dielectric constant of the solvent under those conditions. However, the Born radius is also a function of temperature and pressure (this results from the change in ion hydration and solvation properties with temperature and pressure). The HKF model uses the pressure and temperature derivatives of the Born equation to yield an equation of state to predict the free energy of a solute species as a function of P and T. To use it, we need to know the dielectric constant as a function of P and T. The revised HKF model of Tanger and Helgeson (1988) also incorporates a model for the PT dependence of the Born radius. Since the dielectric constant of water decreases with temperature, Eq. (16) also predicts that the solvation free energy will decrease with temperature. Because of this, we would in general predict that ions of opposite charge will tend to pair up; hence, we expect that strength of complexation should increase with temperature.

The Born model is remarkably useful and modified versions of it are used in molecular simulations of proteins. However, solvation of ions by water is a very strong interaction. As emphasized by Sherman (2010), the primary assumption of the Born model is that the response of the solvent molecules to the solute charge is linear. However, solvent molecules form structured complexes with solute cations; consequently, the dielectric constant of the solvent near the solvent molecules will be different from that of the bulk solution. A good example of this is found in REE^{3+} ions, which due to their high charge to radius ratio cause a strong local structure in the solvent, resulting in substantial polarization of the chloride anions and the water molecules (Petit et al., 2008a). Hence, such ions maintain a high degree of hydration and high charges to high temperatures (Migdisov et al., 2016).

The Born model treats the solvent as a continuum with a constant dielectric constant. This breaks down when describing short-range interactions. The molecular picture provides a much more rigorous (if less convenient) description of the solvent and metal-ligand complexation, and avoids the failures of the continuum model (e.g. electrostriction). Phenomena that are explained by changes in the dielectric constant in the continuum model can be explained in terms of entropy in the molecular model. In current computational approaches, it is convenient to apply the Born model to estimate long-range solvation effects, but treat short range solvation in terms of an explicit molecular picture.

Another pathway to maintaining the apparent stability of charged complexes such as $CuCl_2^-$ and $Au(HS)_2^-$ to high temperature (low dielectric solvent) is via the formation of neutral complexes for example with alkali metals (e.g., $CuCl_2Na(aq)$; $Au(HS)_2Na(aq)$; Zajacz et al., 2010, 2011). These species correspond to outer sphere complexes, where the alkali metals are weakly bound by electrostatic interactions with the ligands. Mei et al. (2014) studied the nature of these outersphere complexes using ab initio molecular dynamics, and found that the Na^+ ion was very weakly bonded, resulting in highly disordered structures with fast (in the order of a few picoseconds) exchange among coordinated and solvent Na^+ ions. Na^+ ion association was correlated linearly to the decrease in solution density, and to a decrease in the hydration of the complex. Mei et al. (2014) concluded that whereas the traditional Born-model description explains the ion association as resulting from the decreased dielectric constant of the solvent, at a molecular level, the increased ion association results from the increase in entropy associated with ion dehydration.

5. Conclusions and perspectives

The complexation of metals by ligands is one of the key factors controlling the solubility of minerals in crustal fluids. The geometry of these complexes can exert a first-order control on the fractionation of these elements in hydrothermal environments. Over the past 20 years, our knowledge of the nature and geometry of the complexes responsible for the solubility of many elements in hydrothermal fluids has been dramatically improved as a result of advances in in situ spectroscopy (most prominently XAS) and ab initio molecular dynamic simulations. This sum of knowledge is improving the robustness and accuracy of reactive-transport models, by delivering thermodynamic models based on sound chemical principles (e.g., Mei et al., 2015b). This new molecular-level understanding of mass transfer also helps us rationalize complex geochemical processes. For example, Louvel et al. (2013) use a coordination-based approach to explore Zr behaviour in subduction environments, and Phillips and Powell (2015) justify a new classification of Au-deposits contrasting *gold-only* and *gold-plus* deposits on the ground that the new classification "*has a sound scientific basis that involves the chemistry of gold in relation to metal complexing, salinity of ore-forming fluids and redox state*".

Acknowledgements

Research funding was provided by the Australian Research Council (ARC) (DP130100471 to J.B.; FT130100510 to W.L.). We are grateful to the European Synchrotron Research Facility (Grenoble, France) for providing beamtime (original XAS data presented in Figs. 15 and 18), and to the Australian International Synchrotron Access Program (ISAP) for travel funding. This work was supported by resources provided by the Pawsey Supercomputing Centre (original MD data presented in Fig. 6c).

Appendix A. Supplementary data

Supplementary data to this article can be found online at http://dx.doi.org/10.1016/j.chemgeo.2016.10.021.

References

Accornero, M., Marini, L., Lelli, M., 2008. The dissociation constant of antimonic acid at 10–40 °C. J. Solut. Chem. 37 (6), 785–800.

Åkesson, R., Persson, I., Sandström, M., Wahlgren, U., 1994. Structure and bonding of solvated mercury(II) and thallium(III) dihalide and dicyanide complexes by XAFS spectroscopic measurements and theoretical calculations. Inorg. Chem. 33, 3715–3723.

Akinfiev, N.N., Tagirov, B.R., 2006. Effect of selenium on silver transport and precipitation by hydrothermal solutions: thermodynamic description of the Ag-Se-S-Cl-O-H system. Geol. Ore Deposits 48, 402–413.

Akinfiev, N.N., Zotov, A.V., 2001. Thermodynamic description of chloride, hydrosulfide, and hydroxo complexes of Ag(I), Cu(I), and Au(I) at temperatures of 25–500 °C and pressures of 1–2000 bar. Geochem. Int. 39 (10), 990–1006.

Altree-Williams, A., Pring, A., Ngothai, Y., Brugger, J., 2015. Textural and compositional complexities resulting from coupled dissolution-reprecipitation reactions in geomaterials. Earth Sci. Rev. 150, 628–651.

Amthauer, G., Pavicevic, M.K., Jelenkovic, R., El Goresy, A., Boev, B., Lazic, P., 2012. State of geoscientific research within the lorandite experiment (LOREX). Mineral. Petrol. 105 (3–4), 157–169.

Anderson, A.J., Mayanovic, R.A., Bajt, S., 1995. Determination of the local-structure and speciation of zinc in individual hypersaline fluid inclusions by micro-XAFS. Can. Mineral. 33, 499–508.

Anderson, A.J., Mayanovic, R.A., Bajt, S., 1998. A microbeam XAFS study of aqueous chlorozinc complexing to 430 °C in fluid inclusions from the Knaumuhle granitic pegmatite, Saxonian Granulite Massif, Germany. Can. Mineral. 36, 511–524.

Anderson, A.J., Jayanetti, S., Mayanovic, R.A., Bassett, W.A., Chou, I.M., 2002. X-ray spectroscopic investigations of fluids in the hydrothermal diamond anvil cell: the hydration structure of aqueous La^{3+} up to 300 °C and 1600 bars. Am. Mineral. 87 (2–3), 262–268.

Antignano, A., Manning, C.E., 2008. Rutile solubility in H_2O, H_2O-SiO_2, and H_2O-$NaAlSi_3O_8$ fluids at 0.7–2.0 GPa and 700–1000 °C: implications for mobility of nominally insoluble elements. Chem. Geol. 255 (1–2), 283–293.

Armunanto, R., Schwenk, C.F., Rode, B.M., 2003. Structure and dynamics of hydrated Ag (I): ab initio quantum mechanical-molecular mechanical molecular dynamics simulation. J. Phys. Chem. A 107 (17), 3132–3138.

Asthagiri, D., Pratt, L.R., Paulaitis, M.E., Rempe, S.B., 2004. Hydration structure and free energy of biomolecularly specific aqueous dications, including Zn^{2+} and first transition row metals. J. Am. Chem. Soc. 126 (4), 1285–1289.

Bailey, E.H., Mosselmans, J.F.W., Schofield, P.F., 2004. Uranyl acetate speciation in aqueous solutions - an XAS study between 25 °C and 250 °C. Geochim. Cosmochim. Acta 68 (8), 1711–1722.

Bailey, E.H., Mosselmans, J.F.W., Schofield, P.F., 2005. Uranyl-citrate speciation in acidic aqueous solutions - an XAS study between 25 and 200 °C. Chem. Geol. 216 (1–2), 1–16.

Bali, E., Audétat, A., Keppler, H., 2011. The mobility of U and Th in subduction zone fluids: an indicator of oxygen fugacity and fluid salinity. Contrib. Mineral. Petrol. 161 (4), 597–613.

Bali, E., Keppler, H., Audetat, A., 2012. The mobility of W and Mo in subduction zone fluids and the Mo–W–Th–U systematics of island arc magmas. Earth Planet. Sci. Lett. 351–352 (0), 195–207.

Ballantyne, J.M., Moore, J.N., 1988. Arsenic geochemistry in geothermal systems. Geochim. Cosmochim. Acta 52 (2), 475–483.

Barnes, S.J., Liu, W., 2012. Pt and Pd mobility in hydrothermal fluids: evidence from komatiites and from thermodynamic modelling. Ore Geol. Rev. 44 (0), 49–58.

Bastrakov, E., Jaireth, S., Mernagh, T., 2010. Solubility of Uranium in Hydrothermal Fluids at 25 °C to 300 °C. Implications for the Formation of Uranium Deposits. Record 2010/029. Geoscience Australia, Canberra (91 pp.).

Bau, M., Dulski, P., 1995. Comparative study of yttrium and rare-earth element behaviours in fluorine-rich hydrothermal fluids. Contrib. Mineral. Petrol. 119, 213–223.

Bazarkina, E.F., Pokrovski, G.S., Zotov, A.V., Hazemann, J.L., 2010. Structure and stability of cadmium chloride complexes in hydrothermal fluids. Chem. Geol. 276 (1–2), 1–17.

Bazarkina, E.F., Pokrovski, G.S., Hazemann, J.L., 2014. Structure, stability and geochemical role of palladium chloride complexes in hydrothermal fluids. Geochim. Cosmochim. Acta 146, 107–131.

Bebie, J., Seward, T.M., Hovey, J.K., 1998. Spectrophotometric determination of the stability of thallium(I) chloride complexes in aqueous solutions up to 200 °C. Geochim. Cosmochim. Acta 62, 1643–1651.

Bebout, G.E., Penniston-Dorland, S.C., 2016. Fluid and mass transfer at subduction interfaces—the field metamorphic record. Lithos 240–243, 228–258.

Belissont, R., Muñoz, M., Boiron, M.-C., Luais, B., Mathon, O., 2016. Distribution and oxidation state of Ge, Cu and Fe in sphalerite by micro-XRF and K-edge micro-XANES: insights into Ge incorporation, partitioning and isotopic fractionation. Geochim. Cosmochim. Acta http://dx.doi.org/10.1016/j.gca.2016.01.001.

Bell, A., Charnock, J., Helz, G., Lennie, A., Livens, F., Mosselmans, J., Pattrick, R., Vaughan, D., 2007. Evidence for dissolved polymeric mercury(II)-sulfur complexes? Chem. Geol. 243 (1–2), 122–127.

Bell, A.S., Burger, P.V., Le, L., Shearer, C.K., Papike, J.J., Sutton, S.R., Newville, M., Jones, J., 2014. XANES measurements of Cr valence in olivine and their applications to planetary basalts. Am. Mineral. 99 (7), 1404–1412.

Benezeth, P., Diakonov, I.I., Pokrovski, G.S., Dandurand, J.L., Schott, J., Khodakovsky, I.L., 1997. Gallium speciation in aqueous solution. Experimental study and modelling .2. Solubility of α-GaOOH in acidic solutions from 150 to 250 °C and hydrolysis constants of gallium (III) to 300 °C. Geochim. Cosmochim. Acta 61 (7), 1345–1357.

Benezeth, P., Palmer, D.A., Wesolowski, D.J., Xiao, C., 2002. New measurements of the solubility of zinc oxide from 150 to 350 °C. J. Solut. Chem. 31, 947–973.

Benfatto, M., Solera, J.A., Chaboy, J., Proietti, M.G., García, J., 1997. Theoretical analysis of X-ray absorption near-edge structure of transition-metal aqueous complexes in solution at the metal K edge. Phys. Rev. B 56, 2447–2452.

Benfatto, M., D'Angelo, P., Della Longa, S., Pavel, N.V., 2002. Evidence of distorted fivefold coordination of the Cu^{2+} aqua ion from an X-ray-absorption spectroscopy quantitative analysis. Phys. Rev. B 65 (17).

Benning, L.G., Seward, T.M., 1996. Hydrosulphide complexing of Au(I) in hydrothermal solutions from 150–400 °C and 500–1500 bar. Geochim. Cosmochim. Acta 60 (11), 1849–1871.

Berry, A.J., Hack, A.C., Mavrogenes, J.A., Newville, M., Sutton, S.R., 2006. A XANES study of Cu speciation in high-temperature brines using synthetic fluid inclusions. Am. Mineral. 91, 1773–1782.

Berry, A.J., Harris, A.C., Kamenetsky, V.S., Newville, M., Sutton, S.R., 2009. The speciation of copper in natural fluid inclusions at temperatures up to 700 °C. Chem. Geol. 259 (1–2), 2–7.

Bethke, C.M., 2008. Geochemical and Biogeochemical Reaction Modeling. 2nd edition. Cambridge University Press, New York (564 pp.).

Bjerrum, N., 1908. Studies on Basic Chromic Compounds. A Contribution to the Theory of Hydrolysis (Dissertation Thesis).

Blumberger, J., 2008. Cuaq^{+}/Cuaq^{2+} redox reaction exhibits strong nonlinear solvent response due to change in coordination number. J. Am. Chem. Soc. 130 (47), 16065–16068.

Blumberger, J., Bernasconi, L., Tavernelli, I., Vuilleumier, R., Sprik, M., 2004. Electronic structure and solvation of copper and silver ions: a theoretical picture of a model aqueous redox reaction. J. Am. Chem. Soc. 126 (12), 3928–3938.

Boctor, N.Z., 1985. Rhodonite solubility and thermodynamic properties of aqueous $MnCl_2$ in the system MnO-SiO_2-HCl-H_2O. Geochim. Cosmochim. Acta 49 (2), 565–575.

Boctor, N.Z., Popp, R.K., Frantz, J.D., 1980. Mineral-solution equilibria; IV, Solubilities and the thermodynamic properties of $FeCl_2^0$ in the system Fe_2O_3-H_2-H_2O-HCl. Geochim. Cosmochim. Acta 44 (10), 1509–1518.

Boily, J.F., Seward, T.M., 2002. Hydrolysis and precipitation of Pd(II) in 0.6 m NaCl. Geochim. Cosmochim. Acta 66 (15A), A88.

Boily, J.F., Seward, T.M., Charnock, J.M., 2007. The hydrolysis and precipitation of Pd(II) in 0.6 mol kg^{-1} NaCl: a potentiometric, spectrophotometric, and EXAFS study. Geochim. Cosmochim. Acta 71, 4834–4845.

Bonnet, J., Mösser-Ruck, R., Cauzid, J., Bailly, L., André, A., 2014. Crystallographic control of trace element (Cu-Ga-Ge-Fe-Cd) distribution in MVT sphalerites, Tennessee, USA. 21st IMA Meeting, 1–5 September 2014, Johannesburg, South Africa, Abstract Volume, p. 129.

Borg, S.J., Liu, W.H., 2010. An XAS study of zinc speciation in aqueous acetate solutions at 25–200 °C. Nucl. Instrum. Methods Phys. Res., Sect. A 619 (1–3), 276–279.

Borg, S., Liu, W., Etschmann, B., Tian, Y., Brugger, J., 2012. An XAS study of molybdenum speciation in hydrothermal chloride solutions from 25–385 °C and 600 bar. Geochim. Cosmochim. Acta 92, 292–307.

Borisenko, A.S., Borovikov, A.A., Vasyukova, E.A., Pavlova, G.G., Ragozin, A.L., Prokop'ev, I.R., Vladykin, N.V., 2011. Oxidized magmatogene fluids: metal-bearing capacity and role in ore formation. Russ. Geol. Geophys. 52 (1), 144–164.

Born, M., 1920. Volumen und Hydratationswärme der Ionen. Z. Phys. 1, 45–48.

Bourcier, W.L., Barnes, H.L., 1987. Ore solution chemistry - VII. Stabilities of chloride and bisulfide complexes of zinc to 350 °C. Econ. Geol. 82, 1839–1863.

Bourke, J.D., Chantler, C.T., Joly, Y., 2016. FDMX: extended X-ray absorption fine structure calculations using the finite difference method. J. Synchrotron Radiat. 23, 551–559.

Bowron, D.T., Beret, E.C., Martin-Zamora, E., Soper, A.K., Sánchez Marcos, E., 2012. Axial structure of the Pd(II) aqua ion in solution. J. Am. Chem. Soc. 134 (2), 962–967.

Bowron, D.T., Amboage, M., Boada, R., Freeman, A., Hayama, S., Diaz-Moreno, S., 2013. The hydration structure of Cu^{2+}: more tetrahedral than octahedral? RSC Adv. 3 (39), 17803–17812.

Brehm, M., Kirchner, B., 2011. TRAVIS - a free analyzer and visualizer for Monte Carlo and molecular dynamics trajectories. J. Chem. Inf. Model. 51 (8), 2007–2023.

Brugger, J., 2007. BeerOz, a set of Matlab routines for the quantitative interpretation of spectrophotometric measurements of metal speciation in solution. Comput. Geosci. 33 (2), 248–261.

Brugger, J., Gieré, R., 2000. Origin and distribution of some trace elements in metamorphosed Fe-Mn deposits, Val Ferrera, eastern Swiss Alps. Can. Mineral. 38, 1075–1101.

Brugger, J., Lahaye, Y., Costa, S., Lambert, D., Bateman, R., 2000. Inhomogeneous distribution of REE in scheelite and dynamics of Archaean hydrothermal systems (Mt. Charlotte and Drysdale gold deposits, Western Australia). Contrib. Mineral. Petrol. 139 (3), 251–264.

Brugger, J., Mcphail, D.C., Black, J., Spiccia, L., 2001. Complexation of metal ions in brines: application of electronic spectroscopy in the study of the Cu(II)-LiCl-H_2O system between 25 and 90 °C. Geochim. Cosmochim. Acta 65 (16), 2691–2708.

Brugger, J., Mcphail, D.C., Wallace, M., Waters, J., 2003. Formation of willemite in hydrothermal environments. Econ. Geol. Bull. Soc. Econ. Geol. 98 (4), 819–835.

Brugger, J., Etschmann, B., Liu, W., Testemale, D., Hazemann, J.-L., van Beek, W., Proux, O., 2007a. An XAS study of the structure and thermodynamics of Cu(I) chloride complexes in brines up to high temperature (400 °C, 600 bar). Geochim. Cosmochim. Acta 71 (20), 4920–4941.

Brugger, J., Meisser, N., Krivovichev, S., Armbruster, T., Favreau, G., 2007b. Mineralogy and crystal structure of bouazzerite from Bou Azzer, Anti-Atlas, Morocco: Bi-As-Fe nanoclusters containing Fe^{3+} in trigonal prismatic coordination. Am. Mineral. 92 (10), 1630–1639.

Brugger, J., Etschmann, B., Pownceby, M., Liu, W., Grundler, P., Brewe, D., 2008. Oxidation state of europium in scheelite: tracking fluid-rock interaction in gold deposits. Chem. Geol. 257 (1–2), 26–33.

Brugger, J., Pring, A., Reith, F., Ryan, C., Etschmann, B., Liu, W., O'Neill, B., Ngothai, Y., 2010. Probing ore deposits formation: new insights and challenges from synchrotron and neutron studies. Radiat. Phys. Chem. 79 (2), 151–161.

Brugger, J., Etschmann, B.E., Grundler, P.V., Liu, W., Testemale, D., Pring, A., 2012. XAS evidence for the stability of polytellurides in hydrothermal fluids up to 599 °C, 800 bar. Am. Mineral. 97 (8–9), 1519–1522.

Brugger, J., Tooth, B., Etschmann, B., Liu, W.H., Testemale, D., Hazemann, J.L., Grundler, P.V., 2014. Structure and thermal stability of Bi(III) oxy-clusters in aqueous solutions. J. Solut. Chem. 43 (2), 314–325.

Bruyère, R., Prat, A., Goujon, C., Hazemann, J.-L., 2008. A new pressure regulation device using high pressure isolation valves. J. Phys. Conf. Ser. 121, 122003–122006.

Bunker, G., 2010. Introduction to xafs. A Practical Guide to X-ray Absorption Fine Structure Spectroscopy. Cambridge University Press, Published in the United States of America by Cambridge University Press, New York (260 pp.).

Burnham, A.D., Berry, A.J., Wood, B.J., Cibin, G., 2012. The oxidation states of niobium and tantalum in mantle melts. Chem. Geol. 330, 228–232.

Burns, P.C., 1999. The crystal chemistry of uranium. In: Burns, P.C., Finch, R. (Eds.), Uranium: Mineralogy, Geochemistry and the Environment. Reviews in Mineralogy. Mineralogical Society of America, Blacksburg, Victoria, pp. 23–90.

Burns, P.C., Finch, R.J., 1999. Wyartite: crystallographic evidence for the first pentavalent-uranium mineral. Am. Mineral. 84 (9), 1456–1460.

Burns, P.C., Ewing, R.C., Hawthorne, F.C., 1997. The crystal chemistry of hexavalent uranium: polyhedron geometries, bond-valence parameters, and polymerization of polyhedra. Can. Mineral. 35, 1551–1570.

Burns, P.C., Ewing, R.C., Navrotsky, A., 2012. Nuclear fuel in a reactor accident. Science 335 (6073), 1184–1188.

Buslaev, Y.A., Petrosyants, S.P., Tarasov, V.P., 1969. Complex germanium fluorides in aqueous solutions. J. Struct. Chem. 10 (3), 338–342.

Butterworth, P., Hillier, I.H., Burton, N.A., Vaughan, D.J., Guest, M.F., Tossell, J.A., 1992. Calculations of the structures, stabilities, Raman spectra, and NMR spectra of cadmium halide hydroxide (CdCln$(OH_2)^{2\,-\,n}$, CdBrn$(OH_2)^{2\,-\,n}$), and zinc chloride hydroxide (ZnCln$(OH_2)^{2\,-\,n}$) species in aqueous solution. J. Phys. Chem. 96 (15), 6494–6500.

Cabral, A.R., Reith, F., Lehmann, B., Brugger, J., Meinhold, G., Tupinamba, M., Kwitko-Ribeiro, R., 2012. Anatase nanoparticles on supergene platinum-palladium aggregates from Brazil: titanium mobility in natural waters. Chem. Geol. 334, 182–188.

Car, R., Parrinello, M., 1985. Unified approach for molecular dynamics and density-functional theory. Phys. Rev. Lett. 55 (22), 2471–2474.

Cardelli, A., Cibin, G., Benfatto, M., Della Longa, S., Brigatti, M.F., Marcelli, A., 2003. A crystal-chemical investigation of Cr substitution in muscovite by XANES spectroscopy. Phys. Chem. Miner. 30 (1), 54–58.

Cauzid, J., Philippot, P., Martinez-Criado, G., Menez, B., Laboure, S., 2007. Contrasting Cu-complexing behaviour in vapour and liquid fluid inclusions from the Yankee Lode tin deposit, Mole Granite, Australia. Chem. Geol. 246, 39–54.

Cempirek, J., Groat, L.A., 2013. Note on the formula of brunogeierite and the first bond-valence parameters for Ge^{2+}. J. Geosci. 58 (1), 71–74.

Chaboy, J., Munoz-Paez, A., Merkling, P.J., Marcos, E.S., 2006. The hydration of Cu^{2+}: can the Jahn-Teller effect be detected in liquid solution? J. Chem. Phys. 124 (6).

Chase, M.W., 1998. NIST-JANAF thermochemical tables. J. Phys. Chem. Ref. Data Monogr. 9 (1961 pp.).

Chen, X., Chu, W., Chen, D., Wu, Z., Marcelli, A., Wu, Z., 2009. Correlation between local structure and molar ratio of Au (III) complexes in aqueous solution: an XAS investigation. Chem. Geol. 268 (1–2), 74–80.

Cheng, H.S., Hsu, C.M., Chang, Y.C., Wei, H.H., 1981. Mössbauer spectroscopic studies of trifluorostannate(II) complexes in frozen aqueous solution. Radiochem. Radioanal. Lett. 49, 167–171.

Cheng, H.S., Hsu, C.M., Shih, L.L., 1984. Mössbauer spectroscopic studies of chlorostannate(II) complexes in frozen aqueous solutions. J. Chin. Chem. Soc. 31, 117–123.

Chou, I.M., Eugster, H.P., 1977. Solubility of magnetite in supercritical chloride solutions. Am. J. Sci. 277 (10), 1296–1314.

Ciobanu, C.L., Cook, N.J., Pring, A., Brugger, J., Danyushevsky, L., Shimizu, M., 2009. 'Invisible gold' in bismuth chalcogenides. Geochim. Cosmochim. Acta 73 (7), 1970–1999.

Clark, C., Grguric, B., Mumm, A.S., 2004. Genetic implications of pyrite chemistry from the Palaeoproterozoic Olary Domain and overlying Neoproterozoic Adelaidean sequences, northeastern South Australia. Ore Geol. Rev. 25 (3–4), 237–257.

Cockerton, A.B.D., Tomkins, A.G., 2012. Insights into the liquid bismuth collector model through analysis of the Bi-Au Stormont Skarn Prospect, northwest Tasmania. Econ. Geol. 107 (4), 667–682.

Collings, M.D., Sherman, D.M., Ragnarsdottir, K.V., 2000. Complexation of Cu^{2+} in oxidised NaCl brines from 25 °C to 175 °C: results from in situ EXAFS spectroscopy. Chem. Geol. 167, 65–73.

Cook, N.J., Ciobanu, C.L., Williams, T., 2011. The mineralogy and mineral chemistry of indium in sulphide deposits and implications for mineral processing. Hydrometallurgy 108 (3–4), 226–228.

Cook, N.J., Ciobanu, C.L., Brugger, J., Etschmann, B., Howard, D.L., de Jonge, M.D., Ryan, C., Paterson, D., 2012. Determination of the oxidation state of Cu in substituted Cu-In-Fe-bearing sphalerite via mu-XANES spectroscopy. Am. Mineral. 97 (2–3), 476–479.

Cook, N.J., Etschmann, B., Ciobanu, C.L., Geraki, K., Howard, D.L., Williams, T., Rae, N., Pring, A., Chen, G., Johannessen, B., Brugger, J., 2015. Distribution and substitution mechanism of Ge in a Ge-(Fe)-bearing sphalerite. Minerals 5 (2), 117–132.

Cooke, D.R., McPhail, D.C., 2001. Epithermal Au-Ag-Te mineralization, Acupan, Baguio District, Philippines; numerical simulations of ore mineral deposition. Econ. Geol. 96, 109–131.

Cotton, F.A., Hall, W.T., 1977. Cesium octachlorodirhenate(III) hydrate - correct structure and its significance with respect to nature of metal-metal multiple bonding. Inorg. Chem. 16 (8), 1867–1871.

Crerar, D.A., Susak, N.J., Borcsik, M., Schwartz, S., 1978. Solubility of buffer assemblage pyrite + pyrrhotite + magnetite in NaCl solutions from 200 to 350 °C. Geochim. Cosmochim. Acta 42 (9), 1427–1437.

Crerar, D.A., Wood, S., Brantley, S., Bocarsly, A., 1985. Chemical controls on solubility of ore-forming minerals in hydrothermal systems. Can. Mineral. 23, 333–352.

Cusanelli, A., Frey, U., Richens, D.T., Merbach, A.E., 1996. The slowest water exchange at a homoleptic mononuclear metal center: variable-temperature and variable-pressure ^{17}O NMR study on $[Ir(H_2O)_6]^{3+}$. J. Am. Chem. Soc. 118 (22), 5265–5271.

Cygan, G.L., Hemley, J.J., D'Angelo, W.M., 1994. An experimental study of zinc chloride speciation from 300 to 600 °C and 0.5 to 2.0 kbar in buffered hydrothermal solutions. Geochim. Cosmochim. Acta 58, 4841–4855.

Da Silva, C., Proux, O., Hazemann, J.-L., James-Smith, J., Testemale, D., Yamaguchi, T., 2009. X-ray absorption spectroscopy study of solvation and ion-pairing in aqueous gallium bromide solutions at supercritical conditions. J. Mol. Liq. 147 (1–2), 83–95.

Dai, S., Wang, P., Ward, C.R., Tang, Y., Song, X., Jiang, J., Hower, J.C., Lia, T., Seredin, V.V., Wagner, N.J., Jiang, Y., Wang, X., Liu, J., 2015. Elemental and mineralogical anomalies in the coal-hosted Ge ore deposit of Lincang, Yunnan, southwestern China: key role of N_2–CO_2-mixed hydrothermal solutions. Int. J. Coal Geol. 19–46.

Dargent, M., Dubessy, J., Truche, L., Bazarkina, E.F., Nguyen-Trung, C., Robert, P., 2013. Experimental study of uranyl(VI) chloride complex formation in acidic LiCl aqueous solutions under hydrothermal conditions (T = 21 °C–350 °C, Psat) using Raman spectroscopy. Eur. J. Mineral. 25, 765–775.

Deditius, A.P., Utsunomiya, S., Renock, D., Ewing, R.C., Ramana, C.V., Becker, U., Kesler, S.E., 2008. A proposed new type of arsenian pyrite: composition, nanostructure and geological significance. Geochim. Cosmochim. Acta 72 (12), 2919–2933.

Dellien, I., Hall, F.M., Hepler, L.G., 1976. Chromium, molybdenum, and tungsten: thermodynamic properties, chemical equilibria, and standard potentials. Chem. Rev. 76, 283–310.

Diakonov, I.I., Pokrovski, G.S., Benezeth, P., Schott, J., Dandurand, J.L., Escalier, J., 1997. Gallium speciation in aqueous solution. Experimental study and modelling .1. Thermodynamic properties of $Ga(OH)_4^-$ to 300 °C. Geochim. Cosmochim. Acta 61 (7), 1333–1343.

Diaz-Moreno, S., Muñoz-Páez, A., Martinez, J.M., Pappalardo, R.R., Sanchez Marcos, E., 1996. EXAFS investigation of inner- and outer-sphere cloroaquo complexes of Cr^{3+} in aqueous solutions. J. Am. Chem. Soc. 118, 12654–12664.

Ding, K., Seyfried, W.E.J., 1992. Determination of Fe-Cl complexing in the low pressure supercritical region (NaCl fluid): iron solubility constraints on pH of subseafloor hydrothermal fluids. Geochim. Cosmochim. Acta 56, 3681–3692.

Driesner, T., Seward, T.M., Tironi, I.G., 1998. Molecular dynamics simulation study of ionic hydration and ion association in dilute and 1 molal aqueous sodium chloride solutions from ambient to supercritical conditions. Geochim. Cosmochim. Acta 62, 3095–3107.

Dutrizac, J.E., Jambor, J.L., Chen, T.T., 1986. Host minerals for the gallium-germanium ores of the Apex Mine, Utah. Econ. Geol. 81 (4), 946–950.

Edwards, A.J., 1972. Crystal-structure of rhenium oxide tetrachloride. J. Chem. Soc. Dalton Trans. (4), 582–584.

Eklund, L., Persson, I., 2014. Structure and hydrogen bonding of the hydrated selenite and selenate ions in aqueous solution. Dalton Trans. 43 (17), 6315–6321.

EnNaciri, A., Barbanson, L., Touray, J.C., 1997. Brine inclusions for the Co-As(Au) Bou Azzer district, Anti-Atlas Mountains, Morocco. Econ. Geol. Bull. Soc. Econ. Geol. 92 (3), 360–367.

Etschmann, B., Liu, W., Testemale, D., Muller, H., Rae, N., Proux, O., Hazemann, J., Brugger, J., 2010. An in situ XAS study of copper(I) transport as hydrosulfide complexes in hydrothermal solutions (25–592 °C, 180–600 bar): speciation and solubility in vapor and liquid phases. Geochim. Cosmochim. Acta 74 (16), 4723–4739.

Etschmann, B.E., Black, J.R., Grundler, P.V., Borg, S., Brewe, D., McPhail, D.C., Spiccia, L., Brugger, J., 2011. Copper(I) speciation in mixed thiosulfate-chloride and ammonia-chloride solutions: XAS and UV–visible spectroscopic studies. RSC Adv. 1 (8), 1554–1566.

Etschmann, B.E., Liu, W., Pring, A., Grundler, P.V., Tooth, B., Borg, S., Testemale, D., Brewe, D., Brugger, J., 2016. The role of Te(IV) and Bi(III) chloride complexes in hydrothermal mass transfer: an X-ray absorption spectroscopic study. Chem. Geol. 425, 37–51.

Evans, H.T.j., Garrels, R.M., 1958. Thermodynamic equilibria of vanadium in aqueous systems as applied to the interpretation of the Colorado Plateau ore deposits. Geochim. Cosmochim. Acta 15, 131–149.

Fan, R., Gerson, A.R., 2011. Nickel geochemistry of a Philippine laterite examined by bulk and microprobe synchrotron analyses. Geochim. Cosmochim. Acta 75 (21), 6400–6415.

Fein, J.B., Hemley, J.J., D'Angelo, W.M., Komninou, A., Sverjensky, D.A., 1992. Experimental study of iron-chloride complexing in hydrothermal fluids. Geochim. Cosmochim. Acta 3179–3190.

Feller, D.F., Glendening, E.D., De Jong, W.A., 1999. Structures and binding enthalpies of $M+\ (H_20)(n)$ clusters, M = Cu, Ag, Au. J. Chem. Phys. 110 (3), 1475–1491 (110(PNNL-SA-30301)).

Ferlat, G., San Miguel, A., Jal, J.F., Soetens, J.C., Bopp, P.A., Hazemann, J.L., Testemale, D., Daniel, I., 2002. The quest for ion pairing in supercritical aqueous electrolytes. J. Mol. Liq. 101 (1–3), 127–136.

Filella, M., Belzile, N., Chen, Y.-W., 2002. Antimony in the environment: a review focused on natural waters: II. Relevant solution chemistry. Earth Sci. Rev. 59 (1–4), 265–285.

Filipponi, A., De Panfilis, S., Oliva, C., Ricci, M.A., D'Angelo, P., Bowron, D.T., 2003. Ion hydration under pressure. Phys. Rev. Lett. 91 (16).

Frick, R.J., Hofer, T.S., Pribil, A.B., Randolf, B.R., Rode, B.M., 2009a. Structure and dynamics of the UO_2^{2+} ion in aqueous solution: an ab initio QMCF MD study. J. Phys. Chem. A 113 (45), 12496–12503.

Frick, R.J., Pribil, A.B., Hofer, T.S., Randolf, B.R., Bhattacharjee, A., Rode, B.M., 2009b. Structure and dynamics of the U^{4+} ion in aqueous solution: an ab initio quantum mechanical charge field molecular dynamics study. Inorg. Chem. 48 (9), 3993–4002.

Fulton, J.L., Hoffmann, M.M., Darab, J.G., 2000a. An X-ray absorption fine structure study of copper(I) chloride coordination structure in water up to 325 °C. Chem. Phys. Lett. 330, 300–308.

Fulton, J.L., Hoffmann, M.M., Darab, J.G., Palmer, B.J., Stern, E.A., 2000b. Copper(I) and copper(II) coordination structure under hydrothermal conditions at 325 °C: an X-ray absorption fine structure and molecular dynamics study. J. Phys. Chem. 104 (49), 11651–11663.

Fulton, J.L., Kathmann, S.M., Schenter, G.K., Balasubramanian, M., 2009. Hydrated structure of Ag(I) ion from symmetry-dependent, K- and L-edge XAFS multiple scattering and molecular dynamics simulations. J. Phys. Chem. A 113 (50), 13976–13984.

Gammons, C.H., 1996. Experimental investigations of the hydrothermal geochemistry of platinum and palladium .5. Equilibria between platinum metal, Pt(II), and Pt(IV) chloride complexes at 25 to 300 °C. Geochim. Cosmochim. Acta 60 (10), 1683–1694.

Gammons, C.H., Bloom, M.S., 1993. Experimental investigation of the hydrothermal geochemistry of platinum and palladium .2. The solubility of PtS and PdS in aqueous sulfide solutions to 300 °C. Geochim. Cosmochim. Acta 57, 2451–2467.

Gammons, C.H., Seward, T.M., 1996. Stability of manganese(II) chloride complexes from 25 to 300 °C. Geochim. Cosmochim. Acta 60 (22), 4295–4311.

Gao, J., John, T., Klemd, R., Xiong, X.M., 2007. Mobilization of Ti–Nb–Ta during subduction: evidence from rutile-bearing dehydration segregations and veins hosted in eclogite, Tianshan, NW China. Geochim. Cosmochim. Acta 71, 4974–4996.

Gibbs, J.W., 1873. A method of geometrical representation of the thermodynamic properties of substances by means of surfaces. Trans. Connecticut Acad. Arts Sci. 2, 382–404.

Gieré, R., 1986. Zirconolite, allanite and hoegbomite in a marble skarn from the Bergell contact aureole: implications for mobility of Ti, Zr and REE. Contrib. Mineral. Petrol. 93, 459–470.

Giggenbach, W., 1971. Blue solutions of sulfur in water at elevated temperatures. Inorg. Chem. 10 (6), 1306–1308.

Gonzalez-Alvarez, I., Pirajno, F., Kerrich, R., 2013. Hydrothermal nickel deposits: secular variation and diversity. Ore Geol. Rev. 52, 1–3.

Gramaccioli, C.M., Diella, V., Demartin, F., 2000. The formation of scandium minerals as an example of the role of complexes in the geochemistry of rare earths and HFS elements. Eur. J. Mineral. 12 (4), 795–808.

Greenwood, N.N., Earnshaw, A., 1984. Chemistry of the Elements. Pergamon Press, Oxford, New York, Toronto, Sydney, Paris, Frankfurt (1542 pp.).

Grenthe, I., Fuger, J., Konings, R.J.M., Lemire, R.J., Muller, A.B., Nguyen-Trung Cregu, C., Wanner, H., 1992. Chemical Thermodynamics, Volume 1: Chemical Thermodynamics of Uranium. Elsevier, North-Holland, Amsterdam (714 pp.).

Grundler, P., Brugger, J., Meisser, N., Ansermet, S., Borg, S., Etschmann, B., Testemale, D., Bolin, T., 2008. Xocolatlite, $Ca_2Mn_{24} + Te_2O_{12}·H_2O$, a new tellurate related to kuranakhite: description and measurement of Te oxidation state by XANES spectroscopy. Am. Mineral. 93 (11–12), 1911–1920.

Grundler, P.V., Brugger, J., Etschmann, B.E., Helm, L., Liu, W.H., Spry, P.G., Tian, Y., Testemale, D., Pring, A., 2013. Speciation of aqueous tellurium(IV) in hydrothermal solutions and vapors, and the role of oxidized tellurium species in Te transport and gold deposition. Geochim. Cosmochim. Acta 120, 298–325.

Grunwaldt, J.D., Wandeler, R., Baiker, A., 2003. Supercritical fluids in catalysis: opportunities of in situ spectroscopic studies and monitoring phase behavior. Catal. Rev. Sci. Eng. 45 (1), 1–96.

Guillaumont, R., Fanghänel, T., Fuger, J., Grenthe, I., Neck, V., Palmer, D.A., Rand, M.H., 2003. Update on the Chemical Thermodynamics of Uranium, Neptunium, Plutonium, Americium and Technetium. OECD Nuclear Energy Agency, Data Bank (959 pp.).

Gysi, A.P., Williams-Jones, A.E., Collins, P., 2016. Lithogeochemical vectors for hydrothermal processes in the Strange Lake peralkaline granitic REE-Zr-Nb deposit. Econ. Geol. 111, 1241–1276.

Haas, J.R., Shock, E.L., Sassani, D.C., 1995. Rare earth elements in hydrothermal systems: estimates of standard partial molal thermodynamic properties of aqueous complexes of the rare earth elements at high pressures and temperatures. Geochim. Cosmochim. Acta 59 (21), 4329–4350.

Hack, A.C., Mavrogenes, J.A., 2006. A synthetic fluid inclusion study of copper solubility in hydrothermal brines from 525 to 725 °C and 0.3 to 1.7 GPa. Geochim. Cosmochim. Acta 70, 3970–3985.

Haigis, V., Salanne, M., Simon, S., Wilke, M., Jahn, S., 2013. Molecular dynamics simulations of Y in silicate melts and implications for trace element partitioning. Chem. Geol. 346 (0), 14–21.

Hanson, B., Jones, J.H., 1998. The systematics of Cr^{3+} and Cr^{2+} partitioning between olivine and liquid in the presence of spinel. Am. Mineral. 83 (7–8), 669–684.

Harris, D.C., 1989. The mineralogy and geochemistry of the Hemlo gold deposit. Ontario. Geol. Surv. Canada Econ. Geol. Rep. 38.

Heinrich, C.A., Seward, T.M., 1990. A spectrophotometric study of aqueous iron (II) chloride complexing from 25 to 200 °C. Geochim. Cosmochim. Acta 54, 2207–2221.

Heinrich, C.A., Walshe, J.L., Harrold, B.P., 1996. Chemical mass transfer modelling of ore-forming hydrothermal systems - current practice and problems [review]. Ore Geol. Rev. 10 (3–6), 319–338.

Heinrich, C.A., Driesner, T., Stefansson, A., Seward, T.M., 2004. Magmatic vapor contraction and the transport of gold from the porphyry environment to epithermal ore deposits. Geology 32 (9), 761–764.

Helgeson, H.C., Kirkham, D.H., Flowers, G.C., 1981. Theoretical prediction of the thermodynamic behavior of aqueous electrolytes at high pressures and temperatures: IV. Calculation of activity coefficients, osmotic coefficients, and apparent molal and standard and relative partial molal properties to 600 °C and 5 kb. Am. J. Sci. 281, 1249–1516.

Henley, R.W., Mavrogenes, J., Tanner, D., 2012. Sulfosalt melts and heavy metal (As-Sb-Bi-Sn-Pb-Tl) fractionation during volcanic gas expansion: the El Indio (Chile) paleo-fumarole. Geofluids 12 (3), 199–215.

Hennig, C., Tutschku, J., Rossberg, A., Bernhard, G., Scheinost, A.C., 2005. Comparative EXAFS investigation of uranium(VI) and -(IV) aquo chloro complexes in solution using a newly developed spectroelectrochemical cell. Inorg. Chem. 44 (19), 6655–6661.

Hennig, C., Schmeide, K., Brendler, V., Moll, H., Tsushima, S., Scheinost, A.C., 2007. EXAFS investigation of U(VI), U(IV), and Th(IV) sulfato complexes in aqueous solution. Inorg. Chem. 46 (15), 5882–5892.

Hofer, T.S., Randolf, B.R., Adnan Ali Shah, S., Rode, B.M., Persson, I., 2007. Structure and dynamics of the hydrated palladium(II) ion in aqueous solution A QMCF MD simulation and EXAFS spectroscopic study. Chem. Phys. Lett. 445 (4–6), 193–197.

Hoffmann, M.M., Addleman, R.S., Fulton, J.L., 2000. Short-pathlength, high-pressure flow cell for static and time-resolved infrared spectroscopy suitable for supercritical fluid solutions including hydrothermal systems. Rev. Sci. Instrum. 71 (3), 1552–1556.

Hoffmann, M.M., Darab, J.G., Fulton, J.L., 2001a. An infrared and X-ray absorption study of the equilibria and structures of chromate, bichromate, and dichromate in ambient aqueous solutions. J. Phys. Chem. 105 (10), 1772–1782.

Hoffmann, M.M., Darab, J.G., Fulton, J.L., 2001b. An infrared and X-ray absorption study of the structure and equilibrium of chromate, bichromate, and dichromate in high-temperature aqueous solutions. J. Phys. Chem. A 105 (28), 6876–6885.

Hsu, C.M., Cheng, H.S., Luh, H., Chen, M.Y., 1984. Mössbauer spectroscopic studies of bromostannate(II) complexes in frozen aqueous solutions. J. Chin. Chem. Soc. 31 (J. Chin. Chem. Soc. (Taipei, Taiwan)).

Hurtig, N.C., Williams-Jones, A.E., 2014a. An experimental study of the solubility of MoO_3 in aqueous vapour and low to intermediate density supercritical fluids. Geochim. Cosmochim. Acta 136 (0), 169–193.

Hurtig, N.C., Williams-Jones, A.E., 2014b. An experimental study of the transport of gold through hydration of AuCl in aqueous vapour and vapour-like fluids. Geochim. Cosmochim. Acta 127, 305–325.

Hurtig, N.C., Williams-Jones, A.E., 2015. Porphyry-epithermal Au-Ag-Mo ore formation by vapor-like fluids: New insights from geochemical modeling. Geology 43 (7), 587–590.

Ikeda, A., Hennig, C., Tsushima, S., Takao, K., Ikeda, Y., Scheinost, A.C., Bernhard, G., 2007. Comparative study of uranyl(VI) and -(V) carbonato complexes in an aqueous solution. Inorg. Chem. 46 (10), 4212–4219.

Ikeda-Ohno, A., Hennig, C., Tsushima, S., Scheinost, A.C., Bernhard, G., Yaita, T., 2009. Speciation and structural study of U(IV) and -(VI) in perchloric and nitric acid solutions. Inorg. Chem. 48 (15), 7201–7210.

Jackson, K.J., Helgeson, H.C., 1985. Chemical and thermodynamic constraints on the hydrothermal transport and deposition of tin: I. Calculation of the solubility of cassiterite at high pressures and temperatures. Geochim. Cosmochim. Acta 49 (1), 1–22.

Jalilehvand, F., Laffin, L.J., 2008. Structure of the hydrated platinum(II) ion and the cis-diammineplatinum(II) complex in acidic aqueous solution: an EXAFS study. Inorg. Chem. 47 (8), 3248–3254.

James-Smith, J., Cauzid, J., Testemale, D., Liu, W., Hazemann, J., Proux, O., Etschmann, B., Philippot, P., Banks, D., Williams, P., Brugger, J., 2010. Arsenic speciation in fluid inclusions using micro-beam X-ray absorption spectroscopy. Am. Mineral. 95 (7), 921–932.

Jayanetti, S., Mayanovic, R.A., Anderson, A.J., Bassett, W.A., Chou, I.-M., 2001. Analysis of radiation-induced small Cu particle cluster formation in aqueous $CuCl_2$. J. Chem. Phys. 115, 954–962.

Joly, Y., 2001. X-ray absorption near-edge structure calculations beyond the muffin-tin approximation. Phys. Rev. (B 63), 125120.

Joly, Y., Bunău, O., Lorenzo, J.E., Galera, R.M., Grenier, S., Thompson, B., 2009. Self-consistency, spin-orbit and other advances in the FDMNES code to simulate XANES and RXD experiments. In: A. DiCicco and A. Filipponi (Editors), 14th International Conference on X-ray Absorption Fine Structure. J. Phys. Conf. Ser. 190 (12 pp.).

Kamona, A.F., Gunzel, A., 2007. Stratigraphy and base metal mineralization in the Otavi Mountain Land, northern Namibia - a review and regional interpretation. Gondwana Res. 11 (3), 396–413.

Keays, R.R., Jowitt, S.M., 2013. The Avebury Ni deposit, Tasmania: a case study of an unconventional nickel deposit. Ore Geol. Rev. 52, 4–17.

Klein, F., Bach, W., 2009. Fe-Ni-Co-O-S phase relations in peridotite-seawater interactions. J. Petrol. 50 (1), 37–59.

Knauss, K.G., Dibley, M.J., Bourcier, W.L., Shaw, H.F., 2001. Ti(IV) hydrolysis constants derived from rutile solubility measurements made from 100 to 300 °C. Appl. Geochem. 16 (9–10), 1115–1128.

Kolonin, G.R., Laptev, Y.V., 1982. Study of process of dissolution of α-Bi_2O_3 (bismite) and complex-formation of bismuth in hydrothermal solutions (in Russian). Geokhimiya 11, 1621–1631.

Koplitz, L.V., Mcclure, D.S., Crerar, D.A., 1987. Spectroscopic study of chloroiron(II) complexes in LiCl-DCl-D_2O solutions. Inorg. Chem. 26 (2), 308–313.

Kovalenko, N.I., Ryzhenko, B.N., 1997. Stability constant of SnFCl0 at 500 °C, 1 kbar, and a constant fugacity of H_2 (Ni/NiO buffer). Geokhimiya (8), 872–875.

Kovalenko, N.I., Ryzhenko, B.N., Dorofeeva, V.A., Bannykh, L.N., 1992. Experimental study of stability of $Sn(OH)_4^{2-}$, $Sn(OH)_2F^-$, and $Sn(OH)_2Cl^-$ complexes at 500 °C, 1 kbar. Geokhimiya (1), 88–98.

Krakowiak, J., Lundberg, D., Persson, I., 2012. A coordination chemistry study of hydrated and solvated cationic vanadium ions in oxidation states +III, +IV, and +V in solution and solid state. Inorg. Chem. 51 (18), 9598–9609.

Kramers, J., Frei, R., Newville, M., Kober, B., Villa, I., 2009. On the valency state of radiogenic lead in zircon and its consequences. Chem. Geol. 261 (1–2), 4–10.

Krupp, R., 1988a. Physicochemical aspects of mercury metallogenesis. Chem. Geol. 69, 345–356.

Krupp, R.E., 1988b. Solubility of stibnite in hydrogen sulfide solutions, speciation, and equilibrium constants, from 25 to 350 °C. Geochim. Cosmochim. Acta 52 (12), 3005–3015.

Lambrecht, G., Diamond, L.W., Pettke, T., 2008. Modification of gas speciation in quartz-hosted fluid inclusions by stray laser radiation during LA-ICPMS analysis. Am. Mineral. 93, 1187–1190.

Lennie, A.R., Charnock, J.M., Pattrick, R.A.D., 2003. Structure of mercury(II)–sulfur complexes by EXAFS spectroscopic measurements. Chem. Geol. 199 (3–4), 199–207.

Leung, K., Nenoff, T.M., 2012. Hydration structures of U(III) and U(IV) ions from ab initio molecular dynamics simulations. J. Chem. Phys. 137 (7).

Lim, L.H.V., Hofer, T.S., Pribil, A.B., Rode, B.M., 2009. The hydration structure of Sn(II): an ab initio quantum mechanical charge field molecular dynamics study. J. Phys. Chem. B 113 (13), 4372–4378.

Lindqvist-Reis, P., Munoz-Paez, A., Diaz-Moreno, S., Pattanaik, S., Persson, I., Sandstrom, M., 1998. The structure of the hydrated gallium(III), indium(III), and chromium(III) ions in aqueous solution. A large angle X-ray scattering and EXAFS study. Inorg. Chem. 37 (26), 6675–6683.

Lipin, B.R., McKay, G.A., 1989. Geochemistry and Mineralogy of Rare Earth Elements. Reviews in Mineralogy. Vol. 21. Mineralogical Society of America (348 pp.).

Liu, W., McPhail, D.C., 2005. Thermodynamic properties of copper chloride complexes and copper transport in magmatic-hydrothermal solutions. Chem. Geol. 221 (1–2), 21–39.

Liu, W., McPhail, D.C., Brugger, J., 2001. An experimental study of copper(I)-chloride and copper(I)-acetate complexing in hydrothermal solutions between 50 °C and 250 °C and vapor-saturated pressure. Geochim. Cosmochim. Acta 65 (17), 2937–2948.

Liu, W., Brugger, J., Mcphail, D.C., Spiccia, L., 2002. A spectrophotometric study of aqueous copper(I)-chloride complexes in LiCl solutions between 100 °C and 250 °C. Geochim. Cosmochim. Acta 66 (20), 3615–3633.

Liu, W., Etschmann, B., Brugger, J., Spiccia, L., Foran, G., McInnes, B., 2006. UV–vis spectrophotometric and XAFS studies of ferric chloride complexes in hyper-saline LiCl solutions at 25–90 °C. Chem. Geol. 231 (4), 326–349.

Liu, W., Etschmann, B., Foran, G., Shelley, M., Brugger, J., 2007. Deriving formation constants for aqueous metal complexes from XANES spectra: Zn^{2+} and Fe^{2+} chloride complexes in hypersaline solutions. Am. Mineral. 92 (5–6), 761–770.

Liu, W., Brugger, J., Etschmann, B., Testemale, D., Hazemann, J.-L., 2008. The solubility of nantokite (CuCl(s)) and Cu speciation in low-density fluids near the critical isochore: an in-situ XAS study. Geochim. Cosmochim. Acta 72 (16), 4094–4106.

Liu, X., Lu, X., Jan Meijer, E., Wang, R., 2010. Hydration mechanisms of Cu^{2+}: tetra-, penta- or hexa-coordinated? Phys. Chem. Chem. Phys. 12 (36), 10801–10804.

Liu, W., Borg, S.J., Testemale, D., Etschmann, B., Hazemann, J.-L., Brugger, J., 2011a. Speciation and thermodynamic properties for cobalt chloride complexes in hydrothermal fluids at 35–440 °C and 600 bar: an in-situ XAS study. Geochim. Cosmochim. Acta 75 (5), 1227–1248.

Liu, X., Lu, X., Wang, R., Zhou, H., Xu, S., 2011b. Speciation of gold in hydrosulphide-rich ore-forming fluids: insights from first-principles molecular dynamics simulations. Geochim. Cosmochim. Acta 75 (1), 185–194.

Liu, X.D., Lu, X.C., Wang, R.C., Meijer, E.J., 2011c. Understanding hydration of Zn^{2+} in hydrothermal fluids with ab initio molecular dynamics. Phys. Chem. Chem. Phys. 13 (29), 13305–13309.

Liu, W., Borg, S., Etschmann, B., Mei, Y., Brugger, J., 2012a. An XAS study of speciation and thermodynamic properties of aqueous zinc bromide complexes at 25–150 °C. Chem. Geol. 298, 57–69.

Liu, X., Lu, X., Wang, R., Zhou, H., 2012b. First-principles molecular dynamics study of stepwise hydrolysis reactions of Y^{3+} cations. Chem. Geol. 334, 37–43.

Liu, X., Lu, X., Wang, R., Zhou, H., 2012c. Silver speciation in chloride-containing hydrothermal solutions from first principles molecular dynamics simulations. Chem. Geol. 294–295, 103–112.

Liu, W., Migdisov, A., Williams-Jones, A., 2012d. The stability of aqueous nickel(II) chloride complexes in hydrothermal solutions: results of UV–visible spectroscopic experiments. Geochim. Cosmochim. Acta 94, 276–290.

Liu, X., Cheng, J., Sprik, M., Lu, X., 2013. Solution structures and acidity constants of molybdic acid. J. Phys. Chem. Lett. 4 (17), 2926–2930.

Liu, W., Etschmann, B., Testemale, D., Hazemann, J.-L., Rempel, K., Mueller, H., Brugger, J., 2014. Gold transport in hydrothermal fluids: competition among the Cl−, Br−, HS− and NH$_3$(aq) ligands. Chem. Geol. 376, 11–19.

Liu, W., Etschmann, B., Migdisov, A., Boukhalfa, H., Testemale, D., Mueller, H., Hazemann, J.-L., Brugger, J., 2016. Europium (II) and Europium (III) in hydrothermal fluids: new insight from in-situ XAS experimental results. Goldschmidt 2016, Yokohama, 26 June–1 July 2016.

Loges, A., Migdisov, A.A., Wagner, T., Williams-Jones, A.E., Markl, G., 2013. An experimental study of the aqueous solubility and speciation of Y(III) fluoride at temperatures up to 250 degrees C. Geochim. Cosmochim. Acta 123, 403–415.

Louvel, M., Sanchez-Valle, C., Malfait, W.J., Testemale, D., Hazemann, J.L., 2013. Zr complexation in high pressure fluids and silicate melts and implications for the mobilization of HFSE in subduction zones. Geochim. Cosmochim. Acta 104, 281–299.

Louvel, M., Sanchez-Valle, C., Malfait, W.J., Cardon, H., Testemale, D., Hazemann, J.L., 2014. Constraints on the mobilization of Zr in magmatic-hydrothermal processes in subduction zones from in situ fluid-melt partitioning experiments. Am. Mineral. 99 (8–9), 1616–1625.

Lüdemann, H.D., Franck, E.U., 1967. Absorptionsspektren bei hohen drucken und temperaturen .I. Wassrige CO$_2^-$ und Ni$_2$-halogenid-losungen bis zu 500 °C und 6 kbar. Berichte Der Bunsen-Gesellschaft Fur Physikalische Chemie 71 (5), 455–460.

Lukanin, O.A., Ryzhenko, B.N., Kurovskaya, N.A., 2013. Zn and Pb solubility and speciation in aqueous chloride fluids at T-P parameters corresponding to granitoid magma degassing and crystallization. Geochem. Int. 51 (10), 802–830.

Lundberg, D., Persson, I., Eriksson, L., D'Angelo, P., De Panfilis, S., 2010. Structural study of the N,N′-dimethylpropyleneurea solvated lanthanoid(III) ions in solution and solid state with an analysis of the ionic radii of lanthanoid(III) ions. Inorg. Chem. 49 (10), 4420–4432.

Mackay, D.A.R., Simandl, G.J., 2014. Geology, market and supply chain of niobium and tantalum-a review. Mineral. Deposita 49 (8), 1025–1047.

Magini, M., 1980. X-ray diffraction study of concentrated chromium (III) chloride solutions. 1. Complex formation analysis in equilibrium conditions. J. Chem. Phys. 73, 2499–2505.

Mann, A.W., Deutscher, R.L., 1978. Genesis principles for the precipitation of carnotite in calcrete drainage in Western Australia. Econ. Geol. 73, 1724–1737.

Martin, R.F., Wulser, P.-A., 2014. Niobium and tantalum in minerals: siderophile, chalcophile or lithophile, and polyvalent. J. Geochem. Explor. 147, 16–25.

Masselmann, S., Meyer, G., 1998. Crystal structure of barium heptachloroeuropate(III), Ba$_2$[EuCl$_7$]. Z. Kristallogr. - New Cryst. Struct. 213 (4), 690.

Mavrogenes, J.A., Berry, A.J., Newville, M., Sutton, S.R., 2002. Copper speciation in vapor-phase fluid inclusions from the Mole Granite, Australia. Am. Mineral. 87, 1360–1364.

Mayanovic, R.A., Anderson, A.J., Bassett, W.A., Chou, I.M., 1999. XAFS measurements on zinc chloride aqueous solutions from ambient to supercritical conditions using the diamond anvil cell. J. Synchrotron Radiat. 6 (Part 3), 195–197.

Mayanovic, R.A., Anderson, A.J., Bassett, W.A., Chou, I.M., 2001. Hydrogen bond breaking in aqueous solutions near the critical point. Chem. Phys. Lett. 336 (3–4), 212–218.

Mayanovic, R.A., Jayanetti, S., Anderson, A.J., Bassett, W.A., Chou, I.M., 2002. The structure of Yb^{3+} aquo ion and chloro complexes in aqueous solutions at up to 500 °C and 270 MPa. J. Phys. Chem. A 106 (28), 6591–6599.

Mayanovic, R.A., Anderson, A.J., Bassett, W.A., Chou, I.M., 2007. On the formation and structure of rare-earth element complexes in aqueous solutions under hydrothermal conditions with new data on gadolinium aqua and chloro complexes. Chem. Geol. 239 (3–4), 266–283.

Mayanovic, R.A., Anderson, A.J., Bassett, W.A., Chou, I.M., 2009a. Steric hindrance and the enhanced stability of light rare-earth elements in hydrothermal fluids. Am. Mineral. 94 (10), 1487–1490.

Mayanovic, R.A., Anderson, A.J., Bassett, W.A., Chou, I.M., 2009b. The structure and stability of aqueous rare-earth elements in hydrothermal fluids: new results on neodymium(III) aqua and chloroaqua complexes in aqueous solutions to 500 °C and 520 MPa. Chem. Geol. 259, 30–38.

Mayanovic, R.A., Anderson, A.J., Dharmagunawardhane, H.A.N., Pascarelli, S., Aquilanti, G., 2012. Monitoring synchrotron X-ray-induced radiolysis effects on metal (Fe, W) ions in high-temperature aqueous fluids. J. Synchrotron Radiat. 19, 797–805.

Mayanovic, R.A., Yan, H., Anderson, A.J., Solferino, G., 2013. Investigation of the structural environment of Ta in a silicate glass and water system under high P-T conditions. J. Non-Cryst. Solids 368, 71–78.

McPhail, D.C., 1995. Thermodynamic properties of aqueous tellurium species between 25 °C and 350 °C. Geochim. Cosmochim. Acta 59, 851–866.

Mei, Y., Sherman, D.M., Liu, W.H., Brugger, J., 2013a. Ab initio molecular dynamics simulation and free energy exploration of copper(I) complexation by chloride and bisulfide in hydrothermal fluids. Geochim. Cosmochim. Acta 102, 45–64.

Mei, Y., Sherman, D.M., Liu, W.H., Brugger, J., 2013b. Complexation of gold in S$_3^-$-rich hydrothermal fluids: evidence from ab-initio molecular dynamics simulations. Chem. Geol. 347, 34–42.

Mei, Y., Liu, W.H., Sherman, D.M., Brugger, J., 2014. Metal complexation and ion hydration in low density hydrothermal fluids: ab initio molecular dynamics simulation of Cu(I) and Au(I) in chloride solutions (25–1000 °C, 1–5000 bar). Geochim. Cosmochim. Acta 131, 196–212.

Mei, Y., Etschmann, B., Liu, W., Sherman, D.M., Barnes, S.J., Fiorentini, M.L., Seward, T.M., Testemale, D., Brugger, J., 2015a. Palladium complexation in chloride- and bisulfide-rich fluids: insights from ab initio molecular dynamics simulations and X-ray absorption spectroscopy. Geochim. Cosmochim. Acta 161, 128–145.

Mei, Y., Sherman, D.M., Liu, W., Etschmann, B., Testemale, D., Brugger, J., 2015b. Zinc complexation in chloride-rich hydrothermal fluids (25–600 °C): a thermodynamic model derived from ab initio molecular dynamics. Geochim. Cosmochim. Acta 150, 265–284.

Mei, Y., Etschmann, B., Liu, W., Sherman, D.M., Testemale, D., Brugger, J., 2016. Speciation and thermodynamic properties of zinc in sulfur-rich hydrothermal fluids: insights from ab initio molecular dynamics simulations and X-ray absorption spectroscopy. Geochim. Cosmochim. Acta 179, 32–52.

Melcher, F., 2003. The Otavi mountain land in Namibia—Tsumeb, germanium and snowball Earth. Mitt. Österr. Mineral. Gesellsch. 148, 413–435.

Melchiorre, E.B., Huss, G.R., Lopez, A., 2014. Carbon and hydrogen stable isotope microanalysis and data correction for rare carbonate minerals: case studies for stichtite ($Mg_6Cr_2(OH)_{16}[CO_3 \cdot H_2O$) and malachite ($Cu_2CO_3(OH)_2$). Chem. Geol. 367, 63–69.

Mesu, J.G., van der Eerden, A.M.J., de Groot, F.M.F., Weckhuysen, B.M., 2005. Synchrotron radiation effects on catalytic systems as probed with a combined in-situ UV–vis/XAFS spectroscopic setup. J. Phys. Chem. B 109, 4042–4047.

Mibe, K., Chou, I.-M., Anderson, A.J., Mayanovic, R.A., Bassett, W.A., 2009. The speciation of aqueous zinc(II) bromide solutions to 500 °C and 900 MPa determined using Raman spectroscopy. Chem. Geol. 259, 48–53.

Migdisov, A.A., Williams-Jones, A.E., 2002. A spectrophotometric study of neodymium (III) complexation in chloride solutions. Geochim. Cosmochim. Acta 66, 4311–4323.

Migdisov, A.A., Williams-Jones, A.E., 2006. A spectrophotometric study of erbium (III) speciation in chloride solutions at elevated temperatures. Chem. Geol. 234, 17–27.

Migdisov, A.A., Williams-Jones, A.E., 2007. An experimental study of the solubility and speciation of neodymium (III) fluoride in F-bearing aqueous solutions. Geochim. Cosmochim. Acta 71, 3056–3069.

Migdisov, A.A., Williams-Jones, A.E., 2008. A spectrophotometric study of Nd(III), Sm(III) and Er(III) complexation in sulfate-bearing solutions at elevated temperatures. Geochim. Cosmochim. Acta 72, 5291–5303.

Migdisov, A.A., Williams-Jones, A.E., 2014. Hydrothermal transport and deposition of the rare earth elements by fluorine-bearing aqueous liquids. Mineral. Deposita 49 (8), 987–997.

Migdisov, A.A., Williams-Jones, A.E., Normand, C., Wood, S.A., 2008. A spectrophotometric study of samarium (III) speciation in chloride solutions at elevated temperatures. Geochim. Cosmochim. Acta 72, 1611–1625.

Migdisov, A.A., Williams-Jones, A.E., Wagner, T., 2009. An experimental study of the solubility and speciation of the rare earth elements (III) in fluoride- and chloride-bearing aqueous solutions at temperatures up to 300 °C. Geochim. Cosmochim. Acta 73 (23), 7087–7109.

Migdisov, A.A., Williams-Jones, A.E., van Hinsberg, V., Salvi, S., 2011a. An experimental study of the solubility of baddeleyite (ZrO_2) in fluoride-bearing solutions at elevated temperature. Geochim. Cosmochim. Acta 75 (23), 7426–7434.

Migdisov, A.A., Zezin, D., Williams-Jones, A.E., 2011b. An experimental study of cobalt(II) complexation in Cl- and H_2S-bearing hydrothermal solutions. Geochim. Cosmochim. Acta 75 (14), 4065–4079.

Migdisov, A.A., Bychkov, A.Y., Williams-Jones, A.E., van Hinsberg, V.J., 2014. A predictive model for the transport of copper by HCl-bearing water vapour in ore-forming magmatic-hydrothermal systems: implications for copper porphyry ore formation. Geochim. Cosmochim. Acta 129, 33–53.

Migdisov, A., Williams-Jones, A.E., Brugger, J., Caporuscio, F., 2016. Hydrothermal transport, deposition, and fractionation of REE: experimental data and thermodynamic calculations. Chem. Geol. 439, 13–42.

Migliorati, V., Mancini, G., Tatoli, S., Zitolo, A., Filipponi, A., De Panfilis, S., Di Cicco, A., D'Angelo, P., 2013. Hydration properties of the Zn^{2+} ion in water at high pressure. Inorg. Chem. 52 (2), 1141–1150.

Minubayeva, Z., Seward, T.M., 2010. Molybdic acid ionisation under hydrothermal conditions to 300 °C. Geochim. Cosmochim. Acta 74 (15), 4365–4374.

Mironova, G.D., Zotov, A.V., Gulko, N.I., 1983. Experimental determination of the orpiment solubility in the acidic solutions at 25–150 °C. Geokhimiya (12), 1762–1768.

Moffett, J.W., 1990. Microbially mediated cerium oxidation in seawater. Nature 345, 421–423.

Moll, H., Denecke, M.A., Jalilehvand, F., Sandström, M., Grenthe, I., 1999. Structure of the aqua ions and fluoride complexes of uranium(IV) and thorium(IV) in aqueous solution an EXAFS study. Inorg. Chem. 38 (8), 1795–1799.

Moreau, G., Helm, L., Purans, J., Merbach, A.E., 2002. Structural investigation of the aqueous Eu^{2+} ion: comparison with Sr^{2+} using the XAFS technique. J. Phys. Chem. A 106 (12), 3034–3043.

Mosselmans, J.F.W., Helz, G.R., Pattrick, R.A.D., Charnock, J.M., Vaughan, D.J., 2000. A study of speciation of Sb in bisulfide solutions by X-ray absorption spectroscopy. Appl. Geochem. 15 (6), 879–889.

Muller, B., Seward, T.M., 2001. Spectrophotometric determination of the stability of tin(II) chloride complexes in aqueous solution up to 300 °C. Geochim. Cosmochim. Acta 65 (22), 4187–4199.

Murphy, P.J., Stevens, G., LaGrange, M.S., 2000. The effects of temperature and pressure on gold-chloride speciation in hydrothermal fluids: a Raman spectroscopic study. Geochim. Cosmochim. Acta 64 (3), 479–494.

Narita, H., Tanaka, M., Shiwaku, H., Okamoto, Y., Suzuki, S., Ikeda-Ohno, A., Yaita, T., 2014. Structural properties of the inner coordination sphere of indium chloride complexes in organic and aqueous solutions. Dalton Trans. 43 (4), 1630–1635.

Natrajan, L.S., Swinburne, A.N., Andrews, M.B., Randall, S., Heath, S.L., 2014. Redox and environmentally relevant aspects of actinide(IV) coordination chemistry. Coord. Chem. Rev. 266, 171–193.

Neilson, G.W., Mason, P.E., Ramos, S., Sullivan, D., 2001. Neutron and X-ray scattering studies of hydration in aqueous solutions. Philos. Transact. Math. Phys. Eng. Sci. 359, 1575–1591.

Nekrasov, S.Y., Migdisov, A.A., Williams-Jones, A.E., Bychkov, A.Y., 2013. An experimental study of the solubility of gallium(III) oxide in HCl-bearing water vapour. Geochim. Cosmochim. Acta 119, 137–148.

Nguyen, T.-N., Duvail, M., Villard, A., Molina, J.J., Guilbaud, P., Dufrêche, J.-F., 2015. Multi-scale modelling of uranyl chloride solutions. J. Chem. Phys. 142 (2), 024501.

Nickel, E.H., 1977. Mineralogy of the “green leader” gold ore at Kalgoorlie, Western Australia. Australas. Inst. Min. Metall. 263, 866–871.

Oelkers, E.H., Sherman, D.M., Ragnarsdottir, K.V., Collins, C., 1998. An EXAFS spectroscopic study of aqueous antimony(III)-chloride complexation at temperatures from 25 to 250 °C. Chem. Geol. 151 (1–4), 21–27.

Ohmoto, H., Hayashi, K.-I., Kajisa, Y., 1994. Experimental study of the solubilities of pyrite in NaCl-bearing aqueous solutions at 250–350 °C. Geochim. Cosmochim. Acta 2169–2185.

Ottonello, G., Zuccolini, M.V., 2005. Ab-initio structure, energy and stable Cr isotopes equilibrium fractionation of some geochemically relevant H-O-Cr-Cl complexes. Geochim. Cosmochim. Acta 69 (4), 851–874.

Pabalan, R.T., 1986. Solubility of Cassiterite (SnO_2) in NaCl Solutions From 200–350 °C, With Geologic Applications. Pennsylvania State University (140 pp.).

Palmer, D.A., Wesolowski, D., Mesmer, R.E., 1987. A potentiometric investigation of the hydrolysis of chromate (VI) ion in NaCl media to 175 °C. J. Solut. Chem. 16 (6), 443–463.

Pan, P., Wood, S.A., 1991. Gold-chloride complexes in very acidic aqueous solutions and at temperatures 25–300 °C: a laser Raman spectroscopy study. Geochim. Cosmochim. Acta 55, 2365–2371.

Pan, P., Wood, S.A., 1994. Solubility of Pt and Pd sulfides and Au metal in aqueous bisulfide solutions .2. Results at 200 °C to 350 °C and saturated vapor pressure. Mineral. Deposita 29 (5), 373–390.

Paquette, K., Helz, G., 1995. Solubility of cinnabar (red HgS) and implications for mercury speciation in sulfidic waters. Water Air Soil Pollut. 80, 1053–1056.

Pasquarello, A., Petri, I., Salmon, P.S., Parisel, O., Car, R., Toth, E., Powell, D.H., Fischer, H.E., Helm, L., Merbach, A.E., 2001. First solvation shell of the Cu(II) aqua ion: evidence for fivefold coordination. Science 291 (5505), 856–859.

Pavlova, G.G., Borovikov, A.A., 2010. Silver-antimony deposits of Central Asia: physico-chemical model of formation and sources of mineralisation. Aust. J. Earth Sci. 57 (6), 755–775.

Pearson, R.G., 1963. Hard and soft acids and bases. J. Am. Chem. Soc. 85 (22), 3533–3539.

Peiffert, C., Cuney, M., Nguyentrung, C., 1994. Uranium in granitic magmas .1. Experimental-determination of uranium solubility and fluid-melt partition-coefficients in the uranium oxide haplogranite H_2O-Na_2CO_3 system at 720–770 °C, 2 kbar. Geochim. Cosmochim. Acta 58 (11), 2495–2507.

Peiffert, C., NguyenTrung, C., Cuney, M., 1996. Uranium in granitic magmas .2. Experimental determination of uranium solubility and fluid-melt partition coefficients in the uranium oxide-haplogranite-H_2O-NaX ($X = Cl, F$) system at 770 °C, 2 kbar. Geochim. Cosmochim. Acta 60 (9), 1515–1529.

Persson, I., 2010. Hydrated metal ions in aqueous solution: how regular are their structures? Pure Appl. Chem. 82, 1901–1917.

Persson, I., Jalilehvand, F., Sandstrom, M., 2002. Structure of the solvated thallium(I) ion in aqueous, dimethyl sulfoxide, N,N′-dimethylpropyleneurea, and N,N-dimethylthioformamide solution. Inorg. Chem. 41 (2), 192–197.

Persson, I., D'Angelo, P., De Panfilis, S., Sandstrom, M., Eriksson, L., 2008. Hydration of lanthanoid(III) ions in aqueous solution and crystalline hydrates studied by EXAFS spectroscopy and crystallography: the myth of the “gadolinium break”. Chem. Eur. J. 14 (10), 3056–3066.

Persson, I., Lyczko, K., Lundberg, D., Eriksson, L., Placzek, A., 2011. Coordination chemistry study of hydrated and solvated lead(II) ions in solution and solid state. Inorg. Chem. 50 (3), 1058–1072.

Pester, N.J., Rough, M., Ding, K., Seyfried Jr., W.E., 2011. A new Fe/Mn geothermometer for hydrothermal systems: implications for high-salinity fluids at 13°N on the East Pacific Rise. Geochim. Cosmochim. Acta 75 (24), 7881–7892.

Petit, L., Vuilleumier, R., Maldivi, P., Adamo, C., 2008a. Ab initio molecular dynamics study of a highly concentrated LiCl aqueous solution. J. Chem. Theory Comput. 4 (7), 1040–1048.

Petit, L., Vuilleumier, R., Maldivi, P., Adamo, C., 2008b. Molecular dynamics study of the coordination sphere of trivalent lanthanum in a highly concentrated LiCl aqueous solution: a combined classical and ab initio approach. J. Phys. Chem. B 112 (34), 10603–10607.

Pfund, D.M., Darab, J.G., Fulton, J.L., Ma, Y., 1994. An XAFS study of strontium ions and krypton in supercritical water. J. Phys. Chem. 98 (50), 13102–13107.

Phillips, G.N., Evans, K.A., 2004. Role of CO_2 in the formation of gold deposits. Nature 429, 860–863.

Phillips, G.N., Powell, R., 2015. A practical classification of gold deposits, with a theoretical basis. Ore Geol. Rev. 65, 568–573.

Picard, A., Testemale, D., Hazemann, J.L., Daniel, I., 2012. The influence of high hydrostatic pressure on bacterial dissimilatory iron reduction. Geochim. Cosmochim. Acta 88, 120–129.

Plyasunov, A.V., Ivanov, I.P., 1991. The solubility of zinc oxide in sodium chloride solutions up to 600 °C and 1000 bar. Geochem. Int. 28 (6), 77–90.

Pohl, W.L., 2011. Economic Geology: Principles and Practice. Wiley-Blackwell (680 pp.).

Pokrovski, G.S., Dubessy, J., 2015a. Stability and abundance of the trisulfur radical ion S3^{-} in hydrothermal fluids. Earth Planet. Sci. Lett. 411, 298–309.

Pokrovski, G.S., Dubrovinsky, L.S., 2011. The S3– ion is stable in geological fluids at elevated temperatures and pressures. Science 331 (6020), 1052–1054.

Pokrovski, G.S., Beny, J.M., Zotov, A.V., 1999. Solubility and Raman spectroscopic study of As(III) speciation in organic compound-water solutions. A hydration approach for aqueous arsenic in complex solutions. J. Solut. Chem. 28 (12), 1307–1327.

Pokrovski, G.S., Zakirov, I.V., Roux, J., Testemale, D., Hazemann, J.L., Bychkov, A.Y., Golikova, G.V., 2002. Experimental study of arsenic speciation in vapor phase to 500 °C: implications for As transport and fractionation in low-density crustal fluids and volcanic gases. Geochim. Cosmochim. Acta 66 (19), 3453–3480.

Pokrovski, G.S., Roux, J., Harrichoury, J.C., 2005a. Fluid density control on vapor-liquid partitioning of metals in hydrothermal systems. Geology 33 (8), 657–660.

Pokrovski, G.S., Roux, J., Hazemann, J.L., Testemale, D., 2005b. An X-ray absorption spectroscopy study of argutite solubility and aqueous Ge(IV) speciation in hydrothermal fluids to 500 °C and 400 bar. Chem. Geol. 217 (1–2), 127–145.

Pokrovski, G.S., Borisova, A.Y., Roux, J., Hazemann, J.L., Petdang, A., Tella, M., Testemale, D., 2006. Antimony speciation in saline hydrothermal fluids: a combined X-ray absorption fine structure spectroscopy and solubility study. Geochim. Cosmochim. Acta 70 (16), 4196–4214.

Pokrovski, G.S., Roux, J., Hazemann, J.L., Borisova, A.Y., Gonchar, A.A., Lemeshko, M.P., 2008. In situ X-ray absorption spectroscopy measurement of vapour-brine fractionation of antimony at hydrothermal conditions. Mineral. Mag. 72 (2), 667–681.

Pokrovski, G.S., Tagirov, B.R., Schott, J., Bazarkina, E.F., Hazermann, J.L., Proux, O., 2009a. An in situ X-ray absorption spectroscopy study of gold-chloride complexing in hydrothermal fluids. Chem. Geol. 259 (1–2), 17–29.

Pokrovski, G.S., Tagirov, B.R., Schott, J., Hazemann, J.L., Proux, O., 2009b. A new view on gold speciation in sulfur-bearing hydrothermal fluids from in situ X-ray absorption spectroscopy and quantum-chemical modeling. Geochim. Cosmochim. Acta 73 (18), 5406–5427.

Pokrovski, G.S., Roux, J., Ferlat, G., Jonchiere, R., Seitsonen, A.P., Vuilleumier, R., Hazemann, J.-L., 2013. Silver in geological fluids from in situ X-ray absorption spectroscopy and first-principles molecular dynamics. Geochim. Cosmochim. Acta 106 (0), 501–523.

Pokrovski, G.S., Akinfiev, N.N., Borisova, A.Y., Zotov, A.V., Kouzmanov, K., 2014. Gold speciation and transport in geological fluids: insights from experiments and physical-chemical modeling. In: Garofalo, P., Ripley, E. (Eds.), Gold-transporting Fluids in the Earth's Crust Vol. 402. Geological Society of London Special Publications, pp. 9–70.

Pokrovski, G.S., Kokh, M.A., Guillaume, D., Borisova, A.Y., Gisquet, P., Hazemann, J.-L., Lahera, E., Del Net, W., Proux, O., Testemale, D., Haigis, V., Jonchière, R., Seitsonen, A.P., Ferlat, G., Vuilleumier, R., Saitta, A.M., Boiron, M.-C., Dubessy, J., 2015b. Sulfur radical species form gold deposits on Earth. Proc. Natl. Acad. Sci.:1–6 http://dx.doi.org/10.1073/pnas.1506378112.

Pourtier, E., Devidal, J.-L., Gibert, F., 2010. Solubility measurements of synthetic neodymium monazite as a function of temperature at 2 kbars, and aqueous neodymium speciation in equilibrium with monazite. Geochim. Cosmochim. Acta 74 (6), 1872–1891.

Qian, G., Brugger, J., Testemale, D., Skinner, W., Pring, A., 2013. Formation of As(II)-pyrite during experimental replacement of magnetite under hydrothermal conditions. Geochim. Cosmochim. Acta 100, 1–10.

Radnai, T., Balint, S., Bako, I., Megyes, T., Grosz, T., Pallagi, A., Peintler, G., Palinko, I., Sipos, P., 2014. The structure of hyperalkaline aqueous solutions containing high concentrations of gallium - a solution X-ray diffraction and computational study. Phys. Chem. Chem. Phys. 16, 4023–4032.

Rae, N., Brugger, J., Etschmann, B.E., Liu, W., Mei, Y., 2015. An XAS Study of Lead Speciation in Chloride Solutions Under Hydrothermal Conditions. Goldschmidt 2015, Prague 16–21 August.

Ragnarsdottir, K.V., Oelkers, E.H., Sherman, D.M., Collins, C.R., 1998. Aqueous speciation of yttrium at temperatures from 25 to 340 °C at Psat - an in situ EXAFS study. Chem. Geol. 151 (1–4), 29–39.

Raiteri, P., Gale, J.D., 2010. Water is the key to nonclassical nucleation of amorphous calcium carbonate. J. Am. Chem. Soc. 132, 17623–17634.

Raiteri, P., Gale, J.D., Quigley, D., Rodger, P.M., 2010. Derivation of an accurate force-field for simulating the growth of calcium carbonate from aqueous solution: a new model for the calcite–water interface. J. Phys. Chem. C 114 (13), 5997–6010.

Ravel, B., Newville, M., 2005. ATHENA, ARTEMIS, HEPHAESTUS: data analysis for X-ray absorption spectroscopy using IFEFFIT. J. Synchrotron Radiat. 12, 537–541.

Redkin, A.F., Kostromin, N.P., 2010. On the problem of transport species of tungsten by hydrothermal solutions. Geochem. Int. 48 (10), 988–998.

Rehr, J.J., Kas, J.J., Vila, F.D., Prange, M.P., Jorissen, K., 2010. Parameter-free calculations of X-ray spectra with FEFF9. Phys. Chem. Chem. Phys. 12 (21), 5503–5513.

Reith, F., Campbell, S.G., Ball, A.S., Pring, A., Southam, G., 2014. Platinum in Earth surface environments. Earth-Sci. Rev. 131, 1–21.

Rempel, K.U., Migdisov, A.A., Williams-Jones, A.E., 2006. The solubility and speciation of molybdenum in water vapour at elevated temperatures and pressures: implications for ore genesis. Geochim. Cosmochim. Acta 70 (3), 687–696.

Rempel, K.U., Williams-Jones, A.E., Migdisov, A.A., 2008. The solubility of molybdenum dioxide and trioxide in HCl-bearing water vapour at 350 °C and pressures up to 160 bars. Geochim. Cosmochim. Acta 72 (13), 3074–3083.

Rempel, K.U., Williams-Jones, A.E., Migdisov, A.A., 2009. The partitioning of molybdenum(VI) between aqueous liquid and vapour at temperatures up to 370 °C. Geochim. Cosmochim. Acta 73 (11), 3381–3392.

Renshaw, J.C., Butchins, L.J.C., Livens, F.R., May, I., Charnock, J.M., Lloyd, J.R., 2005. Bioreduction of uranium: environmental implications of a pentavalent intermediate. Environ. Sci. Technol. 39 (15), 5657–5660.

Richard, A., Rozsypal, C., Mercadier, J., Banks, D.A., Cuney, M., Boiron, M.-C., Cathelineau, M., 2012. Giant uranium deposits formed from exceptionally uranium-rich acidic brines. Nat. Geosci. 5 (2), 142–146.

Roberts, M.A., Sankar, G., Thomas, J.M., Jones, R.H., Du, H., Chen, J., Pang, W., Xu, R., 1996. Synthesis and structure of a layered titanosilicate catalyst with five-coordinate titanium. Nature 381 (6581), 401–404.

Robie, R.A., Hemingway, B.S., 1995. Thermodynamic properties of minerals and related substances at 298.15 K and 1 bar (105 pascals) pressure and higher temperatures. U.S. Geol. Surv. Bull. 2131.

Ruaya, J.R., Seward, T.M., 1986. The stability of chlorozinc(II) complexes in hydrothermal solutions up to 350 °C. Geochim. Cosmochim. Acta 50, 651–661.

Rubatto, D., Hermann, J., 2003. Zircon formation during fluid circulation in eclogites (Monviso, Western Alps): implications for Zr and Hf budget in subduction zones. Geochim. Cosmochim. Acta 67, 2173–2187.

Rudolph, W.W., Irmer, G., 2015. Hydration and ion pair formation in aqueous Y^{3+}-salt solutions. Dalton Trans. 44 (42), 18492–18505.

Rudolph, W.W., Pye, C.C., 2000. Raman spectroscopic measurements of scandium(III) hydration in aqueous perchlorate solution and ab initio molecular orbital studies of scandium(III) water clusters: does Sc(III) occur as a hexaaqua complex? J. Phys. Chem. A 104 (8), 1627–1639.

Rudolph, W., Brooker, M.H., Tremaine, P.R., 1997. Raman spectroscopic investigation of aqueous $FeSO_4$ in neutral and acidic solutions from 25 °C to 303 °C - inner- and outer-sphere complexes. J. Solut. Chem. 26 (8), 757–777.

Rudolph, W.W., Brooker, M.H., Tremaine, P., 1999a. Raman- and infrared spectroscopic investigation of aqueous $ZnSO_4$ solutions from 8 °C to 165 °C: inner- and outer-sphere complexes. Z. Phys. Che. Int. J. Res. Phys. Chem. Chem. Phys. 209 (Part 2), 181–207.

Rudolph, W.W., Brooker, M.H., Tremaine, P.R., 1999b. Raman spectroscopy of aqueous $ZnSO_4$ solutions under hydrothermal conditions: solubility, hydrolysis, and sulfate ion pairing. J. Solut. Chem. 28 (5), 621–630.

Saffré, D., Atinault, E., Pin, S., Renault, J.P., Hazemann, J.L., Baldacchino, G., 2011. In-situ UV–visible spectrum acquisition of Br_3^-. Investigations of concentrated HBr aqueous solutions under 13 keV X-rays. J. Phys. Conf. Ser. 261, 12013.

Salvi, S., Williams-Jones, A.E., 1996. The role of hydrothermal processes in concentrating high-field strength elements in the Strange Lake peralkaline complex, northeastern Canada. Geochim. Cosmochim. Acta 60 (11), 1917–1932.

Schwarz-Schampera, U., Herzig, P.M., 2002. Indium: Geology, Mineralogy, and Economics. Springer, Heidelberg.

Schweitzer, G.K., Pesterfield, L.L., 2010. The Aqueous Chemistry of the Elements. Oxford University Press, USA (447 pp.).

Seward, T.M., 1976. The stability of chloride complexes of silver in hydrothermal solutions up to 350 °C. Geochim. Cosmochim. Acta 40 (11), 1329–1341.

Seward, T.M., 1981. Metal complex formation in aqueous solutions at elevated temperatures and pressures. Phys. Chem. Earth 13–14 (0), 113–132.

Seward, T.M., 1984. The formation of lead(II) chloride complexes to 300 °C - a spectrophotometric study. Geochim. Cosmochim. Acta 48 (1), 121–134.

Seward, T.M., Barnes, H.L., 1997. Chapter 9: metal transport by hydrothermal ore fluids. In: Barnes, H.L. (Ed.), Geochemistry of Hydrothermal Ore Deposits. John Wiley & Sons, pp. 435–486.

Seward, T.M., Driesner, T., 2004. Hydrothermal solution structure: experiments and computer simulations. In: Palmer, D.A., Fernández-Prini, R., Havey, A.H. (Eds.), Aqueous Systems at Elevated Temperatures and Pressures: Physical Chemistry in Water, Steam and Hydrothermal Solutions. Elsevier, pp. 149–182.

Seward, T.M., Rickard, D.T., Wickman, F.E., 1981. Metal complex formation in aqueous solutions at elevated temperatures and pressures. Chemistry and geochemistry of solutions at high temperatures and pressures. Proceedings of a Nobel Symposium Organised by the Royal Swedish Academy of Sciences. Chemistry and Geochemistry of Solutions at High Temperatures and Pressures. Nobel Symposium Vols. 13–14, pp. 113–132.

Seward, T.M., Henderson, C.M.B., Charnock, J.M., 1993. An X-ray absorption spectroscopic study of aqueous $CdCl_2$ to 250 °C. In: Dobson, B.R.e., Lorrain., p.-I., Cathelineau, M.C.a.M. (Eds.), Proceedings of the 4th International Symposium on Hydrothetmal Reactions. Institut Lorrain, pp. 231–233.

Seward, T.M., Henderson, C.M.B., Charnock, J.M., Dobson, B.R., 1995. The hydration of metal cations in hydrothermal solutions: recent EXAFS results. Water-Rock Interact. 8, 43–46.

Seward, T.M., Henderson, C.M.B., Charnock, J.M., Dobson, B.R., 1996. An X-ray absorption (EXAFS) spectroscopic study of aquated Ag^+ in hydrothermal solutions to 350 °C. Geochim. Cosmochim. Acta 60 (13), 2273–2282.

Seward, T.M., Henderson, C.M.B., Charnock, J.M., 2000. Indium(III) chloride complexing and solvation in hydrothermal solutions to 350 °C: an EXAFS study. Chem. Geol. 167 (1–2), 117–127.

Shannon, R.D., 1976. Revised effective ionic radii and systematic studies of interatomic distances in halides and chalcogenides. Acta Crystallogr. A32, 751–767.

Sheard, E.R., Williams-Jones, A.E., Heiligmann, M., Pederson, C., Trueman, D.L., 2012. Controls on the concentration of zirconium, niobium, and the rare earth elements in the Thor Lake rare metal deposit, Northwest Territories, Canada. Econ. Geol. 107 (1), 81–104.

Sherman, D.M., 2007. Complexation of Cu^+ in hydrothermal NaCl brines: ab initio molecular dynamics and energetics. Geochim. Cosmochim. Acta 71 (3), 714–722.

Sherman, D.M., 2010. Metal complexation and ion association in hydrothermal fluids: insights from quantum chemistry and molecular dynamics. Geofluids 10 (1–2), 41–57.

Sherman, D.M., Collings, M.D., 2002. Ion association in concentrated NaCl brines from ambient to supercritical conditions: results from classical molecular dynamics simulations. Geochem. Trans. 3 (11), 102–107.

Sherman, D.M., Ragnarsdottir, K.V., Oelkers, E.H., 2000a. Antimony transport in hydrothermal solutions: an EXAFS study of antimony(V) complexation in alkaline sulfide and sulfide–chloride brines at temperatures from 25 °C to 300 °C at Psat. Chem. Geol. 167 (1–2), 161–167.

Sherman, D.M., Ragnarsdottir, K.V., Oelkers, E.H., Collins, C.R., 2000b. Speciation of tin (Sn^{2+} and Sn^{4+}) in aqueous Cl solutions from 25 °C to 350 °C: an in situ EXAFS study. Chem. Geol. 167 (1–2), 169–176.

Shock, E.L., Sassani, D.C., Betz, H., 1997a. Uranium in geologic fluids - estimates of standard partial molal properties, oxidation potentials, and hydrolysis constants at high temperatures and pressures. Geochim. Cosmochim. Acta 61 (20), 4245–4266.

Shock, E.L., Sassani, D.C., Willis, M., Sverjensky, D.A., 1997b. Inorganic species in geologic fluids - correlations among standard molal thermodynamic properties of aqueous ions and hydroxide complexes. Geochim. Cosmochim. Acta 61 (5), 907–950.

Shvarov, Y., Bastrakov, E., 1999. HCh: a software package for geochemical modelling. User's Guide. AGSO Record. Vol. 1999/25 (60 pp.).

Simon, G., Essene, E.J., 1996. Phase relations among selenides, sulfides, tellurides, and oxides; I, thermodynamic properties and calculated equilibria. Econ. Geol. 91 (7), 1183–1208.

Simon, A.C., Pettke, T., Candela, P.A., Piccoli, P.M., Heinrich, C.A., 2007. The partitioning behavior of As and Au in S-free and S-bearing magmatic assemblages. Geochim. Cosmochim. Acta 71 (7), 1764–1782.

Skirrow, R.G., Walshe, J.L., 2002. Reduced and oxidized Au-Cu-Bi iron oxide deposits of the Tennant Creek inlier, Australia: an integrated geologic and chemical model. Econ. Geol. Bull. Soc. Econ. Geol. 97 (6), 1167–1202.

Smith, D.W., 1976. Chlorocuprates(II). Coord. Chem. Rev. 21, 93–158.

Smith, C.G., 2001. Always the bridesmaid, never the bride: cobalt geology and resources. Trans. Inst. Min. Metall., Sect. B Appl. Earth Sci. 110, B75–B80.

Smith, D.E., Dang, L.X., 1994. Computer simulations of NaCl association in polarizable water. J. Chem. Phys. 100 (5), 3757–3766.

Spieker, W.A., Liu, J., Miller, J.T., Kropf, A.J., Regalbuto, J.R., 2002. An EXAFS study of the coordination chemistry of hydrogen hexachloroplatinate(IV): 1. Speciation in aqueous solution. Appl. Catal. A Gen. 232 (1–2), 219–235.

Spry, P.G., Scherbarth, N.L., 2006. The gold–vanadium–tellurium association at the Tuvatu gold–silver prospect, Fiji: conditions of ore deposition. Mineral. Petrol. 87 (3–4), 171–186.

Spycher, N.F., Reed, M.H., 1989. As (III) and Sb(III) sulfide complexes: an evaluation of stoichiometry and stability from existing experimental data. Geochim. Cosmochim. Acta 53 (9), 2185–2194.

Stefánsson, A., Seward, T.M., 2003a. Experimental determination of the stability and stoichiometry of sulphide complexes of silver(I) in hydrothermal solutions to 400 °C. Geochim. Cosmochim. Acta 67 (7), 1395–1413.

Stefánsson, A., Seward, T.M., 2003b. The hydrolysis of gold(I) in aqueous solutions to 600 °C and 1500 bar. Geochim. Cosmochim. Acta 9, 1677–1688.

Stefánsson, A., Seward, T.M., 2003c. Stability of chloridogold(I) complexes in aqueous solutions from 300 to 600 °C and from 500 to 1800 bar. Geochim. Cosmochim. Acta 67, 4559–4576.

Stefánsson, A., Seward, T.M., 2004. Gold(I) complexing in aqueous sulphide solutions to 500 °C at 500 bar. Geochim. Cosmochim. Acta 68, 4121–4143.

Stünzi, H., Marty, W., 1983. Early stages of the hydrolysis of chromium(III) in aqueous solution. 1. Characterization of a tetrameric species. Inorg. Chem. 33, 2145–2150.

Suleimenov, O.M., 2004. Simple, compact, flow-through, high temperature high pressure cell for UV–vis spectrophotometry. Rev. Sci. Instrum. 75, 3363–3364.

Suleimenov, O.M., Seward, T.M., 2000. Spectrophotometric measurements of metal complex formation at high temperatures: the stability of Mn(II) chloride species. Chem. Geol. 167, 177–192.

Susak, N.J., Crerar, D.A., 1985. Spectra and coordination changes of transition metals in hydrothermal solutions: implications for ore genesis. Geochim. Cosmochim. Acta 49 (2), 555–564.

Sutton, S.R., Karner, J., Papike, J., Delaney, J.S., Shearer, C., Newville, M., Eng, P., Rivers, M., Dyar, M.D., 2005. Vanadium K edge XANES of synthetic and natural basaltic glasses and application to microscale oxygen barometry. Geochim. Cosmochim. Acta 69 (9), 2333–2348.

Sverjensky, D.A., 1984. Europium redox equilibria in aqueous solution. Earth and planet. Sci. Lett. 67 (1), 70–78.

Sverjensky, D.A., 1986. Genesis of Mississippi Valley type lead-zinc deposits. Annu. Rev. Earth Planet. Sci. 14, 177–199.

Sverjensky, D.A., 1987. The role of migrating oil field brines in the formation of sediment-hosted Cu-rich deposits. Econ. Geol. 82, 1130–1141.

Sverjensky, D., Shock, E., Helgeson, H., 1997. Prediction of the thermodynamic properties of aqueous metal complexes to 1000 °C and 5 kbar. Geochim. Cosmochim. Acta 61 (7), 1359–1412.

Sverjensky, D.A., Harrison, B., Azzolini, D., 2014a. Water in the deep Earth: the dielectric constant and the solubilities of quartz and corundum to 60 kb and 1200 °C. Geochim. Cosmochim. Acta 129, 125–145.

Sverjensky, D.A., Stagno, V., Huang, F., 2014b. Important role for organic carbon in subduction-zone fluids in the deep carbon cycle. Nat. Geosci. 7 (12), 909–913.

Ta, C., Reith, F., Brugger, J., Pring, A., Lenehan, C.E., 2014. Analysis of gold(I/III)-complexes by HPLC–ICP-MS demonstrates gold(III) stability in surface waters. Environ. Sci. Technol. 48 (10), 5737–5744.

Ta, C., Brugger, J., Pring, A., Hocking, R.K., Lenehan, C.E., Reith, F., 2015. Effect of manganese oxide minerals and complexes on gold mobilization and speciation. Chem. Geol. 407, 10–20.

Tagirov, B.R., Seward, T.M., 2010. Hydrosulfide/sulfide complexes of zinc to 250 °C and the thermodynamic properties of sphalerite. Chem. Geol. 269, 301–311.

Tagirov, B.R., Baranova, N.N., Zotov, A.V., Akinfiev, N.N., Polotnyanko, N.A., Shikina, N.D., Koroleva, L.A., Shvarov, Y.V., Bastrakov, E.N., 2013. The speciation and transport of palladium in hydrothermal fluids: experimental modeling and thermodynamic constraints. Geochim. Cosmochim. Acta 117, 348–373.

Tanis, E.A., Simon, A., Tschauner, O., Chow, P., Xiao, Y., Burnley, P., Cline II, C.J., Hanchar, J.M., Pettke, T., Shen, G., Zhao, Y., 2015. The mobility of Nb in rutile-saturated $NaCl^-$ and NaF-bearing aqueous fluids from 1–6.5 GPa and 300–800 degrees C. Am. Mineral. 100 (7), 1600–1609.

Tanger, J.C., Helgeson, H.C., 1988. Calculation of the thermodynamic and transport properties of aqueous species at high pressures and temperatures: Revised equations of state for the standard partial molal properties of ions and electrolytes. Am. J. Sci. 288, 19–98.

Tarnopolskaia, M.E., Bychkov, A.Y., Shvarov, Y.V., 2016. Experimental study of gallium oxide solubility in chloride solutions at 300–400 °C. Geochem. Int. 54 (7), 640–644.

Taylor, M.J., Coddington, J.M., 1992. The constitution of aqueous tin(IV) chloride and bromide solutions and solvent extracts studied by ^{119}Sn NMR and vibrational spectroscopy. Polyhedron 11, 1531–1544.

Taylor, J.R., Wall, V.J., 1993. Cassiterite solubility, tin speciation, and transport in a magmatic aqueous phase. Econ. Geol. Bull. Soc. Econ. Geol. 88 (2), 437–460.

Tella, M., Pokrovski, G.S., 2008. Antimony(V) complexing with O-bearing organic ligands in aqueous solution: an X-ray absorption fine structure spectroscopy and potentiometric study. Mineral. Mag. 72 (1), 205–209.

Testemale, D., Hazemann, J.L., Pokrovski, G.S., Joly, Y., Roux, J., Argoud, R., Geaymond, O., 2004. Structural and electronic evolution of the $As(OH)_3$ molecule in high temperature aqueous solutions: an X-ray absorption investigation. J. Chem. Phys. 121 (18), 8973–8982.

Testemale, D., Argoud, R., Geaymond, O., Hazemann, J.L., 2005. High pressure high temperature cell for X-ray absorption and scattering techniques. Rev. Sci. Instrum. 76 (4).

Testemale, D., Brugger, J., Liu, W., Etschmann, B., Hazemann, J., 2009a. In-situ X-ray absorption study of iron(II) speciation in brines up to supercritical conditions. Chem. Geol. 264 (1–4), 295–310.

Testemale, D., Dufaud, F., Martinez, I., Benezeth, P., Hazemann, J.L., Schott, J., Guyot, F., 2009b. An X-ray absorption study of the dissolution of siderite at 300 bar between 50 °C and 100 °C. Chem. Geol. 259 (1–2), 8–16.

Testemale, D., Pokrovski, G.S., Hazemann, J.L., 2011. Speciation of As(III) and As(V) in hydrothermal fluids by in situ X-ray absorption spectroscopy. Eur. J. Mineral. 23 (3), 379–390.

Testemale, D., Prat, A., Lahera, E., Hazemann, J.-L., 2016a. Novel high-pressure windows made of glass-like carbon for X-ray analysis. Rev. Sci. Instrum. 87, 75115.

Testemale, D., Sanchez-Valle, C., Goujon, C., Pokrovski, G.S., Guyot, F., 2016b. Speciation and solubility of Fe(III) in crustal fluids. Goldschmidt Conference Abstract, Yokohama 2016.

Tian, Y., Etschmann, B., Liu, W., Borg, S., Mei, Y., Testemale, D., O'Neill, B., Rae, N., Sherman, D.M., Ngothai, Y., Johannessen, B., Glover, C., Brugger, J., 2012. Speciation of nickel (II) chloride complexes in hydrothermal fluids: in situ XAS study. Chem. Geol. 334, 345–363.

Tian, Y., Etschmann, B., Mei, Y., Grundler, P.V., Testemale, D., Hazemann, J.-L., Elliott, P., Ngothai, Y., Brugger, J., 2014. Speciation and thermodynamic properties of manganese(II) chloride complexes in hydrothermal fluids: in situ XAS study. Geochim. Cosmochim. Acta 129, 77–95.

Timofeev, A., Migdisov, A.A., Williams-Jones, A.E., 2015. An experimental study of the solubility and speciation of niobium in fluoride-bearing aqueous solutions at elevated temperature. Geochim. Cosmochim. Acta 158, 103–111.

Tomkins, A.G., Mavrogenes, J.A., 2002. Mobilization of gold as a polymetallic melt during pelite anatexis at the Challenger deposit, South Australia: a metamorphosed Archean gold deposit. Econ. Geol. Bull. Soc. Econ. Geol. 97 (6), 1249–1271.

Tomkins, A.G., Pattison, D.R.M., Zaleski, E., 2004. The Hemlo gold deposit, Ontario: an example of melting and mobilization of a precious metal-sulfosalt assemblage during amphibolite facies metamorphism and deformation. Econ. Geol. 99 (6), 1063–1084.

Tooth, B., Ciobanu, C.L., Green, L., O'Neill, B., Brugger, J., 2011. Bi-melt formation and gold scavenging from hydrothermal fluids: an experimental study. Geochim. Cosmochim. Acta 75 (19), 5423–5443.

Tooth, B., Etschmann, B., Pokrovski, G.S., Testemale, D., Hazemann, J.L., Grundler, P.V., Brugger, J., 2013. Bismuth speciation in hydrothermal fluids: an X-ray absorption spectroscopy and solubility study. Geochim. Cosmochim. Acta 101, 156–172.

Tormanen, T.O., Koski, R.A., 2005. Gold enrichment and the Bi-Au association in pyrrhotite-rich massive sulfide deposits, Escanaba trough, southern Gorda Ridge. Econ. Geol. 100 (6), 1135–1150.

Tossell, J.A., 1991. Calculations of the structures, stabilities, and Raman and zinc NMR spectra of zinc aqua chloride $ZnCln(OH_2)_a^{2-n}$ species in aqueous solution. J. Phys. Chem. 95 (1), 366–371.

Tossell, J.A., 1994. The speciation of antimony in sulfidic solutions: a theoretical study. Geochim. Cosmochim. Acta 58 (23), 5093–5104.

Tossell, J.A., Vaughan, D.J., 1993. Bisulfide complexes of zinc and cadmium in aqueous solution: calculation of structure, stability, vibrational, and NMR spectra, and of speciation on sulfide mineral surfaces. Geochim. Cosmochim. Acta 57 (9), 1935–1945.

Trefry, J.H., Metz, S., 1989. Role of hydrothermal precipitates in the geochemical cycling of vanadium. Nature 342, 531–533.

Ulrich, T., Mavrogenes, J., 2008. An experimental study of the solubility of molybdenum in H_2O and KCl-H_2O solutions from 500 °C to 800 °C, and 150 to 300 MPa. Geochim. Cosmochim. Acta 72 (9), 2316–2330.

Underwood, C.C., McMillen, C.D., Chen, H.Y., Anker, J.N., Kolis, J.W., 2013. Hydrothermal chemistry, structures, and luminescence studies of alkali hafnium fluorides. Inorg. Chem. 52 (1), 237–244.

Usher, A., Mcphail, D., Brugger, J., 2009. A spectrophotometric study of aqueous Au(III) halide-hydroxide complexes at 25–80 °C. Geochim. Cosmochim. Acta 73 (11), 3359–3380.

Vallet, V., Wahlgren, U., Schimmelpfennig, B., Moll, H., Szabo, Z., Grenthe, I., 2001. Solvent effects on uranium(VI) fluoride and hydroxide complexes studied by EXAFS and quantum chemistry. Inorg. Chem. 40 (14), 3516–3525.

Van Baalen, M.R., 1993. Titanium mobility in metamorphic systems: a review. Chem. Geol. 110, 233–249.

van Sijl, J., Allan, N.L., Davies, G.R., Westrenen, W.v., 2009. Molecular modelling of rare earth element complexation in subduction zone fluids. Geochim. Cosmochim. Acta 73 (13), 3934–3947.

van Sijl, J., Allan, N.L., Davies, G.R., van Westrenen, W., 2010. Titanium in subduction zone fluids: first insights from ab initio molecular metadynamics simulations. Geochim. Cosmochim. Acta 74 (9), 2797–2810.

van Sijl, J., Allan, N.L., Davies, G.R., van Westrenen, W., 2011. Solvation of Ti(IV) in aqueous solution under ambient and supercritical conditions. Phys. Chem. Chem. Phys. 13 (16), 7371–7377.

Vanýsek, P., 2011. Electrochemical Series, Handbook of Chemistry and Physics. 92nd Edition. Chemical Rubber Company.

Varekamp, J.C., Buseck, P.R., 1984. The speciation of mercury in hydrothermal systems, with applications to ore deposition. Geochim. Cosmochim. Acta 48, 177–185.

Vchirawongkwin, V., Hofer, T.S., Randolf, B.R., Rode, B.M., 2007. Tl(I) - the strongest structure-breaking metal ion in water? A quantum mechanical/molecular mechanical simulation study. J. Comput. Chem. 28 (6), 1006–1016.

VillafuerteCastrejon, M.E., Estrada, M.R., GomezLara, J., Duque, J., Pomes, R., 1997. Crystal structure of Cs_2KTbCl_6 and Cs_2KEuCl_6 by powder X-ray diffraction. J. Solid State Chem. 132 (1), 1–5.

Vogel, D.J., Kilin, D.S., 2014. Electron Dynamics of Solvated $Ti(OH)_4$. MRS Proceedings, 1647.

Von Damm, K.L., 1995. Controls on the chemistry and temporal variability of seafloor hydrothermal fluids. In: Humphris, S.E.e., Zierenberg, R.A.e., Mullineaux, L.S.e., Thomson, R.E.e. (Eds.), Seafloor Hydrothermal Systems; Physical, Chemical, Biological, and Geological Interactions. Geophysical Monograph, Big Sky, MT, United States, pp. 222–247.

Wagman, D.D., Evans, W.H., Parker, V.B., Schumm, R.H., Halow, I., Bailey, S.M., Churney, K.L., Nuttall, R.L., 1982. The NBS tables of chemical thermodynamic properties, selected values for inorganic and C1 and C2 organic substances in SI units. J. Phys. Chem. Ref. Data 11 (Suppl. 2) (392 pp.).

Wallen, S.L., Pfund, D.M., Fulton, J.L., Yonker, C.R., Newville, M., Ma, Y.J., 1996. High-pressure, capillary X-ray absorption fine structure cell for studies of liquid and supercritical fluid solutions. Rev. Sci. Instrum. 67 (8), 2843–2845.

Watenphul, A., Schmidt, C., Jahn, S., 2014. Cr(III) solubility in aqueous fluids at high pressures and temperatures. Geochim. Cosmochim. Acta 126, 212–227.

Werner, A., 1893. Beitrag zur Konstitution anorganischer Verbindungen (in German). Z. Anorg. Chem. 3, 267–330.

Wesolowski, D., Drummond, S.E., Mesmer, R.E., Ohmoto, H., 1984. Hydrolysis equilibria of tungsten(VI) in aqueous sodium chloride solutions to 300 °C. Inorg. Chem. 23 (8), 1120–1132.

Wilke, M., Schmidt, C., Dubrail, J., Appel, K., Borchert, M., Kvashnina, K., Manning, C.E., 2012. Zircon solubility and zirconium complexation in $H_2O + Na_2O + SiO_2 \pm Al_2O_3$ fluids at high pressure and temperature. Earth Planet. Sci. Lett. 349, 15–25.

Williams-Jones, A.E., Heinrich, C.A., 2005. 100th anniversary special paper: vapor transport of metals and the formation of magmatic-hydrothermal ore deposits. Econ. Geol. 100 (7), 1287–1312.

Williams-Jones, A.E., Bowell, R.J., Migdisov, A.A., 2009. Gold in solution. Elements 5 (5), 281–287.

Williams-Jones, A.E., Migdisov, A.A., Samson, I.M., 2012. Hydrothermal mobilisation of the rare earth elements - a tale of “Ceria” and “Yttria”. Elements 8 (5), 355–360.

Wilson, G.A., Eugster, H.P., 1990. Cassiterite solubility and tin speciation in supercritical chloride solutions. Geochem. Soc. Spec. Pub. Geochem. Soc. 2, 179–195.

Wilson, N., Webster-Brown, J., Brown, K., 2007. Controls on stibnite precipitation at two New Zealand geothermal power stations. Geothermics 36 (4), 330–347.

Wong, J., Lytle, F.W., Messmer, R.P., Maylotte, D.H., 1984. X-edge absorption spectra of selected vanadium compounds. Phys. Rev. B 30, 5596–5610.

Wood, S.A., 1989. Raman spectroscopic determination of the speciation of ore metals in hydrothermal solutions: I. Speciation of antimony in alkaline sulfide solutions at 25 °C. Geochim. Cosmochim. Acta 53 (2), 237–244.

Wood, S.A., 1992. Experimental determination of the solubility of $WO_3(s)$ and the thermodynamic properties of $H_2WO_4(aq)$ in the range 300–600 °C at 1 kbar: calculation of scheelite solubility. Geochim. Cosmochim. Acta 56 (5), 1827–1836.

Wood, S.A., Samson, I.M., 2000. The hydrothermal geochemistry of tungsten in granitoid environments: I. Relative solubilities of ferberite and scheelite as a function of T, P, pH, and m(NaCl). Econ. Geol. Bull. Soc. Econ. Geol. 95 (1), 143–182.

Wood, S.A., Samson, I.M., 2006. The aqueous geochemistry of gallium, germanium, indium and scandium. Ore Geol. Rev. 28 (1), 57–102.

Wood, S.A., Vlassopoulos, D., 1989. Experimental determination of the hydrothermal solubility and speciation of tungsten at 500 °C and 1 kbar. Geochim. Cosmochim. Acta 53 (2), 303–312.

Wood, S.A., Mountain, B.W., Pan, P., 1992. The aqueous geochemistry of platinum, palladium and gold - recent experimental constraints and a reevaluation of theoretical predictions. Can. Mineral. 30, 955–982.

Wood, S.A., Pan, P., Zhang, Y., Mucci, A., 1994. The solubility of Pt and Pd sulfides and Au in bisulfide solutions .1. Results at 25–90 °C and 1 bar pressure. Mineral. Deposita 29 (4), 309–317.

Woodward, L.A., Nord, A.A., 1956. Raman spectrum of tetrachlorogallate ion ($GaCl_4^{2-}$) in aqueous solution. J. Chem. Soc. Econ. Geol. Spec. Pub. 3721–3722.

Xiong, Y.L., 2003. Predicted equilibrium constants for solid and aqueous selenium species to 300 °C: applications to selenium-rich mineral deposits. Ore Geol. Rev. 23 (3–4), 259–276.

Xiong, Y., 2007. Hydrothermal thallium mineralization up to 300 °C: a thermodynamic approach. Ore Geol. Rev. 32 (1–2), 291–313.

Xiong, Y., Wood, S.A., 1998. Experimental evidence for the mobility of Os under hydrothermal conditions. The Geological Society of South Africa and the South African Institute of Mining and Metallurgy: 8th International Platinum Symposium. Symp. Ser. S18, 457–459.

Xiong, Y.L., Wood, S.A., 1999. Experimental determination of the solubility of ReO_2 and the dominant oxidation state of rhenium in hydrothermal solutions. Chem. Geol. 158 (3–4), 245–256.

Xiong, Y.L., Wood, S.A., 2001. Hydrothermal transport and deposition of rhenium under subcritical conditions (up to 200 °C) in light of experimental studies. Econ. Geol. Bull. Soc. Econ. Geol. 96 (6), 1429–1444.

Yamaguchi, T., Lindqvist, O., Claeson, T., Boyce, J.B., 1982. EXAFS and X-ray-diffraction studies of the hydration structure of stereochemically active Sn(II) ions in aqueous-solution. Chem. Phys. Lett. 93 (6), 528–532.

Yamaguchi, T., Lindqvist, O., Boyce, J.B., Claeson, T., 1984. Determination of the hydration structure of silver ions in aqueous silver perchlorate and nitrate solutions from EXAFS using synchrotron radiation. Acta Chem. Scand. Ser. A 38 (6), 423–428.

Yang, T., Tsushima, S., Suzuki, A., 2002. Chloride concentration and temperature effects on the hydration of Th(IV) ion: a molecular dynamics simulation. Chem. Phys. Lett. 360 (5–6), 534–542.

Yardley, B.W.D., 2005. Metal concentrations in crustal fluids and their relationship to ore formation. Econ. Geol. 100, 613–632.

Yin, R., Wang, R.C., Zhang, A.-C., Hu, H., Zhu, J.C., Rao, C., Zhang, H., 2013. Extreme fractionation from zircon to hafnon in the Koktokay No. 1 granitic pegmatite, Altai, northwestern China. Am. Mineral. 98 (10), 1714–1724.

Zajacz, Z., Seo, J.H., Candela, P.A., Piccoli, P.M., Heinrich, C.A., Guillong, M., 2010. Alkali metals control the release of gold from volatile-rich magmas. Earth Planet. Sci. Lett. 297 (1–2), 50–56.

Zajacz, Z., Seo, J.H., Candela, P.A., Piccoli, P.M., Tossell, J.A., 2011. The solubility of copper in high-temperature magmatic vapors: a quest for the significance of various chloride and sulfide complexes. Geochim. Cosmochim. Acta 75 (10), 2811–2827.

Zakaznova-Herzog, V.P., Seward, T.M., Suleimenov, O.M., 2006. Arsenous acid ionisation in aqueous solutions from 25 to 300 °C. Geochim. Cosmochim. Acta 70 (8), 1928–1938.

Zaraisky, G.P., Korzhinskaya, V., Kotova, N., 2010. Experimental studies of Ta_2O_5 and columbite-tantalite solubility in fluoride solutions from 300 to 550 °C and 50 to 100 MPa. Mineral. Petrol. 99 (3–4), 287–300.

Zhang, L., Audétat, A., Dolejš, D., 2012. Solubility of molybdenite (MoS_2) in aqueous fluids at 600–800 °C, 200 MPa: a synthetic fluid inclusion study. Geochim. Cosmochim. Acta 77, 175–185.

Zhang, N., Brugger, J., Etschmann, B., Ngothai, Y., Zeng, D., 2015a. Thermodynamic modeling of poorly complexing metals in concentrated electrolyte solutions: an X-ray absorption and UV–vis spectroscopic study of Ni(II) in the $NiCl_2$-$MgCl_2$-H_2O system. PLoS One 10 (4).

Zhang, N., Zeng, D., Brugger, J., Zhou, Q., Ngothai, Y., 2015b. Effect of solvent activity on solute association: the formation of aqueous nickel(II) chloride complexes studied by UV–vis and EXAFS spectroscopy. J. Solut. Chem. 44, 1320–1338.

Zhao, R., Pan, P., 2001. A spectrophotometric study of Fe(II)-chloride complexes in aqueous solutions from 10 to 100 °C. Can. J. Chem. 79, 131–144.

Zhong, R., Brugger, J., Chen, Y., Li, W., 2015a. Contrasting regimes of Cu, Zn and Pb transport in ore-forming hydrothermal fluids. Chem. Geol. 395, 154–164.

Zhong, R., Brugger, J., Tomkins, A.G., Chen, Y., Li, W., 2015b. Fate of gold and base metals during metamorphic devolatilization of a pelite. Geochim. Cosmochim. Acta 171, 338–352.

Zotov, A., Kudrin, A., Levin, K., Shikina, N., Var'yash, L., 1995. Experimental studies of the solubility and complexing of selected ore elements (Au, Ag, Cu, Mo, As, Sb, Hg) in aqueous solutions. In: Shmulovich, K.I., Yardley, B.W.D., Gonchar, G.G. (Eds.), Fluids in the Crust. Springer, Netherlands, pp. 95–137.

1.4.3 The autoclave equipment installed at FAME beamlines

Collaborations:

- *Local: FAME staff (E. Lahera, W. Delnet, I. Kieffer, O. Proux)*

As a complement to the above review, and to comply with the objective of this section to summarize the last 15 years studying metal speciation by XAS, figure 1.10 is an adaptation of the figure 16 from reference (25) above, that visually shows the different elements that were investigated in this period with our equipment at FAME beamlines. Transition metals and metalloids are the most investigated, and the trend is now on Rare Earth Elements and Lanthanides (see the perspectives further down). A study was also recently published (independently from me and my collaborators) by B. von der Heyden in *Ore Geology Reviews* (42) which (sic) "*seeks to critically review and highlight the power and affordances of synchrotron X-ray techniques specifically to the fields of fundamental- and applied ore geology*". In this work, the author compiled a database of the ore related studies which made use of synchrotron techniques. From this database it is indeed obvious that from year 2005 the most used beamline in that scientific field is FAME (BM30-B at ESRF). The reason is quite simple: we took our autoclave set-up which was operational, and made it available to the users of the beamline. And from that period, the many requirements by the users and thousands of hours of operation forced us to improve its safety, its reliability, its user-friendliness, its cost effectivity, etc. These improvements in turn motivated the users to come back, and so on. FAME beamlines are a national CNRS Earth Sciences platform, and as such we are firm believers in the relevance and effectiveness of open access and collaboration. Based on his quite exhaustive database (available as a spreadsheet in the supplementary material of the publication (42)), B. von der Heyden concludes that

> "certain beamlines are favoured for ore related research because their associated end-stations are equipped with unique experimental equipment or with unique detectors. From the compiled database (Supplementary Material), BM30-B at the ESRF is the most highly utilised beamline for ore related research. This is attributed to the large number of XANES and EXAFS experiments that have conducted at this beamline using the available high pressure/high temperature autoclave equipment (Fig. 6a; (Testemale et al., 2005)). These experiments investigate the solubility, redox chemistry, and coordination environment of metal ligand complexes under temperature and pressure conditions typical of ore-forming hydrothermal fluids (e.g., 30–600 °C and 0.1–200 MPa). This experimental design has been useful in establishing the stability and complexation behaviour of complexes of gold (Pokrovski et al., 2009a,b, 2015), platinum group elements (Bazarkina et al., 2014; Mei et al., 2015a; Scholten et al., 2018), and copper (Brugger et al., 2007; Liu et al., 2008; Etschmann et al., 2010), as well as a host of other elements of economic interest (see Supplementary Material)*"*.

Finally, this HDR manuscript also provides an opportunity to establish the statistics of the usage of our set-up at FAME (and FAME-UHD beamlines). Figure 1.11 shows the number of publications involving the use of our autoclaves in the period 2000-2019: that's a total of 71 publications (I co-authored ~60 of them). A complement to this statistical analysis is to consider our 2005 technological publication that describes our autoclave (43): it has been cited 75 times since 2005. Finally, in the period 2002-2019 where FAME was fully operational, ~100 experiments (~6 days each) using the autoclaves were conducted on our beamlines.

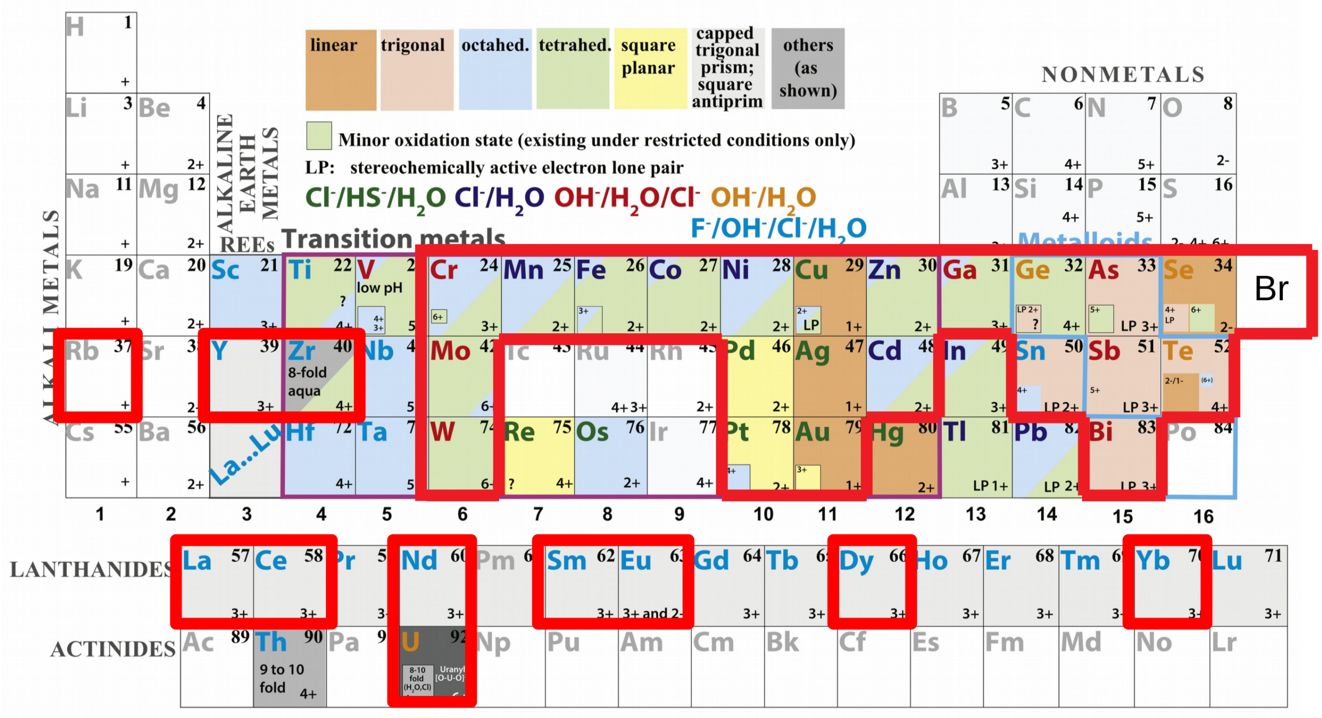

Figure 1.10: Periodic table adapted from reference (25) to highlight the metallic elements that were studied by XAS at FAME and FAME-UHD beamlines in the last 15 years, making use of our autoclave installation.

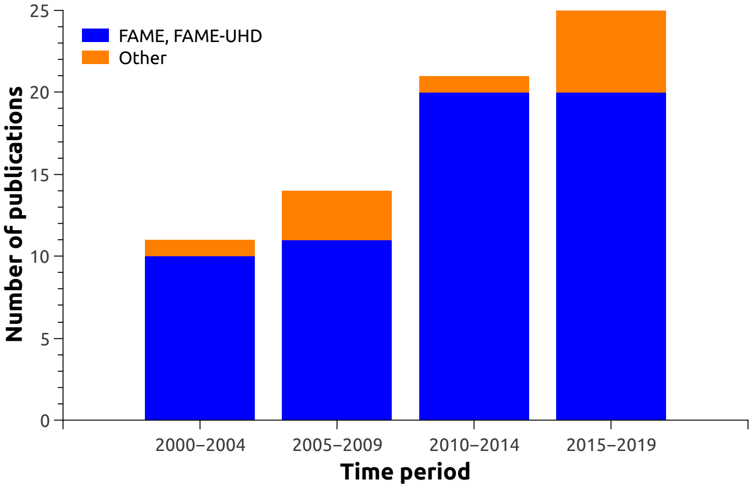

Figure 1.11: Blue: Number of publications that involve the use of our autoclaves at FAME or FAME-UHD beamlines. Orange: Number of publications (that I co-authored) and which involve the use of our autoclaves in non-XAS experiments (Raman, IXS, SAXS, HP synthesis, etc.). The numbers for the period 2000-2004 include the studies that used the previous version of the autoclave, and the experiments conducted on the BM32 EXAFS station before it was moved on BM30B-FAME.

Chapter 2

High-pressure and high-temperature technological developments.

2.1 Context

The scientific rationale behind the technological development of autoclaves has been established above in the chapter dedicated to XAS studies of hydrothermal metal transport. It can be synthesized in 3 ideas: the *in situ* study of hydrothermal fluids of metallogeny relevance, by spectroscopy. The corresponding technological challenges can be summarized as follows:

Hydrothermal fluids These fluids are under high pressure and temperature which require the use of specific materials; the fluids can be chemically reactive with the sample holder; their densities cover a wide range from liquid to vapor (0.1-1) $g.cm^{-3}$ in the same experimental run; the metal concentration relevant for transport studies can be very low (10s of ppm).

Spectroscopy Windows need to be used in the autoclave in order to collect photons; for XAS studies, X-rays energies as low as 5 keV are considered, strongly absorbed by the HP/HT materials mentioned above.

In situ The need for *in situ* measurements is challenging by itself (HT/HP, potential chemical reactivity of fluids, etc.), but it is made even more complex by the necessity of precise and stable pressures and temperatures.

Recently I co-authored with J. Brugger a section of the upcoming volume of International Tables of Crystallography dedicated to XAS (and related techniques) (2). It is entitled "Reaction cells" and describes the use of cells for the *in situ* study of fluids at elevated temperatures and pressures (both old designs and the current set-ups), the related experimental constraints that need to be addressed in the design of cells, and some scientific applications. This manuscript was accepted almost 2 years ago (but the publishing timescale of International Tables is very slow): I include it here because it is very useful to describe the context of the technological development of autoclaves.

Key ideas of the publication:

I highlighted (yellow) some interesting ideas. In particular, what I consider the very distinctive features of this manuscript are:

- it constitutes a comprehensive **listing of existing design** for *in situ* spectroscopic cells, with attention given to detailing their advantages and disadvantages;
- Figure 2 is an original figure that describes the **ranges of pressure and sample volume** for existing reaction cells. It also includes the footprint of typical synchrotron beams to highlight the importance of beam/sample volume ratio in order to limit **beam damage**...
- ... which is discussed in a dedicated paragraph.

International Tables for Crystallography:
Volume I, X-ray Absorption Spectroscopy and Related Techniques

3. Experimental Methods

3.37. Cells for spectroscopy of fluids at elevated pressure and temperature

Denis Testemale[a] & Joël Brugger[b]

[a]CNRS, Université Grenoble Alpes, Institut NEEL, F-38000Grenoble, France

[b]School of Earth, Atmosphere and the Environment, Monash University, Clayton, 3800, VIC, Australia

Keywords: high pressure / high temperature; hydrothermal; melts; *in situ*; reaction cells.

Abstract

The study of reactions involving liquids at elevated temperatures and/or pressures is important for a wide range of disciplines, including Earth and Planetary sciences, corrosion, materials, geo-engineering, and biological/environmental studies. *In situ* XAS measurements have had a profound impact on the field, by providing direct insights into the molecular-level reaction mechanisms at elevated P, T. This chapter summarizes the various approaches underpinning the design of reaction cells suitable for the study of these reactions at extreme conditions via XAS methods.

3.37.1. XAS and *in situ* studies of liquids at high pressure and temperature

Liquids (e.g., supercritical aqueous fluids; melts) under extreme conditions (temperature, pressure, composition) play an important role in both natural and man-made systems, e.g., planetary sciences; economic geology and hydrometallurgy; corrosion in power plants; catalysis; geo-engineering (e.g., geothermal energy, CO_2 sequestration) and material sciences (Brugger et al., 2010; Darr and Poliakoff, 1999). These applications rely on our understanding of the structure of the liquids, the nature and thermodynamic stability of relevant inorganic and organometallic complexes, and of the mechanisms and kinetics of reactions over a wide range in pressures and temperatures.

The increased availability of XAS combined with developments in spectroscopic cell designs have had a profound impact on the study of melts and aqueous fluids at high PT (Filipponi, 2001; Brugger et al., 2016), similarly to its impact on catalysis (section 3.38) and high pressure research (section 3.42). X-rays make it possible to probe the electronic structure of atoms in fluids *in situ* under extreme conditions. XAS is sensitive to the short-range structure about a specific atom, and hence is ideally suited for studying complex, multi-component liquids, such as those encountered in nature. The capacity of EXAFS to provide direct quantitative information about the hydration and structure of metal complexes (including metal-ligand distances) in dilute solutions motivated much of the early work on hydrothermal solutions (e.g., Pfund et al., 1994; Seward et al., 1993, 1995, 1996; Wallen et al., 1996). The quantitative nature of EXAFS and XANES (e.g., Benfatto et al., 2002; Liu et al., 2007) remains one of the main strengths of the technique. A recurrent theme in the field is the drive to exploit the unique features offered by X-ray beams at synchrotrons fully. For example, XAS studies were combined (**i**) with quantitative measurements of mineral solubility via measurements of X-ray fluorescence or step-height (Figure 1; e.g., Daval et al., 2010; Liu et al., 2008; Pokrovski et al., 2005; Sanchez-Valle et al., 2004; Wilke et al. 2012); and (**ii**) with measurements of absolute absorbance used to measure the density of the fluid (e.g., Etschmann et al., 2010; Pokrovski et al. 2008); such measurements also offer a convenient way to calibrate the temperature and pressure at the beam-position by comparison with the known equation of state of a sample (Figure 1); (**iii**) time-resolved measurements were used to investigate the kinetics of redox reactions (Cochain et al., 2013), either beam- or biologically-induced (Mayanovic et al., 2012; Picard et al., 2012) and the kinetics of mineral dissolution (Daval et al., 2010; Testemale et al., 2009a); (**iv**) the spatial resolution offered by focussed X-ray beams was used to probe separated phases such as fluid/melt (Louvel et al., 2013) and liquid/vapour (‘boiling’; Pokrovski et al., 2008), or to limit effects of beam-induced photo-reduction (e.g., Tooth et al., 2013).

The three main challenges that need to be addressed for measuring high quality XAS data on liquids at elevated temperature and/or pressure include: (**i**) the choice of materials, which need to be X-ray transparent and yet resistant to extremes in pressure and temperature; inert relative to samples that are commonly highly corrosive (e.g., acid; strongly oxidizing or reducing); able to contain the liquid; and sufficiently pure not to spoil the data with an unwanted contribution to the signal. (**ii**) A reliable control of reaction parameters, in particular pressure, temperature, and sample composition, for long period of times and at suitable precision. Collection of EXAFS data on dilute samples can take up to >10 hours (e.g., Pokrovski et al., 2009), and for low density (<0.8 g/cm^3) aqueous fluids, small fluctuations in pressure will cause sufficient density fluctuations as to affect the quality of the EXAFS data. (**iii**) Safety in beamline environment.

Many types of experimental devices have been used for *in situ* XAS measurements of liquids at high temperature and/or pressure (see exhaustive review by Filipponi, 2001), and some of them are succinctly presented below to illustrate the various approaches used and highlight their advantages and limitations.

3.37.2. Cells for *in situ* high temperature (HT) XAS measurements of melts

Cells operating at ambient or low pressure, under a controlled atmosphere, or under vacuum, have been used extensively to study solids at high temperatures, and their temperature-driven structural and redox modifications (phase transitions, melting mechanisms, kinetics of oxidation-reduction reactions, etc.). The same cell designs can be adapted for the study of melts, and most are based on resistive-heating. The graphite crucible based “L'Aquila-Camerino oven” (Filipponi et al., 1994) allows measurements up to 2250°C. The “heating wire” design (Mysen and Frantz, 1992) has been replicated and optimized (Richet et al., 1993; Farges et al., 1995) and makes EXAFS measurements of melts possible up to 3500°C (under vacuum). These designs benefit from very short heating and cooling times (> 100°C/s). High photon fluxes allow collection of time-resolved XAS measurements at very high temperatures (Cochain et al., 2013).

The levitation technique is a noticeable alternative method for HT measurements at low pressures; coupled with laser heating, it offers an efficient, simple and compact container-less method to place a sample in an X-ray or neutron beam (Hennet et al., 2011), and is suitable for XAS fluorescence measurements (Landron et al., 1997).

3.37.3. Cells for *in situ* XAS measurements of liquids

Figure 2 shows the different families of cells that are frequently used for XAS measurements at high temperature and moderate to very high pressures.

3.37.3.1 Very high pressures

The very high pressure cells are the Hydrothermal Diamond Anvil Cell (HyDAC) and the Paris-Edinburgh cells, described in detail in section 3.42. In the context of hydrothermal fluids, they are capable of much higher pressures than other current XAS cells: even the Paris-Edinburgh cells were occasionally adapted with success to aqueous fluids up to ~6.4 Gpa/275°C (Filipponi et al., 2003; Migliorati et al., 2013). The minuscule-to-very small volumes (<100 nl in DAC), the high density of the materials crossed by the X-rays, and the difficulty to control pressure accurately are their limitations for hydrothermal fluids.

3.37.3.2 Fluid inclusions

Fluid inclusions are mentioned here, even if they are not experimental cells *per se*, as they allow investigating HP/HT fluids (Roedder, 1984) and are sometimes considered as micro-batch reactors for the *in situ* investigation of hydrothermal fluids by XAS (Frantz et al., 1988). They consist of small quantities of fluids trapped in a host mineral during its crystallisation. They can be either natural (recording the fluids from which hydrothermal minerals form) or synthetic inclusions prepared in controlled conditions. At room temperature and pressure, fluid inclusions may contain several phases (fluid, gas bubble, precipitated mineral), but they still hold the original bulk composition, and upon heating the original speciation can be analysed, for example by XAS (e.g., Cauzid et al. 2007; Sanchez-Valle et al. 2004). Disadvantages include the impossibility to control the pressure (the volume is constant) and the very small volume (<1 nl), which can lead to significant issues with beam damage (e.g., James-Smith et al. 2010; see below).

3.37.3.3 Moderate pressure

A simple and safe cell design is based on the use of Fused Silica glass Capillary Capsules (FSCC; Chou, 2012). This design has been used in many optical spectroscopy studies (e.g., Raman) and has been adapted successfully to XAS measurements (Wallen et al., 1996; Hoffmann et al., 2000). The small beam size and high flux offered by synchrotron sources are essential given the small internal diameter (a few hundreds µm) of the capillaries. FSCC are inherently safe, have a large opening for fluorescence measurements, and allow for optical observation of the sample during the collection of XAS data. One obvious handicap is the reactivity of silica at temperatures ≥~400°C (Hoffmann et al., 2000) that hinders the study of hydrothermal fluids in those conditions.

The main group of cells for *in situ* XAS measurements of hydrothermal fluids includes various autoclave-type designs, which offer easy sample loading, flexible geometric design (in particular to measure the transmitted and/or fluorescence photons, see Figure 1) and accurate control over temperature and pressure. Pressure is typically limited to < ~2 kbar (Figure 2).

In a pioneering study, Seward et al. (1996) used an externally heated autoclave fitted with 2 mm silica windows to explore the evolution of Ag^+ coordination from ambient to 350°C via EXAFS. Such a design is limited to high X-ray energies (Ag K-edge is 25.514 keV) due to the strong absorption of the thick silica windows and does not allow pressure control (the cell operates at the equilibrium vapour pressure). Similar cells with simple design where the container is sealed and the pressure not regulated were also developed in the same period (e.g., thick silica tubes or alloy body closed by Kapton windows, Mosselmans et al., 1996).

At the Pacific Northwest National Laboratories, a number of flow-through cells were built based on a design featuring an externally heated body fitted with diamond windows, and 2 ports for incoming and outgoing solution flow (Pfund et al., 1994; Fulton et al., 2000, 2004; Hoffman et al., 2000). Compared to closed-system designs, flow-through reaction cells have the advantage of reduced beam damage, and offer flexibility for changing or controlling fluid composition over time, such as keeping the pH of the solution constant. By reducing the diamond thickness and the length of the beam path, EXAFS spectra could even be measured at very low X-ray energies for hydrothermal solutions up to supercritical conditions (Ca K-edge @ 4038 eV; Fulton et al., 2004). Diamond is one of the few materials able to withstand the chemically aggressive character of hydrothermal solutions, but its use comes at the price of the presence of diffraction peaks in the XAS signal, like in the case of DAC cells (section 3.42), and small unsupported diameter of the windows.

An internally heated autoclave was developed at Néel Intitute (CNRS, France) and installed at the FAME XAS beamline at ESRF (Testemale et al., 2005, 2016). It is to date the only system that is fully integrated in a beamline and available as a user facility. The autoclave is based on the design of Tamura et al. (1995), which introduced the separation of the needs for heat and chemical resistance from the requirements for physical strength (containment pressure). An internal cell of varying volume (i.e., pressure is equal to the externally imposed pressure) was placed in a He-pressurized autoclave, enabling for example EXAFS measurements of liquid selenium up to 1600°C/600 bar (Tamura et al., 1995; Soldo et al., 1998). The design is flexible in that both transmission and fluorescence (with high solid angle) signals can be measured concurrently (Figure 1), and the materials and thickness of the internal cell and autoclave windows can be easily customized for specific applications, e.g. minimize beam absorbance to access low-energy edges, down to ~6 keV (MnKα fluorescence @ 5.9 keV, Tian et al., 2014); or maximize mechanical strength to reach higher pressures, up to 150 MPa/500°C (Ranieri et al., 2012). The key materials of this design are beryllium and glassy carbon. The former has a low-Z, a small density and good mechanical strength, and thus is used to build the autoclave windows. The latter is extremely chemically resistant (e.g., HCl, H_2S, …) to high temperatures (>1000˚C), it contains few impurities, has a low density, and can be machined; it is used for the internal cell, and recently for HP autoclave windows (Testemale et al., 2016). Pressure and temperature are controlled independently and precisely (Bruyère et al., 2008), which opens the way to the study of phase separation and low-density fluids of importance for example in Economic Geology, e.g., down to fluid densities of ~0.1 $g.cm^{-3}$ (Liu et al., 2008). A sample area of about 5 mm diameter is accessible to the X-ray beam; this allows for checking sample homogeneity, measurements in multiphase systems, or minimisation of beam damage. This autoclave to date has achieved temperatures to ~1000°C and pressures to ~200 MPa.

All those autoclave-type designs offer relatively large sample volumes (~1-1000 µl). This situation brings a number of benefits for *in situ* spectroscopy: it reduces the risk of beam damage (see below); it removes the need for micro-focussed beams; it allows for direct measurements of temperature and pressure without the use of calibrant; and it allows sample recovery for further measurements, such as cell counting in bacterial cultures (Picard et al., 2012).

3.37.4. Beam damage in reaction cells

Ionizing radiation induces radiolysis of water, thus producing radiolytic species such as H^+, H, OH, OH^- and hydrated electron, e^-_{aq}, which upon reaction with one another produce redox-active species such as hydrogen peroxide, dissolved hydrogen ($H_2(aq)$) and oxygen ($O_2(aq)$) (Jayanetti et al., 2001;

Saffré et al., 2011). As reviewed recently by Brugger et al. (2016), the effects of radiolytic species on the oxidation states of metal ions in solutions within spectroscopic cell under X-ray illumination are well established yet difficult to predict. The nature of the effect (e.g., reduction versus oxidation) and the rate of the photoreaction depend upon solution composition, temperature, and the volume of the fluid compared to the volume affected by the beam (Figure 2). The effects of beam damage need to be carefully considered when interpreting XAS data on hydrothermal reactions. These effects are particularly extreme in the case of small sample volumes, such as fluid inclusions and DAC micro-beam experiments (e.g., Mayanovic et al., 2012) where the sample volume is a few nanoliters and the beam flux very high at insertion devices beamlines. In the case of larger sample volumes (relative to the volume of fluid within the beam), and/or lower flux bending magnet beamlines, beam damage can have beneficial effects, e.g. by promoting the rate of conversion of the ion in solution to the thermodynamically stable species (e.g., Fulton et al., 2000) or the rate of mineral dissolution in the case of *in situ* solubility experiments

3.37.5. Future developments

The study of fluids under extreme conditions is a rapidly evolving field. Current trends include: (i) co-measurements of EXAFS and other spectroscopy (e.g., optical and vibrational spectroscopy; small angle scattering), as well as better control of solution chemistry parameters, in particular pH and redox; (ii) accessing higher pressures with autoclave designs, since deep earth processes is a current hot topic in hydrothermal geochemistry (e.g., Sverjensky et al. 2014); (iii) lower energy (lower Z elements) spectroscopy enabled by new materials; and (iv) adapt to the next detection methods of XAS beamlines, in particular high spectral resolution spectroscopy (Hazemann et al. 2009).

3.37.6. References

Bassett, W.A., Anderson, A.J., Mayanovic, R.A., and Chou, I.M. (2000) Hydrothermal diamond anvil cell for XAFS studies of first-row transition elements in aqueous solution up to supercritical conditions. Chemical Geology, 167(1-2), 3-10.

Benfatto, M., D'Angelo, P., Della Longa, S., and Pavel, N.V. (2002) Evidence of distorted fivefold coordination of the Cu^{2+} aqua ion from an x-ray-absorption spectroscopy quantitative analysis. Physical Review B, 65(17).

Brugger, J., Liu, W.H., Etschmann, B., Mei, Y., Sherman, D.M., and Testemale, D. (2016) A review of the coordination chemistry of hydrothermal systems, or do coordination changes make ore deposits? Chemical Geology, 447, 219-253.

Brugger, J., Pring, A., Reith, F., Ryan, C., Etschmann, B., Liu, W., O'Neill, B., and Ngothai, Y. (2010) Probing ore deposits formation: New insights and challenges from synchrotron and neutron studies. Radiation Physics and Chemistry, 79(2), 151-161.

Bruyère, R., Prat, A., Goujon, C., and Hazemann, J.-L. (2008) A new pressure regulation device using high pressure isolation valves. J. Phys.: Conf. Ser., 121, 122003-6.

Cauzid, J., Philippot, P., Martinez-Criado, G., Menez, B. and Laboure, S. (2007) Contrasting Cu-complexing behaviour in vapour and liquid fluid inclusions from the Yankee Lode tin deposit, Mole Granite, Australia. Chemical Geology 246, 39-54.

Chou, I.-M. (2012) Optical cells with fused silica windows for the study of geological fluids, in: Ferraris, G., Dubessy, J., Caumon, M.-C., Rull, F. (Eds.), Raman Spectroscopy Applied to Earth Sciences and Cultural Heritage. European Mineralogical Union, pp. 227–247.

Cochain, B., Neuville, D.R., de Ligny, D., Malki, M., Testemale, D., Pinet, O., Richet, P. (2013) Dynamics of iron-bearing borosilicate melts: Effects of melt structure and composition on viscosity, electrical conductivity and kinetics of redox reactions. Journal of Non-Crystalline Solids 373–374, 18–27.

Daval, D., Testemale, D., Recham, N., Tarascon, J.-M., Siebert, J., Martinez, I., and Guyot, F. (2010) Fayalite (Fe_2SiO_4) dissolution kinetics determined by X-ray absorption spectroscopy. Chemical Geology, 275, 161–175.

Darr, J.A., and Poliakoff, M. (1999) New directions in inorganic and metal-organic coordination chemistry in supercritical fluids. Chemical Reviews, 99(2), 495-541.

Etschmann, B., Liu, W., Testemale, D., Muller, H., Rae, N., Proux, O., Hazemann, J., and Brugger, J. (2010) An in situ XAS study of copper(I) transport as hydrosulfide complexes in hydrothermal solutions (25-592 ˚C, 180-600 bar): Speciation and solubility in vapor and liquid phases. Geochimica Et Cosmochimica Acta, 74(16), 4723-4739.

Farges, F., Itié, J.-P., Fiquet, G., Andrault, D. (1995) A new device for XAFS data collection up to 2000 K (or 3700 K under vacuum). Nuclear Instruments and Methods in Physics Research Section B: Beam Interactions with Materials and Atoms 101, 493–498.

Filipponi, A., Di Cicco, A. (1994) Development of an oven for X-ray absorption measurements under extremely high temperature conditions. Nuclear Instruments and Methods in Physics Research Section B: Beam Interactions with Materials and Atoms 93, 302–310.

Filipponi, A. (2001) EXAFS for liquids. Journal of Physics: Condensed Matter 13, R23.

Filipponi, A., De Panfilis, S., Oliva, C., Ricci, M., D'Angelo, P., Bowron, D. (2003) Ion Hydration under Pressure. Physical Review Letters 91.

Frantz, J.D., Mao, H.K., Zhang, Y.-G., Wu, Y., Thompson, A.C., Underwood, J.H., Giauque, R.D., Jones, K.W., Rivers, M.L. (1988) Analysis of fluid inclusions by X-ray fluorescence using synchrotron radiation. Chemical Geology 69, 235–244.

Fulton, J.L., Chen, Y., Heald, S.M., and Balasubramanian, M. (2004) High-pressure, high-temperature x-ray absorption fine structure transmission cell for the study of aqueous ions with low absorption-edge energies. Review of Scientific Instruments, 75(12), 5228-5231.

Fulton, J.L., Hoffmann, M.M., Darab, J.G., Palmer, B.J., and Stern, E.A. (2000) Copper(I) and copper(II) coordination structure under hydrothermal conditions at 325 ˚C: An X-ray absorption fine structure and molecular dynamics study. Journal of Physical Chemistry, 104(49), 11651-11663.

Hazemann, J.-L., Proux, O., Nassif, V., Palancher, H., Lahera, E., Da Silva, C., Braillard, A., Testemale, D., Diot, M.-A., Alliot, I., Del Net, W., Manceau, A., Gelebart, F., Morand, M., Dermigny, Q. and Shukla, A. (2009) High-resolution spectroscopy on an X-ray absorption beamline. J. Synchrotron Radiat. 16, 283-292.

Hennet, L., Cristiglio, V., Kozaily, J., Pozdnyakova, I., Fischer, H.E., Bytchkov, A., Drewitt, J.W.E., Leydier, M., Thiaudière, D., Gruner, S., Brassamin, S., Zanghi, D., Cuello, G.J., Koza, M., Magazù, S., Greaves, G.N., Price, D.L. (2011) Aerodynamic levitation and laser heating: Eur. Phys. J. Spec. Top. 196, 151.

Hoffmann, M.M., Darab, J.G., Heald, S.M., Yonker, C.R., Fulton, J.L. (2000) New experimental developments for in situ XAFS studies of chemical reactions under hydrothermal conditions. Chemical Geology 167, 89–103.

James-Smith, J., Cauzid, J., Testemale, D., Liu, W., Hazemann, J., Proux, O., Etschmann, B., Philippot, P., Banks, D., Williams, P. and Brugger, J. (2010) Arsenic speciation in fluid inclusions using micro-beam X-ray absorption spectroscopy. American Mineralogist 95, 921-932.

Jayanetti, S., Mayanovic, R.A., Anderson, A.J., Bassett, W.A., and Chou, I.-M. (2001) Analysis of radiation-induced small Cu particle cluster formation in aqueous $CuCl_2$. Journal of Chemical Physics, 115, 954-962.

Landron, C., Launay, X., Rifflet, J.C., Echegut, P., Auger, Y., Ruffier, D., Coutures, J.P., Lemonier, M., Gailhanou, M., Bessiere, M., Bazin, D., Dexpert, H. (1997) Development of a levitation cell for synchrotron radiation experiments at very high temperature. Nuclear Instruments and Methods in Physics Research Section B: Beam Interactions with Materials and Atoms 124, 627–632.

Liu, W., Etschmann, B., Foran, G., Shelley, M., and Brugger, J. (2007) Deriving formation constants for aqueous metal complexes from XANES spectra: Zn^{2+} and Fe^{2+} chloride complexes in hypersaline solutions. American Mineralogist, 92(5-6), 761-770.

Liu, W.H., Brugger, J., Etschmann, B., Testemale, D., and Hazemann, J.-L. (2008) The solubility of nantokite (CuCl(s)) and Cu speciation in low-density fluids near the critical isochore: An in-situ XAS study. Geochimica Cosmochima Acta, 72(16), 4094-4106.

Louvel, M., Sanchez-Valle, C., Malfait, W.J., Testemale, D., Hazemann, J.-L. (2013) Zr complexation in high pressure fluids and silicate melts and implications for the mobilization of HFSE in subduction zones. Geochimica et Cosmochimica Acta 104, 281–299.

Mayanovic, R.A., Anderson, A.J., Dharmagunawardhane, H.A.N., Pascarelli, S., and Aquilanti, G. (2012) Monitoring synchrotron X-ray-induced radiolysis effects on metal (Fe, W) ions in high-temperature aqueous fluids. Journal of Synchrotron Radiation, 19, 797-805.

Migliorati, V., Mancini, G., Tatoli, S., Zitolo, A., Filipponi, A., De Panfilis, S., Di Cicco, A., and D'Angelo, P. (2013) Hydration Properties of the Zn^{2+} Ion in Water at High Pressure. Inorganic Chemistry, 52(2), 1141-1150.

Mosselmans, J.F.W., Schofield, P.F., Charnock, J.M., Garner, C.D., Pattrick, R.A.D., Vaughan, D.J. (1996) X-ray absorption studies of metal complexes in aqueous solution at elevated temperatures. Chemical Geology 127, 339–350.

Mysen, B.O., Frantz, J.D. (1992) Raman spectroscopy of silicate melts at magmatic temperatures: Na_2O-SiO_2, K_2O-SiO_2 and Li_2O-SiO_2 binary compositions in the temperature range 25–1475 °C. Chemical Geology 96, 321–332.

Pfund, D.M., Darab, J.G., Fulton, J.L., and Ma, Y. (1994) An XAFS study of strontium ions and krypton in supercritical water. The Journal of Physical Chemistry, 98(50), 13102-13107.

Picard, A., Testemale, D., Hazemann, J.L., and Daniel, I. (2012) The influence of high hydrostatic pressure on bacterial dissimilatory iron reduction. Geochimica Et Cosmochimica Acta, 88, 120-129.

Pokrovski, G.S., Roux, J., Hazemann, J.L., Borisova, A.Y., Gonchar, A.A., and Lemeshko, M.P. (2008) In situ X-ray absorption spectroscopy measurement of vapour-brine fractionation of antimony at hydrothermal conditions. Mineralogical Magazine, 72(2), 667-681.

Pokrovski, G.S., Roux, J., Hazemann, J.L., and Testemale, D. (2005) An X-ray absorption spectroscopy study of argutite solubility and aqueous Ge(IV) speciation in hydrothermal fluids to 500 ˚C and 400 bar. Chemical Geology, 217(1-2), 127-145.

Pokrovski, G.S., Tagirov, B.R., Schott, J., Hazemann, J.L., and Proux, O. (2009) A new view on gold speciation in sulfur-bearing hydrothermal fluids from in situ X-ray absorption spectroscopy and quantum-chemical modeling. Geochimica et Cosmochimica Acta, 73(18), 5406-5427.

Ranieri, V., Haines, J., Cambon, O., Levelut, C., Le Parc, R., Cambon, M., Hazemann, J.-L. (2012) In Situ X-ray Absorption Spectroscopy Study of $Si_{1-x}Ge_xO_2$ Dissolution and Germanium Aqueous Speciation under Hydrothermal Conditions. Inorganic Chemistry 51, 414–419.

Richet, P., Gillet, P., Pierre, A., Bouhifd, M.A., Daniel, I., Fiquet, G. (1993) Raman spectroscopy, x-ray diffraction, and phase relationship determinations with a versatile heating cell for measurements up to 3600 K (or 2700 K in air). Journal of Applied Physics 74, 5451–5456.

Roedder, E. (1984) Fluid inclusions. Reviews in Mineralogy, 12. Mineralogical Society of America, 644 pp.

Saffré, D., Atinault, E., Pin, S., Renault, J.P., Hazemann, J.L., Baldacchino, G. (2011) In-situ UV-visible spectrum acquisition of Br_3^-. Investigations of concentrated HBr aqueous solutions under 13 keV X-rays. Journal of Physics: Conference Series 261, 012013.

Sanchez-Valle, C., Daniel, I., Martinez, I., Simionovici, A., Reynard, B. (2004) Progress in quantitative elemental analyses in high P–T fluids using synchrotron x-ray fluorescence (SXRF). J. Phys.: Condens. Matter 16, S1197.

Seward, T.M., Henderson, C.M.B., Charnock, J.M., and Dobson, B.R. (1995) The hydration of metal cations in hydrothermal solutions: recent EXAFS results. Water-Rock Interaction, 8, 43-46.

Seward, T.M., Henderson, C.M.B., Charnock, J.M., and Dobson, B.R. (1996) An X-ray absorption (EXAFS) spectroscopic study of aquated Ag^+ in hydrothermal solutions to 350 ˚C. Geochimica et Cosmochimica Acta, 60(13), 2273-2282.

Seward, T.M., Henderson, C.M.B., Charnock, J.M., Dobson, B.R.e., and Lorrain., p.-I. (1993) An X-ray absorption spectroscopic study of aqueous CdCl2 to 250 °C. In M.C.a.M. Cathelineau, Ed. Proceedings of the 4th International Symposium on Hydrothermal Reactions, p. 231-233. Institut Lorrain.

Soldo, Y., Hazemann, J.L., Aberdam, D., Inui, M., Tamura, K., Raoux, D., Pernot, E., Jal, J.F., Dupuy-Philon, J. (1998) Semiconductor-to-metal transition in fluid selenium at high pressure and high temperature: an investigation using x-ray-absorption spectroscopy. Phys. Rev. B 57, 258–268.

Sverjensky, D.A., Stagno, V. and Huang, F. (2014) Important role for organic carbon in subduction-zone fluids in the deep carbon cycle. Nature Geoscience 7, 909-913.

Tamura, K., Inui, M., and Hosokawa, S. (1995) XAFS measurements at high-temperatures and pressures. Review of Scientific Instruments, 66(2), 1382-1384.

Testemale, D., Argoud, R., Geaymond, O., and Hazemann, J.L. (2005) High pressure high temperature cell for x-ray absorption and scattering techniques. Review Of Scientific Instruments, 76(4).

Testemale, D., Dufaud, F., Martinez, I., Benezeth, P., Hazemann, J.L., Schott, J., and Guyot, F. (2009a) An X-ray absorption study of the dissolution of siderite at 300 bar between 50 ˚C and 100 ˚C. Chemical Geology, 259(1-2), 8-16.

Testemale, D., Brugger, J., Liu, W., Etschmann, B., Hazemann, J.-L. (2009b). In-situ X-ray absorption study of iron(II) speciation in brines up to supercritical conditions. Chemical Geology 264, 295–310.

Testemale, D., Prat, A., Lahera, E., and Hazemann, J.L. (2016) Novel high-pressure windows made of glass-like carbon for x-ray analysis. Review of Scientific Instruments, 87(7).

Tian, Y., Etschmann, B., Mei, Y., Grundler, P.V., Testemale, D., Hazemann, J.-L., Elliott, P., Ngothai, Y., and Brugger, J. (2014) Speciation and thermodynamic properties of manganese(II) chloride complexes in hydrothermal fluids: *in situ* XAS study. Geochimica Et Cosmochimica Acta, 129, 77-95.

Tooth, B., Etschmann, B., Pokrovski, G.S., Testemale, D., Hazemann, J.L., Grundler, P.V., and Brugger, J. (2013) Bismuth speciation in hydrothermal fluids: An X-ray absorption spectroscopy and solubility study. Geochimica Et Cosmochimica Acta, 101, 156-172.

Wallen, S.L., Pfund, D.M., Fulton, J.L., Yonker, C.R., Newville, M., and Ma, Y.J. (1996) High-pressure, capillary x-ray absorption fine structure cell for studies of liquid and supercritical fluid solutions. Review of Scientific Instruments, 67(8), 2843-2845.

Wilke, M., Schmidt, C., Dubrail, J., Appel, K., Borchert, M., Kvashnina, K. and Manning, C.E. (2012) Zircon solubility and zirconium complexation in H_2O + Na_2O + SiO_2 +/- Al_2O_3 fluids at high pressure and temperature. Earth and Planetary Science Letters 349, 15-25.

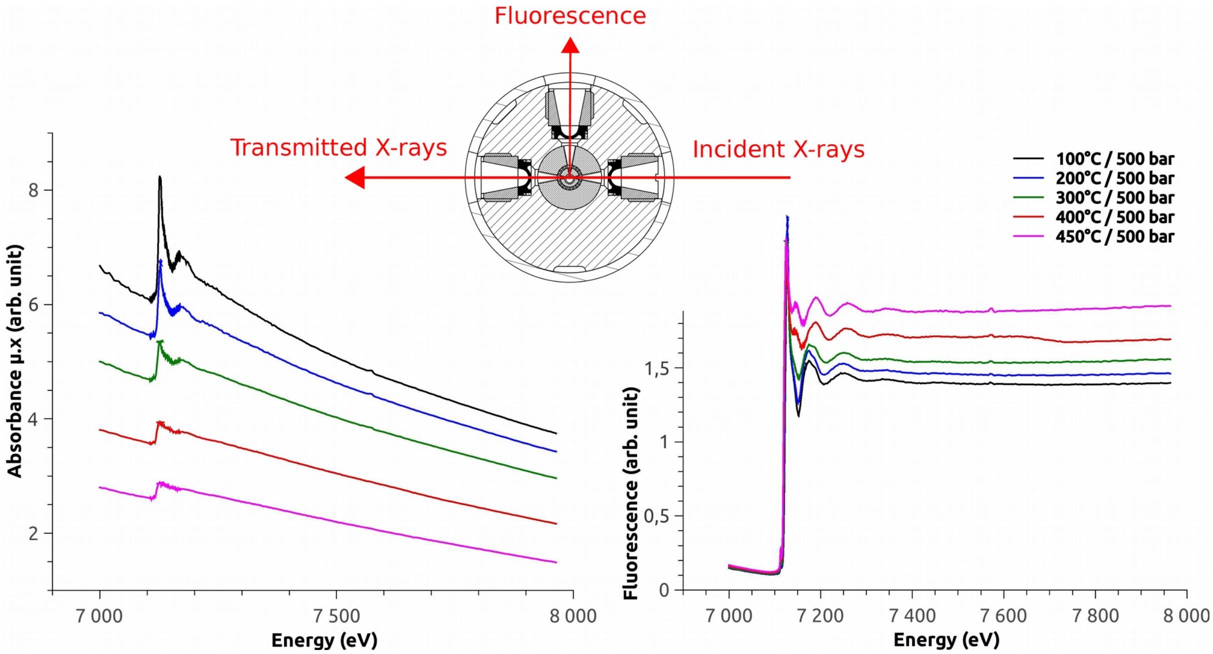

Figure 1: XAS data for metals in hydrothermal fluids. In this example aqueous solutions contain 0.045 m Fe^{2+}, 0.35 m NaCl and 0.1 m HCl were measured in an autoclave at 500 bar from 100°C to 450°C (Testemale et al., 2009b). Both transmission (left) and fluorescence spectra (right) were measured concurrently thanks to the geometry of the autoclave (cross-section on top). This is a typical example of low concentration measurements where the fluorescence spectra are essential for good spectral data quality (XANES and EXAFS analysis), but the absorbance spectra (transmission) are useful for the quantitative determination of fluid density (the absolute absorbance levels are directly proportional to the fluid density), and of the dissolved metal concentration (derived from the variation of absorbance over the absorption edge).

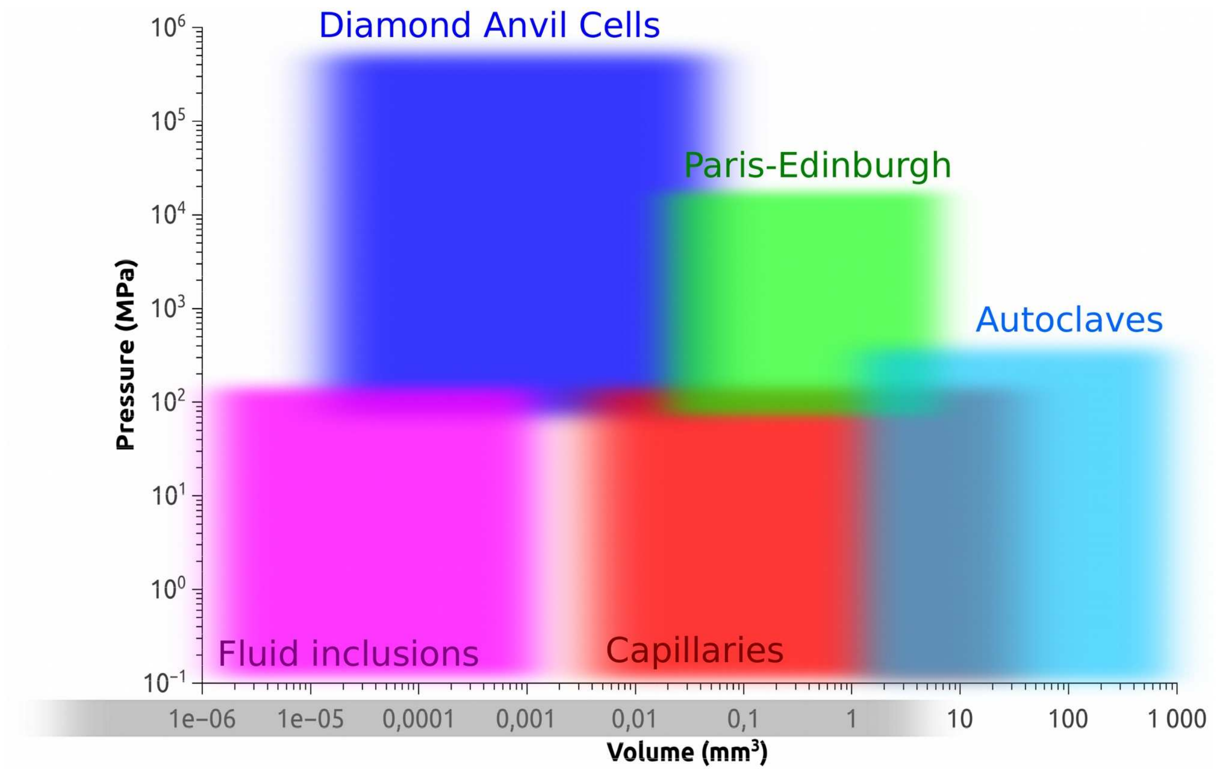

Figure 2: Summary of the pressure range versus volume of the various families of high pressure cells used for XAS *in situ* measurements of liquids. The temperature domains are imposed by the heating technology: <800°C, heating stage for fluid inclusions and capillaries; <1200°C, resistive heating for autoclaves and PE cells; <3000°C, laser heating for DAC. The grey band along the volume axis depicts the range of volumes probed with synchrotron beams.

2.2 The Néel autoclave

Collaboration:

- *Local: Néel Institute X'Press technological group (A. Prat, R. Bruyère, C. Bouchard, C. Goujon, M. Legendre)*
- *Local: FAME staff (E. Lahera, W. Delnet)*

Supervision:

- *S. Neufselle, M1 trainingship (Joseph Fourier University, 2011)*
- *M. Louvel, Swiss National Science Foundation post-doctoral (2011-2012)*
- *L. Creon-Bocquet, ANR post-doctoral (2015)*

A preliminary remark needs to be done: if it was not for the Néel Institute (department PLUM, formerly the 'Laboratoire de Cristallgraphie') and the FAME beamlines, and all the technical staff there, the development of our autoclave set-up would have been impossible. Indeed, the expertise in high pressure technology at Néel Institute and FAME beamlines is second to none, in particular within the staff of the dedicated technological pools (X'Press pole). This strong HP activity mirrors the very active and collaborative HP community in France, structured in the 'Réseau des Hautes Pressions'[1], which regularly brings together the HP community (once every two years) during the national HP conferences, 'Forum des Hautes Pressions': I attend them assiduously to benefit from sharp expertise, up-to-date information, and a friendly atmosphere.

2.2.1 Introduction, general principles

The design of the autoclave was done during the period of my PhD, which led to our major publication of 2005 (43) (included below). During the ~5 following years an intense development followed, in particular with a constant improvement of the internal cell that holds the sample, both in terms of geometry and materials. Since then, the regular use of the autoclave on FAME and FAME-UHD beamlines, and the challenging experimental conditions explored by the users, are the driver for a constant optimisation.

In this section of the manuscript, I chose to include below the 2005 publication about our autoclave, because it explains clearly the technological principles of its design. In the following sub-sections I briefly highlight some key ideas of both its design and its usage. Finally, a short description of the new version of the autoclave is done.

Key ideas of the publication:

I highlighted (yellow) some interesting ideas. In particular, what I consider the very distinctive features of this manuscript are:

- the **design of the HP windows** (Be material and large solid angle) allows for very good data collection, and the 3 windows enable to collect transmission and fluorescence data simultaneously;
- **pressure and temperature are controlled independently** (sample volume is not constant): the P-T phase diagram can be explored more easily;
- thanks to 2 different X-ray and optical set-ups, the **autoclave is very versatile** and can be used for many absorption, scattering and optical techniques.

---

[1] `www.reseauhp.org/`

REVIEW OF SCIENTIFIC INSTRUMENTS **76**, 043905 (2005)

High pressure/high temperature cell for x-ray absorption and scattering techniques

Denis Testemale
Laboratoire de Cristallographie, UPR5031, 25 Avenue des Martyrs, 38042 Grenoble Cedex 09, France and SNBL/ESRF, 6 Rue Jules Horowitz, BP 220, 38043 Grenoble Cedex 09, France

Roger Argoud, Olivier Geaymond, and Jean-Louis Hazemann
Laboratoire de Cristallographie, UPR5031, 25 Avenue des Martyrs, 38042 Grenoble Cedex 09, France

(Received 19 November 2004; accepted 31 January 2005; published online 23 March 2005)

A high pressure/high temperature cell dedicated to x-ray absorption spectroscopy, small angle x-ray scattering, and inelastic x-ray scattering techniques is presented. The P and T parameters are controlled independently and their range allow the study of aqueous solutions ($T \leqslant 500$ °C and $P \leqslant 2000$ bar) and liquid metals and glasses ($T \leqslant 1700$ °C and $P \leqslant 2000$ bar). The autoclave technology is inspired from previous high pressure/high temperature equipments but great improvements are achieved. Original high pressure windows have been developed to ensure both pressure resistance and low absorbance combined with large angular aperture. Different configurations are available for the internal cell that contains the sample whether it is aqueous or not. As an example of the efficiency of the set-up, we present preliminary x-ray absorption results on 0.01 m $FeCl_3$ aqueous solutions from ambient to supercritical conditions (375 °C and 300 bar). These low concentrations samples and low energy spectra (Fe K-edge is at 7112 eV) represent challenging experimental conditions. © *2005 American Institute of Physics.*

[DOI: 10.1063/1.1884188]

I. INTRODUCTION

Structural investigation of the disordered states of matter under extreme conditions of pressure and temperature is an attractive scientific domain. The reason stems from the importance of characterizing the dependence of the structure of matter upon temperature and pressure to get a deep understanding of the bonding interactions at stake. With the emergence of synchrotron sources that provide an extremely bright and well focussed beam, the compatibility of high pressure (HP) equipments with diffraction or spectroscopic techniques is now well established.[1,2] In the frame of our program of synchrotron based structural investigation of liquids in supercritical conditions, our team develops high pressure and high temperature (HP/HT) autoclave set-ups. The first ones were built in collaboration with Pr. Tamura (Hiroshima University)[3,4] and several x-ray absorption spectroscopy (XAS) and small angle x-ray scattering (SAXS) studies have been successfully conducted. The topics investigated are the study of ion pairing in aqueous supercritical solutions,[5–8] and structural studies of liquid metals, either by XAS (Ref. 3 and 9) or by SAXS.[10] The experimental difficulties inherent to the combination of x-ray techniques (especially x-ray absorption spectroscopy) with HP/HT sample environments have been exhaustively described by Filipponi.[2] In the present document, we describe a HP/HT set-up developed in order to be compatible with x-ray absorption spectroscopy (XAS), small angle x-ray scattering and inelastic x-ray scattering (IXS) techniques, both for aqueous and metal liquids samples. The interest of using these three techniques for samples at extreme conditions relies on their complementarity. Although XAS provides for information at the atomic scale around a specific atom,[2] SAXS is sensitive to the size and the amplitude of the density fluctuations that appear in the compressible regime of liquids.[10] IXS refers to various specific techniques, among which we can quote the measurement of the dynamic structure factor $S(q,\omega)$ to determine the parameters of the structural relaxation in hydrogen-bonded liquids,[11] the measurement of Compton profiles to determine the ground-state momentum probability and thus elucidate the nature of the hydrogen bond,[12] and the Raman IXS which has been used recently to measure the K-edge absorption spectra of oxygen in water.[13,14] In particular, when it comes to measure such low energy absorption spectra in HP/HT conditions, this technique is compulsory to overcome the limiting absorbance of the HP/HT equipments.

One of the main features of the cell is that the temperature and the pressure are varied independently in the ranges 30–1700 °C and 1–2000 bar. Furthermore, the versatility of this set-up makes manifold studies possible, from electrolytic or proteines aqueous solutions (up to 2000 bar and 600 °C at least) to liquid metals and metallic glasses under high temperature ($T \leqslant 1700$ °C). The general principle of this cell consists of an internally heated helium-pressurized autoclave with cold walls.[4,15] Such a configuration is necessary to be able to choose an internal sample container, chemically inert, and it avoids the optical windows to support the severe corrosive attacks of the supercritical samples. The present description of the technological specificities of this instrument is outlined along two main axis. First we will deal with the

HP part which consists of describing the HP vessel and particularly its windows. Then we will describe the internal set-up (heater and sample container).

As an example of the capabilities of the set-up, we present preliminary results of XAS measurements, both x-ray absorption near edge structure (XANES) and extended x-ray absorption fine structure (EXAFS) obtained recently on Fe^{III} aqueous solutions at high temperature and high pressure. Iron is one of the main element in the Earth composition. Its abundance in the outer mantle and the crust calls for a good understanding of its speciation in hydrothermal aqueous solutions since the fluid phase is the transport agent of minerals. High temperature and high pressure, as well as low concentration are necessary to reproduce these hydrothermal conditions. One of the most limiting constraint to study iron by x-ray absorption spectroscopy in HP/HT conditions is the relatively low energy of the iron *K*-edge (7112 eV) highly absorbed by HP/HT set-ups. That is the reason why we claim that these preliminary results are a good indicator of the capabilities of our cell.

II. PRESSURE/VESSEL

From a geochemical and geophysical point of view, the pressure range of our instrument (1–2000 bar) is an intermediate range corresponding to the few hundreds of bar characterizing the hydrothermal fluids and the sub- and supercritical natural solutions. This is a soft range compared to the maximal static pressures obtained with diamond anvil cells (DAC) or multianvils cells, necessary to investigate the pressure issues in the mantle and crust science.[2] However, it enables a 1 bar precision control of the pressure which is not the case in the DAC set-ups. Indeed, the high-pressure (HP) technology of our set-up is based on an helium pressurization of the vessel in which the sample and the furnace are placed. We develop, in the present part, a description of this HP vessel, with a special attention to the windows.

A. HP vessel

Figure 1 shows a drawing of the HP vessel. In this drawing, all the main elements of the apparatus are displayed: the HP vessel, two of the three HP windows, the plug, and the internal set-up attached to it. The HP vessel is cooled by a circulation of water. It has been made in X13 stainless steel, which does not oxidize and present interesting mechanical properties. The HP seal between the vessel and the plug is achieved with a vitton seal and an antiextrusion brass Δ-ring located in the area 9 in Fig. 1. The role of the plug is to introduce the He inlet, the thermocouples and electrical leads into the internal part. The technological solution chosen is conical pyrophyllite leadthroughs.

B. Windows

In the present case where the HP windows are not in contact with the sample, the choice of their material and their design is imposed by resistance to pressure, spectroscopic and ease of use constraints.

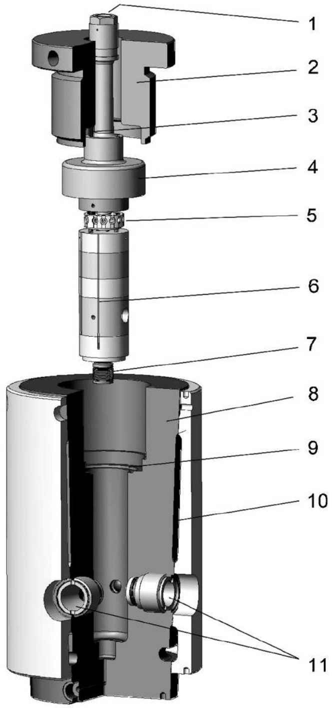

FIG. 1. 3D drawing of the newly developed high pressure/high temperature (HP/HT) set-up. (1) He inlet through the HP vessel plug. (2) HP vessel nut to hold tight the vessel plug. (3) Pyrophyllite leadthroughs. (4) HP vessel plug. (5) Thermocouples and electrical leads connections to the internal part. (6) Thermocouple (one visible out of two). (7) Bellows of the internal cell. (8) HP vessel. (9) Vitton seal. (10) Water cooling circulation. (11) Windows (two out of three): the visible parts are the locknuts. The size of the HP vessel (8) is 242 mm × 150 mm.

1. Vessel design

As it can be seen in the drawing in Fig. 2, the vessel has been designed with three windows, two on the beam axis (one entrance, one exit) and one at 90°. The former are used to collect transmission absoption spectra and SAXS signals. The latter is dedicated to the collection of fluorescence or inelastic scattering photons. In Fig. 3, one can see the assem-

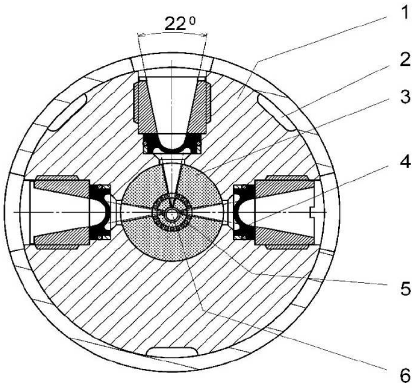

FIG. 2. Drawing of the general windows geometry (two on the beam axis, and one at 90°). The setup is drawn with Be windows in (1) HP vessel main part (piece 8 in Fig. 1). (2) Water cooling circulation (piece 10 in Fig. 1). (3) Alumina insulating pieces. (4) Beryllium window. (5+6) Furnace and internal cell.

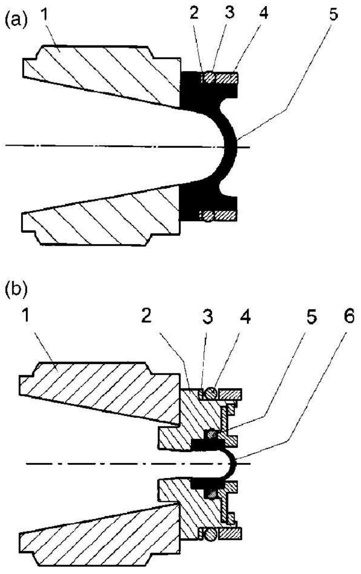

FIG. 3. (a) Drawing of the assembly of a beryllium HP window. (1) Locknut to hold tight the windows in the HP vessel orifice. (2) Antiextrusion Teflon ring. (3) Viton O-ring gasket. (4) centering brass ring. (5) beryllium window. (b) Drawing of the assembly of a sapphire HP window. (1) Locknut to hold tight the windows in the HP vessel orifice. (2) Adaptation element. (3) Antiextrusion Teflon ring. (4+5) Viton O-ring gaskets. (6) Sapphire window.

bly of the windows in their orifice: a locknut coupled with an O-ring seal guarantee an efficient HP tightness and an easy-to-change adaptation of the different windows. Another significant interest of this narrow confinement of the windows is the cooling they benefit by contact with the water cooled vessel and from the convective circulation of pressurized helium due to the internal heating.[15]

2. Design

Considering the low count-rate that fluorescence and inelastic scattering experiments produce, and the global need for the best signal-to-noise ratio, the width of the three windows must be optimized. A large angular opening is also of major importance to increase the detection solid angle. For all these reasons, the windows are dome shaped as it is visible in Fig. 3. The resulting angular opening is either 22° (XAS, IXS) and 5° for the SAXS windows that have a smaller diameter; these angles are defined by the solid angle, centered at the sample, available for the detection setups. It is worth noting the very weak variation of the windows thickness within this angular range: there is no angular dependence of the transmitted intensity.

3. Material

The windows materials are chosen according to the experimental technique. The most polyvalent windows, for XAS and IXS techniques, are made in Be. Extruded Be SR200 is chosen for its compromise between good mechanical properties and low absorption properties. Opposite, SAXS technique needs a monocrystalline material to dispose of the Bragg peaks that would pollute the scattering signal at low q. Monocrystalline sapphire Al_2O_3, with the window axis coincident to the $\vec{c}$ axis of the monocristal piece, suits very well. Real systematic tests were made to know the pressure limit of the different types of windows. For both Be and sapphire cases, the failure was localized in the convex thin part of the windows, as it is apparent in Fig. 4. The pressure limit for a 1.5 mm Be window is about 4000 bar, and about 2400 bar for a 0.6 mm sapphire window.

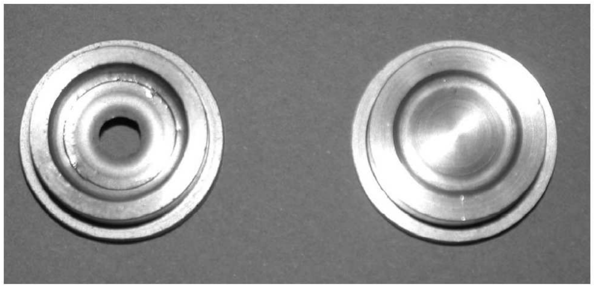

FIG. 4. Picture showing the 1.5 mm Be window before (right) and after (left) a test of pressure explosion (4000 bar). The window exploded in the top part of the profile and a crack is visible in the convex thinnest part of this profile.

III. INTERNAL HEATING/SAMPLE

Two technological functions are accomplished in the internal part of the cell (drawn in Fig. 5): sample containing in a so-called internal cell and sample heating in a furnace.

A. Heating elements

The heating elements design is based on the one developed by Tamura *et al.*[4] It consists of placing the sample container in a copper tube which is heated up to the experimental temperature with a resistive metallic wire (molybde-

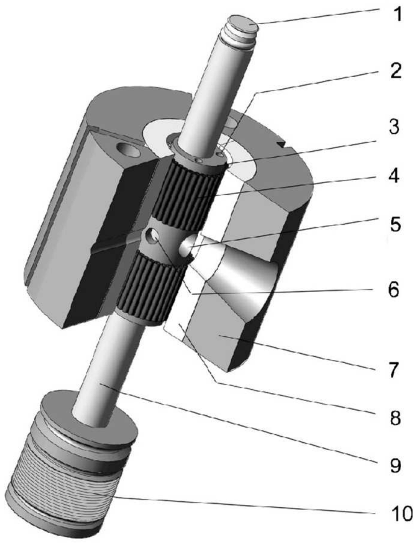

FIG. 5. 3D drawing of the internal part in the configuration for aqueous samples. (1) Internal cell cap. (2) Thermocouple housing in the copper tube. (3) Copper tube. (4) Resistive furnace. (5+6) Beam windows in the copper tube. (7+8) insulating ceramic elements. (9) Alumina internal cell. (10) Bellows for aqueous samples. Note that the heating principle is identical in the case of nonaqueous samples.

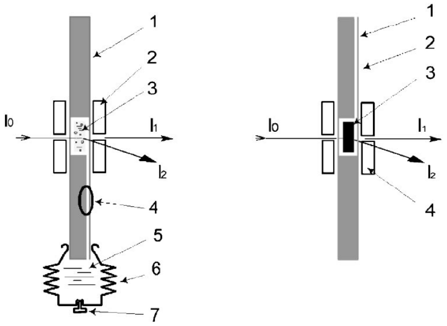

FIG. 6. Sketch of the two internal set-up. I_0, I_1, and I_2 correspond to the incident, transmitted, and fluorescence (or scattered) beams. Left for the aqueous samples. (1) Cylindrical internal cell with two inner tubes (in gray) above and below the sample. (2) Furnace. (3) Heated aqueous sample. (4) Canal connecting the sample to the bellows. (5) Ambient aqueous sample. (6) Bellows. (7) Sealing screw. Right for the liquid metals samples. (1) Cylindrical internal cell with two inner tubes (in gray) above and below the sample. (2) Canal for the expanding sample. (3) Liquid metal sample. (4) Furnace.

num, tungsten or tantalum). The role of this copper tube is to uniformize the temperature in its inner part and thus in the internal cell itself. *K*-type thermocouples are housed in holes drilled in the tube in order to measure the temperature as close to the sample as possible. The resulting temperature gradient between the thermocouples holes and the inner part of the internal cell has been determined precisely. As it is visible in Fig. 5, all these elements are confined in insulating ceramic elements both to avoid heat outflow and for high-pressure safety reasons. Since the sample region probed by the photons beam is at the center of the heating zone, all the heating elements have three apertures corresponding to the three windows of the HP vessel.

B. Internal cell

It is worth recalling that the walls of the cylindrical sample container (internal cell) do not have to support any relative pressure, since the whole HP vessel is He pressurized. The resulting benefit is that the selection of the material is not made under resistance to pressure considerations but dictated by its chemical neutrality with the sample, its low absorption properties, its resistance to high temperatures, and its compatibility with easy machining. According to each spectroscopic or scattering technique, specific container shape and material are chosen. The constraints to be considered are the photons energy, the amplitude of the cross section of the physical process (and thus the countrate), and the angular dependence of the outcoming intensity of photons. Very versatile materials are polycrystalline sapphire Al_2O_3 or glassy carbon and are used for most of experiments. For the study of melting glasses or metallic liquid samples, quartz is also successfully used.

C. Internal cell setup

There are two main experimental configurations of the internal setup, corresponding to the two types of samples: either liquid metals or aqueous samples (Fig. 6). In the former case, the melting liquid expands upwards in the cell in an expansion canal, however remaining in the heated volume to avoid any partial solidification of the sample. The same canal is also used to trap the escaping metallic vapor that could otherwise deposit elsewhere in the vessel, on the beam pathway (HP windows, heater, …). Such an experimental configuration is used, for example, for EXAFS investigations of liquid metal.[16]

For the aqueous samples, the main cylindrical sapphire tube is the same, but a pair of bellows are placed at the bottom that transfer pressure to the sample. This element enables to isolate the aqueous sample from the He atmosphere. Furthermore, it acts as a reservoir, since its contact with the water cooled HP vessel cools it down and allows the liquid inside to remain at the ambient density. With such a set-up, pressure and temperature prospection of the phase diagram with strong variations of the sample density can be achieved in the (30–600 °C) and (1–2000 bar) ranges.

IV. GEOCHEMICAL APPLICATION: EXAFS/XANES INVESTIGATION OF Fe^{III} ENVIRONMENT IN HYDROTHERMAL CONDITIONS

We present in this part results obtained with beryllium windows. Although pressure tests have been conducted on the SAXS sapphire windows (see above), they have still not been put in an x-ray beam.

A. Experiment

The samples studied were 0.01 m $FeCl_3$ aqueous solutions. They were prepared by dissolving solid $FeCl_3$ (Sigma-Aldrich Chemie GmbH) in deionized water (18 MΩ). The spectra were recorded at 300 bar from 30 °C to 375 °C, giving solvent densities from 1 to 0.32 g cm^{-3}.

XAS spectra at the Fe *K*-edge (7112 eV) were obtained at the European Synchrotron Radiation Facility (Grenoble, France) at the Collaborative Research Group FAME beamline (French Absorption spectroscopy beamline in Material and Environmental science). This beamline is installed on a bending magnet (0.8 T). It is constituted of two parabolic Rh-coated mirror, a Si (111) double-crystal monochromator and an experimental setup for different XAS acquisition modes (transmission and fluorescence). The spot size ($200 \times 300\ \mu m^2$) is kept constant on the sample with the dynamical sagittal focusing of the second crystal of the monochromator.[17] The spectra were recorded at the Fe *K*-edge in fluorescence mode with a 13 Ge elements Canberra detector. For each temperature, three spectra were accumulated for a total counting time of 2 h.

B. Qualitative analysis

The EXAFS oscillations extracted from the fluorescence spectra are displayed in Fig. 7 and the XANES spectra in Fig. 8. In Fig. 7, it is clearly visible that in spite of the low energy, low concentration and relatively low counting time, valid EXAFS spectra are obtained. A qualitative observation of this figure indicates a clear evolution with temperature that has to be quantify with a precise EXAFS data processing as it will be done in the next future. The decrease of the amplitude of the oscillations in the (3–5 Å^{-1}) region strongly

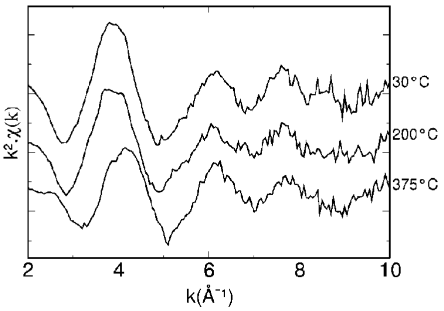

FIG. 7. EXAFS $k^2 \times \chi(k)$ oscillations extracted from the fluorescence spectra of 0.01 m $FeCl_3$ solutions at 300 bar. The oscillations are plotted for three temperatures: 30 °C is the lowest and 375 °C the highest temperature analyzed.

suggests an evolution of the number of oxygen neighbors around the Fe^{3+} ion. The evolution of the frequency of the oscillations indicates an evolution of the Fe–O distance. This structural modification could also be accompanied with an ion pairing effect between Fe^{3+} and Cl^- ions as it is observed in these conditions of temperature and pressure.[5,6,18–20] All these first EXAFS qualitative results are confirmed by the inspection of the XANES spectra in Fig. 8. XANES spectroscopy is a powerful tool to elucidate the precise three-dimensional structure of a molecular cluster. It provides also for additional electronic information on the absorbing atom. This XANES spectroscopy was recently applied to the study of the hydration of ions[21,22] and of molecules in supercritical conditions.[23] In the latter reference, authors used the cell presented here for part of the measurements. In Fig. 8, the change in the shape of the spectra suggests a modification of the environment of Fe^{III} at high temperatures. This change is most likely due to a modification of the oxygen shell around the iron ion.

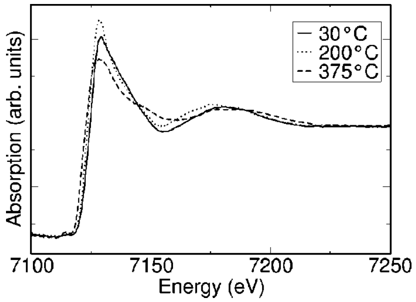

FIG. 8. XANES spectra of the $FeCl_3$ aqueous solutions at 300 bar at three temperatures. The spectra have been normalized to the density of the solvent.

[1] M. I. Eremets, *High Pressure Experimental Methods* (Oxford University Press, Oxford, 1996).
[2] A. Filipponi, J. Phys.: Condens. Matter **13**, 23 (2001).
[3] Y. Soldo, J.-L. Hazemann, D. Aberdam, M. Inui, K. Tamura, D. Raoux, E. Pernot, J.-F. Jal, and J. Dupuy-Philon, Phys. Rev. B **57**, 258 (1998).
[4] K. Tamura, M. Inui, and S. Hosokawa, Rev. Sci. Instrum. **66**, 1382 (1995).
[5] V. Simonet, Y. Calzavara, J.-L. Hazemann, R. Argoud, O. Geaymond, and D. Raoux, J. Chem. Phys. **117**, 2771 (2002).
[6] V. Simonet, Y. Calzavara, J.-L. Hazemann, R. Argoud, O. Geaymond, and D. Raoux, J. Chem. Phys. **116**, 2997 (2002).
[7] G. Ferlat, A. S. Miguel, J.-F. Jal, J.-C. Soetens, P. A. Bopp, J.-L. Hazemann, D. Testemale, and I. Daniel, J. Mol. Liq. **101**, 127 (2002).
[8] G. Ferlat, A. S. Miguel, J.-F. Jal, J.-C. Soetens, P. A. Bopp, I. Daniel, S. Guillot, J.-L. Hazemann, and R. Argoud, Phys. Rev. B **63**, 134202 (2001).
[9] Y. Soldo, J.-L. Hazemann, D. Aberdam, M. Inui, K. Tamura, D. Raoux, E. Pernot, J.-F. Jal, and J. Dupuy-Philon, Phys. Rev. B **57**, 258 (1998).
[10] M. V. Coulet, V. Simonet, Y. Calzavara, D. Testemale, J.-L. Hazemann, D. Raoux, F. Bley, and J.-P. Simon, J. Chem. Phys. **118**, 11235 (2003).
[11] A. Cunsolo, G. Ruocco, F. Sette, C. Masciovecchio, A. Mermet, G. Monaco, M. Sampoli, and R. Verbeni, Phys. Rev. Lett. **82**, 775 (1999).
[12] E. D. Isaacs, A. Shukla, P. M. Platzman, D. R. Hamann, B. Barbiellini, and C. A. Tulk, Phys. Rev. Lett. **82**, 600 (1999).
[13] U. Bergmann, P. Wernet, P. Glatzel, M. Cavalleri, L. G. Pettersson, A. Nilsson, and S. P. Cramer, Phys. Rev. B **66**, 092107 (2002).
[14] D. T. Bowron, M. H. Krisch, A. C. Barnes, J. L. Finney, A. Kaprolat, and M. Lorenzen, Phys. Rev. B **62**, R9223 (2000).
[15] D. S. Tsiklis, *Handbook of Techniques in High-Pressure Research and Engineering* (Plenum, New York, 1968).
[16] M. V. Coulet (unpublished).
[17] J.-L. Hazemann, K. Nayouf, and F. D. Bergevin, Nucl. Instrum. Methods Phys. Res. B **97**, 547 (1995).
[18] M. M. Hoffmann, J. G. Darab, B. J. Palmer, and J. L. Fulton, J. Phys. Chem. **103**, 8471 (1999).
[19] T. M. Seward, C. M. B. Henderson, J. M. Charnock, and B. R. Dobson, Geochim. Cosmochim. Acta **60**, 2273 (1996).
[20] S. L. Wallen, B. J. Palmer, and J. L. Fulton, J. Chem. Phys. **108**, 4039 (1998).
[21] M. Benfatto, P. D'Angelo, S. DellaLonga, and N. V. Pavel, Phys. Rev. B **65**, 174205 (2002).
[22] P. D'Angelo, M. Benfatto, S. DellaLonga, and N. V. Pavel, Phys. Rev. B **66**, 064209 (2002).
[23] D. Testemale, J.-L. Hazemann, G. S. Pokrovski, J. Roux, Y. Joly, R. Argoud, and O. Geaymond, J. Chem. Phys. **121**, 8973 (2004).

2.2.2 Design and usage highlights

In complement to the above publication, in this sub-section I succinctly highlight a few important design and usage ideas that have come up along the 15 years of use of the autoclaves. Here again the idea is to critically review this period and synthesize the main strengthes and weaknesses of our technology. Some of them were already touched upon earlier in this manuscript, but I still find worthwhile to list them here, in order to make this technological chapter complete and self-consistent.

Glass-like carbon internal cells: the use of glass-like (or glassy) carbon was a real game changer that opened the possibility of low X-ray energy spectroscopy. Before its introduction in 2005, we used to make internal cells in alumina but the strong absorption of X-rays of this material imposed to machine the cells down to very thin thickness: the process was complex, not reliable, time consuming, and the resulting cells were fragile. By comparison, glassy carbon is much more transparent to X-rays, is (kind of) cheap, easy to machine, inert chemically, and has low impurities. This point is explained in the section of International Tables of Crystallography (included above). In short, if it was not for this material, XAS experiments below ~9 keV would have been impossible, i.e., no access to 3d transition metals. The main drawbacks of glassy carbon in the context of hydrothermal geochemistry is its chemical reactivity with sulfur rich solutions, and its oxydation/destruction above 700°C in aqueous solutions.

High-pressure windows material As explained in our publication (43) (included above), beryllium is best for its low X-ray absorption and mechanical resistance. In our design the HP windows are not in contact with the sample and are constantly cooled: so they are totally safe (no beryllium-related risks) and have a long life. Nevertheless, the (very) annoying problem with beryllium is the high impurities content: the figure 2.2.2 (left) shows a fluorescence spectrum of different HP windows material, where it is obvious that the beryllium one contains many impurities, in large quantities; and most of them are relevant elements for hydrothermal geochemistry. These impurities add a parasitic signal in measurements acquired in transmission through the HP windows, as it is visible in figure 2.2.2 (right, the red curve is the signature of Be windows at the copper K-edge), and thus harms the signal quality from the sample (black curve).

Because some specific experiments needed a very clean base line, for example in the case of very low metal concentrations, we designed and built some glassy carbon HP windows to take advantage of the purity of this material (figure 2.2.2, left), its low absorption and low cost. However assessing its mechanical resistance was a bit "terra incognita" as we didn't know of any HP equipment built in glassy carbon. It did work and was published in reference (44). Figure 2.2.2 (right) shows that the low signal from low concentration samples can be measured in transmission (blue and green curves), whereas it could not have been extracted reliably otherwise (red and black curves).

Beam damage and sample volume One interesting feature of our set-up is the (relatively) large sample volume, in the range (0.05-1) ml. It allows to load and unload easily the samples, to load millimetric solid samples (for dissolution experiments, or mineral buffering), to recover liquid and solid samples for *post mortem* analysis, and also to ensure that the sample/beam volume ratio is large. The importance of having such a large ratio to avoid beam damage (or redox modification of the sample) has already been discussed in this manuscript: in our recent review (25), which is included in section 1.4 (page 51 of this manuscript), the discussion about beam damage can be found page 223 of this publication; and just above in our "International Tables of Crystallography" contribution, included in the section 2.1 (page 91) of this manuscript. In the latter publication, figure 2 is a compelling demonstration that autoclaves have usually a more favorable volume ratio sample vs beam size.

HP and HT stability The temperature control is done with a resistive heater: this is a classical design that is easily and reliably regulated. On the contrary, the pressure control is more complex, and specific valves and a regulation apparatus were developed at Néel Institute: see reference (45). This system was optimised over the years for the following reasons.

In the case of aqueous samples, the stability of pressure and temperature regulation over time (i.e., during measurements) is crucial. This is especially true in the case of experimental conditions where the sample density varies strongly with P and T. Indeed, in our set-up (autoclave+FAME beamline

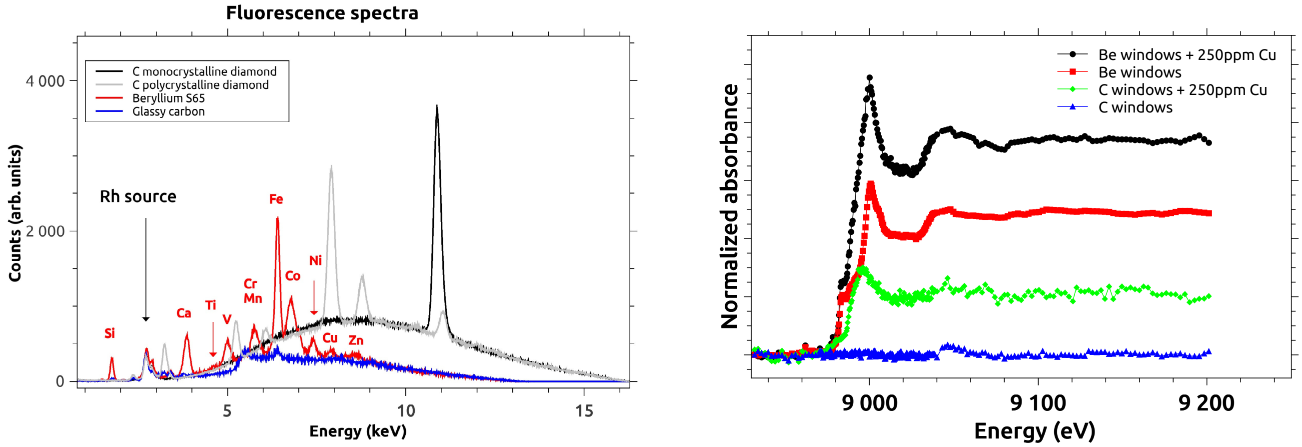

Figure 2.1: Figures extracted from reference (44). Left: Fluorescence spectra from monocrystalline and polycrystalline diamonds, glass-like carbon and beryllium. The acquisition time is 1200s for all spectra and they are normalized to the rhodium source L alpha and beta fluorescence intensity. The elements indicated in red correspond to the tagging of the fluorescence peaks of the beryllium impurities; beryllium is polycrystalline not textured and does not diffract. The diamond spectra contain only diffraction peaks over an inelastic background. Right: Absorption spectra measured in transmission of 4.5 mm beryllium and dome shaped glass-like carbon windows, with and without a 250 ppm Cu(II) solution in the autoclave. The spectra were flattened and aligned at 8960 eV for clarity and comparison purposes.

acquisition chain), we can detect very small variations of the sample density: about ±0.001 $g.cm^{-3}$. This is all nice and good when one wants to measure densities with precision, but is less than ideal when the sample density oscillates during a measurement, and this variation translates into signal oscillation as well: EXAFS is all about oscillations, so parasitic ones should be removed at all cost. As an example, for a measurement done at 300 bar/400°C on an aqueous sample (the density of which is considered equal to that of water), a variation of its density of ±0.001 $g.cm^{-3}$ corresponds to a variation of 0.2 bar: in other terms, to avoid a parasitic oscillation in the XAS data, a stability of ±0.2 bar or better is needed, which is about what we manage to do (see figure 2.2).

Visual observation As described in the original publication (43), the versatility of the autoclave set-up relies on the possibility to swap the materials of the HP windows and internal cell. Basically, there is an "X-ray configuration" that consists of beryllium windows and glassy carbon cells, and an "optical configuration" that consists of sapphire windows and cells. The latter allows for visual observation of the sample which is useful in some situations where it helps conducting the running experiment: tracking the color change of the sample, monitoring the melting of a solid sample, checking the position of liquid and vapor during a phase separation, simple curiosity, etc. In figure 2.3 three pictures of a phase separation in water are showed as an example.

2.2.3 Autoclave MarkII

Collaborations:

- *ISTO Orléans (R. Champallier, A. Slodczik)*

This is a brief paragraph about the recently developed new version of our autoclave. No technological detail are given here, only a summary and a scientific example.

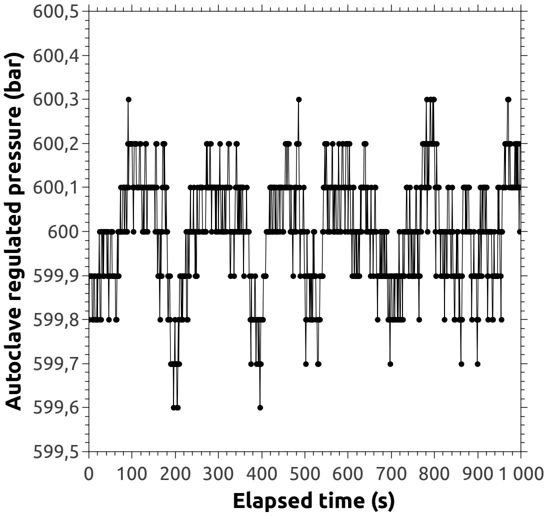

Figure 2.2: Variation of the pressure in the autoclave, regulated by the control system described in (45).

Figure 2.3: Visualisation of the phase separation of water occuring at 200 bar/365°C. Top and bottom pistons are visible, the sample is between the pistons in the clear area.

The objective of designing a "MarkII version" of our set-up was mainly to improve two thermal aspects: better internal geometry for a smaller temperature offset, and better efficiency to reach higher temperatures). Some small improvements were also added to the different elements, either practical or cosmetic. What is interesting to note after about one year of use is that all the new equipments, even some with a familiar design (like here), need some commissioning and tuning. Maybe we are spoiled by the routine, reliable and friendly use of the "MarkI" version, but each new technological change or improvement indeed needs to be optimised. Nevertheless, even if some modifications still need to be done, the goals are mostly reached with clearly a better thermal behaviour, and new scientific possibilities.

We now use this new version for all autoclave experiments, including the "classical" measurements of aqueous solutions below 600°C; but here I show a scientific example to illustrate the new possibilities offered by the better thermal capacities, a study conducted by M. Louvel (Münster University) in collaboration with us. The general idea is to study metal speciation in magmatic fluids and melts, i.e., to transfer our methodology to higher temperatures and to fluids deeper in the crust. In this specific study, the goal was to evaluate how much bromide could transfer from the fluid (the initial aqueous sample was a NaBr aqueous solution) to an haplogranite melt. Figure 2.4 shows the geometry of the internal assembly that enables to collect both transmission and fluorescence signals from both the fluid and the

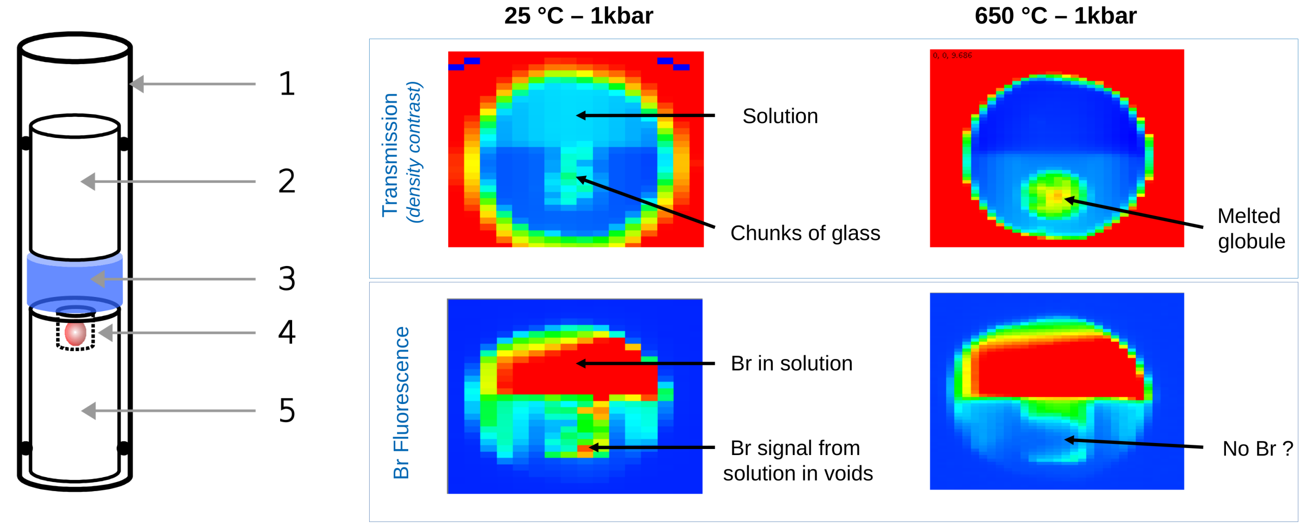

Figure 2.4: Graphical summary of M. Louvel's experiment to study Br speciation in magmatic melts and fluids. Left: schematic drawing of the internal cell assembly. 1: glassy carbon internal cell; 2: top piston; 3: sample NaBr-rich aqueous fluid; 4: crucible machined in the bottom piston, with a spherical glass sample inside; 5: bottom piston. Right: 2D cartographs of the sample at 1 kbar/250°C (left) and 1 kbar/650°C (right). The circular shape corresponds to the entrance HP window accessible to the photons: the top half of this shape shows the fluid, the bottom half shows the top part of the bottom piston, with the crucible fully visible. The cartographs are obtained either by transmission measurements (density contrast, top row), or by Br fluorescence signal (bottom row).

melt. The figure also displays the 2D cartographs that were measured, and on which the fluid and melts are clearly distinguishable, with the respective presence and absence of bromide. XAS spectra were also collected in both phases.

This was a preliminary experiment, already successful and promising, and which immediately provided for numerous areas of improvement that are underway.

2.3 Autoclave collaborations

We often describe our equipment as being versatile. In this section I wish to document this aspect by describing briefly several studies that used our autoclaves differently from the classical "XAS of hydrothermal aqueous solutions" configuration, that I mainly discussed in this manuscript. All these works needed specific technological developments. For each example I describe the scientific background context (by copying elements of the publications), and also list the key technological elements/tools that proved beneficial to the experiments.

2.3.1 Generation of organic compounds in hydrothermal fluids

Collaborations:

- *IFREMER, Brest (C. Konn, J. Querellou)*

The global scientific context was the study of the abiotic production of hydrocarbons in the Earth's crust. The specific objective of this experiment was to determine the chemical products of hydrothermal degradation of biomass (conducted in our autoclave) and compare it to the nature of organic compounds that are found above Mid-Ocean Ridge hydrothermal systems. The abstract of the publication (46) reads:

> *Experiments on hydrothermal degradation of Pyrococcus abyssi biomass were conducted at elevated pressure (40 MPa) over a 200–450°C temperature range in sapphire reaction cells. Few organic compounds could be detected in the 200°C experiment. This lack was attributed to an incomplete degradation of P. abyssi cells. On the contrary, a wide range of soluble organic molecules were generated at temperatures >350°C including toluene, styrene, C8–C16 alkyl-benzenes, naphthalene, C11–C16 alkyl-naphthalenes, even carbon number C12–C18 polycyclic aromatic hydrocarbons, C15–C18 alkyl-phenanthrenes and C8:0–C16:0 n-carboxylic acids. The effect of time on the final organic composition of the degraded P. abyssi solutions at 350°C was also investigated. For that purpose the biomass was exposed for 10, 20, 60, 90, 270 and 720 min at 350°C. We observed a similar effect of temperature and time on the chemical diversity obtained. In addition, temperature and time increased the degree of alkylation of alkyl-benzenes. This study offers additional evidence that a portion of the aliphatic hydrocarbons present in the fluids from the Rainbow ultramafic-hosted hydrothermal field may be abiogenic whereas a portion of the aromatic hydrocarbons and n-carboxylic acids may have a biogenic origin. We suggest that aromatic hydrocarbons and linear fatty acids at the Rainbow site may be derived directly from thermogenic alteration of material from the sub-seafloor biosphere. Yet we infer that the formation and dissolution of carboxylic acids in hydrothermal fluids may be controlled by other processes than in our experiments.*

The 2 important experimental requirements were:

- the need to pressurize/heat and later de-pressurize/cool very quickly in order to reproduce the expected natural scenario of biomass suddenly carried away by seafloor hydrothermal circulation: we managed to reach increasing rates of 600 bar/min and 660°C/min;
- the necessity to recover the fluid samples to analyse them by gas chromatography mass spectrometry: the very tight diameter specifications of our sapphire cells ensure that no fluid is lost when unloading and can be collected *post mortem*, as shown in figure 2.5.

2.3.2 Microbial redox transformation of metals under subsurface pressure and temperature conditions

Collaborations:

- *University of Nevada, Las Vegas (A. Picard), LGL, Lyon (I. Daniel)*

The global scientific context was the study of geochemical redox cycles of metals under the oceanic subsurface, and the potential role of microorganisms. The specific objectives of the experiments (47, 48, 49) were the monitoring by XAS of the intensity and kinetics of reduction of selenium and iron by microorganisms under high pressure, in order to estimate the pressure range of their redox activity. The abstract of the publication (47) reads:

> *The impact of deep-subsurface pressure conditions on microbial activity is still poorly constrained. In particular it is unknown how pressure of deep environments affects microbial transformations of iron. We investigated the effects of high hydrostatic pressure (HHP) on the rate and the extent of bacterial dissimilatory iron reduction (DIR). We employed a novel experimental setup that enables in situ monitoring of Fe oxidation state and speciation in bacterial cultures in an optimized HHP incubation system using X-ray Absorption Near-Edge Structure (XANES) spectroscopy. The iron-reducing bacterium Shewanella oneidensis MR-1 was incubated at 30°C with Fe(III) citrate and tryptone at pressures between 0.1 and 100 MPa. For pressures up to 70 MPa strain MR-1 (10^8 cells ml^{-1}) was able to reduce all 5 mM Fe(III) provided. Above 70 MPa, the final amount of Fe(III) that MR-1 could reduce decreased linearly and DIR was estimated to stop at 109 ± 7 MPa. The decrease in the reduction yield was correlated*

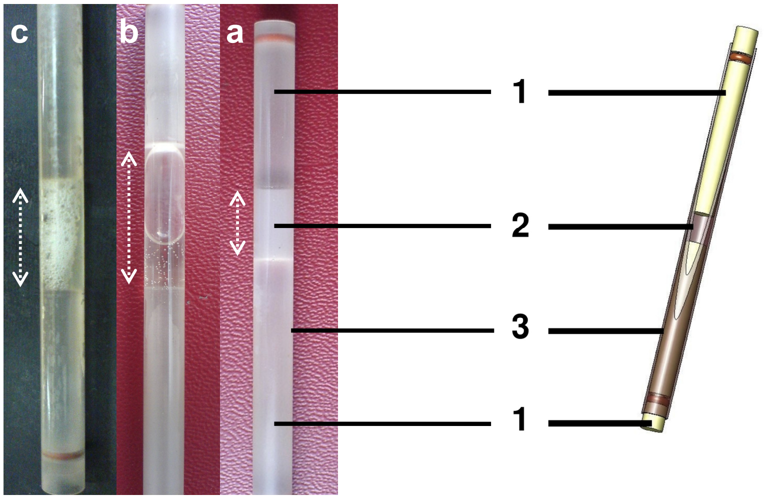

Figure 2.5: Figure and legend extracted from reference (46). On the right, schematic view of the internal cell that contains the sample. (1) Top and bottom sapphire pistons with a sealing silicone ring visible on each; (2) sample room between top and bottom pistons (2 cm maximum in our experiments); (3) sapphire tube (partly cut for clarity reasons). The total length of the cell is 85 mm. The internal diameter is 5 mm. On the left, picture of the internal cell before (A) and after a degradation experiment at 350°C/40 MPa (B) and 200°C/40 MPa (C). The arrows show the sample room between the two pistons. One can see the evolution of the sample: blurred before degradation, clear after (B) and frothy when treated at low temperature 200°C (C). A helium bubble is visible in (B).

> *with the dramatic decrease in survival (as determined by CFU counts) above 70 MPa. The initial rate of DIR increased with pressure up to 40 MPa, then decreased to reach zero at about 110 MPa. Increased rates of DIR activity and relatively high growth rates for pressures below 40 MPa would potentially ensure the maintenance of MR-1 in most of deep subsurface environments where moderate pressures occur, i.e. deep-sea environments. This study not only provides the first in situ quantitative results for microbial iron metabolism under HHP conditions but also sets the stage for future investigations of deep-sea pressure-adapted iron reducers. Moreover it demonstrates for the first time that XANES at the Fe K-edge is a powerful probe for in vivo monitoring of iron transformations in living microbial cultures.*

The 3 important experimental constraints were:

- the necessity to recover the fluid samples in order to do *post mortem* cell counting;
- the metal concentrations were low (about 250 ppm of iron for example) and the iron impurities of beryllium HP windows would impair the signal quality, all the more so as only one XANES spectrum (i.e., low statistics) could be measured in order to limit beam exposure (see below): this study triggered the design of glassy carbon HP windows that could hold 2000 bar (the maximum pressure that would be explored), which were mentioned earlier in this manuscript (in section 2.2.2, page 112);
- the necessity to limit beam exposure and increase the volume ratio sample/beam as much as possible, otherwise the beam damage on cell activity would bias the results. The users' previous experiments were conducted with diamon anvil cells (DAC) where this ratio is much less favorable, but given that experiments were conducted at room temperature sample volumes as large as 1ml could be used (compared to the 100 nl, at best, in DAC). This aspect was already discussed earlier in this manuscript.

2.3.3 Solvothermal synthesis of size-controlled single-nanocrystals and *in situ* monitoring

Collaborations:

- *Néel Institute, Grenoble (G. Dantelle, A. Ibañez)*

The global scientific context of this on-going collaboration is the synthesis of size-controlled doped nanocrystals that can be used in LED technology and nanothermometry. This collaboration is rich (50, 51, 52) and consists of several axes of research. The abstract of reference (52) is a good summary of the objectives and first results:

> Ce^{3+}*-doped* $Y_3Al_5O_{12}$ *(YAG:Ce) nanocrystals were synthesized by a unique solvothermal method, under sub-critical conditions. A home-made autoclave was used, operating in a larger pressure and temperature range than that with conventional commercial equipment and allowing direct in situ photoluminescence (PL) and X-ray absorption characterizations. The study of various synthesis conditions (pressure, temperature, precursor concentration, reaction time) allowed the best reaction conditions to be pinpointed to control YAG:Ce nanocrystal size, as well as crystal quality, and to get efficient optical properties. Without any post thermal treatment, we succeeded in obtaining well- crystallized YAG:Ce nanocrystals (30–200 nm), displaying typical PL properties of YAG:Ce with a maximal emission at 550 nm. The pristine 100 nm-sized YAG:Ce nanoparticles present an internal quantum yield of about 40±5%. In situ X-ray absorption near edge spectroscopy demonstrates the presence of* Ce^{4+} *in nanocrystals elaborated at high temperature, resulting from the oxidation of* Ce^{3+} *during the crystallization process.*

The important experimental features (that, again, prove the versatility of our set-up) are:

- Despite the low sample volume in our autoclaves (compared to the milliliters available in commercial autoclaves), the quantity of products that are recovered (synthesized nanoparticles) is enough to permit *post mortem* analysis (TEM, photoluminescence, etc.), see figure 2.6.
- What initiated this work was the need for a synthesis autoclave that would allow for a better control of synthesis parameters: indeed the conventional commercial autoclaves can usually only be heated and the pressure would build up autogenously and varies along with the evolution of the chemical reactions. Immediately, the possibility to use higher pressures improved the crystallinity of the particles (figure 2.6).
- *In situ* characterization. After this initial synthesis step, the logical next step we explored was *in situ* optical characterization through the HP windows: photo-luminescence measurements and visualization (figure 2.6). And obviously we proceeded to *in situ* XAS measurements to quantify the hydrothermal oxydation of Ce^{3+} to Ce^{4+} in doped nano-YAG:Ce (figure 2.6). Eventually, very recent *in situ* DLS (Dynamic Light Scattering) measurements were also conducted successfully.

2.3.4 Technology transfer

Finally, I also collaborated with research teams interested in copying our autoclaves. I reckon there is room for everyone, and withholding information is never a good solution in the long term. Several groups of research approached us and managed to develop their own version of our set-up, among which:

- Adelaide University: J. Brugger et al. designed and commissioned in 2010 a similar autoclave to be installed on the XAS beamline of the australian synhrotron (53).
- Münster University: S. Klemme and his collaborators have been building and have recently commissioned their own version of the autoclave.

For information, it is interesting to list the elements where they chose to use exactly the same elements as in our design: pressure regulation system, beryllium windows, glassy carbon cells. This is in line with the technological features that I highlighted above, and confirms their importance for the success of such hydrothermal experiments.

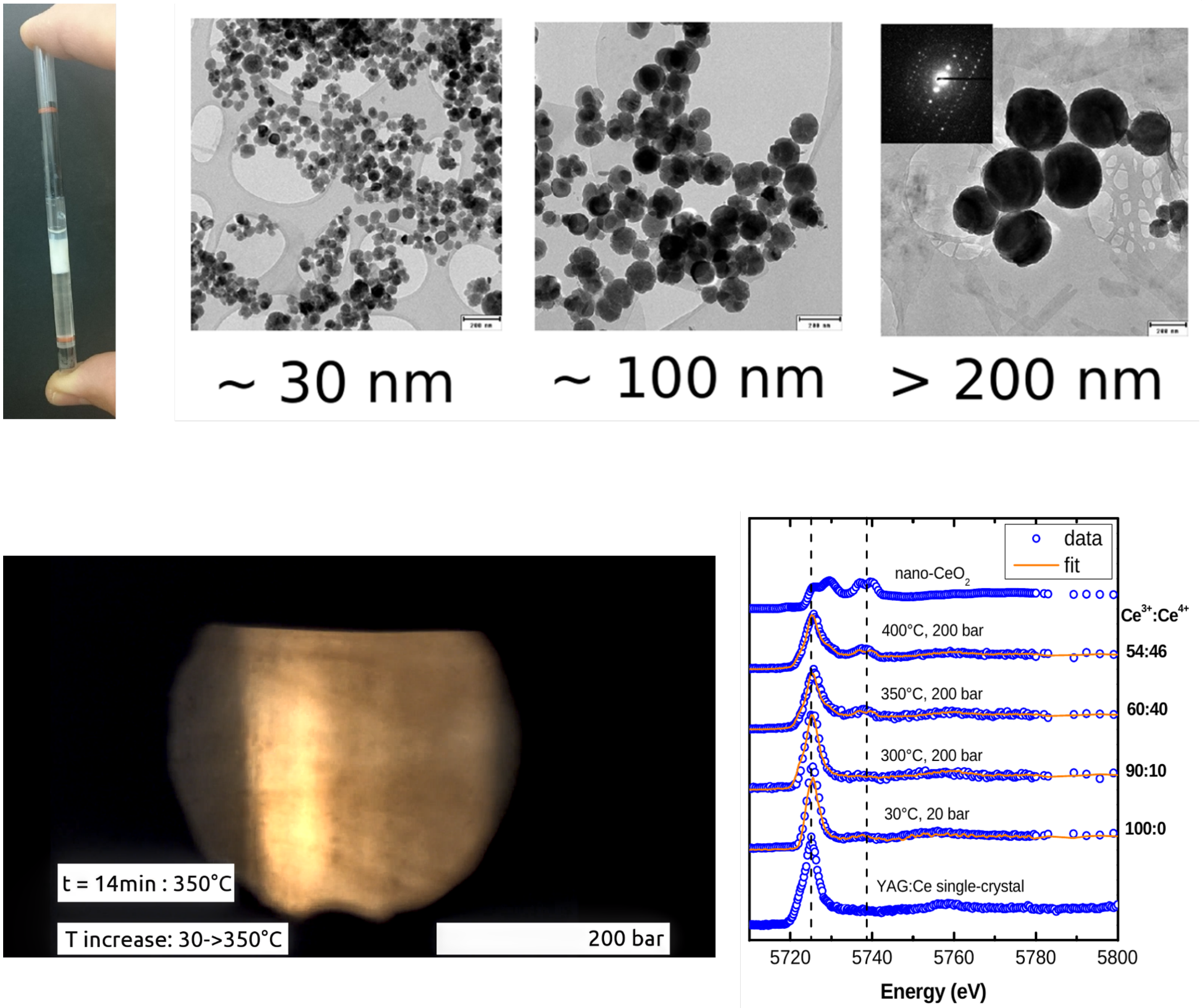

Figure 2.6: Top, left: Picture of the sapphire cell after a synthesis; the sample is fully recovered, both the transparent fluid phase and the solid white phase made of nanoparticles. Top, right: TEM images of synthesized nanoparticles YAG:Ce; different experimental conditions lead to different size characteristics. Bottom, left: picture of the sample volume in the autoclave during a synthesis, at 200 bar/350°C; the smoke-like texture in the fluid is formed by growing nanoparticles, their photoluminescence is at the origin of the orange tint. Bottom, right: *in situ* XANES spectra measured in the autoclave at FAME-UHD beamline (blue) and the corresponding linear combination fits (red) which allow for the quantitative determination of the Ce^{3+}/Ce^{4+} ratio. The oxydation of Ce^{3+} is demonstrated.

Chapter 3

Beamline scientist

Supervision:

- *the beamline users!*

This is a peculiar chapter, since it doesn't describe a scientific topic on its own, but still describe a real scientific activity. I'm involved at the FAME and FAME-UHD beamlines as a scientist. I don't mean to detail whithin this manuscript the day-to-day actions and requirements, but I'd rather take this opportunity to ponder the relevance for a CNRS research scientist to occupy this specific position. Indeed, a big part of the job is to provide user support, but not only...

3.1 User support

The role of user support (commonly known as "local contact") consists of helping the users of our beamline at the different stages of their experiment:

Before the experiment feasibility assessment, writing of the proposal, preparation of the experiment (mechanical integration, optimal sample preparation, planning, etc.);

During the experiment setup of the beamline (optics, sample environment), technical and/or methodological and/or strategical and/or psychological support;

After the experiment spectra analysis, publication.

Obviously the involvement of the beamline scientist depends on the expertise of the users: new users clearly need guidance to conduct their experiment in good conditions and make the best of their precious beamtime; whereas a long-time experienced synchrotron veteran needs mainly a correctly aligned beamline, a properly documented wiki page, and coins for the coffee machine. This "local contact" function clearly matches my curriculum (physics engineering school + PhD), skills and personal taste; which is a prerequisite for being doing this job for 15 years now. Another attractive aspect of this synchrotron work is the different timescale than in the laboratory: experiments usually run for one week, 24/24, and such a time pressure is both challenging and invigorating... as long as it is well balanced with more thoughtful laboratory periods.

3.2 Outreach and teaching

Outreach communication and teaching are crucial elements of the scientific activity of FAME beamlines. We interact with 2 types of students/visitors: non specialists curious about the large facilities (and ESRF) and looking for a general visit of the installations, and scientists specifically interested by the possibility to conduct a synchrotron experiment and XAS in particular. I'll also discuss autoclave teaching.

General visit Synchrotron installations (and large facilities in general, such as the ILL neutron source on the same EPN campus as ESRF) attracts quite a lot of curious students/scientists/people. The reasons

are manifold. First such large installations are noticeable, both visually (the EPN campus is located in the city and is quite peculiar with the CEA formerly doing nuclear research, the ILL nuclear reactor and the synchrotron with its donut shape) and economically because they drain a lot of public money. Then, they are interesting to visit for the large number of trades and specific technical jobs involved, not only purely scientific. Finally, Grenoble universities are particularly active, in many scientific courses, in including the X-rays and neutrons tools available at Grenoble.
For this type of visits, ESRF is very well prepared and I regularly organize visits, and interact with the ESRF communication group.

Synchrotron and XAS introduction For scientists interested in doing synchrotron experiments, and in particular XAS measurements at FAME, it goes beyond a simple visit and is real teaching with more time. First I've been teaching within the european HERCULES course[1] for 12 years now. Then, FAME has been organizing a one week teaching course[2] since 2004. It includes lectures (XAS, detectors, optics, etc.), practicals on the beamline (beamline set-up, measurement) and analysis tutorials (EXAFS and XANES). Our idea was both to demystify access to synchrotron (which can be a bit intimidating and difficult for scientists with no experience), and to train power users who would then make their FAME experiments smooth, and who would also preach the XAS and FAME word in their respective labs.
This teaching is a very efficient way to interact with the community and facilitate the access to FAME beamlines, and as such is an important aspect of my position as a beamline scientist. The constant filling of our workshop is also an indication that there is clearly a need for XAS teaching in France.

HP autoclave teaching Whithin our FAME training course we introduce the use of autoclaves among other sample environments, but it is definitely not a proper workshop. Another teaching channel is through the biennial french HP workshop/conference organized by the "Réseau français des hautes pressions"[3], where we regularly communicate and demonstrate our autoclaves; but we hardly reach "autoclave newbies" because the attendees are mainly HP (french) scientists already experienced. Finally, ESRF recently organized a one week workshop to train the (established or potential) users to the use of HP equipments, through lectures, scientific highlights, and practicals; we were involved for the autoclaves. This was an interesting opportunity in terms of teaching and interaction with the users, but also because the attendees were coming mainly from foreign countries and were not aware of our autoclaves. It turns out that in this small panel of HP users Diamond Anvil Cells (DAC) were the stars of the show and the corresponding workshops could not accept all the registrations; on the contrary our autoclave practicals did not attract a lot of students (the ones we had ticked autoclaves mainly as a second choice). This is an interesting outcome, which shows that the autoclave community might be much smaller that the higher pressure ones (DAC, Paris-Edinburgh, etc.), or that more communication needs to be done outside France.

3.3 XAS database

Collaborations:

- *OSUG (B. Schmitt, P. Bollard, D. Albert)*

Over the period 2015-2019, I have carried the project of setting up a spectral database for FAME and FAME-UHD. The motivation was two-fold:

- to fill the database gap in the field of X-ray absorption spectroscopy. Indeed, some databases exist but there are few of them (54, 55), and the description of the samples is often too vague for the spectra to be effectively reused, leading users to measure very regularly the same references and thus leading to a loss of overall beam time;

---

[1] `http://hercules-school.eu/`

[2] `www.esrf.eu/home/UsersAndScience/Experiments/CRG/BM30/fame-training-course.html`

[3] `www.reseauhp.org/`

- to anticipate the current political trend requiring data to be made public (Europe is gradually imposing the concept of FAIR: Findable Accessible Interoperable Reusable data); but our objective was also to go beyond this, and to ensure that the data are indeed accessible, but also reusable, indexed and containing sufficient detail to serve as a repository for sets of spectra (useful for calculation codes using artificial intelligence methods, for example). I think that meeting these requirements is essential for a national instrument, and this was lacking on FAME.

We chose to join the SSHADE project [4], led by Bernard Schmitt (IPAG, Grenoble): this database infrastructure hosts spectral data from many types of materials (minerals, meteorites, organic matter, etc.), as well as simulated spectra covering the whole electromagnetic spectrum from gamma rays to radio waves. Our first task was to make the data model compatible with the X-absorption data from our beamlines. Benefiting from the SSHADE infrastructure, the SSHADE/FAME database is perennial (INSU label as National Observation Service). It is based on a very elaborated data model which allows to describe very precisely all the elements (from the sample to the measurement) and to make an efficient research. Moreover, by assigning a DOI (Digital Object Identifier) to each dataset, it offers the possibility to disseminate the spectra in a robust way and in accordance with current publication requirements[5]. Its search, visualization and export interface has been open to users since February 2018: one example (based on reference (7)) is shown in figure 3.1. The SSHADE consortium currently brings together 21 laboratories from 11 different countries. The SSHADE/FAME database currently contains about 400 spectra. Now that it is in production, a major current task is to convince and help users to deposit their data. To do so as smoothly and efficiently as possible we (I. Kieffer for the technical part) developed Python tools to convert spreadsheet-style information (i.e., user compatible) into the xml SSHADE format.

3.4 Pivotal role

In conclusion, my function at the FAME beamlines is both scientific and technical, which reflects my training as a scientist and engineer. The scientist positions at large facilities always have a strong technical aspect, by nature, but I strongly believe that staffing synchrotron beamlines with scientists, and not only engineers (i.e. technical staff), is extremely beneficial for everybody. When writing 'scientists', I'm refering to researchers in connection with non-synchrotron laboratories. Indeed, beyond the role of user beamline support, my function sits at the interface between the beamline and the HP (autoclave) communities. By actively participating in the technical integration of the autoclaves on the beamlines, in their maintenance, by providing user support during experiments, by spreading the words about our installation, but also by conducting my own research, I ensure that our HP equipments are efficiently used, for everyone's interest and good use of public fundings.

For all these reasons, the different missions of my beamline scientist position need to be pursued and reinforced.

---

[4] www.sshade.eu

[5] So far some publications (such as Geochimica Cosmochimica Acta) politely invite authors to submit data along with the manuscript, but time will come when this will be compulsory.

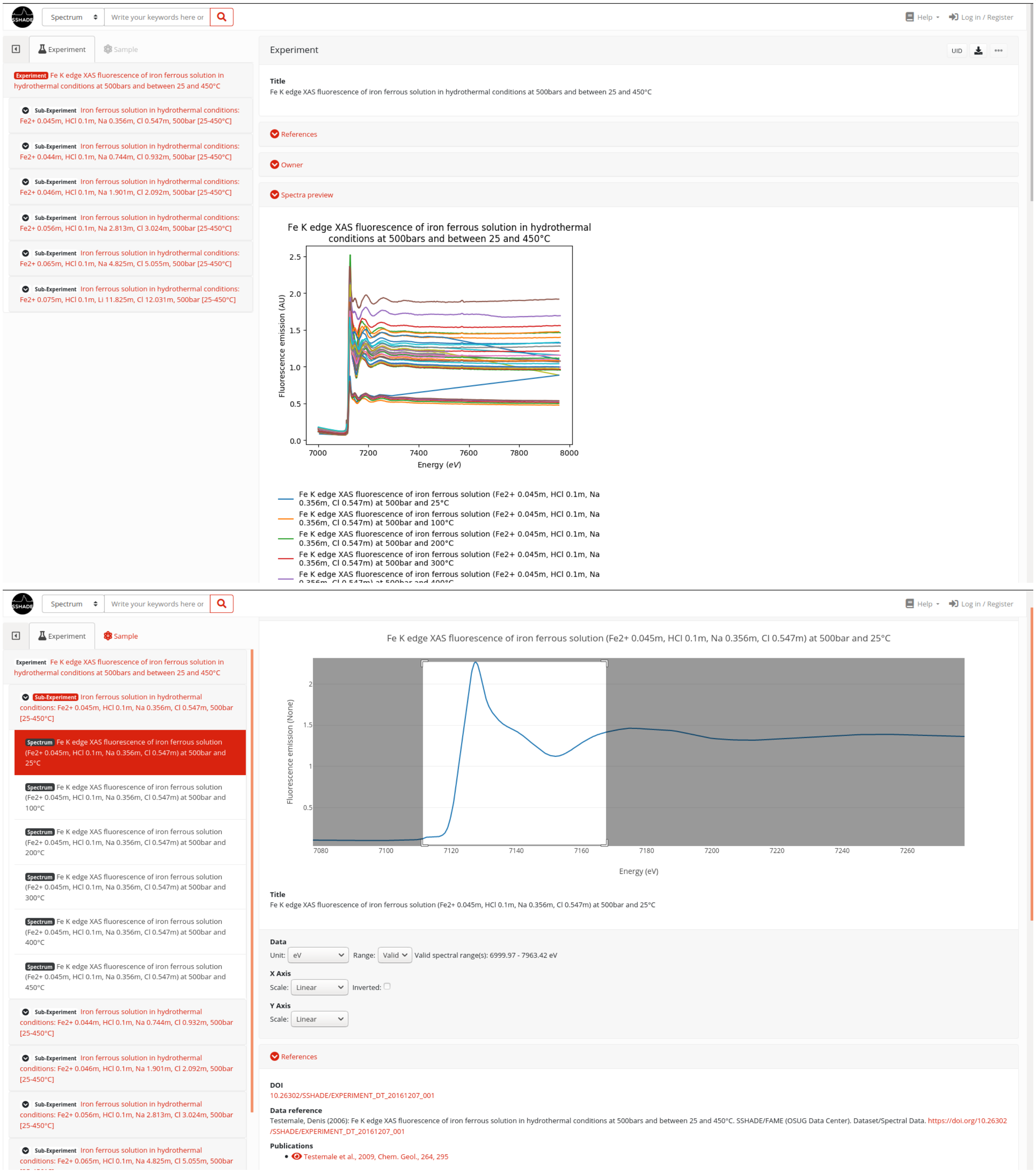

Experiment Fe K edge XAS fluorescence of iron ferrous solution in hydrothermal conditions at 500bars and between 25 and 450°C

Sub-Experiment Iron ferrous solution in hydrothermal conditions: Fe2+ 0.045m, HCl 0.1m, Na 0.356m, Cl 0.547m, 500bar [25-450°C]

Sub-Experiment Iron ferrous solution in hydrothermal conditions: Fe2+ 0.044m, HCl 0.1m, Na 0.744m, Cl 0.932m, 500bar [25-450°C]

Sub-Experiment Iron ferrous solution in hydrothermal conditions: Fe2+ 0.046m, HCl 0.1m, Na 1.901m, Cl 2.092m, 500bar [25-450°C]

Sub-Experiment Iron ferrous solution in hydrothermal conditions: Fe2+ 0.056m, HCl 0.1m, Na 2.813m, Cl 3.024m, 500bar [25-450°C]

Sub-Experiment Iron ferrous solution in hydrothermal conditions: Fe2+ 0.065m, HCl 0.1m, Na 4.825m, Cl 5.055m, 500bar [25-450°C]

Sub-Experiment Iron ferrous solution in hydrothermal conditions: Fe2+ 0.075m, HCl 0.1m, Li 11.825m, Cl 12.031m, 500bar [25-450°C]

Experiment

Title
Fe K edge XAS fluorescence of iron ferrous solution in hydrothermal conditions at 500bars and between 25 and 450°C

References

Owner

Spectra preview

Fe K edge XAS fluorescence of iron ferrous solution in hydrothermal conditions at 500bars and between 25 and 450°C

Fe K edge XAS fluorescence of iron ferrous solution (Fe2+ 0.045m, HCl 0.1m, Na 0.356m, Cl 0.547m) at 500bar and 25°C
Fe K edge XAS fluorescence of iron ferrous solution (Fe2+ 0.045m, HCl 0.1m, Na 0.356m, Cl 0.547m) at 500bar and 100°C
Fe K edge XAS fluorescence of iron ferrous solution (Fe2+ 0.045m, HCl 0.1m, Na 0.356m, Cl 0.547m) at 500bar and 200°C
Fe K edge XAS fluorescence of iron ferrous solution (Fe2+ 0.045m, HCl 0.1m, Na 0.356m, Cl 0.547m) at 500bar and 300°C
Fe K edge XAS fluorescence of iron ferrous solution (Fe2+ 0.045m, HCl 0.1m, Na

Experiment Fe K edge XAS fluorescence of iron ferrous solution in hydrothermal conditions at 500bars and between 25 and 450°C

Sub-Experiment Iron ferrous solution in hydrothermal conditions: Fe2+ 0.045m, HCl 0.1m, Na 0.356m, Cl 0.547m, 500bar [25-450°C]

Spectrum Fe K edge XAS fluorescence of iron ferrous solution (Fe2+ 0.045m, HCl 0.1m, Na 0.356m, Cl 0.547m) at 500bar and 25°C

Spectrum Fe K edge XAS fluorescence of iron ferrous solution (Fe2+ 0.045m, HCl 0.1m, Na 0.356m, Cl 0.547m) at 500bar and 100°C

Spectrum Fe K edge XAS fluorescence of iron ferrous solution (Fe2+ 0.045m, HCl 0.1m, Na 0.356m, Cl 0.547m) at 500bar and 200°C

Spectrum Fe K edge XAS fluorescence of iron ferrous solution (Fe2+ 0.045m, HCl 0.1m, Na 0.356m, Cl 0.547m) at 500bar and 300°C

Spectrum Fe K edge XAS fluorescence of iron ferrous solution (Fe2+ 0.045m, HCl 0.1m, Na 0.356m, Cl 0.547m) at 500bar and 400°C

Spectrum Fe K edge XAS fluorescence of iron ferrous solution (Fe2+ 0.045m, HCl 0.1m, Na 0.356m, Cl 0.547m) at 500bar and 450°C

Sub-Experiment Iron ferrous solution in hydrothermal conditions: Fe2+ 0.044m, HCl 0.1m, Na 0.744m, Cl 0.932m, 500bar [25-450°C]

Sub-Experiment Iron ferrous solution in hydrothermal conditions: Fe2+ 0.046m, HCl 0.1m, Na 1.901m, Cl 2.092m, 500bar [25-450°C]

Sub-Experiment Iron ferrous solution in hydrothermal conditions: Fe2+ 0.056m, HCl 0.1m, Na 2.813m, Cl 3.024m, 500bar [25-450°C]

Sub-Experiment Iron ferrous solution in hydrothermal conditions: Fe2+ 0.065m, HCl 0.1m, Na 4.825m, Cl 5.055m, 500bar

Fe K edge XAS fluorescence of iron ferrous solution (Fe2+ 0.045m, HCl 0.1m, Na 0.356m, Cl 0.547m) at 500bar and 25°C

Title
Fe K edge XAS fluorescence of iron ferrous solution (Fe2+ 0.045m, HCl 0.1m, Na 0.356m, Cl 0.547m) at 500bar and 25°C

Data
Unit: eV Range: Valid Valid spectral range(s): 6999.97 - 7963.42 eV

X Axis
Scale: Linear Inverted: ☐

Y Axis
Scale: Linear

References

DOI
10.26302/SSHADE/EXPERIMENT_DT_20161207_001

Data reference
Testemale, Denis (2006): Fe K edge XAS fluorescence of iron ferrous solution in hydrothermal conditions at 500bars and between 25 and 450°C. SSHADE/FAME (OSUG Data Center). Dataset/Spectral Data. https://doi.org/10.26302/SSHADE/EXPERIMENT_DT_20161207_001

Publications
- Testemale et al., 2009, Chem. Geol., 264, 295

Figure 3.1: Snapshots of the SSHADE/FAME database webpage. Top: all the spectra of the reference (7) are accessible and shown here. Bottom: one individual spectrum shown with the very useful graphical interface at the top, and the DOI and reference shown at the bottom.

Chapter 4

Perspectives

Before detailing the perspectives of my research, and because this HDR is a perfect opportunity to look back on the job done, I'll introduce this chapter by briefly exposing my scientific project to be recruited at CNRS (that I joined in 2007).

> CNRS project, 2007. *In situ* study of hydrothermal fluids: relationship between fluid structure and properties.
>
> This project is part of the study of matter transfer and the formation/dissolution of crustal minerals in the presence of hydrothermal fluids. Very few direct observations of these fluids exist to date. The objective of my project is, based on ***in situ* studies using mainly synchrotron resources**, to describe them structurally at the atomic scale, by varying temperature, pressure and density. **The systems studied will be solvents and solvent/solute systems: water, H2O-NaCl brines and CO2/H2O mixtures for which data are scarce, as well as solutions containing ions of the elements present in the crustal minerals.** The methodology will be to study model solutions in order to move towards more complex solutions, including direct *in situ* observation of mineral dissolution and analysis of fluid inclusions under appropriate temperature and pressure conditions. From an experimental point of view, **the techniques that will be implemented are optical or X-ray spectroscopies, sensitive to the atomic structure, and which will also make it possible to determine the speciation and solubility of an element**. These data will be used in the development of thermodynamic and kinetic models, particularly adapted to the conditions of deep geological storage.

It's safe to say that the part of this project dedicated to the study of speciation and solubility of metals in hydrothermal conditions, by *in situ* X-ray spectroscopic methods, has been carried out successfully. And hopefully this is demonstrated in this manuscript by the description of the strong collaborations and exhaustive results, of the robust methods and technological developments, and of their facilitated access for the scientific community at FAME beamlines. In comparison, the study of the structure of solvents and mixture of solvents, in particular through the use of optical and x-ray spectroscopies, was not addressed in the manuscript. This does not mean that nothing was done (far from it!), but I considered that this body of work was not complete and consistent enough to be included as a chapter[1]. Also, if I'm honest, there's a lot of unfinished business.

In this context, establishing the scientific perspectives for the next years is quite obvious. I'll organize them along two axes: hydrothermal transport of metals, and physical-chemistry of supercritical solvents/fluids. I'll also distinguish between topics that are the logical continuation of previous works and that I expect to be doable without complications, and topics that are more exploratory and may face strong experimental challenges or lead to dead-ends.

---

[1] And I definitely wanted to reduce the size of this manuscript, which is getting way too big!

4.1 Hydrothermal transport of metals

4.1.1 X-ray absorption spectroscopies

As stated above this aspect of my CNRS project has been exhaustively addressed during the last 15 years, and I consider that a personal cycle comes to an end; but this doesn't mean that all the methods, tools and equipment should be discarded. In fact, we clearly have the ambition to maintain FAME/Néel position as a leader in hydrothermal synchrotron research. This will be done by following several guidelines that all derive from the results and information presented in the previous chapters:

- we'll keep on offering the best data quality and user experience at FAME, but will also reinforce the installation of autoclaves at FAME-UHD beamline. Indeed, with the continuous advances in XANES calculations and the growing input from molecular dynamics, it is more relevant to study small features in XANES spectra, for which the higher resolution of crystal analyser beamlines comes in handy. Reference (56) is a very neat review we wrote about the principles and benefits of HERFD in the context of environmental biogeochemistry, but most of the information applies to all scientific fields.
- As stated earlier, we still need to optimize the recent version of our autoclaves, to offer a better thermal behaviour. Some improvements will also benefit to the efficiency and friendliness of its use, for power users and newcomers as well.
- The database of XAS spectra (FAME and FAME-UHD beamlines) SSHADE/FAME is a project that is really mature now: the SSHADE infrastructure is in production, and the software tools are available at FAME for the upload of data. Now the database needs to be populated with a sustained data ingestion policy, where the biggest hurdle is to motivate the users sufficiently that they free up time for this task (me included!).
- We need to set up training actions for users of HP autoclaves, that shall take place outside the periods of beamtime.

The list above is more about methods and tools. In terms of research topics, after the period of (mostly) transition metals and metalloids, the momentum is now whithin Rare Earth Elements (REE): even if it is limited to our autoclaves at FAME, the figure 1.10 (page 90) provides a graphical summary of the situation, where all 3d transition metals have been studied, and the REEs are attracting the attention of many research groups. In our case, in the context of hydrothermal geochemistry, the first REEs were studied a few years ago: ytterbium by M. Louvel (Münster University) (57) and europium with my australian colleagues (58). Since then, things are moving forward with the same collaborators, and the speciation of yttrium was investigated (the *Geochim. Cosmochim. Acta* manuscript is accepted), and analysis is ongoing for other REEs (samarium, neodymium, etc.). I also refer here to the chemistry example of cerium nanoparticles synthesis I explained above (section 2.3.3, page 118): this is not in the context of hydrothermal geochemistry, but REEs have so many applications in nanotechnology, biotechnology, chemistry, etc., that studies in all these scientific fields are being conducted.

4.1.2 Raman spectroscopy

One topic I'd like to explore in the next years is the use of Raman spectroscopy to derive speciation information in hydrothermal fluids; in some cases it might be complementary to XAS data. In the context of geological fluids, Raman is being mainly used for organic and inorganic molecules (59, 60), where it shines as a very powerful probe. Though in the case of metal speciation, the signal from ion contact pairs is much weaker, such as in a recent example that combines XAS (FAME) and Raman data (61). A consequence is the need of high metal concentrations which are less relevant when compared to low concentrations of natural samples (25). Another drawback is the difficulty to interpret vibration frequencies (i.e., the position of the Raman peaks) without the support from *ab initio* calculations, either previously published or to be done. When metal transport at hydrothermal conditions is done by covalent molecules, the Raman signal is strong, such as in the example of U transport as uranyl-chloro-complexes $UO_2Cl_n^{2-n}$ (62, 63), or As(III) monovalent species $As(OH)_3^0$ (64).

That's a lot of negatives that may disqualify the use of Raman for this purpose, but I'm intrigued by some studies where ion metal contact species have a not-so-weak Raman signal, like in the case

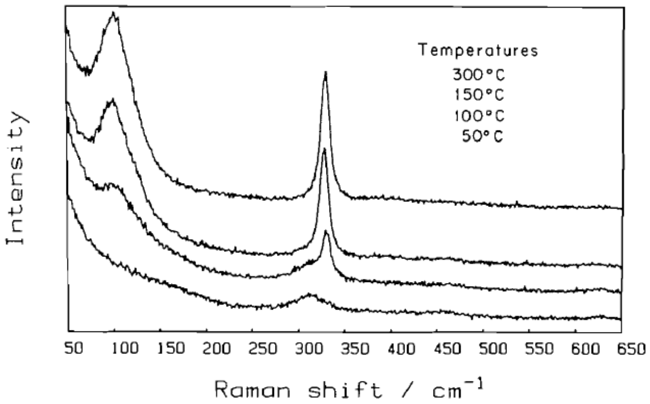

Raman spectra of 1.0 *m* $FeCl_3$, 5 *m* HCl, 1 *m* $NaClO_4$, solution E, recorded at 50, 100, 150, and 300°C and 9 MPa.

Figure 4.1: Figure extracted from reference (66) that shows the Raman signature of $Fe^{III} - Cl$ complexes with a very characteristic and intense peak at 332 cm^{-1} attributed to the $FeCl_4^-$ end-member.

of $Zn - Br$ interactions (65) and more interestingly (for me) of $Fe^{III} - Cl$ complexes (66). In the latter example, it is noteworthy that only one Fe species is detected, namely $FeCl_4^-$, at 300°C/90 bar, with a very characteristic and strong Raman signature (figure 4.1). I plan to harness this idea by *i)* determining what iron concentration is needed to measure a useful Raman signal, and *ii)* reproducing the same conditions as in the XAS experiments to evaluate if the $FeCl_4^-$ end-member is also detected (alone). If this experiment proves to be conclusive, it could be a very useful complement to the XAS results.

4.2 Physical-chemistry of supercritical fluids

Note: In this section I'm about to present scientific perspectives on a topic that I did not address previously in the manuscript. For that reason, in order to make things understandable, before exposing my ideas and objectives for the coming years I'll include very briefly the results already obtained since my PhD. The reason I chose to structure the manuscript this way is because this axis of research has so far been little productive in terms of publications, and I wanted to make this 'Perspectives' chapter a bit thicker, and not a short (christmas) list.

Supervision:

- *A. Bordage, ANR post-doctoral (2013)*
- *E. Boulard, ANR post-doctoral (2014)*
- *D. Perice, M1 trainingship (INPG, 2018)*

4.2.1 Supercritical water: short and medium scale structure

During my PhD (experiments) and the first post-doctoral years (analysis and publication), we studied the short and medium-scale structure of supercritical water. This work consisted of small angle x-ray scattering (SAXS, reference (67)) and resonant inelastic x-ray scattering (RIXS, reference (68); and Compton scattering, reference (69)) experiments, that were conducted independently but complemented each other. The objective of the former was to determine the size and the amplitude of the density fluctuations that occur in supercritical fluids, and are maximal along the critical isochore, i.e., the analytic extension of the liquid-vapor coexistence curve where the water density is constant and equal to the critical density 0.332 $g.cm^{-3}$ (see figure 4.2, left). In the same study we evaluated the influence of these fluctuations

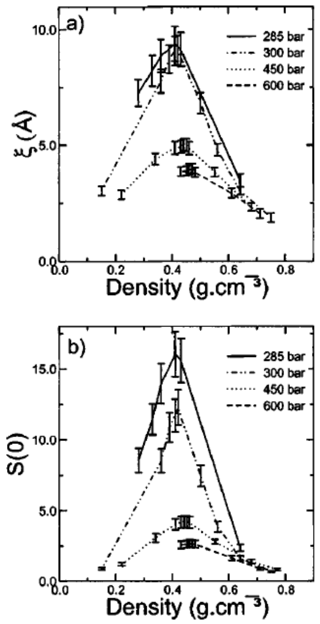

FIG. 3. Values of correlation length (a) and structure factor $S(0)$ (b) for supercritical water along four isobars as a function of density. The shift of the maxima with respect to the critical density ρ_C=0.32 g cm^{-3} is explained in the text. The lines are a guide for the eye.

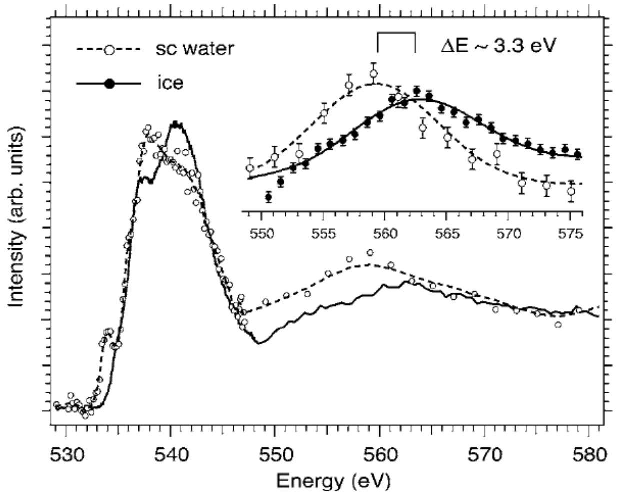

FIG. 2. Extended oxygen K-edge spectra of sc water and ice as measured with x-ray Raman scattering (XRS). sc water, open circles and dashed line (data points and smoothed curve, respectively). Crystalline ice, solid line. Inset, second maxima in the spectra at around 560 eV with data as open (sc water) and solid circles (ice) with relative intensities emphasizing the energy shift and calculated Gaussian fits as lines. The Gaussian profiles are centered at 559.2 eV for sc water (dashed line) and 562.5 eV for ice (solid line) (12 eV full width at half maximum in both cases).

Figure 4.2: Left: Extracted from reference (67): the graph shows the size and amplitude of the density fluctuations determined by SAXS. Right: Extracted from reference (68), the graph shows (open circles) the experimental RIXS XANES spectrum of supercritical water.

on the hydration of dissolved ions. In parallel, a XANES of supercritical water at the oxygen K-edge was measured by RIXS (figure 4.2, right), and interpreted based on a structural model of the distribution of hydrogen bonding. This latter experiment was conducted at APS (Chicago, US) where we brought our autoclave to install it on one of the first synchrotron beamline equipped with crystal analyzers. At the time, this measurement was experimentally very challenging and was one of the very few spectroscopic *in situ* measurement in high temperature and pressure conditions. Thus it provided additional and useful information in a controversial and heated scientific debate. Also, in terms of research strategy, it provided a solid basis (both technical and scientific) for further work... But this further work never occured, because no beamtime was granted to us at ESRF on RIXS beamlines. Meanwhile, the scientific debate went on, but with no experimental *in situ* spectroscopic measurements of supercritical water until the work of Sahle et al. (70). In this study they used a Diamond Anvil Cell on ESRF ID16 beamline, to measure XANES RIXS spectra at the oxygen K-edge. Like for all similar studies, data were interpreted with the use of MD calculations, in order to propose a structural model that describes the evolution of hydrogen bonding.

Perspectives:

There are several elements that lead me to believe that it might be worth considering again this type of experiment. The technical arguments are that we still have autoclaves that work even better, and we now also have direct access to a crystal analyzer beamline (FAME-UHD). Furthermore, we have a privileged access to the FDMNES software which can calculate RIXS spectra (FDMNES is developed by Y. Joly at Néel Institute). Then, the scientific argument is that more P/T conditions of supercritical water still have to be explored, in particular the crossing of the critical isochore studied in details by SAXS, where density fluctuations arise and are prone to strong modifications of the local water structure and hydrogen bondings. Another idea is to investigate the influence of co-solvents and/or dissolved species, also sources of H-bonding modifications. The 2 main difficulties that I anticipate are:

- Will the signal be strong enough to explore many P/T conditions? The S/N ratio of our previous RIXS experiment (see figure 4.2) was not very good, but I don't know of similar experiments (indeed there are very few) where the S/N is better. Furthermore, we improved (i.e., reduced) the absorbance of the autoclave materials and expect more photons today.
- We will definitely need theoretical support to interpret the data, in particular to obtain a structural model over which FDMNES calculations can be done and compared to experimental data. The recent example of the similar work of Sahle at al (70) is a perfect demonstration that a robust interpretation of such RIXS data has to be supported by top-notch MD calculations. Since this work is about soft-condensed matter, such theoretical support cannot be found at Néel Institute: some prospecting has to be done.

4.2.2 $H_2O - CO_2$ hydrothermal solvents

As stated in the introduction of this chapter, the study of hydrothermal solvents (H_2O, $H_2O - salts$ and $H_2O - CO_2$ mixed solvents) by *in situ* optical spectroscopy was in my CNRS scenario of research. The main topic I've been involved in is Raman spectroscopy on $H_2O - CO_2$ mixed solvents. CO_2 is the second most abundant component in natural fluids and is therefore involved in a wide variety of processes spanning from photosynthesis and greenhouse effect to ore deposits formation and volcanic degassing. Recently, the interactions between supercritical carbon dioxide, brines and rocks have also received considerable attention in order to develop viable carbon dioxide sequestration scenarios for long-term carbon storage into deep geological formations. Finally, CO_2 is also widely used in the industry because it has the potential to significantly modify the properties of water (density, electrolytic conductivity, corrosivity). Overall, accurate modeling of the thermodynamic properties of $H_2O - CO_2$ mixtures requires a better understanding of the intermolecular interactions between the CO_2 and H_2O molecules and of the extent of hydrogen bonding in $H_2O - CO_2$ mixtures at the relevant pressure and temperature conditions.

A lot of work has been done, only partly published so far. In the technical reference (71), we presented the Raman set-up installed at Néel Institute, with preliminary results on supercritical water and $H_2O - CO_2$.[2] A summary of this work is shown in figure 4.3. The key elements from this figure and the publication (71), that shall be highlighted are: ***i)*** the quality of the data; ***ii)*** the possibility to measure Raman scattering from two co-existing phases; ***iii)*** the possibility to visualize the fluids inside the cell, thanks to the use of monocrystalline sapphire cells and HP windows. Since then the measurements and analysis continued, but were slowed down by various experimental and analytical hurdles. First, the biggest difficulty of this type of HT Raman measurements is the occurence of an intense photo-luminescence (PL) signal that contaminates (at best) or kills the sample signal; this fight against PL has been draining a lot of our time and energy and is not over, yet. Another difficulty, specific to this study, is to find the best method to load CO_2 in the cell. In reference (71) oxalic acid was used; more recently we loaded silver oxalate powder that is thermally degraded into CO_2 with no carbon by-products. In both cases, the quantity of powder that can be loaded is limited, which prevents from reaching CO_2 concentrations above 20% (atomic). Finally, the number of experimental runs conducted at different conditions (temperature, pressure, CO_2 concentration) is very big and provided a very large quantity of data that need to be integrated and evaluated globally: for this purpose, complementary data needs to be collected (for example calculations of density and CO_2 concentration). At the end of the day, the results consisted of a multi-dimensional dataset, that could only be processed by using Python-based data mining. Which we had to learn.

Nevertheless, we obtained interesting results that can be summarized in the following way. As long as 2 phases co-exist (L+V in figure 4.3) water and carbon dioxide Raman signatures in the liquid phase are different from their 'pure' counterpart (at similar concentrations), which can be interpreted as molecular interactions between H_2O and CO_2 molecules. But when the system becomes monophasic (F in figure 4.3), everything changes: water (resp. carbon dioxide) Raman signature is identical to pure water (resp. carbon dioxide) and indicate that no molecular interactions take place.

Perspectives:

Besides completing the ongoing analysis, I can see two evolutions for this study.

---

[2] Since then, an improved Raman set-up was developed, with better optics.

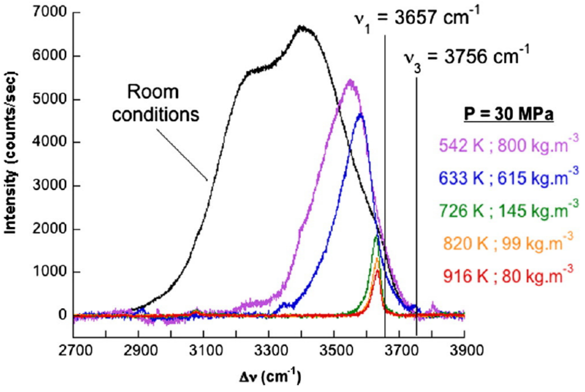

Fig. 4. Raman spectra of water at room-temperature and at P = 30 MPa for temperature ranging from 542 K to 916 K; each spectrum was background subtracted. From 648 K, water is in the supercritical state. The position of the stretching modes of the OH band for the isolated molecule is given as references. The evolution of the spectral features with temperature reflects the changes of the H bond in the supercritical state.

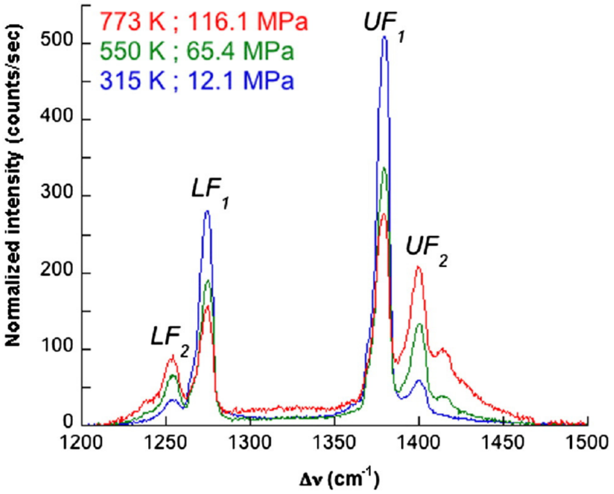

Fig. 5. Density-normalized Raman spectra of carbon dioxide obtained for three supercritical conditions (T = 315 K, P = 12.1 MPa, ρ = 700 kg·m^{-3}; T = 550 K, P = 65.4 MPa, ρ = 560 kg·m^{-3}; T = 773 K, P = 116.1 MPa, ρ = 560 kg·m^{-3}).

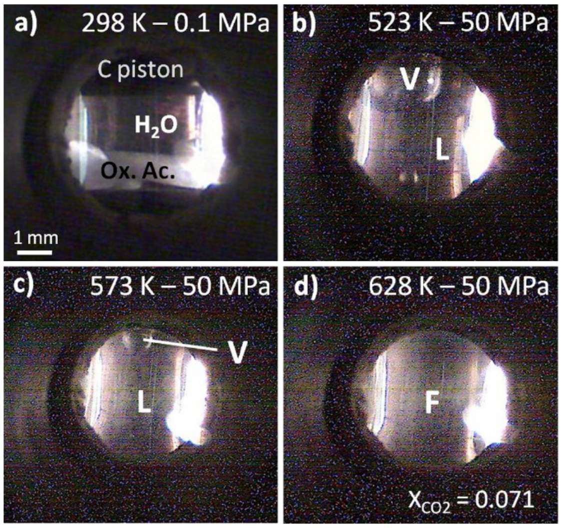

Fig. 7. Visual observation inside the autoclave of the evolution of the H_2O–CO_2 binary system with temperature, for a 7.1 mol% CO_2 concentration. (a) Starting load with the oxalic acid pellet in the sapphire cell at room conditions. (b) H_2O-rich liquid (L) and a CO_2-rich vapor phase (V) formed upon oxalic acid decomposition at 523 K and 50 MPa. (c) Decrease of the V phase proportion with the increase of the CO_2 solubility in H_2O at 573 K and 50 MPa. (d) Formation of a single fluid phase (F) at 628 K and 50 MPa.

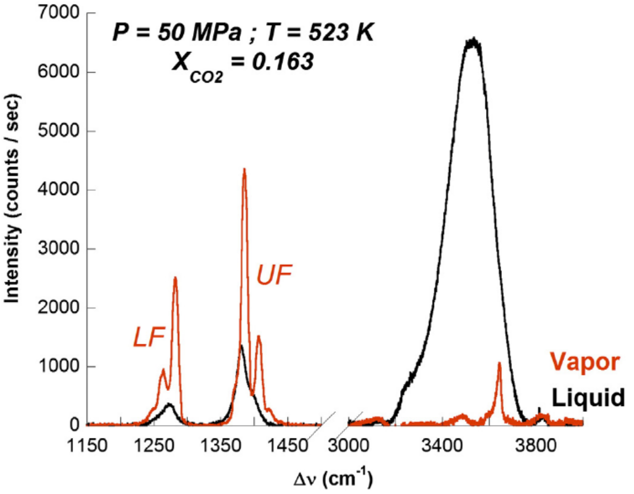

Fig. 8. Raman spectra collected in coexisting CO_2-rich vapor phase and H_2O-rich liquid phase at 523 K and 50 MPa, for a 16.3 mol% CO_2 concentration. Both the CO_2 Fermi diad (1150–1500 cm^{-1}) and the OH stretching band (3000–4000 cm^{-1}) are presented.

Figure 4.3: Figures extracted from reference (71), with their legends for a detailed explanation. Top: the Raman spectra of H_2O and CO_2 singles phases at hydrothermal conditions are shown. Bottom : two phases co-exist (liquid L and vapour V), are observed, and their Raman scattering is measured; at higher temperatures, the fluid becomes monophasic (F).

- Once again, I'll mention that theoretical support is crucially needed to exploit this type of data: with so many variables (pressure, temperature, density, concentration), a reliable interpretation of the spectroscopic features cannot be done without the input from MD calculated structures. What I find interesting nowadays is that the theoricians (start to?) think the same: having access to experimental data is really useful to test the molecular structures they calculate. Actually, the pure CO_2 data from reference **(71)** (see figure 4.3) was integrated in a theoretical paper (72). I wish to proceed similarly. And one outcome I anticipate is that interacting with theory people will triger new ideas of experiments.
- A logical extension of the existing dataset is towards higher CO_2 concentrations. In order to go beyond the existing 20% limit it seems obligatory to turn to cryogenic loading (water ice and dry ice) which will allow much larger concentrations of carbon dioxide. We did some unsuccessful (and costly) tests some years ago but I'd like to have a second look.

4.2.3 Supercritical solvents and Small Organic Molecules (SOM)

This last perspective is really more exploratory than the ones exposed above. The idea is to monitor the hydrothermal formation, stability and/or degradation of Small Organic Molecules (SOM) by *in situ* Raman spectroscopy. This is inspired by studies such as the one by Marocchi et al. (73): they used Raman spectroscopy to monitor the onset of carbon compounds during the dissolution of siderite, in connection with our previous study about siderite dissolution by XAS (10). The fate of carbon compounds at hydrothermal conditions has been largely investigated (see for example references (74, 75, 76)), mainly by flexible reactor (and sampling+chromatography) experimentation. But similar *in situ* investigations by Raman spectrometry are (to my knowledge) scarce. Another source of inspiration is the study about the generation of organic compounds in hydrothermal fluids, that I was involved in recently (46) (see the brief description in section 2.3.1, page 115). We demonstrated that among organic molecules commonly found in natural hydrothermal plumes some may have a biogenic origin, while some others may originate from abiogenic processes. The characterization was based on *ex situ* chromatography. Logically, we had initiated an experimental program on the monitoring of such organic species by Raman, with many measurements conducted on reference samples, but the preliminary attempt of *in situ* investigation at hydrothermal conditions was a failure, mainly because of a (very) annoying photo-luminescence signal and contamination by a bad quality notch filter.

- Practically, the first technical research to be done, and that will be beneficial to all Raman measurements, is the reduction of this luminescence contamination. This point was already mentioned in the previous section several times, but is critical for SOM Raman measurements. Major improvements were done to our Raman installation, in particular with better optics and the possibility to use several laser wavelengths. But an exhaustive assessment of these improvements still needs to be done. Then, more specifically to the SOM topic, it is necessary to determine what is the concentation limit to measure safely their Raman signal at *in situ* hydrothermal conditions.
- Then, the first research objects that could be targeted are "simple" molecules, such as methanol or formic acid/H_2O mixtures. They are known systems which will enable to calibrate our technique (Raman sensitivity, determination of relative concentrations, etc.). For example, the stability of formic acid $HCOOH$ could be studied, with special attention to the reaction $HCOOH \leftrightarrow H_2 + CO_2$, which is far from being the only one occurring in the system but for which all molecules involved can be monitored using in situ Raman spectroscopy.

Remerciements

Je souhaite remercier tous les membres du jury qui ont accepté, de façon enthousiaste, d'évaluer mon travail; notamment Carmen Sanchez-Valle, Max Wilke et Laurent Truche pour leur lecture du manuscrit pendant une période de confinement particulière et compliquée.

Je pense suffisamment avoir insisté dans ce manuscrit sur l'importance du travail collectif à l'origine de la réussite de nos installations synchrotron et de nos équipements de haute pression. Il me semble donc indispensable de remercier les acteurs de cette réussite, qui en plus d'être (très) compétents ont la qualité d'être (très) sympathiques. Jean-Louis, Olivier P., les deux "historiques" aux caractères si différents; Eric, Alain et William, en charge de la partie technique et mon assurance tous risques en cas ~~de casse matérielle~~ d'aléa expérimental; Isabelle et tout le staff de FAME et FAME-UHD, et plus largement des CRG françaises à l'ESRF qui constituent une belle équipe; et les membres du pôle X-Press de l'Institut Néel, qui font de ce laboratoire un acteur majeur de la haute pression en France.

Depuis mon doctorat j'ai effectué la majorité de mon parcours à l'Institut Néel: les 20 années passées ont forcément créé des liens, professionnels et personnels, trop nombreux pour être détaillés ici. Toutefois je mentionne ici les membres de l'équipe synchrotron-SPMCE-MRS, dont la diversité de thématiques rend les discussions scientifiques très riches, et consituée de chercheuses et chercheurs sur qui s'appuyer; Corinne F. et Pierre B. ont su m'initier à la spectrométrie Raman et m'ont donné confiance dans cette nouvelle activité; évidemment j'ai une pensée pour Muriel B., pour son efficacité et sa gentillesse; enfin comment ne pas s'enthousiasmer devant l'ambiance du deuxième étage (côté sud) et la spontanéité et franchise de ses protagonistes, qui savent rendre la recherche scientifique terre à terre, presque rustique, et sacrément amicale! :-)

Un autre élément de mon activité de recherche que j'ai fortement mis en avant dans mon manuscrit est mon goût pour les collaborations, à la fois parce que c'est intrinsèque au travail sur les lignes de lumière et par choix personnel. De fortes connexions se sont donc établies avec des collègues, devenus amis, au gré d'expériences plus ou moins réussies (mais jamais ratées!). Je cite succinctement ici le gang des australiens (Joël, Barbara, Weihua, Mei, etc.) qui ont fait mon post-doc australien une parenthèse très enrichissante et sont toujours aujourd'hui de fidèles collaborateurs; le toulousain Gleb (un gang à lui tout seul) et son fameux stylo rouge (sa correction en rouge de notre premier article commun, qui était également mon premier article, reste un souvenir marquant...); François G. à Paris, trop poli pour être membre d'un gang mais dont les connaissances scientifiques et la gentillesse sont à chacune de nos rencontres extrêmement revigorantes; Cécile K. et Géraldine D. avec qui j'ai toujours plaisir à parler aussi d'autre chose que de science. Et plein d'autres collaborateurs dont j'oublie maintenant les noms en bouclant ce manuscrit, mais qui me reviendront ensuite.

Enfin, malgré toutes ces manips synchrotron et HP compliquées, la vie serait bien trop simple et fade sans le gang de la rue des Roses. Marie, Lise et Leo, c'est bien vous qui me faites avancer, je vous embrasse.

Bibliography

(1) S. D. Kelly, D. Hesterberg, B. Ravel, April L. Ulery, and L. Richard Drees. Analysis of Soils and Minerals Using X-ray Absorption Spectroscopy. In *SSSA Book Series*. Soil Science Society of America, 2008.

(2) Denis Testemale and Joël Brugger. 3.37: Cells for spectroscopy of fluids at elevated pressure and temperature. Reaction Cells. volume I: X-ray Absorption Spectroscopy and related techniques of *International Tables for Crystallography*. 2020.

(3) V. Simonet, Y. Calzavara, J. L. Hazemann, R. Argoud, O. Geaymond, and D. Raoux. X-ray absorption spectroscopy studies of ionic association in aqueous solutions of zinc bromide from normal to critical conditions. *The Journal of Chemical Physics*, 117(6):2771, 2002.

(4) V. Simonet, Y. Calzavara, J. L. Hazemann, R. Argoud, O. Geaymond, and D. Raoux. Structure of aqueous ZnBr(sub 2) solution probed by x-ray absorption spectroscopy in normal and hydrothermal conditions. *The Journal of Chemical Physics*, 116(7):2997, 2002.

(5) Gleb S Pokrovski, Ildar V Zakirov, Jacques Roux, Denis Testemale, Jean-Louis Hazemann, Andrew Y. u Bychkov, and Galina V Golikova. Experimental study of arsenic speciation in vapor phase to 500°C: implications for As transport and fractionation in low-density crustal fluids and volcanic gases. *Geochimica et Cosmochimica Acta*, 66(19):3453–3480, October 2002.

(6) Denis Testemale, Jean-Louis Hazemann, Gleb S. Pokrovski, Yves Joly, Jacques Roux, Roger Argoud, and Olivier Geaymond. Structural and electronic evolution of the As(OH)3 molecule in high temperature aqueous solutions: An x-ray absorption investigation. *The Journal of Chemical Physics*, 121(18):8973–8982, November 2004.

(7) Denis Testemale, Joel Brugger, Weihua Liu, Barbara Etschmann, and Jean-Louis Hazemann. In-situ X-ray absorption study of Iron(II) speciation in brines up to supercritical conditions. *Chemical Geology*, 264(1-4):295–310, June 2009.

(8) Weihua Liu, Barbara Etschmann, Joël Brugger, Leone Spiccia, Garry Foran, and Brent McInnes. UV–Vis spectrophotometric and XAFS studies of ferric chloride complexes in hyper-saline LiCl solutions at 25–90 °C. *Chemical Geology*, 231(4):326–349, August 2006.

(9) C. A. Heinrich and T. M. Seward. A spectrophotometric study of aqueous iron (II) chloride complexing from 25 to 200 C. *Geochimica et Cosmochimica Acta*, 54(8):2207–2221, 1990.

(10) Denis Testemale, Fabien Dufaud, Isabelle Martinez, Pascale Bénézeth, Jean-Louis Hazemann, Jacques Schott, and François Guyot. An X-ray absorption study of the dissolution of siderite at 300 bar between 50 °C and 100 °C. *Chemical Geology*, 259(1-2):8–16, February 2009.

(11) Damien Daval, Denis Testemale, Nadir Recham, Jean-Marie Tarascon, Julien Siebert, Isabelle Martinez, and François Guyot. Fayalite (Fe2SiO4) dissolution kinetics determined by X-ray absorption spectroscopy. *Chemical Geology*, 275(3-4):161–175, August 2010.

(12) Joël Brugger. BeerOz, a set of Matlab routines for the quantitative interpretation of spectrophotometric measurements of metal speciation in solution. *Computers & Geosciences*, 33(2):248–261, February 2007.

(13) J. James-Smith, J. Cauzid, D. Testemale, W. Liu, J.-L. Hazemann, O. Proux, B. Etschmann, P. Philippot, D. Banks, P. Williams, and J. Brugger. Arsenic speciation in fluid inclusions using micro-beam X-ray absorption spectroscopy. *American Mineralogist*, 95(7):921–932, June 2010.

(14) Denis Testemale, Gleb S. Pokrovski, and Jean-Louis Hazemann. Speciation of AsIII and AsV in hydrothermal fluids by in situ X-ray absorption spectroscopy. *European Journal of Mineralogy*, 23(3):379–390, July 2011.

(15) Gleb S Pokrovski, Jacques Schott, François Farges, and Jean-Louis Hazemann. Iron (III)-silica interactions in aqueous solution: insights from X-ray absorption fine structure spectroscopy. *Geochimica et Cosmochimica Acta*, 67(19):3559–3573, October 2003.

(16) Bernard J. Wood, L. Taras Bryndzia, and Kathleen E. Johnson. Mantle Oxidation State and Its Relationship to Tectonic Environment and Fluid Speciation. *Science*, 248(4953):337–345, April 1990.

(17) Katherine A. Kelley and Elizabeth Cottrell. Water and the Oxidation State of Subduction Zone Magmas. *Science*, 325(5940):605–607, July 2009.

(18) Yanlu Xing, Barbara Etschmann, Weihua Liu, Yuan Mei, Yuri Shvarov, Denis Testemale, Andrew Tomkins, and Joël Brugger. The role of fluorine in hydrothermal mobilization and transportation of Fe, U and REE and the formation of IOCG deposits. *Chemical Geology*, 504:158–176, January 2019.

(19) Weihua Liu, Stacey J. Borg, Denis Testemale, Barbara Etschmann, Jean-Louis Hazemann, and Joël Brugger. Speciation and thermodynamic properties for cobalt chloride complexes in hydrothermal fluids at 35–440°C and 600bar: An in-situ XAS study. *Geochimica et Cosmochimica Acta*, 75(5):1227–1248, March 2011.

(20) Yuan Mei, David M. Sherman, Weihua Liu, Barbara Etschmann, Denis Testemale, and Joël Brugger. Zinc complexation in chloride-rich hydrothermal fluids (25–600°C): A thermodynamic model derived from ab initio molecular dynamics. *Geochimica et Cosmochimica Acta*, 150:265–284, February 2015.

(21) Elena F. Bazarkina, Gleb S. Pokrovski, Alexander V. Zotov, and Jean-Louis Hazemann. Structure and stability of cadmium chloride complexes in hydrothermal fluids. *Chemical Geology*, 276(1):1–17, September 2010.

(22) Yuan Tian, Barbara Etschmann, Yuan Mei, Pascal V. Grundler, Denis Testemale, Jean-Louis Hazeman, Peter Elliott, Yung Ngothai, and Joël Brugger. Speciation and thermodynamic properties of manganese(II) chloride complexes in hydrothermal fluids: In situ XAS study. *Geochimica et Cosmochimica Acta*, 129:77–95, March 2014.

(23) Yuan Tian, Barbara Etschmann, Weihua Liu, Stacey Borg, Yuan Mei, Denis Testemale, Brian O'Neill, Nick Rae, David M. Sherman, Yung Ngothai, Bernt Johannessen, Chris Glover, and Joël Brugger. Speciation of nickel (II) chloride complexes in hydrothermal fluids: In situ XAS study. *Chemical Geology*, 334:345–363, December 2012.

(24) B. Ravel and M. Newville. ATHENA, ARTEMIS, HEPHAESTUS: data analysis for X-ray absorption spectroscopy using IFEFFIT. *Journal of Synchrotron Radiation*, 12(4):537–541, June 2005.

(25) Joël Brugger, Weihua Liu, Barbara Etschmann, Yuan Mei, David M. Sherman, and Denis Testemale. A review of the coordination chemistry of hydrothermal systems, or do coordination changes make ore deposits? *Chemical Geology*, 447:219–253, December 2016.

(26) John L. Fulton, Markus M. Hoffmann, John G. Darab, Bruce J. Palmer, and Edward A. Stern. Copper(I) and Copper(II) Coordination Structure under Hydrothermal Conditions at 325 °C: An X-ray Absorption Fine Structure and Molecular Dynamics Study. *The Journal of Physical Chemistry A*, 104(49):11651–11663, December 2000.

(27) Weihua Liu, Joel Brugger, Barbara Etschmann, Denis Testemale, and Jean-Louis Hazemann. The solubility of nantokite (CuCl(s)) and Cu speciation in low-density fluids near the critical isochore: An in-situ XAS study. *GEOCHIMICA ET COSMOCHIMICA ACTA*, 72(16):4094–4106, August 2008.

(28) Blake Tooth, Barbara Etschmann, Gleb S. Pokrovski, Denis Testemale, Jean-Louis Hazemann, Pascal V. Grundler, and Joël Brugger. Bismuth speciation in hydrothermal fluids: An X-ray absorption spectroscopy and solubility study. *Geochimica et Cosmochimica Acta*, 101:156–172, January 2013.

(29) Weihua Liu, Barbara Etschmann, Denis Testemale, Jean-Louis Hazemann, Kirsten Rempel, Harald Müller, and Joël Brugger. Gold transport in hydrothermal fluids: Competition among the Cl-, Br-, HS- and NH3(aq) ligands. *Chemical Geology*, 376:11–19, May 2014.

(30) P. D'Angelo, M. Benfatto, S. Della Longa, and N. Pavel. Combined XANES and EXAFS analysis of Co2+, Ni2+, and Zn2+ aqueous solutions. *Physical Review B*, 66(6), August 2002.

(31) M. Benfatto, P. D'Angelo, S. Della Longa, and N. Pavel. Evidence of distorted fivefold coordination of the Cu2+ aqua ion from an x-ray-absorption spectroscopy quantitative analysis. *Physical Review B*, 65(17), May 2002.

(32) Sofía Díaz-Moreno, Adela Muñoz-Páez, and Jesús Chaboy. X-ray Absorption Spectroscopy (XAS) Study of the Hydration Structure of Yttrium(III) Cations in Liquid and Glassy States: Eight or Nine-Fold Coordination? *The Journal of Physical Chemistry A*, 104(6):1278–1286, February 2000.

(33) M. Benfatto and S. Della Longa. Geometrical fitting of experimental XANES spectra by a full multiple-scattering procedure. *Journal of Synchrotron Radiation*, 8(4):1087–1094, July 2001.

(34) Y. Joly. X-ray absorption near-edge structure calculations beyond the muffin-tin approximation. *Physical Review B*, 63(12), March 2001.

(35) Denis Testemale. *Structures locales en solution aqueuse supercritique*. PhD thesis, Université Joseph Fourier, 2003.

(36) B.E. Etschmann, W. Liu, D. Testemale, H. Müller, N.A. Rae, O. Proux, J.L. Hazemann, and J. Brugger. An in situ XAS study of copper(I) transport as hydrosulfide complexes in hydrothermal solutions (25–592°C, 180–600bar): Speciation and solubility in vapor and liquid phases. *Geochimica et Cosmochimica Acta*, 74(16):4723–4739, August 2010.

(37) J. Brugger, B. Etschmann, W. Liu, D. Testemale, J.L. Hazemann, H. Emerich, W. van Beek, and O. Proux. An XAS study of the structure and thermodynamics of Cu(I) chloride complexes in brines up to high temperature (400°C, 600bar). *Geochimica et Cosmochimica Acta*, 71(20):4920–4941, October 2007.

(38) Paola D'Angelo, Otello Maria Roscioni, Giovanni Chillemi, Stefano Della Longa, and Maurizio Benfatto. Detection of Second Hydration Shells in Ionic Solutions by XANES: Computed Spectra for Ni 2+ in Water Based on Molecular Dynamics. *Journal of the American Chemical Society*, 128(6):1853–1858, February 2006.

(39) G. J. Ackland, K. D'Mellow, S. L. Daraszewicz, D. J. Hepburn, M. Uhrin, and K. Stratford. The MOLDY short-range molecular dynamics package. *Computer Physics Communications*, 182(12):2587–2604, December 2011.

(40) G. S. Pokrovski, J. Roux, J. L. Hazemann, and D. Testemale. An X-ray absorption spectroscopy study of argutite solubility and aqueous Ge(IV) speciation in hydrothermal fluids to 500 degrees C and 400 bar. *CHEMICAL GEOLOGY*, 217(1-2):127–145, April 2005.

(41) G. S. Pokrovski, J. Roux, J.-L. Hazemann, A. Yu Borisova, A. A. Gonchar, and M. P. Lemesiiko. In situ X-ray absorption spectroscopy measurement of vapour-brine fractionation of antimony at hydrothermal conditions. *Mineralogical Magazine*, 72(2):667–681, April 2008.

(42) Bjorn P. von der Heyden. Shedding light on ore deposits: A review of synchrotron X-ray radiation use in ore geology research. *Ore Geology Reviews*, 117:103328, February 2020.

(43) Denis Testemale, Roger Argoud, Olivier Geaymond, and Jean-Louis Hazemann. High pressure/high temperature cell for x-ray absorption and scattering techniques. *Review of Scientific Instruments*, 76(4):043905, April 2005.

(44) Denis Testemale, Alain Prat, Eric Lahera, and Jean-Louis Hazemann. Novel high-pressure windows made of glass-like carbon for x-ray analysis. *Review of Scientific Instruments*, 87(7):075115, July 2016.

(45) R Bruyère, A Prat, C Goujon, and J-L Hazemann. A new pressure regulation device using high pressure isolation valves. *Journal of Physics: Conference Series*, 121(12):122003, July 2008.

(46) C. Konn, D. Testemale, J. Querellou, N. G. Holm, and J. L. Charlou. New insight into the contributions of thermogenic processes and biogenic sources to the generation of organic compounds in hydrothermal fluids: On the origin of organic compounds in hydrothermal fluids. *Geobiology*, 9(1):79–93, January 2011.

(47) Aude Picard, Denis Testemale, Laura Wagenknecht, Rachael Hazael, and Isabelle Daniel. Iron reduction by the deep-sea bacterium Shewanella profunda LT13a under subsurface pressure and temperature conditions. *Frontiers in Microbiology*, 5:796, January 2015.

(48) Aude Picard, Denis Testemale, Jean-Louis Hazemann, and Isabelle Daniel. The influence of high hydrostatic pressure on bacterial dissimilatory iron reduction. *Geochimica et Cosmochimica Acta*, 88(0):120–129, July 2012.

(49) A. Picard, I. Daniel, D. Testemale, I. Kieffer, P. Bleuet, H. Cardon, and P. M. Oger. Monitoring microbial redox transformations of metal and metalloid elements under high pressure using in situ X-ray absorption spectroscopy: XANES on microbes under pressure. *Geobiology*, pages no–no, January 2011.

(50) Geraldine Dantelle, Marija Matulionyte, Denis Testemale, Alexandra Cantarano, Alain Ibanez, and Fiorenzo Vetrone. Nd3+ doped Gd3Sc2Al3O12 nanoparticles: towards efficient nanoprobes for temperature sensing. *Physical Chemistry Chemical Physics*, 21(21):11132–11141, May 2019.

(51) Geraldine Dantelle, Denis Testemale, Stephanie Kodjikian, and Alain Ibanez. Synthesis of high-quality garnet-type Gd3Sc2Al3O12:Ce3+ nanocrystals. In *Oxide-based Materials and Devices IX*, volume 10533, page 1053322. International Society for Optics and Photonics, February 2018.

(52) Géraldine Dantelle, Denis Testemale, Estelle Homeyer, Alexandra Cantarano, Stéphanie Kodjikian, Christophe Dujardin, Jean-Louis Hazemann, and Alain Ibanez. A new solvothermal method for the synthesis of size-controlled YAG:Ce single-nanocrystals. *RSC Advances*, 8(47):26857–26870, 2018.

(53) Yuan Tian, Joel Brugger, Weihua Liu, Stacey Borg, Barbara Etschmann, Brian O'Neill, Denis Testemale, Jean-Louis Hazemann, Chris Glover, Yung Ngothai, Michael Jung, and Jason Peak. High-temperature and Pressure Spectroscopic Cell for In-situ XAS Study of Supercritical Fluids at the Australian Synchrotron. *Chemeca 2010: Engineering at the Edge; 26-29 September 2010, Hilton Adelaide, South Australia*, page 3425, 2010. Publisher: Engineers Australia.

(54) Kiyotaka Asakura, Hitoshi Abe, and Masao Kimura. The challenge of constructing an international XAFS database. *Journal of Synchrotron Radiation*, 25(4):967–971, July 2018.

(55) B. Ravel and M. Newville. XAFS Data Interchange: A single spectrum XAFS data file format. *Journal of Physics: Conference Series*, 712:012148, May 2016.

(56) Olivier Proux, Eric Lahera, William Del Net, Isabelle Kieffer, Mauro Rovezzi, Denis Testemale, Mohammed Irar, Sara Thomas, Antonio Aguilar-Tapia, Elena F. Bazarkina, Alain Prat, Marie Tella, Mélanie Auffan, Jérôme Rose, and Jean-Louis Hazemann. High-Energy Resolution Fluorescence Detected X-Ray Absorption Spectroscopy: A Powerful New Structural Tool in Environmental Biogeochemistry Sciences. *Journal of Environmental Quality*, 46(6):1146–1157, November 2017.

(57) Marion Louvel, Amélie Bordage, Denis Testemale, Li Zhou, and John Mavrogenes. Hydrothermal controls on the genesis of REE deposits: Insights from an in situ XAS study of Yb solubility and speciation in high temperature fluids (T<400°C). *Chemical Geology*, 417:228–237, December 2015.

(58) Weihua Liu, Barbara Etschmann, Artas Migdisov, Hakim Boukhalfa, Denis Testemale, Harald Müller, Jean-Louis Hazemann, and Joël Brugger. Revisiting the hydrothermal geochemistry of europium(II/III) in light of new in-situ XAS spectroscopy results. *Chemical Geology*, 459:61–74, May 2017.

(59) Christian Schmidt and I-Ming Chou. The Hydrothermal Diamond Anvil Cell (HDAC) for Raman spectroscopic studies of geological fluids at high pressures and temperatures. In Giovanni Ferraris, J. Dubessy, M.-C. Caumon, and F. Rull, editors, *Raman spectroscopy applied to Earth sciences and cultural heritage*, pages 249–278. European Mineralogical Union, 2012.

(60) G. S. Pokrovski and L. S. Dubrovinsky. The S3- Ion Is Stable in Geological Fluids at Elevated Temperatures and Pressures. *Science*, 331(6020):1052–1054, February 2011.

(61) Lea Scholten, Anke Watenphul, Oliver Beermann, Denis Testemale, Doreen Ames, and Christian Schmidt. Nickel and platinum in high-temperature H2O + HCl fluids: Implications for hydrothermal mobilization. *Geochimica et Cosmochimica Acta*, 224:187–199, March 2018.

(62) Maxime Dargent. *Spéciation et réduction de l'U (VI) dans les fluides chlorurés acides en conditions hydrothermales: Du transport au dépôt de l'uranium dans les gisements sous discordance*. PhD thesis.

(63) Maxime Dargent, Jean Dubessy, Laurent Truche, Elena F. Bazarkina, Chinh Nguyen-Trung, and Pascal Robert. Experimental study of uranyl(VI) chloride complex formation in acidic LiCl aqueous solutions under hydrothermal conditions (T = 21 C?350 °C, Psat) using Raman spectroscopy. *European Journal of Mineralogy*, 25(5):765–775, January 2014.

(64) Robert Gout, Gleb Pokrovski, Jacques Schott, and Antoine Zwick. Raman spectroscopic study of arsenic speciation in aqueous solutions up to 275°C. *Journal of Raman Spectroscopy*, 28(9):725–730, September 1997.

(65) Kenji Mibe, I-Ming Chou, Alan J. Anderson, Robert A. Mayanovic, and William A. Bassett. The speciation of aqueous zinc(II) bromide solutions to 500 °C and 900 MPa determined using Raman spectroscopy. *Chemical Geology*, 259(1):48–53, February 2009.

(66) Katsuo Murata, Donald E. Irish, and Gerald E. Toogood. Vibrational spectral studies of solutions at elevated temperatures and pressures. 11. A Raman spectral study of aqueous iron (III) chloride solutions between 25 and 300° C. *Canadian Journal of Chemistry*, 67(3):517–524, 1989.

(67) D. Testemale, M. V. Coulet, J. L. Hazemann, J. P. Simon, F. Bley, O. Geaymond, and R. Argoud. Small angle x-ray scattering of a supercritical electrolyte solution: The effect of density fluctuations on the hydration of ions. *JOURNAL OF CHEMICAL PHYSICS*, 122(19), May 2005.

(68) P. Wernet, D. Testemale, J. L. Hazemann, R. Argoud, P. Glatzel, L. G. M. Pettersson, A. Nilsson, and U. Bergmann. Spectroscopic characterization of microscopic hydrogen-bonding disparities in supercritical water. *Journal of Chemical Physics*, 123(15):154503, October 2005. WOS:000232697900025.

(69) Patrick H.-L. Sit, Christophe Bellin, Bernardo Barbiellini, D. Testemale, J.-L. Hazemann, T. Buslaps, Nicola Marzari, and Abhay Shukla. Hydrogen bonding and coordination in normal and supercritical water from x-ray inelastic scattering. *PHYSICAL REVIEW B*, 76(24):245413, December 2007.

(70) C. J. Sahle, C. Sternemann, C. Schmidt, S. Lehtola, S. Jahn, L. Simonelli, S. Huotari, M. Hakala, T. Pylkkanen, A. Nyrow, K. Mende, M. Tolan, K. Hamalainen, and M. Wilke. Microscopic structure of water at elevated pressures and temperatures. *Proceedings of the National Academy of Sciences*, 110(16):6301–6306, April 2013.

(71) Marion Louvel, Amélie Bordage, Cécile Da Silva-Cadoux, Denis Testemale, Eric Lahera, William Del Net, Olivier Geaymond, Jean Dubessy, Roger Argoud, and Jean-Louis Hazemann. A high-pressure high-temperature setup for in situ Raman spectroscopy of supercritical fluids. *Journal of Molecular Liquids*, 205:54–60, May 2015.

(72) Marie Basire, Félix Mouhat, Guillaume Fraux, Amélie Bordage, Jean-Louis Hazemann, Marion Louvel, Riccardo Spezia, Sara Bonella, and Rodolphe Vuilleumier. Fermi resonance in CO $_2$: Mode assignment and quantum nuclear effects from first principles molecular dynamics. *The Journal of Chemical Physics*, 146(13):134102, April 2017.

(73) Marta Marocchi, Hélène Bureau, Guillaume Fiquet, and François Guyot. In-situ monitoring of the formation of carbon compounds during the dissolution of iron(II) carbonate (siderite). *Chemical Geology*, 290(3-4):145–155, November 2011.

(74) S. Huotari, T. Pylkkänen, R. Verbeni, G. Monaco, and K. Hämäläinen. Direct tomography with chemical-bond contrast. *Nature materials*, 10(7):489–493, 2011.

(75) Jeffrey S. Seewald, Mikhail Yu. Zolotov, and Thomas McCollom. Experimental investigation of single carbon compounds under hydrothermal conditions. *Geochimica et Cosmochimica Acta*, 70(2):446–460, January 2006.

(76) Thomas M. McCollom and Jeffrey S. Seewald. Experimental constraints on the hydrothermal reactivity of organic acids and acid anions: I. Formic acid and formate. *Geochimica et Cosmochimica Acta*, 67(19):3625–3644, October 2003.